ANNUAL REPORT 2017

CENTER FOR EXPERIMENTAL NUCLEAR PHYSICS AND ASTROPHYSICS

UNIVERSITY OF WASHINGTON

CENPA

Center for Experimental Nuclear Physics and Astrophysics

Annual Report 2017

University of Washington

ANNUAL REPORT

Center for Experimental Nuclear Physics and Astrophysics
University of Washington
April 1, 2017

Sponsored in part by the United States Department of Energy
under Grant #DE-FG02-97ER41020.

Cover design by Gary Holman. The images show students, postdocs and staff working on one of the many research projects at CENPA.

INTRODUCTION

The Center for Experimental Nuclear Physics and Astrophysics, CENPA, was established in 1998 at the University of Washington as the institutional home for a broad program of research in nuclear physics and related fields. Research activities are conducted locally and at remote sites. The research program emphasis is fundamental symmetries and neutrinos. In neutrino physics, CENPA is the lead US institution in the KATRIN tritium beta decay experiment, the site for experimental work on Project 8, and a collaborating institution in the MAJORANA ^{76}Ge double beta decay experiment. The Muon Physics group has developed the MuSun experiment to measure muon capture in deuterium at the Paul Scherrer Institute in Switzerland. The group has a leadership role in the new project to measure the anomalous magnetic moment of the muon at Fermilab to even higher precision than it is presently known from the collaboration's previous work at Brookhaven. The fundamental symmetries program also includes "in-house" research on the search for a static electric dipole moment in ^{199}Hg, and an experiment using the local tandem Van de Graaff accelerator to measure the electron-neutrino correlation and Fierz interference in ^{6}He decay.

In addition to the research directly supported by DOE's Office of Nuclear Physics through the CENPA core grant, other important programs are located at CENPA, forming a broader intellectual center with valuable synergies. The "Gravity" group, as it is known, carries out with both DOE and NSF support studies of the weak and strong Equivalence Principles, fundamental precepts of General Relativity, as well as searches for non-Newtonian weak forces such as are predicted by theories with extra dimensions. In addition, they participate in advanced LIGO. The DOE Office of High Energy Physics supports a unique experiment, the ADMX axion search. An unusual spin-off from basic nuclear physics is our program on nanopore sequencing, supported by NIH.

Notable

The LIGO Scientific Collaboration, which UW is a part of, was awarded the 2016 Special Breakthrough Prize in Fundamental Physics and the 2016 Gruber Cosmology Prize for the detection of gravitational waves from two black holes colliding over a billion light years away. The UW contribution to Advanced LIGO has been in characterizing charge and pressure noise on the LIGO test masses and in low-frequency seismic isolation using high-precision ground-rotation sensors (NSF support).

Transitions

CENPA Director, Hamish Robertson, is now Professor Emeritus. Peter Doe has assumed the role of US spokesperson for the KATRIN experiment. Fortunately Hamish continues his unique contributions to the KATRIN, Project 8 and TRIMS experiments. David Hertzog has been appointed Interim Director.

Associate Director, Diana Parno, has assumed the position of Assistant Research Professor at Carnegie Mellon University. Her legendary organizational talent and comradeship will be greatly missed. Fortunately Diana will continue her physics input to the KATRIN project and connections to CENPA, having established an active CMU group. Gary Holman has been appointed Acting Associate Director. Research Engineer Hannah LeTourneau, who supported the helium liquifier, left to go to graduate school. Research Engineer Joben Pdersen is now a full-time staff member working on the accelerator and ion source.

Postdoc Clara Cuesta has taken a new position as AIDA2020 postdoctoral fellow at CIEMAT in Madrid, Spain. Postdoc Ana Malagon left the ADMX group in December 2016. She is now in private industry in the Seattle area. Postdocs Walter Pettus and Mathieu Guigue joined the lab this past year. Walter has been working on Project 8 and Mathieu on ADMX.

Graduate students Christian Boutan (ADMX), Michael Murray (MuSun), and Tim Winchester (SNO) completed their theses this past year. Christian will begin a position at Pacific Northwest National Laboratory. Graduate student Julieta Gruszko was awarded a prestigious MIT Pappalardo Fellowship and Graduate student Matthias Smith was awarded a prestigious INFN Fellowship. Julieta will move to Boston and Matthias to Pisa, Italy to start their new positions in early fall, after completing their theses. Finally, Master's students Kerkira Stockton defended her thesis with the Gravity group this March and Diana Thompson defended her thesis in October 2016.

Highlights

- In October, KATRIN achieved a major milestone with Director Robertson among those pressing the "First Light" button to send electrons down the entire length of the KATRIN apparatus.
- As tritium operation approaches for KATRIN, major upgrades to the detector veto hardware and DAQ rate capability have been implemented that will better meet and extend the physics reach of the experiment.
- For newly proposed high-rate measurements with KATRIN, such as a keV-scale sterile neutrino search and an extensive calibration scan of the source properties with a high-intensity e-gun, a new signal shaping filter logic was developed at CENPA and then implemented into the FPGA of the detector readout system. An initial test with an e-gun shows good agreement in performance with the design predictions.
- The KATRIN collaboration adopted the UW-group design of overall analysis structure to integrate detector data, slow-control readings, simulation and statistical analysis, as well as our design for quality assurance and data blinding. The first version of the software suite was implemented at CENPA and is being evaluated by the collaboration. The UW group periodically provides training sessions on KATRIN data analysis to the collaboration.
- The MAJORANA DEMONSTRATOR (MJD) Collaboration has successfully completed construction of the second of the two modules of enriched Ge detectors, and both modules are now running in a completed shield at the Sanford Underground Research Facility in Lead, SD.
- Using data from MJD, we published in PRL a search for low-energy signals from pseudoscalar and vector Dark Matter and other exotic phenomena

- The MJD Collaboration released preliminary results at Neutrino 2016 and Neutrino Telescopes 2017 showing achievement within uncertainty of reaching the primary background goal. The Collaboration is joining forces with their European counterparts, GERDA, to achieve the highest-sensitivity neutrinoless double-beta decay search to date, and to mount a ton-scale experiment, dubbed LEGEND.
- Project 8 has successfully commissioned a Cyclotron Radiation Emission Spectroscopy (CRES) cell with increased gas volume and better signal-to-noise ratio, compatible with first tritium operation. The vacuum manifold to safely handle the tritium gas was built and passed review by the radiation safety committee. The understanding of the rich CRES frequency spectrum is well advanced.
- A new analysis of data from the 3 phases of SNO that makes use of a 30% larger fiducial volume and 18% larger live time with the aid of a new event fitter has been completed. The *hep* neutrino flux is found to be non-zero at more than 95% CL, with a most probable value about 3 times larger than the theoretical prediction.
- We finished analyzing and published our determination of a gamma branch in ^{22}Na aimed at resolving a puzzle, but the puzzle remains after our measurement. The analysis did reveal an interesting story regarding the role of collective motion in ^{22}Na.
- We have two achievements related to our little-a experiment with laser-trapped ^{6}He. We published a careful analysis of the position determination properties of our MCP detector showing 8-μm precision, an important step towards the determination of the $\beta - \nu$ correlation. We also finished our first physics paper, presenting data on the charge distribution of Li ions, a solid benchmark for atomic theory calculations of similar problems.
- We have put together a collaboration and written a proposal for applying the CRES technique developed by Project 8 to measure the ^{6}He beta spectrum. The analysis of systematics uncertainties indicates this could be the most sensitive way of searching for chirality-flipping currents ever proposed.
- The Muon $g-2$ project is 97% complete. Beam commissioning has started and experiment commissioning is schedule for June, 2017. Substantive UW contributions include: muon storage modeling; NMR probes, electronics and DAQ; shimming the precision magnetic field; and, the construction of the full calorimeter system. We are presently designing and installing a set of novel beam imaging detectors to help steer the muons into the storage ring. Six UW Ph.D. students are involved.
- Our $g - 2$ calorimeter subgroup led a third test beam experiment at SLAC, which featured the final designs of the calibration system, calorimeters, readout electronics, waveform digitizers, DAQ, GPU farm, and offline analysis framework. A technical paper is in preparation.
- The UW field group played a leading role in shimming the Storage Ring magnet field to a uniformity that exceeds by a factor of 3 that realized in the BNL E821 experiment. We also developed the instrumentation and measured the radial and longitudinal magnetic field components in the storage ring.

- Our MuSun experiment concluded its data taking on μd capture with a final run at PSI that was focussed on measuring specific systematic uncertainties. With that, our full statistics has been achieved and the necessary corresponding test measurements have been made.

- After reporting a new upper limit on the Hg EDM in 2016, our group has embarked upon an upgrade to the experimental apparatus to both increase its sensitivity and reduce the source of the dominant systematic error.

- The ADMX Gen2 experiment — located at CENPA — began data taking operations with unprecedented sensitivity to axion dark matter.

- The UW LIGO team members successfully installed a second ground-rotation-sensor at the LIGO Hanford Observatory improving its robustness against wind and consequently improving duty cycle for the second observation run.

As always, we encourage outside applications for the use of our facilities. As a convenient reference for potential users, the table on the following page lists the capabilities of our accelerators. For further information, please contact Gary Holman, Acting Associate Director (holman@uw.edu) or Eric Smith, Research Engineer (esmith66@u.washington.edu) CENPA, Box 354290, University of Washington, Seattle, WA 98195; (206) 543 4080. Further information is also available on our web page: `http://www.npl.washington.edu`.

We close this introduction with a reminder that the articles in this report describe work in progress and are not to be regarded as publications nor to be quoted without permission of the authors. In each article the names of the investigators are listed alphabetically, with the primary author underlined in the case of multiple authors, to whom inquiries should be addressed.

David Hertzog, Interim Director   Gary Holman, Acting Associate Director and Editor
Daniel Salvat and Walter Pettus, Technical Editors   Victoria Clarkson, Assistant Editor

TANDEM VAN DE GRAAFF ACCELERATOR

Our tandem accelerator facility is centered around a High Voltage Engineering Corporation Model FN purchased in 1966 with NSF funds, with operation funded primarily by the U.S. Department of Energy. See W. G. Weitkamp and F. H. Schmidt, "The University of Washington Three Stage Van de Graaff Accelerator," *Nucl. Instrum. Methods* **122**, 65 (1974). The tandem was adapted in 1996 to an (optional) terminal ion source and a non-inclined tube #3, which enables the accelerator to produce high intensity beams of hydrogen and helium isotopes at energies from 100 keV to 7.5 MeV.

Some Available Energy Analyzed Beams

Ion	Max. Current (particle μA)	Max. Energy (MeV)	Ion Source
^{1}H or ^{2}H	50	18	DEIS or 860
^{3}He or ^{4}He	2	27	Double Charge-Exchange Source
^{3}He or ^{4}He	30	7.5	Tandem Terminal Source
^{6}Li or ^{7}Li	1	36	860
^{11}B	5	54	860
^{12}C or ^{13}C	10	63	860
*^{14}N	1	63	DEIS or 860
^{16}O or ^{18}O	10	72	DEIS or 860
F	10	72	DEIS or 860
* Ca	0.5	99	860
Ni	0.2	99	860
I	0.001	108	860

*Negative ion is the hydride, dihydride, or trihydride.

Several additional ion species are available including the following: Mg, Al, Si, P, S, Cl, Fe, Cu, Ge, Se, Br and Ag. Less common isotopes are generated from enriched material. We recently have been producing the positive ion beams of the noble gases He, Ne, Ar, and Kr at ion source energies from 10 keV to 100 keV for implantation, in particular the rare isotopes ^{21}Ne and ^{36}Ar. We have also produced a separated beam of 15-MeV ^{8}B at 6 particles/second.

Contents

1 Neutrino Research

KATRIN

1.1 KATRIN status

J. F. Amsbaugh, J. Barrett*, A. Beglarian†, T. Bergmann†, L. I. Bodine, T. H. Burritt, P. J. Doe, S. Enomoto, N. Fong, J. A. Formaggio*, F. M. Fränkle†, F. Harms†, L. Kippenbrock, A. Kopmann†, E. L. Martin, A. Müller†, N. S. Oblath*, R. Ostertag†, D. S. Parno‡, D. A. Peterson, A. W. P. Poon§, R. G. H. Robertson, A. Seher†, D. Tcherniakhovski†, T. D. Van Wechel, K. J. Wierman¶, J. F. Wilkerson¶, and S. Wüstling†

By making a precise measure of the end point of the electron energy spectrum from tritium beta decay, KATRIN will probe the neutrino mass to a planned sensitivity of 200 meV. The experimental technique, drawing on the experiences of several earlier experiments, uses a windowless, gaseous tritium source and two electrostatic spectrometers which measure the electron energy. Initially proposed in 2001, all major components, shown in Fig. 1.1-1, are now in place and in the final stages of commissioning.

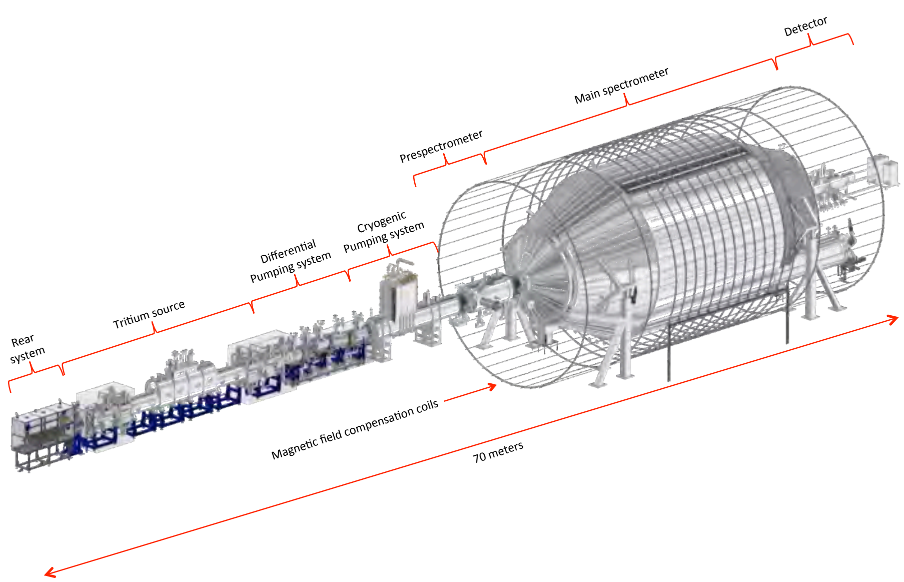

Figure 1.1-1. Arrangement of the principal components of the KATRIN apparatus.

*Massachusetts Institute of Technology, Cambridge, MA.
†Karlsruhe Institute of Technology, Karlsruhe, Germany.
‡Presently at Carnegie Mellon University, Pittsburgh, PA.
§Lawrence Berkeley National Laboratory, Berkeley, CA.
¶University of North Carolina, Chapel Hill, NC.

There have been two data-taking campaigns over the past year: June - August, which focused on studying spectrometer backgrounds and October - December 2016, during which the entire KATRIN beam line was operated for the first time and the focus was on alignment of the beam line components.

The two spectrometers were operated in unison for the first time during the autumn campaign. The pre-spectrometer operates at a potential several hundred volts below that of the main spectrometer in order to prevent the intense flux of lower energy beta electrons from entering and overwhelming the main analyzing spectrometer. This potential difference, in combination with the magnetic flux tube, results in a Penning trap between the two spectrometers. Electrons stored in this trap produce backgrounds through ionization interactions and intermittent discharges. To empty this trap in a controlled fashion, Penning wipers periodically sweep through the trap. The efficacy of this technique to control the trap is reported below. The background in the main spectrometer was a factor of approximately 40 higher than the design goal. After lengthy investigation, the contribution of possible sources has now been quantified and it has been demonstrated that the primary background results from Rydberg atoms distributed throughout the volume of the spectrometer. The origin of this background and the plans to control it are presented below.

On 14th October, with the entire beam line evacuated and the source and transport magnets energized, 'First Light' operation was possible, whereby electrons from a gun placed upstream of the source traveled the entire 70-meter length of the apparatus. This enabled the individual components of KATRIN to be aligned, centering the unobstructed flux tube onto the focal plane detector. The magnetic flux tube passes through cylindrical electrodes positioned along the electron transport system. These electrodes are designed to prevent ions in the source from entering and contaminating the spectrometers. The electron gun, which was also capable of producing ions, demonstrated that the electrodes successfully exclude the ions from the spectrometers, which is a necessary requirement for tritium operation.

1.2 Focal-plane-detector system operation and upgrades

J. F. Amsbaugh, J. Barrett*, A. Beglarian†, T. Bergmann†, L. I. Bodine, T. H. Burritt, P. J. Doe, S. Enomoto, N. Fong, J. A. Formaggio*, F. M. Fränkle†, F. Harms†, L. Kippenbrock, A. Kopmann†, E. L. Martin, A. Müller†, N. S. Oblath*, R. Ostertag†, D. S. Parno‡, D. A. Peterson, A. W. P. Poon§, R. G. H. Robertson, A. Seher†, D. Tcherniakhovski†, T. D. Van Wechel, K. J. Wierman¶, J. F. Wilkerson¶, and S. Wüstling†

The Focal Plane Detector (FPD) system saw approximately 4 months of 24/7 operation during this year's commissioning of the source, transport system, and spectrometers. Over

*Massachusetts Institute of Technology, Cambridge, MA.
†Karlsruhe Institute of Technology, Karlsruhe, Germany.
‡Presently at Carnegie Mellon University, Pittsburgh, PA.
§Lawrence Berkeley National Laboratory, Berkeley, CA.
¶University of North Carolina, Chapel Hill, NC.

the remaining 8 months, maintenance and upgrades of the FPD were performed as described below.

- *Magnet maintenance*: The detector magnet has been operating reliably since 2009. As the magnet must function reliably for another 6 years, the magnet manufacturer replaced the cold head and performed required maintenance. The magnet has since been successfully operated at the nominal field of 3.6 T in conjunction with the 6 T pinch magnet. The current feedthrough plugs on the vacuum cryostat of both the two-year old pinch magnet and the nine-year old detector magnet suffered from overheating. Design issues have been identified, repairs were carried out, and design improvements are being investigated. This is particularly important since a total of eight of these magnets are employed in the KATRIN beam line.

- *Detector resolution*: It has been observed during recent data runs that the FPD energy resolution has degraded since initial commissioning measurements at CENPA and KIT several years ago. To trace the origin of this deterioration, an effort was made to analyze ^{241}Am calibration runs regularly taken during detector operation in order to construct a detailed time evolution of the energy resolution. Although stable during the course of previous measurement phases, the temperature-corrected energy resolution appears to have worsened during specific maintenance breaks in which invasive work was done on the FPD system, including the removal of the detector wafer from the system. A separate noise analysis indicates that a source of parallel resistance, likely located near the detector wafer itself, is responsible for the resolution degradation. To enable further studies of the energy resolution, there is a plan to upgrade a test stand at KIT to allow for additional testing of detector components apart from the FPD system.

- *PAE potential*: The design criteria of the post acceleration electrode (PAE) is to provide up to 30-kV energy to charged particles of either polarity. Since its initial testing in 2010, the PAE cannot exceed approximately 10 kV without suffering high voltage breakdown. This breakdown is independent of the polarity, or the presence of the 3.6-T magnetic field. Using a mock-up of the PAE at UW, visiting KIT students Agnes Seher and Raphael Ostertag identified the problem as being a 'triple junction' resulting from the contact of a conductor (metal foil electrodes) with an insulator (a quartz tube) in the presence of the PAE vacuum. Removing the electrodes from the quartz tubes and performing a glow discharge conditioning of the system allowed 30-kV potentials without breakdown. These tests were not conducted with magnetic fields. The foils were placed over the quartz to remove a Penning trap at the PAE. Removing the foil electrodes will be carried out at KIT to determine if high potentials may be reached without the Penning trap being a problem.

- *Pulcinella tests*: Pulcinella is a titanium disk that can be inserted into the flux tube and illuminated with UV light, providing photoelectrons whose energy can be varied according to the potential applied to the disk. By attaching a femto-ammeter to the disk, the photoelectron current measured by the ammeter can be compared to the electron flux recorded by the detector. The disk may also be used as a 'fire wall' to protect the sensitive detector from unexpected, high current events occurring upstream. If the system is acceptably quiet, then the disk can be retracted, exposing the detector. This was tested with both electrons and ions and Pulcinella was found to be a sensitive monitor that may be used as a bellwether for activities upstream of the detector.

- *DAQ system upgrade*: The Data Acquisition System (DAQ) was designed to operate at a maximum rate of $\sim$ 150 kHz, or about 1 kHz per pixel. This is more than adequate for the region of interest where the rate is not expected to exceed a few mHz. However, to minimize the amount of time spent calibrating the detector and to allow it to be used for investigating the lower energy regions of the spectrum for evidence of sterile neutrinos, it must be capable of higher rate operation without suffering the energy distortions and event counting inaccuracies resulting from event pile-up at high rates. This was achieved by incorporating a second layer of bipolar shaping into the FPGA. The initial results obtained using an electron gun are in good agreement with simulations, indicating that the DAQ can operate at 2 MHz without suffering problems due to event pile-up. These results are described in detail below.

- *Veto upgrade*: The new, simpler and more robust veto system has been operated in its entirety. Final installation of the scintillator end caps will be completed during the next maintenance period. The performance of the system is described below.

- *Alignment and shadowing*: Using the electron gun upstream of the tritium source, the 90-mm diameter sensitive area of the detector was aligned to 1.8 mm of the center of the flux tube. During this exercise it was discovered that the lower segment of the detector appeared to be shadowed. This shadowing was located to a region between the two spectrometers and was initially attributed to the flapper of the valve between the two spectrometers not being fully open. This was found to be not the case. By running the electron gun at a fixed potential of 100 V and applying an adjustable potential to the valve, it was found that only the low energy electrons were being removed, suggesting that the shadowing was due to an electrostatic charging in the region of the valve. Investigations continue, but it is not thought that this will influence the neutrino mass sensitivity.

- *Summary and future*: The FPD continues to perform well for commissioning the KATRIN hardware. The ongoing upgrades and maintenance schedule is expected to meet the needs of tritium running and to allow for initial investigation of additional physics.

1.3 Study of the control of the inter-spectrometer Penning trap

M. Fedkevych*, F. Fränkle†, L. Kippenbrock, D. S. Parno‡, and P. C.-O. Ranitzsch*

A Penning trap is formed by the electromagnetic conditions in the region connecting the KATRIN pre- and main spectrometers. Here, the combination of a strong magnetic field and a positive electric potential well results in the trapping of negative particles. Any low-energy electrons produced between the spectrometers will be confined to the Penning trap, but these electrons can ionize residual gas, producing additional trapped electrons as well as positive ions. Because the main spectrometer is operated at a negative high voltage, the positive ions can be accelerated into the vessel. Here, the positive ions have a probability to ionize residual gas, thereby producing ionization electrons that can reach the detector with energies indistinguishable from the signal beta electrons. Thus, if left undisturbed, the Penning trap will result in the production of an unacceptably high rate of background electrons.

The creation of the Penning trap cannot be avoided as long as both spectrometer vessels are operated at negative high voltage (near -18 kV), which is the designed mode of operation for KATRIN[1]. A mechanical means of emptying the Penning trap has been designed by collaborators at the University of Münster. In 2016, this device was installed on-site in the inter-spectrometer valve, which was built at CENPA. Known as the "Penning wiper", the apparatus consists of a metal rod that can be periodically swept through the magnetic flux tube in order to remove trapped electrons. Three of these Penning wipers were installed in the system. During standard KATRIN operation, it is planned to insert a Penning wiper into the flux tube at regular intervals. However, the optimal frequency of this motion must be determined experimentally.

During First Light measurements in Nov. and Dec. 2016, the inter-spectrometer Penning trap was investigated for the first time. With the main spectrometer set near to its nominal voltage (-18.6 kV), the pre-spectrometer voltage was incrementally ramped while the detector rate was monitored. When the measured detector rate surpassed a pre-defined value, the Penning wiper was automatically inserted in the flux tube. Rate spikes consistent with a filled Penning trap (Penning "discharges") were observed when the pre-spectrometer was ramped to -2 kV (when operating the pre-spectrometer magnets at 80% of their nominal field). At this voltage, several frequency settings for the Penning wiper were also tested. No setting was able to prevent the production of a Penning discharge, but the movement of the wiper into the flux tube was generally able to quench a Penning discharge already in progress.

Additionally, the wiper was also operated in a static configuration in which the wiper was fixed within the flux tube. This mode of operation is not ideal since the wiper obscures a sizable fraction of the flux tube and results in a reduction of the number of usable detector pixels for the neutrino mass analysis. However, measurements taken with the static Pen-

---

*University of Münster, Münster, Germany.
†Karlsruhe Institute of Technology, Karlsruhe, Germany.
‡Presently at Carnegie Mellon University, Pittsburgh, PA.

[1] M. Prall *et al.*, New Journal of Physics, **14**, 073054 (2012).

ning wiper showed no Penning discharges when both spectrometers were operated near their nominal voltage settings.

Since the measurements last year, a few upgrades have been made to the system. The position of the Penning wiper has been adjusted, since run data indicated that the wiper did not previously reach the center of the flux tube. This modification should help to ensure that all trapped electrons will be emptied by the movement of the Penning wiper. Additionally, upgrades to the electronics will allow for the simultaneous operation of all three Penning wipers. Further measurements with the Penning wiper are planned for the next data-taking phase: additional operating conditions to be studied include the effect of an increased magnetic field in the beam line and a lower residual gas pressure (after the planned bake-out of the spectrometer vessels). In preparation for future tests, we have begun to implement routines related to ion transport and scattering in Kassiopeia, the KATRIN simulation code. We have also performed preliminary simulations of the trapped electrons in this region with various pre-spectrometer potential settings.

1.4 Main spectrometer background studies

G. Drexlin*, F. Fränkle*, L. Kippenbrock, M. Kleesiek*, D. S. Parno†, and N. Trost*

A background level of less than 10 millicounts per second is required in order for KATRIN to reach its design sensitivity[1]. However, the observed background rate from the main spectrometer is over an order of magnitude larger than this value. A number of potential background sources have been studied to discover the origin of this background rate.

One background of concern is due to the passage of cosmic ray muons through the walls of the main spectrometer vessel. Simulations indicate that over 35,000 muons pass through the main spectrometer every second[2]. Muons produce secondary electrons when traveling through the steel walls of the vessel. A combination of magnetic and electrostatic shielding has been implemented to limit the effect of secondary electrons emitted from the surface, but only during commissioning measurements could the effectiveness of the shielding be determined. By looking at the correlation and coincidence between muon events (detected via nearby plastic scintillator panels) and FPD electron events, no measurable effect on the background rate could attributed to the cosmic ray muon flux with standard KATRIN field settings. A paper describing the muon background for KATRIN is currently in the final stages of preparation.

The mechanism thought to be responsible for the majority of the observed background in the main spectrometer is due to the implantation of ^{210}Pb in the vessel walls[3]. This

*Karlsruhe Institute of Technology, Karlsruhe, Germany.
†Presently at Carnegie Mellon University, Pittsburgh, PA.

[1] J. Angrik *et al.*, "KATRIN Design Report", 2005.
[2] B. Leiber, "Investigations of background due to secondary electron emission in the KATRIN-experiment", PhD thesis, KIT, 2014.
[3] F. Harms, "Characterization and Minimization of Background Processes in the KATRIN Main Spectrometer", PhD thesis, KIT, 2015.

isotope is a daughter of ^{222}Rn, which is present in ambient air, to which the interior of the main spectrometer was exposed for some time. The decay chain of ^{210}Pb includes the alpha decay of ^{210}Po, which can sputter atoms from the vessel walls. Specifically, this decay seems to cause the expulsion of hydrogen Rydberg atoms from the surface. Rydberg atoms are highly excited but neutral atoms. Their neutrality allows them to bypass the magnetic and electrostatic shielding that blocks most charged particles originating from the vessel walls. Upon entering the volume of the main spectrometer, Rydberg atoms can be easily ionized, even by blackbody radiation, thereby resulting in the production of low-energy ionization electrons that are indistinguishable from signal β electrons.

To verify that the previously mentioned process is responsible for the observed background rate, a measurement was performed by collaborators at KIT in December 2016 in which the Rydberg background was temporarily enhanced using an isotope of lead with a much shorter half-life than that of ^{210}Pb. A ^{228}Th source was connected to the main spectrometer in order to expose the vessel to ^{220}Rn, which causes the implantation of ^{212}Pb in the spectrometer walls, eventually leading to the alpha decay of ^{212}Po on the surface. Assuming that the observed background comes from Rydberg atoms produced following the alpha decays on the surface, one expects to see a sizable increase in the background rate. Indeed, measurements showed an larger background rate, and, more importantly, it was observed that the increased background decayed away at a rate consistent with the half-life of ^{212}Pb. This experimental test, along with other measurements of the spectrometer background, confirms the above-mentioned background model.

The effect of the high background rate on the sensitivity of KATRIN can be largely mitigated by reducing the size of the magnetic flux tube used during neutrino mass measurements and measuring a larger portion of the β electron spectrum near the endpoint. Additionally, there is a plan during the next measurement phase to test the use of a UV light source to irradiate the spectrometer surface and thereby reduce the available hydrogen that can be excited into Rydberg states.

1.5 Electron detection for time-of-flight operation

T. H. Burritt, P. J. Doe, E. L. Martin, D. A. Peterson, R. G. H. Robertson, and T. D. Van Wechel

Implementing a time-of-flight measurement in the KATRIN experiment could allow measurement of the energy spectrum above each retarding potential, instead of only measuring the total rate of electrons above each retarding potential. This could significantly reduce the data collection time required to attain the same statistical uncertainty[1].

In time-of-flight mode the energy of each electron is determined from the time it takes to pass through the main spectrometer. As flight time is mostly determined by the slow movement through the analyzing plane, where the remaining transverse momentum of the electron results in reduced energy resolution similar to high pass filter mode, the energy

[1]Nicholas Steinbrink *et al.*, New J. Phys. **15** 113020 (2013).

resolution in time of flight mode could be nearly as good as the normal high-pass filter mode. The stop signal for time of flight is already available from electron impact on the focal plane detector, but a start signal is still required. The best place for the start signal is between the pre-spectrometer and main spectrometer.

Multiple methods of detecting the passage of an electron have been explored, but none have been found suitable so far. A resonant cavity structure was tested that would exchange energy with the passing electrons through interaction with the cavity's electric field, though the signal-to-noise ratio was too small even averaging millions of events. The signal from the cavities was a change in cavity oscillation amplitude, but it could be either an increase or decrease depending on cavity phase on arrival of the electron. As the method of trying to draw the signal from the noise was straight averaging of the signal, the signal to noise ratio was only improved as the fourth power of the number of events.

An alternate signal filtering scheme was devised that would produce a unipolar signal by sampling at quarter waves of the carrier frequency and taking the sum of the square of the differences half periods apart. A new front end amplifier using pseudomorphic high-electron-mobility transistors (pHEMTs) is being explored. The amplifier is still in the design stage and needs additional refinement; simulations still put the signal to noise ratio at around 10^{-3}. A method of increasing cavity quality by using positive feedback is also being explored as a possible method of improving performance.

Electrons trapped between the main spectrometer and pre-spectrometer would cause backgrounds too large for time-of-flight mode to be implemented. A removal method using a wiper that sweeps across the beam line was constructed and installed in the valve between the pre-spectrometer and main spectrometer. An alternative use of a passing electron detector, which would not require single electron sensitivity, may be to detect filling of the penning trap and trigger-wiper activation.

1.6 Firmware upgrade for high-rate measurements

T. Bergmann*, S. Enomoto, and D. Tcherniakhovski*

In the KATRIN neutrino-mass measurement, the rate of tritium β electrons at the detector is expected to be less than 1 cps (corresponds to $\sim$10 mcps/pixel), and the detector system is optimized for this low rate. For example, the charge-integrating preamplifiers are of the CR discharging type (as opposed to the "reset" type) with a long time constant of 1 ms, and the pulse shaping time is in the range of 1 to 10 μs. If two electrons arrive within the discharging time scale (1 ms), the second one will be affected by the tail of the first one, resulting in a lower estimated energy (tail pile-up). If two electrons arrive within the shaping-time time scale (1 to 10 μs), they will make only one pulse after shaping, resulting in a lower summed-energy and inaccurate electron counting (peak pile-up). If more than two electrons arrive within these time-scales, the behavior is further complicated.

*Karlsruhe Institute of Technology, Karlsruhe, Germany.

Although the expected electron rate for the normal tritium runs is small, the need for high-rate operation has emerged. Calibrations with an e-gun, such as for the tritium gas density measurement and energy-loss measurement, directly benefit from high-rate measurements, and currently measurements at >50 kcps/pixel are proposed. To facilitate a new program to search for keV-scale sterile neutrinos with KATRIN, the apparatus will operate at very low retarding potentials, and the rate at the detector will reach $\sim$ 1 Mcps or more.

Fig. 1.6-1 shows energy spectra of 18 keV electrons from an e-gun at two different per-pixel rates. At a low rate (left; 4 kcps), the energy peak is clear at 18 keV (there is a tiny peak at 36 keV from double-electron bunch from the e-gun) and electron counting is straightforward, although there is some constant contamination of noise events at low energy. At a high rate (right; 150 kcps), tail pile-up broadens and shifts the peak down to $\sim$14 keV, causing detection loss by pushing events below threahold. Peak pile-up causes a plateau-shaped spectrum between $\sim$14 keV and $\sim$32 keV for double-electron events. The overlap of single-electron events and double-electron events at around 14 keV makes electron counting difficult. Another plateau from triple-electron events is also visible above 35 keV (which actually extends from $\sim$14 keV to $\sim$40 keV, according to DRIPS simulation[1]).

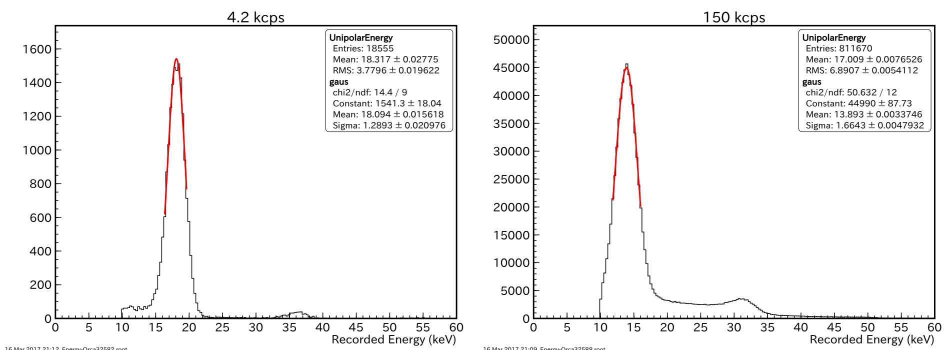

Figure 1.6-1. Energy spectra for 18 keV electrons from an e-gun at a rate of 4 kcps (*left*) and 150 kcps (*right*). Pile-up effects are visible in the high rate spectrum.

The pole-zero cancellation technique, a common remedy for tail pile-up, cannot be used for this case because of multiple A/C couplings between the preamp and the ADC. Using two shapers in parallel, one with a short shaping time and one with a long (nominal) shaping time, is a common construct to reject peak pile-up; however, this is not feasible as our shaping time is limited by the ADC sampling interval and signal-to-noise ratio. On top of that, making a major modification to the current system was not acceptable given that the total detector system had already been thoroughly tested and the KATRIN tritium measurement had been scheduled in two years, as of 2013 when this upgrade was discussed.

We solved these problems by developing a new bipolar shaping (trapezoidal) filter. The filter introduces another differentiation stage (a trapezoidal filter is a kind of differentiation filter) after standard pulse shaping which is "unipolar" in the sense that common CR-(RC)$_n$ filters produce gaussian-like pulse shapes, and the trapezoidal filter, which the KATRIN detector system implements in the FPGA, provides a trapezoidal shape, both of which are

[1]CENPA Annual Report, University of Washington (2013) p. 13.

unipolar (pulses grow only in a more positive direction). Adding another differential stage makes the unipolar pulse bipolar, where one signal makes one positive pulse followed by one negative pulse.

These bipolar pulses do not accumulate (because of vanishing net sum) and therefore no tail pile-up occurs. The time between the positive and negative components of the bipolar pulse depends upon the pulse rise-time, and is sensitive to the presence of multiple signals within one bipolar event. This can be used to resolve peak pile-up. In addition, the implementation of bipolar shaping is purely an addition of another shaping stage and it will not affect the existing system in principle. The downside for this is inflated noise at low rate, which is ∼40% higher in equivalent noise charge (ENC) compared to the optimal unipolar shaping for the same shaping time. Further, compensation for ballistic loss is not straightforward compared to trapezoidal shaping.

Fig. 1.6-2 shows the energy spectra with bipolar shaping for the same data as in Fig. 1.6-1. The upgraded system can record both unipolar-shaped and bipolar-shaped energies for every event. Although the peak at low rate is wider (as predicted), the peak position remains unchanged at high rate. For low rates, we can simply use the unipolar-shaped energy for better energy resolution.

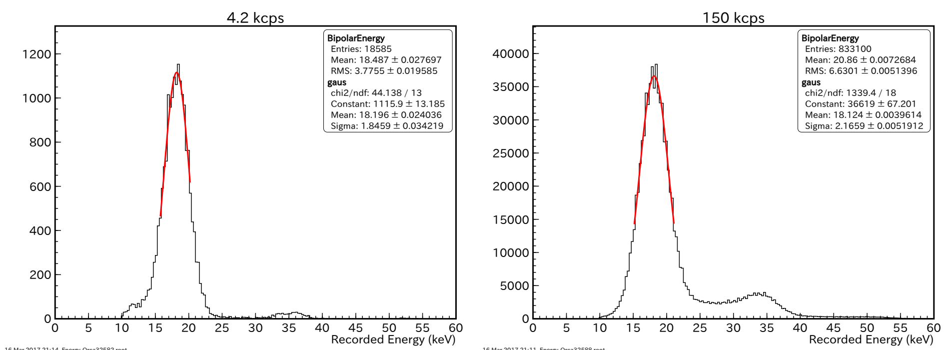

Figure 1.6-2. Bipolar-shaped energy spectra for 18 keV electrons from an e-gun at 4 kcps (*left*) and 150 kcps (*right*), showing that the peak position remains unchanged at high rate.

Fig. 1.6-3 shows a two-dimensional plot of energy and peak-to-valley-time (i.e. the time between the bipolar positive and negative pulses) for 18 keV electrons at 150 kcps (the same dataset as in Fig. 1.6-2 right). The double-electron plateau structure in the energy spectrum (projection to the horizontal axis; equivalent to Fig. 1.6-2, right plot) between 18 keV and 36 keV has a distinguishably large peak-to-valley time at the energy of single-electron peak, ∼18 keV, enabling us to resolve the overlap in the energy spectrum. The well-separated cluster of triple-electron events is also visible on the right side.

Overall, the new bipolar shaping filter behaves exactly as designed, and accurate electron counting is possible with the bipolar filter even above 100 kcps per pixel. Agreement with DRIPS simulation prediction (not shown here) is quite good and our next step is to use the simulation to develop an analysis method for electron counting.

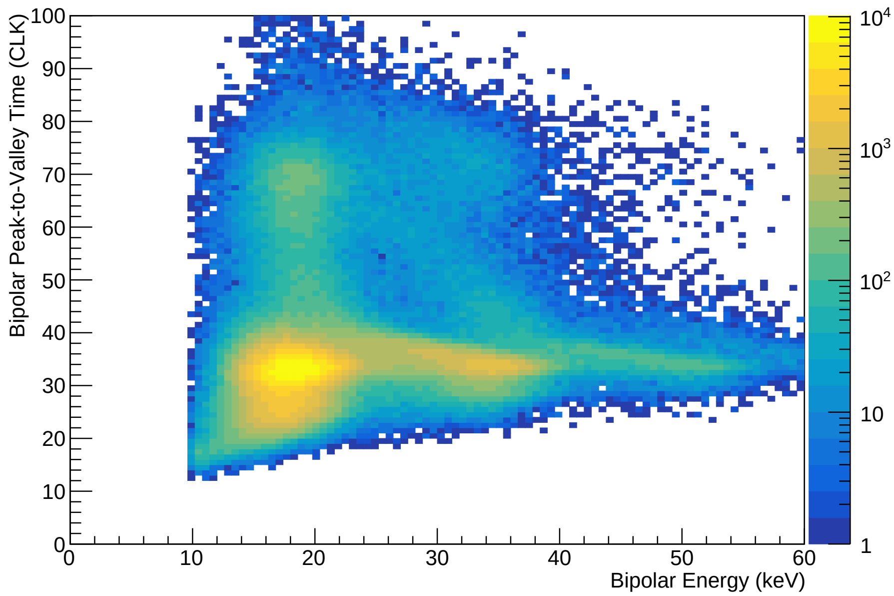

Figure 1.6-3. Peak pile-up separation using bipolar peak-to-valley time, for 18 keV electrons at 150 kcps from an e-gun. The color scale indicates the number of DAQ events per bin for the entire run.

1.7 Progress on veto upgrade

T. H. Burritt, P. J. Doe, S. Enomoto, N. Fong, A. Müller*, D. A. Peterson, and T. D. Van Wechel

The cosmic muon veto for the KATRIN FPD is being upgraded to take advantage of new silicon photo-multiplier (SiPM) models and recent technical advancements from other experiments. The current KATRIN veto yields two to three detected photons per cosmic muon per SiPM, while other experiments typically report much higher numbers such as 20 detected photons per muon per SiPM, even with similar detector construction. Due to the high dark rate of SiPMs at ∼100 kHz, 99% of our recorded data is currently dominated by accidental coincidences from dark noise, even with precise control of the SiPM temperature with Peltier coolers in a box with carefully regulated dry nitrogen flow. An upgrade to a high light-yield system will not only reduce the data size by ∼ 90% but will also improve the system's robustness, stability, and ease of operation by eliminating the cooling system and associated temperature regulation. It will then reduce systematic effects associated with the instability.

The design of the new veto system and the results from prototype tests were reported last year[1]. Based on the demonstrated superior performance (more than an order of magnitude higher light-yield compared to the existing veto), stability (no cooling necessary, stable against

*Karlsruhe Institute of Technology, Karlsruhe, Germany.

[1]CENPA Annual Report, University of Washington (2016) p. 6.

operating condition fluctuations) and robustness (the fibers, the most fragile part of the system, are replaceable even after installation), we produced 12 stave panels, 3 end-cap panels, 6 front-end electronics modules, and 2 controller modules, as well as FPGA firmware and embedded software for control, monitoring, and automated calibration. The system was shipped to KIT in June 2016, then assembled and installed into the detector system. Fig. 1.7-1 shows the installation of the panels and electronics.

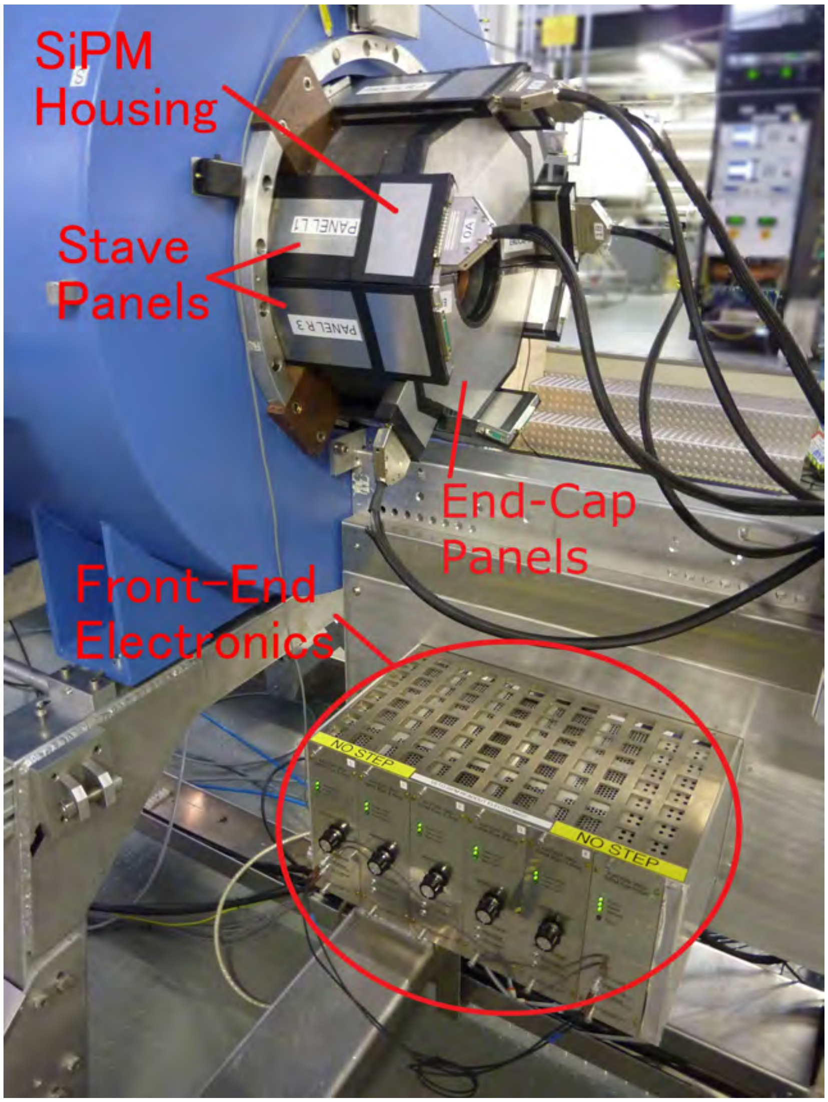

Figure 1.7-1. Installation of the new veto panels and electronics.

Prior to installation, all assembled panels were tested and characterized. Fig. 1.7-2 shows the SiPM hit rates for various coincidence conditions with two stacked stave panels. Neglecting accidental coincidence events, forming coincidences among different SiPMs eliminates SiPM dark hits, as SiPM dark hits are local to each SiPM. If coincidences are formed for SiPMs on different panels, it also eliminates panel-contained events, typically due to environmental γ-rays, and remaining events are only due to through-going cosmic muons (plus the neglected accidentals). As can be seen in Fig. 1.7-2, an ADC threshold of 200 will select almost all cosmic muon events while the contamination from accidental coincidence of SiPM dark hits and environmental gammas can be strongly suppressed.

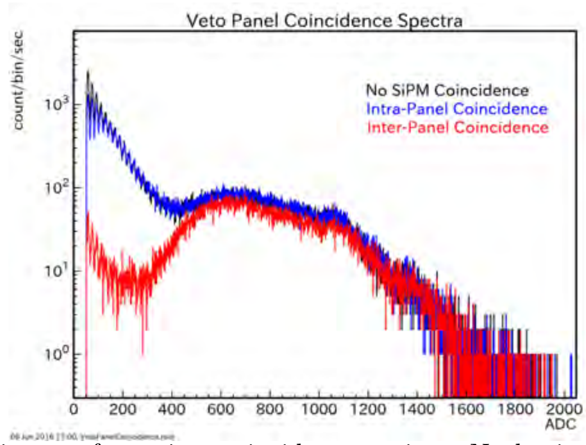

Figure 1.7-2. SiPM hit rates for various coincidence settings. Neglecting accidentals, red is by cosmic muons, the difference between blue and red is from environmental gammas, and the difference between black and blue is by SiPM dark noise. The lower part (ADC<200) of red is due to accidentals.

The per-panel muon detection efficiency and the total event rate with the ADC<200 cut were measured with three stacked stave panels, where the coincidence of the top and bottom panels triggers through-going cosmic muons and the central panel is for evaluation. The result is summarized in Table 1.7-1. Note that the coincidence here is among SiPMs within one panel (central panel), where the panel-contained events such as environmental gammas are not suppressed. Given that the rate in the table is comparable to the actual cosmic muon rate (i.e., the contribution from the other sources does not inflate the data rate), we will record all the intra-panel coincidence events. Inter-panel coincidences will be applied in offline analysis; in this way, optimization of the cut can be performed based on the detection efficiency of the as-installed multi-panel geometry for the actual muon angular distribution, in order to achieve the optimal balance between live-time loss and other background sources.

Table 1.7-1. Per-panel muon detection efficiency and event rates, for various coincidence settings.

Coincidence Threshold	Detection Efficiency (%)	Hit Rate (cps/panel)
1	99.83 ± 0.01	178
2	99.75 ± 0.02	160
3	97.72 ± 0.05	136
4	94.30 ± 0.09	112

During the installation of the detector system, we found that the end-cap panels needed some slight modification to fit into the space. The modified end-cap panels were shipped to KIT in February 2017, and are waiting for the next detector service period scheduled in summer 2017.

1.8 Data quality for the KATRIN experiment

S. Enomoto, L. Kippenbrock, and D. S. Parno*

We are continuing to develop a system to ensure the quality of the data used during the final KATRIN analysis[1]. Our primary goals are to exclude data taken during times when the apparatus is operating out of specification and could introduce unacceptable systematic effects, and to identify data for which special care is necessary in the analysis stage.

In the last year, we have coordinated with the various subsystem task groups to generate a nearly complete draft list of several hundred sensors (out of more than 10,000 in the experiment) whose readings could indicate a critical problem with data quality. In certain cases, the data-quality indicators are not simple sensor readings, but the products of specialized offline analyses; laser Raman spectroscopy results, which give the isotopic composition of the source gas, are a prime example. This list of indicators is the first step toward building a database of data-quality criteria, which cannot be finalized until the completion of commissioning and sensitivity studies for all subsystems.

With other collaboration members, we are leading a task group to draft an overall data-quality policy for the experiment, including sensor categorization and procedures for setting, documenting, and changing validity ranges. Several aspects of the data-quality infrastructure have now been implemented in KATRIN analysis code, including fine-grained, numerical alert levels that could provide early warning of dangerous drifts in operational parameters.

We have also completed a stability study of data-quality indicators in the FPD system, based on a week of data-taking during a summer 2015 commissioning period. Fig. 1.8-1 shows the results for a typical indicator, the current drawn by the front-end electronics on the 8V supply line. Variation over time was quite small, with almost all readback values contained within a range of 1 mA. No correlation of the sensor value with detector rate was observed. We have proposed a fairly wide validity range that would have invalidated only 40 s of data over the weeklong test period.

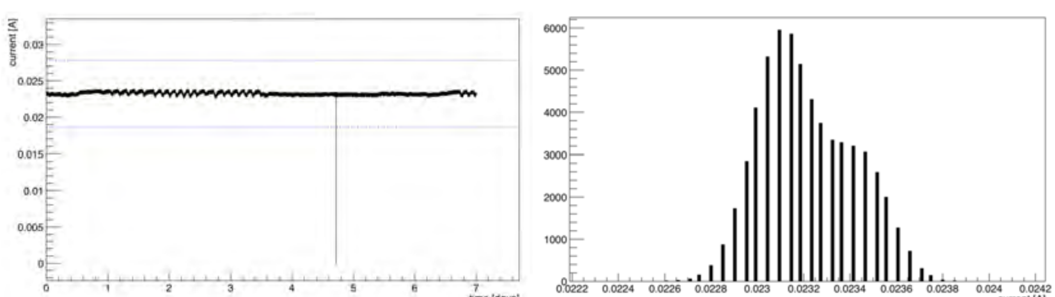

Figure 1.8-1. Stability data for a sensor in the focal-plane detector system, the current drawn by the front-end electronics on the 8V supply line. *Left:* Weeklong time series of readings in Summer 2015; blue dashed lines indicate the proposed validity window. The isolated spike to 0 A is due to a readback error. *Right:* Histogram of current readings.

*Presently at Carnegie Mellon University, Pittsburgh, PA.

[1] CENPA Annual Report, University of Washington (2016) p. 3.

TRIMS

1.9 Status of the Tritium Recoil-Ion Mass Spectrometer (TRIMS)

L. I. Bodine*, T. H. Burritt, C. Claessens†, S. Enomoto, M. Kallander, Y. -T. Lin, E. Machado, R. Ostertag‡, D. S. Parno§, D. A. Peterson, R. F. H. Robertson E. B. Smith, T. D. Van Wechel, and D. I. Will

The Tritium Recoil-Ion Mass Spectrometer (TRIMS) experiment is designed to measure the branching ratio to the molecular bound state ^{3}HeT$^+$ following the β-decay of the molecule T_2[1]. This branching ratio has been predicted by modern molecular final state theories, but the prediction disagrees with experimental results from the 1950s. Many other predictions from the same theoretical framework, however, do agree with the experiments. The TRIMS experiment will use modern instrumentation and analysis methods to re-examine this observable, so that the discrepancy can be addressed. The knowledge of this branching ratio will provided a verification of the theoretical framework which has been applied to describe the final state distribution of the β-decay spectrum measured by KATRIN.

In March 2016, the TRIMS apparatus was moved from the Physics/Astronomy Building to CENPA Hot Lab[2]. We completed the vacuum system reconstruction and reconnected the external electronics. We carried out performance tests for our equipments, such as leak-checking our vacuum system and testing the stability of our magnet power supplies and high-voltage power supply; the system has been stable. We have resumed data-taking with a CAEN DT5720 digitizer and run slow controls with a LabJack12 through the ORCA data-acquisition system[3]. The BEANS and KAFFEE analysis codes from KATRIN[4] were integrated into the TRIMS data-processing chain. We use BEANS to convert data, both the PIPS detector waveform data and slow-control data, from ORCA to ROOT and digitally process the waveforms through a pair of offline trapezoidal filters. We use KAFFEE to upload the processed data to a dedicated server. A new preamp was also designed to improve the resolution of the detectors. Currently, our best PIPS detector has an energy resolution of FWHM $= 2.5 \pm 0.4$ keV, which essentially meets our stringent requirement of FWHM $= 2.3$ keV.

In attempt to mitigate the high-voltage micro-discharges reported last year[2], we made several design changes during the reconstruction. Most importantly, we replaced the stainless-steel internal electrodes with a gold-plated electrode and a negative 100V-biased mesh electrode. The gold-plated electrode on the 60 kV end was designed to reduce the number of ions knocked out by β particles, whereas the mesh on the ground end was designed to prevent

*Departed March, 2016.
†University of Mainz, Mainz, Germany.
‡Karlsruhe Institute of Technology, Karlsruhe, Germany.
§Presently at Carnegie Mellon University, Pittsburgh, PA.

[1]CENPA Annual Report, University of Washington (2013) p. 15.
[2]CENPA Annual Report, University of Washington (2016) p. 12.
[3]CENPA Annual Report, University of Washington (2012) p. 25.
[4]CENPA Annual Report, University of Washington (2014) p. 5.

the secondary electrons produced at ground from being accelerated by the high voltage. The mesh design also removes a Penning trap that arose in the previous design. The assembly work was done in a laminar flow cabinet to assure the requirements for ultra-high vacuum compatibility.

While the performance was significantly better than that achieved in 2015, our high-voltage commissioning revealed that micro-discharges persisted. Analyzing the energy spectrum, we observed that these micro-discharge events resemble proton (or hydrogen ion) events. We therefore performed a glow-discharge cleaning by supplying 3 kV to a decay chamber filled with 2×10^{-2} Torr of argon in order to drive out residual hydrogen on the β electrode. The cleaning removed almost all micro-discharge events, but it also sputtered gold atoms from the electrode to the inside surface of the decay chamber. We replaced the chamber and substituted a bakeout procedure for the glow-discharge cleaning. The bakeout, which should serve to remove residual hydrogen from the entire vacuum system, has been successfully completed. We are preparing for further high-voltage commissioning tests.

1.10 The tritium and ^{83m}Kr gas-handling system for the TRIMS experiment

M. Kallander, Y.-T. Lin, E. M. Machado, D. S. Parno*, and R. G. H. Robertson

The TRIMS T_2 gas-handling manifold was originally designed to diffuse three types of gases through a leak valve into the main vacuum system of the apparatus. The original gas system was a three-legged manifold constructed entirely of VCR4 and VCR8 hardware. T_2 and H_2 were to come from 50 cc cells on two of the legs, and a dry, neutral gas such as Ar or N_2 would come through the third leg from a large compressed gas cylinder. The only means of pumping the manifold was through a leak valve, which was the single point of connection between the vacuum system and the manifold. In the course of using the manifold, this revealed itself to be an unanticipated shortcoming of the gas-handling system.

Additionally, early on in the experiment, it was known that ^{83m}Kr was going to be used as a calibration source of mono-energetic conversion electrons to test the silicon detectors used by TRIMS. It was envisioned that this testing could occur only once, at the very beginning of the experiment, after which the generator would be removed from a leg of the gas manifold. Later, it was decided that TRIMS should have a permanent, in situ ^{83m}Kr generator to allow calibration of the detectors, as well as to allow for mapping of the electric field inside the decay chamber. The generator, previously used by the Project 8 experiment, takes the form of zeolite beads embedded with ^{83}Rb.

The design of the gas-handling manifold has been modified to include this ^{83m}Kr generator, as well as a separate pumping line for the gas manifold. Fig. 1.10-1 shows a diagram of the TRIMS apparatus. The section labeled “Hydrogen Bottle” will eventually be replaced with the T_2 cell. The addition of the section labeled “B” allows the gas-handling manifold to be pumped independently of the main vacuum system. The system is now assembled, pumped,

*Presently at Carnegie Mellon University, Pittsburgh, PA.

baked, and ready to receive T_2. The TRIMS experiment underwent a UW Radiation Safety Office panel review, and was approved for the usage of T_2 and ^{83}Rb.

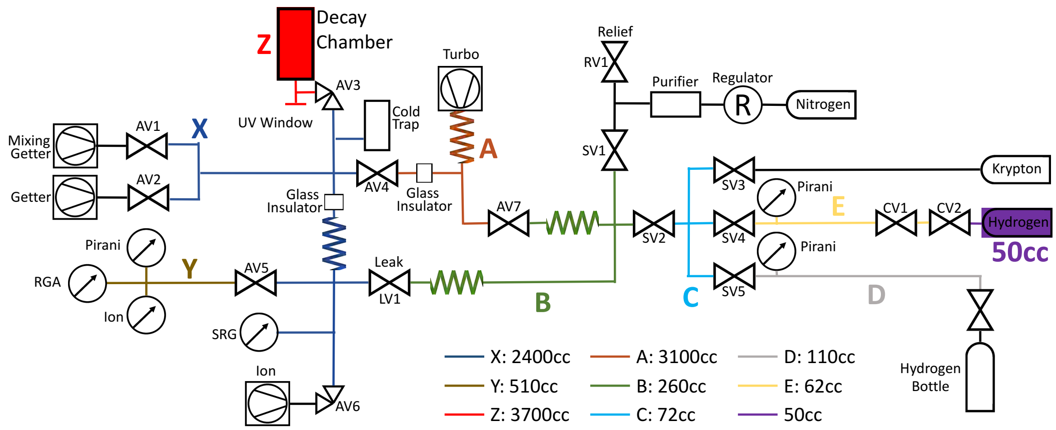

Figure 1.10-1. A schematic diagram of the TRIMS apparatus with calibrated volumes

MAJORANA

1.11 Overview of the MAJORANA DEMONSTRATOR

T. H. Burritt, M. Buuck, C. Cuesta*, J. A. Detwiler, Z. Fu, J. Gruszko, I. Guinn, D. A. Peterson, R. G. H. Robertson, K. Ton†, and T. D. Van Wechel

The MAJORANA DEMONSTRATOR is a neutrinoless double-beta ($0\nu\beta\beta$) decay search employing a 44.1-kg array of high-purity germanium (HPGe) detectors, 29.7 kg of which are enriched in ^{76}Ge. The experiment is currently running at the Sanford Underground Research Facility (SURF) in Lead, SD. The detectors are arranged in strings of 4 to 5 on low-background electroformed copper supports which are then placed in two cryogenic lead- and copper-shielded modules (see Fig. 1.11-2). The primary technical goal of the DEMONSTRATOR is the achievement of a radioactive background of 3 counts/ton/year within a 4-keV region of interest surrounding the 2039-keV Q-value for ^{76}Ge $0\nu\beta\beta$ decay. Such a low background level would justify deeper investment in a much larger ton-scale experiment with sufficient sensitivity to definitively search for $0\nu\beta\beta$ decay for inverted hierarchical neutrino masses.

In the past year, the collaboration completed construction of the second module of HPGe detectors, and the experiment is now running in low-background mode with both modules in a completed shield. The radioassay program instituted to minimize natural radioactivity in MAJORANA detector materials was published in 2016[1]. A first measurement of the total muon flux in the underground laboratory using the MAJORANA DEMONSTRATOR veto system was

*Presently at Centro de Investigaciones Energéticas, Medio Ambientales Y Tecnológicas, Madrid, Spain.
†Departed in June, 2016.

[1] N. Abgrall *et al.*, Nucl. Instr. Meth. Phys. Res. A, **828**, 22-36 (2016).

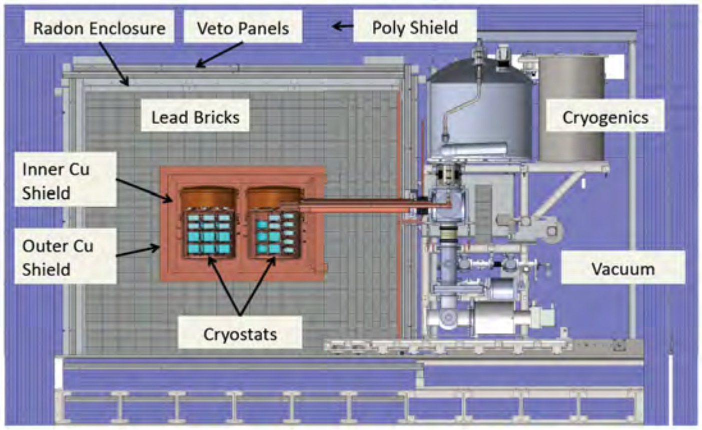

Figure 1.11-2. Schematic of the MAJORANA DEMONSTRATOR apparatus.

recently accepted for publication[1]. More recently we published a search for mono-energetic peaks in our low-energy data (5-100 keV), placing new limits on models of pseudoscalar and vector Dark Matter, solar axions, electron decay, and Pauli Exclusion Principle violation [2]. We have recently submitted a manuscript on our calibration system[3], and are preparing a submission on our enriched germanium processing R&D, as well as a number of other technical topics. We hope to release our first $0\nu\beta\beta$ decay limit in the coming months, and a full analysis of MAJORANA DEMONSTRATOR backgrounds later this fall. We are also preparing for joint analysis activities with the GERDA collaboration; this combination should achieve unprecedented sensitivity for $0\nu\beta\beta$ decay searches. The two experiments are already proceeding with plans to combine to build a larger, ton-scale apparatus, the Large Enriched Germanium Experiment for Neutrinoless $\beta\beta$ Decay ("LEGEND").

1.12 Summary of recent results from the MAJORANA DEMONSTRATOR

M. Buuck, C. Cuesta*, J. A. Detwiler, Z. Fu, J. Gruszko, and I. Guinn

The MAJORANA DEMONSTRATOR was finished with assembly in 2016. The first module came online after the 2015 rework on December 31st, 2015 and the second module came online in August 2016. Both modules took data from August 25$^{\text{th}}$ to September 27$^{\text{th}}$ 2016 in order to establish the region-of-interest (1900 keV to 3000 keV) background for Critical Decision 4 (CD4). The background in this region is predicted to be independent of the energy, so it is used to determine the projected background for the neutrinoless double-beta ($0\nu\beta\beta$) decay region-of-interest (ROI), which is a small window around the $Q_{\beta\beta}$ -value of 2039 keV. Because the modules were constructed and commissioned independently, each module used separate data acquisition systems and the data were kept separate and analyzed independently. Data

*Presently at Centro de Investigaciones Energéticas, Medio Ambientales Y Tecnológicas, Madrid, Spain.

[1] N. Abgrall *et al.*, Astropart. Phys. **0927-6505** (2017).
[2] N. Abgrall *et al.*, arXiv:1612.00886 [nucl-ex], to appear in Phys. Rev. Lett. (2017).
[3] N. Abgrall *et al.*, arXiv:1702.02466 [nucl-ex] (2017).

from Module 1 is labeled as Dataset 3 and data from Module 2 is labeled as Dataset 4. After analysis of these datasets showed no major problems with the running of both modules, we unified their DAQ systems and are now acquiring only one dataset at a time.

Summary statistics of Datasets 3 and 4

Dataset 3 was acquired over a period of 32.37 days, of which 31.67 days was live (97.8%). Of that livetime, energy calibration of Module 1 or 2 took up 1.18 days and disruptive commissioning tests took up 0.57 days, with the remaining 29.91 days devoted to the $0\nu\beta\beta$-decay search and background level estimation.

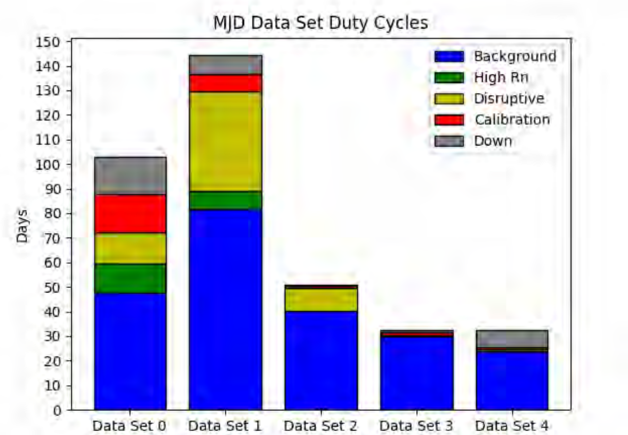

Figure 1.12-1. Duty cycles of all complete datasets taken so far with the MAJORANA DEMONSTRATOR. Datasets 0, 1, 2, and 3 are with Module 1 only and Dataset 4 is with Module 2 only. Datasets 3 and 4 were acquired simultaneously and are used in this analysis.

Of the livetime devoted to the $0\nu\beta\beta$-decay search, some fraction is lost to a few sources of deadtime. In Dataset 3, 0.0025 days were lost due to dead time during the periodic ($\sim$ 0.1 Hz/detector) firing of the pulser system. This pulser is implemented primarily to ensure that the detectors remain live during data collection. A further 0.0127 days were cut by the muon veto, and 0.0003 days were lost due to rare events such as digitizer channel dropout. Finally, removal of junk waveforms from the acquired data (pulser retriggers, transient electronic noise, etc.) has an estimated efficiency to retain events in the ROI of 0.9995. This leaves effectively 29.88 days live for Dataset 3. The duty cycles of all complete datasets acquired so far are shown in Fig. 1.12-1.

Module 1 contains 20 detectors enriched to approximately 88% ^{76}Ge and 9 detectors made from natural Ge. Of the enriched detectors, 16 are used in this analysis and have a combined active mass of 12.63 $\pm$ 0.19 kg, while 4 of the natural detectors are used in this analysis and have a combined active mass of 2.79 $\pm$ 0.06 kg. Multiplying the enriched active mass by the livetime for Dataset 3 gives the exposure used to determine the background level for CD4: 377.41 kg-days.

The Dataset 4 exposure is computed in the same way as the Dataset 3 exposure. Dataset 4 was live for 25.65 days (79.3%), with 1.17 days calibrating, 0.78 days commissioning, and 23.69 days taking $0\nu\beta\beta$ data. After subtractions for pulsers, the muon veto, channel dropout, and the data cleaning framework efficiency, the total livetime for DS4 is 23.57 days. Module 2 contains 15 enriched (with 7 used in DS4) and 14 natural (with 7 used in DS4) detectors for a total active mass of 5.47 ± 0.08 kg enriched and 3.95 ± 0.09 kg natural. These values produce an exposure of 128.85 kg-days for Dataset 4.

Background level of Datasets 3 and 4

Several standard cuts are applied to the data before generating a final spectrum. First, only events occurring in a single detector are retained, because $0\nu\beta\beta$-decay only occurs in one detector at a time. Some detectors are not fully depleted and so are only used to veto events with high multiplicity; these are removed from the analysis. Any waveform that is tagged as "junk" by the data cleaning process is removed, and every event tagged as simultaneous with a cosmogenic muon interaction by the muon veto is also removed. A tag called A vs. E that identifies events interacting multiple times within a single detector is also applied and tagged events are removed. Finally, the delayed-charge-recovery (DCR) tag (Sec. 1.13) is applied. This tag identifies degraded alpha particle interactions along the passivated surfaces of the detectors by detecting the delayed collection of the electrons liberated in the interaction. After all of these tags are applied and the tagged events are removed, 2 events remain in Dataset 3 between 1900 keV and 3000 keV. This corresponds to an expected background of $0.16^{+0.18}_{-0.10}$ counts/kg/month using Feldman-Cousins[1] errors. In Dataset 4, zero events remain after applying these cuts, which gives an expected background of $0^{+0.31}_{-0}$ counts/kg/month. A histogram showing the energy spectrum of the sum of Dataset 3 and Dataset 4 is shown in Fig. 1.12-2.

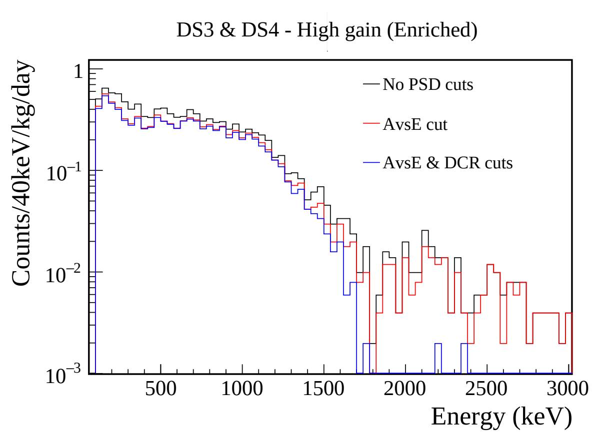

Figure 1.12-2. Full energy spectrum for sum of DS3 and DS4. The black line is the spectrum with all cuts except for A vs. E and DCR applied. The red line is the spectrum with all cuts except for DCR applied, and the blue line is with all cuts applied.

[1] *Unified approach to the classical statistical analysis of small signals*, Gary J. Feldman and Robert D. Cousins, Phys. Rev. D **57**, 3873 (1998).

This can be compared to the background measured in Dataset 1, which was taken with the same module before the copper external radiation shield was fully installed. In Dataset 1, we obtained a projected background of $0.24^{+0.18}_{-0.10}$ counts/kg/month. The energy spectra from Dataset 1, Dataset 3, and Dataset 4 obtained after applying all cuts are shown overlaid in Fig. 1.12-3. The result from Datasets 3 and 4 can also be compared to the Department of Energy's Optimal Performance Parameter goal for background which was 0.6 counts/kg/month after all cuts. We also had an internal design goal of 3 counts/ton/year in the small ROI around $Q_{\beta\beta}$ (2039 keV). In those units, the result from DS3 is $5.1^{+5.7}_{-3.2}$ counts/ton/year and the result from DS4 is $0^{+8.6}_{-0}$ counts/ton/year in the 2039 keV ROI. The combined dataset gives a rate of $3.7^{+4.1}_{-2.3}$ counts/ROI/ton/year. As more data is collected, we will obtain a more precise measurement of our background levels, and will eventually be able to determine whether or not we have hit our goal of 3 counts/ROI/ton/year. As most of the events near the ROI appear to be from degraded alpha-particle interactions, our background could potentially be further reduced by improving pulse-shape or other kinds of tags of those events. It is also important to understand the ultimate source of these particles so that they can be better mitigated in a future experiment.

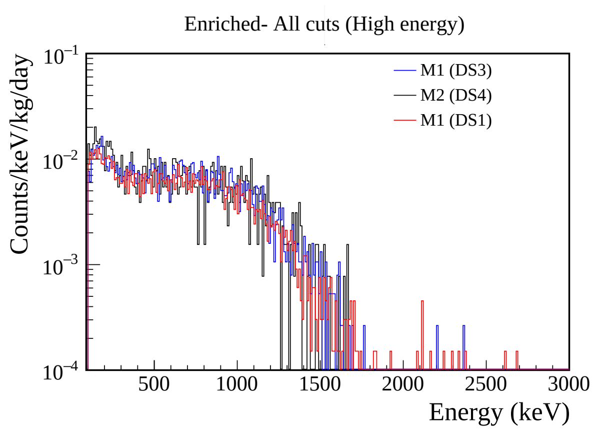

Figure 1.12-3. Comparison of energy spectrum for DS1 (Module 1 only), DS3 (Module 1 only), and DS4 (Module 2 only). Of particular interest is the significant reduction in activity near the $0\nu\beta\beta$ region-of-interest from DS1 to DS3 and DS4.

1.13 Alpha particle discrimination and TUBE

T. Bode*†, M. Buuck, C. Cuesta‡, J. A. Detwiler, J. Gruszko, I. Guinn, S. Mertens*†, and M. Willers*

Alpha particles pose a problematic background in large granular detector arrays, particularly those alphas that originate from Rn progeny that plate out on the detector surfaces during manufacturing and assembly. The geometry of the p-type point contact (PPC) detectors

*Technical University of Munich, Munich, Germany.

†Max Planck Institute, Munich, Germany.

‡Presently at Centro de Investigaciones Energéticas, Medio Ambientales Y Tecnológicas, Madrid, Spain.

implemented in the MAJORANA DEMONSTRATOR make the DEMONSTRATOR relatively insensitive to alphas, with the exception of a contribution coming from the passivated surface between the point contact and outer dead layer. In this region, the response to alphas is difficult to characterize. The charge collection properties near this surface can differ for different detector models. In the MAJORANA DEMONSTRATOR, events have been observed in which alphas incident on or originating from this surface are significantly degraded in energy, leading to a potential background contribution in the ROI for $0\nu\beta\beta$.

However, it is also observed that charge mobility is drastically reduced on or near the passivated surface, and is slowly released on the timescale of waveform digitization, leading to a measurable change in slope of the tail of a recorded pulse. It is expected that this effect is due to surface propagation of the electron contribution to the signal, while the holes are collected normally. This matches the model developed by Mullowney *et al*[1]. Using a filter that can identify the occurrence of this delayed charge recovery (DCR), these events can be identified, allowing for the efficient rejection of passivated surface alpha events in analysis.

Validating this model and fully characterizing the alpha interaction rejection efficiency of such a filter requires alpha source scans of the specific detector geometries used. To that end, the CENPA group has collaborated with the GERDA and MAJORANA groups at Technical University of Munich (TUM) to rebuild and adapt an existing alpha-source scanner. This internal scanning cryostat, the TUM Upside down BEGe (TUBE) experiment, is currently being used to take an alpha source scan of a MAJORANA detector. The early results from these measurements have confirmed our model of alpha interactions and validated the use of the DCR pulse shape discrimination technique.

The Delayed Charge Recovery (DCR) Cut for Alpha Particle Interactions

An alpha interaction cut, which identifies waveforms with a low-mobility charge component like those of Fig. 1.13-1, was developed in 2016 using commissioning data from Module 1 of the DEMONSTRATOR. Based on the results of signal-to-background optimization studies of these commissioning runs, it has been implemented with a single-site bulk (gamma and double-beta decay) event acceptance efficiency of 90% $\pm$ 4.1%. The bulk acceptance is determined using calibration spectra. The uncertainty in the acceptance is driven by pulse shape deviations, and is quantified by comparing the acceptance in the ^{228}Th double-escape peak (a known sample of single-site events without significant charge loss) to the acceptance over a range of energies. A new version of the DCR discriminator, which corrects for the effect of charge trapping in the detector bulk and thus reduces this systematic uncertainty, has been developed and is currently being tested.

[1] P. Mullowney, M. C. Lin, K. Paul, *et al*, NIM A, **662**, 1 (2012) 33-44.

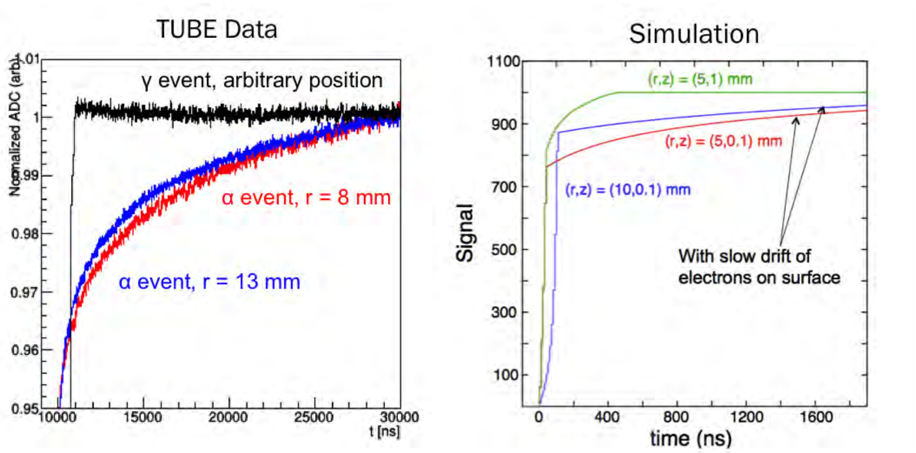

Figure 1.13-1. *Left:* Sample average normalized TUBE waveforms with pole-zero (pulse decay) correction. Waveforms are from alpha source scans with the source incident on the detector surface at different distances (r) from the point-contact, in red and blue, and from a run without the alpha source incident on the detector, in black. The alpha event waveforms show a slow component contribution from the drift of charge along the passivated surface, which is used to identify these events. The shape of the waveforms closely matches that predicted in simulations. *Right:* Sample simulated waveforms, incorporating passivated surface drift of electrons. The interactions originate at different radii (r) and depths (z) in the detector, with (r,z) = (0,0) mm being the center of the point-contact.

The use of the DCR discriminator in the MAJORANA DEMONSTRATOR data sets reduces the rate of background events in the $0\nu\beta\beta$ region-of-interest by a factor of 25 (Sec. 1.12). Further improvement is expected from the switch to data-taking incorporating multisampling, which will allow longer waveforms to be recorded, and from future improvements to the DCR analysis.

Characterizing Alpha Interactions with TUBE

Given the importance of the DCR discriminator to the MAJORANA DEMONSTRATOR's results, the decision was made to scan a MAJORANA detector using the existing TUBE scanner[1] while continuing preparations to build a similar scanner at CENPA. The TUBE scanner was adapted to accept the dimensions and IR-shine sensitivity of PONaMA-1, a natural-abundance detector made by ORTEC for the MAJORANA Collaboration that has the same geometry as the ^{76}Ge-enriched detectors currently taking data in the MAJORANA DEMONSTRATOR. In February 2017, a spectral-grade ^{241}Am source was installed in the system and high-quality data-taking began.

Analysis of the TUBE scanning data has begun, and early results (see Fig. 1.13-2) confirm that the DCR parameter identifies alpha event waveforms effectively at a range of radial scanning positions, even when the events cannot be clearly identified by their energy. The

[1]M. Agostini, Dissertation, Technical University Munich (2013).

waveforms of TUBE alpha scan events confirm the interaction model used in our simulations (see Fig. 1.13-1).

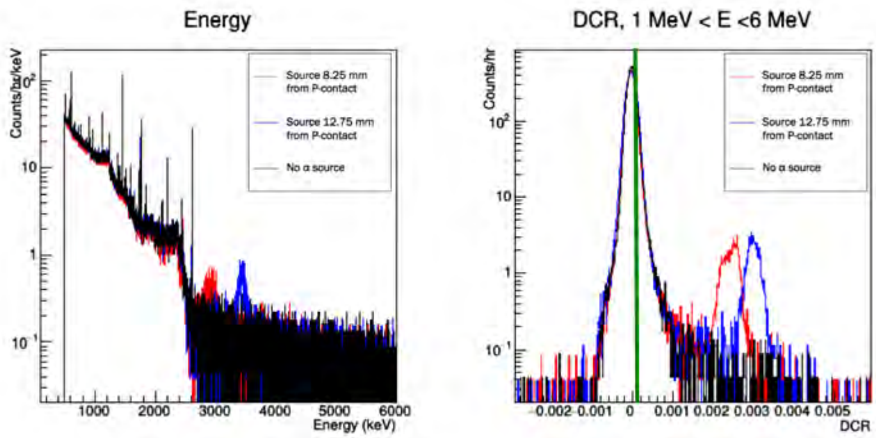

Figure 1.13-2. Data from TUBE taken without the alpha source incident on the detector, in black, with the source incident on the passivated surface 8.25 mm from the point-contact, in red, and 12.75 mm from the point-contact, in blue. *Left:* Energy spectra taken with TUBE. The energy of the alpha peak increases with increased scanning radius, as is expected if the electrons are the primary source of delayed charge. *Right:* The DCR distribution in TUBE. The 90% DCR cut falls at the green line; events falling to the right of this line are rejected. Alpha scan distributions show a clear excess of events at high values of DCR.

1.14 Searching for $2\nu\beta\beta$ to excited states

T. H. Burritt, M. Buuck, C. Cuesta*, J. A. Detwiler, Z. Fu J. Gruszko, I. Guinn, D. A. Peterson, R. G. H. Robertson, and T. D. Van Wechel

While $2\nu\beta\beta$ from ^{76}Ge to the ground state of ^{76}Se has been observed, the same decay into an excited state of ^{76}Se has not yet been seen. The MAJORANA DEMONSTRATOR is searching for $2\nu\beta\beta$ to excited states in ^{76}Ge. There are three possible excited state decay modes allowed, as shown in Fig. 1.14-1. Due to the reduced Q-values of these modes, these modes have much longer half-lives than the ground state mode. The $0^+_{\text{g.s.}} - 0^+_1$ decay has the shortest half-life of all the excited state decay modes, expected to be between 1.2×10^{23} yrs $- 6.7 \times 10^{24}$ yrs. The excited state decay modes are accompanied by at least one γ-ray each (at 559.1 keV and 563.2 keV for $0^+_{\text{g.s.}} - 0^+_1$). These photons give the excited state decay modes a unique signature that reduces their backgrounds significantly, making detection by the DEMONSTRATOR feasible. A candidate event would be a multi-detector event, with at least one event falling in a region of interest around the 559.1-keV and 563.2-keV γ energies. Recognizing these events requires identification of multi-detector coincidence events and proper calibration of the detectors.

The MAJORANA event builder is the software that detects coincidence events. The event

*Presently at Centro de Investigaciones Energéticas, Medio Ambientales Y Tecnológicas, Madrid, Spain.

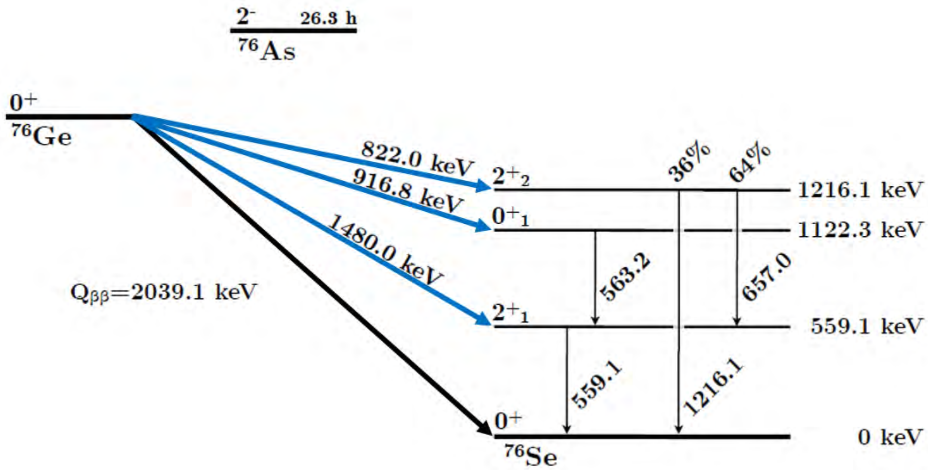

Figure 1.14-1. Level diagram for $2\nu\beta\beta$ in ^{76}Ge. The $0^+_{\mathrm{g.s.}} - 0^+_1$ mode is the most common excited state decay.

builder is responsible for converting raw binary files produced by the ORCA DAQ software into ROOT files that are usable by the Majorana Demonstrator anaylsis software. The builder also detects and removes waveforms that have been corrupted. Finally, the builder combines waveforms from multiple detectors that are nearby in time into events. In the last year, the event builder has been upgraded in order to support multi-sampled waveforms from the Gretina digitizers. These digitizers use different sampling rates for the baselines and the falling edge of the waveform than the rising edge, enabling a longer timing window for each waveform without sacrificing information useful for discriminating multi-site events. The event builder has also been upgraded to support ORCA's quick start mode, which enables dead-time free data collection. The event builder is currently being used to process all of the data for the Majorana Demonstrator.

The Majorana Demonstrator's detectors are calibrated using γ-ray peaks from a ^{228}Th line source. The spectral lines from these peaks are fit to a peakshape function that is the sum of a gaussian component, low- and high-energy exponentially modified gaussian tail components, and a step component. Multiple peaks from a calibration spectrum are simultaneously fit, with the peakshape parameters describing the calibration constants and resolution as functions of peak energy. The results of such a fit are shown in Fig. 1.14-2. This technique enables the fitting of small spectral peaks that would not converge if fit on their own. More peaks allows easier study of calibration systematics, such as nonlinearities in the digitizer response. The simultaneous fit is performed using an adaptive Hybrid Monte Carlo (HMC) algorithm. HMC is a gradient-based Markov Chain Monte Carlo (MCMC) technique, which has a convergence time that scales well with number of correlated parameters compared to other MCMC methods. This is necessary due to the large number of parameters, many of which experience strong correlations, involved in a simultaneous fit.

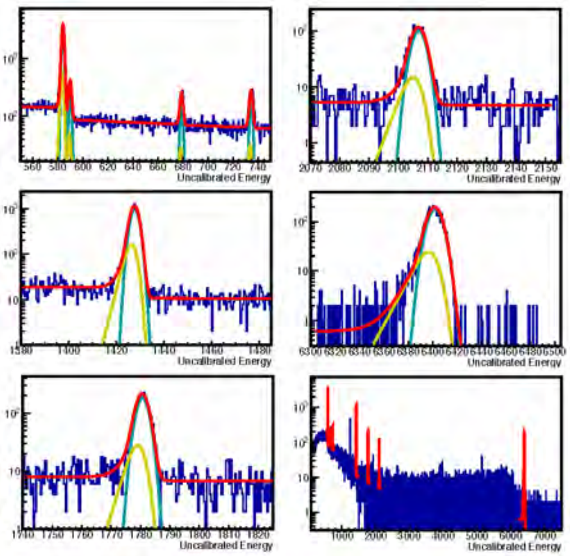

Figure 1.14-2. The results of the multipeak fitter run on uncalibrated data. Peaks were fit using the Gaussian (teal) and low-energy tail (gold) components. Peaks were fit at 238.6 keV, 241.0 keV, 277.4 keV, 300.1 keV, 583.2 keV, 727.3 keV, 860.6 keV, and 2614.5 keV.

Project 8

1.15 Status of the Project 8 neutrino-mass experiment

A. Ashtari Esfahani, S. Böser*, R. Cervantes, C. Claessens*, L. de Viveiros†‡ P. J. Doe, S. Doeleman§, M. Fertl, E. C. Finn‖, J. A. Formaggio¶, M. Guigue‖, K. M. Heeger**, A. M. Jones‖, K. Kazkaz††, B. H. LaRoque†, A. Lindman*, E. Machado, B. Monreal‡‡†, J. A. Nikkel**, N. S. Oblath¶‖, W. Pettus, R. G. H. Robertson, L. J. Rosenberg, G. Rybka, L. Saldaña**, P. Slocum**, J. R. Tedeschi‖, T. Thümmler§§, B. A. VanDevender‖, M. Wachtendonk, M. Walter§§, J. Weintrub§, A. Young§, and E. Zayas¶

Project 8 is an effort toward an improved neutrino mass determination by measuring the frequency of the cyclotron radiation emitted by tritium beta decay electrons spiraling in a magnetic field. The technique, called Cyclotron Radiation Emission Spectroscopy (CRES),

*Institut für Physik, Johannes-Gutenberg Universität Mainz, Germany.
†University of California, Santa Barbara, CA.
‡Pennsylvania State University State College, PA.
§Harvard-Smithsonian Center for Astrophysics, Cambridge, MA.
‖Pacific Northwest National Laboratory, Richland, WA.
¶Massachusetts Institute of Technology, Cambridge, MA.
**Yale University, New Haven, CT.
††Lawrence Livermore National Laboratory, Livermore, CA.
‡‡Case Western Reserve University, Cleveland, OH.
§§Institut für Kernphysik, Karlsruher Institut für Technologie, Karlsruhe, Germany.

combines the rich history of single-electron trapping with high precision frequency analysis techniques to provide a unique avenue to high resolution electron spectroscopy. The project is organized into four phases to reach the anticipated sensitivity to the neutrino mass of 40 meV.

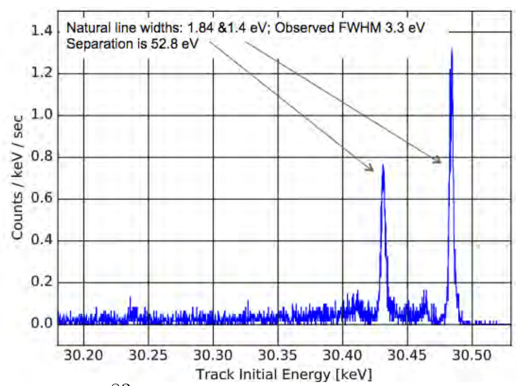

Figure 1.15-1. Spectrogram of the ^{83m}Kr lines at 30.4 keV demonstrated resolution of 3.3 eV approaching the natural line widths[1].

The publication of a high resolution ^{83m}Kr conversion electron spectrum (Fig. 1.15-1) spanning over the K, L, M, and N shells of krypton marked the success of phase I of the experimental effort[1]. This was the first demonstration of the CRES technique. More sophisticated analysis schemes are being developed to facilitate more accurate energy reconstruction[2].

Building on the success of phase I, an upgraded tritium compatible cell was developed and built. The new cell, shown in Fig. 1.15-2, is based on a waveguide with a circular cross section increasing both the signal-to-noise ratio and effective volume of the system. The magnetic trap consists of five "z^2" coils, which can act independently as harmonic traps, or in concert to form a broad flat region with pinches at the end (termed a "bathtub" trap). To probe the magnetic field generated by the trapping coil, a new Electron Spin Resonance (ESR) magnetometer has been installed on the insert. The new insert was installed last summer and is currently being commissioned with conversion electrons from ^{83m}Kr. Later, the cell will be filled with molecular tritium gas.

The microwave background noise in the phase II experiment has also vastly improved compared to phase I, as can be seen in Fig. 1.15-3. Installation of a cryogenic circulator prevents the amplifier noise from being reinjected into the cell. As a result, the overall noise level for the apparatus has decreased. The new circulator has also smoothed noise oscillations by terminating the standing wave in between the first amplifier and waveguide short, which was placed at the bottom end of the waveguide to increase the SNR level by reflecting electron signal back to amplifiers.

Another phase II milestone was the development of a tritium handling system. The gas-handling manifold, initially constructed at Yale University, allows the safe handling of the

[1]D.M. Asner *et al.*, Phys. Rev. Lett. 114, 1162501 (2015).
[2]A. Ashtari Esfahani *et al.* J Phys. G. 44 054004 (2017).

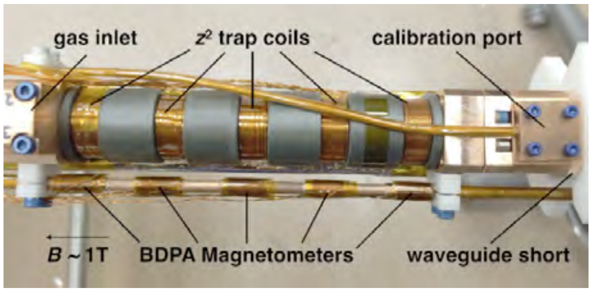

Figure 1.15-2. Phase II cell with five trapping coils and ESR probes. The gas will be loaded into the cell through the gas inlet. The calibration port is also being used to inject signals into the waveguide for calibration purposes. This cell is compatible with both Krypton and Tritium data taking.

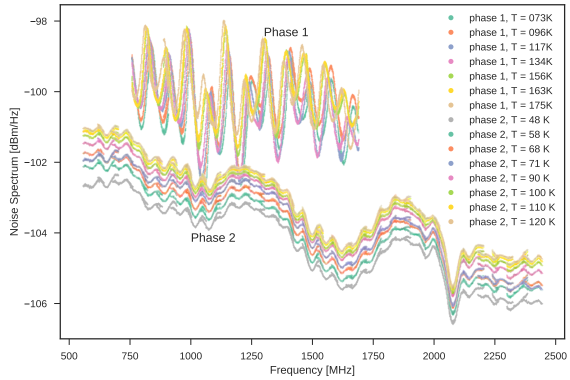

Figure 1.15-3. Noise level comparison between phase I and II over a frequency band of 2 GHz. Each curve in the plot represents the noise power at a specific temperature. The direct relation between the noise level and temperature is apparent in the plot. The phase II apparatus has also demonstrated a clear reduction in both noise level and its oscillation.

tritium gas. In addition, it provides an ^{83m}Kr calibration source of monoenergetic conversion electrons with energies near the tritium β-decay end point. The design of the system was modified such that the gas-handling system would attach to the existing Project 8 phase II apparatus. Project 8 underwent a UW Radiation Safety Office review panel of the gas-handling manifold and received permission to use T_2. The gas manifold will contain a 2 Ci inventory of T_2 and 5 mCi inventory of ^{83}Rb which serves as a generator for the ^{83m}Kr. The new system also has the capability to be used in phase III (Fig. 1.15-4).

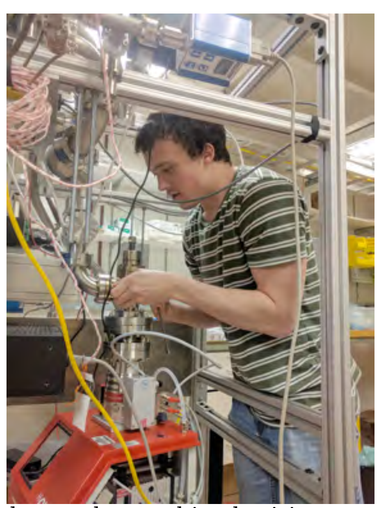

Figure 1.15-4. Evan Zayas works on the combined tritium and krypton gas system. This system will be used to source and probe both krypton and tritium in the system. It has been designed for use in both Phase II and III of the experiment.

One of the current efforts of the Project 8 collaboration is the integration of a more sophisticated data acquisition system with a significantly higher trigger rate and a multi channel approach that can be extended to the phase III and IV data acquisition requirements. For this purpose the collaboration is currently commissioning a ROACH2 board (Reconfigurable Open Architecture Computing Hardware) which was developed for antenna arrays in radio astronomy. On the ROACH2 board, the incoming signal is digitized at 3.2 GSPS (after the signal has been downsampled by 24.2 GHz). The signal is then fed to an FPGA with three band widths that can be individually tuned to different central frequencies. Following down-conversion, the signal is split and its Fourier transform is computed. Both the time- and frequency domain representation of the signal are then streamed to a server via 10 GbE. With this combination of real-time Fourier transform computation and fast data packet reception and processing on the server it is possible to operate either in streaming or triggered mode with no dead-time.

Since January 2017 the ROACH2 is connected to the analog signal of the Project 8 experiment and first sets of data have been acquired using the streaming mode of the DAQ software. Fig. 1.15-5 shows 1 second of data with many electron tracks visible. This data has an event rate of a few tracks per second, which could not be recorded with the former Real-time Spectrum Analyzer due to its long dead time and high trigger threshold.

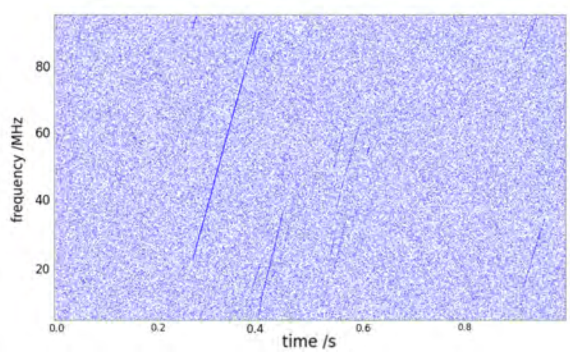

Figure 1.15-5. One second of data recorded by the new DAQ system, ROACH2. The spectrogram shows the power in each bin of time and frequency. The lines of higher power are the signal from individual electrons.

Phase III planning efforts are underway and will require a larger volume of magnetic field, which requires a new method for harvesting the microwave signal using a phased array of antennas. With the larger instrumented volume we can achieve a neutrino mass sensitivity $m_\nu < 2$ eV, competitive with current limits from Mainz[1] and Troitsk[2]. To acquire the necessary statistics over a period of one year, we estimated a required volume of 200 cm^3. It is therefore not practical to conduct this experiment in an enclosed waveguide detector as in phases I and II. For phase III, Project 8 must enlarge its tritium volume so that trapped electrons will emit cyclotron radiation into free space. A used MRI magnet has been acquired and is on site to accommodate the larger experiment, with an open bore of 90 cm.

[1]C. Kraus *et al.* 2005 Eur. Phys. J.C 40:447 (2005).
[2]V.N. Aseev *et al.* Phys. Rev. D 84(11) 112003 (2011).

A phased array of antenna elements is an effective means to collect free-space radiation. We are investigating one or more ring-shaped arrays of antenna elements with each element amplified and digitized independently. The total available (coherent) signal power increases linearly with the number of instrumented channels N, while the incoherent noise of each channel contributes only $\sqrt{N}$ to the total noise. Performance has been modeled for an 8-cm-radius ring with 48 channels, the maximum that will fit around the circumference (Fig. 1.15-6). A SNR of 9 dB can be attained in this design.

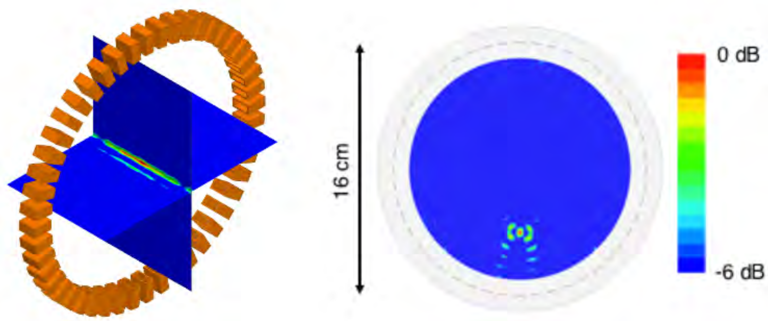

Figure 1.15-6. An 8-cm-radius ring array composed of 48 open-ended waveguide antenna elements in free space. Phases are tuned such that the focus is on the cylindrical axis (*left*) or 4 cm from the center (*right*).

The goal of phase IV is sensitivity to the full range of neutrino masses allowed by the assumption of an inverted mass hierarchy. An idealized estimate of the Project 8 sensitivity is $m_\nu < 40$ meV (90% C.L.). In order to circumvent the fundamental limit set by final-state broadening with a molecular T_2 source, the Project 8 collaboration is planning to make use of atomic tritium for the first time.

1.16 Development of an atomic source for Project 8

S. Böser*, J.Ȧ. Formaggio†, M. Guigue‡, A. Lindman*, E. Machado, R. G. H. Robertson

A very attractive feature of the Project 8 method, and the goal of its fourth phase, is the possibility of performing a tritium beta decay experiment with atomic tritium. Doing so removes the line-broadening contribution caused by zero-point motion in the T_2 molecule, about a 1-eV FWHM line-width contribution with both statistical and systematic penalties for molecular-based experiments. Fig. 1.16-1 compares the atomic and molecular line-widths [1]. The endpoint energy for the atomic decay is about 10 eV smaller than the molecular decay, which places stringent requirements on the purity of an atomic source. A molecular

*Institut für Physik, Johannes-Gutenberg Universität Mainz, Germany.
†Massachusetts Institute of Technology, Cambridge, MA.
‡Pacific Northwest National Laboratory, Richland, WA.

[1] L. I. Bodine, D. S. Parno, and R. G. H. Robertson; Phys. Rev. C **91** 035505 (2015).

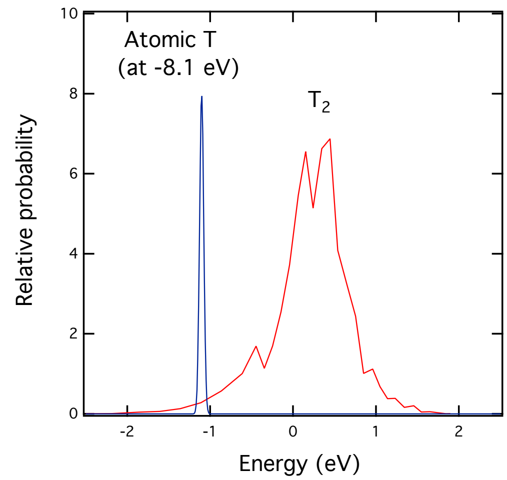

Figure 1.16-1. Line-width contributions for atomic and molecular tritium. The atomic line is Doppler-broadened, as shown for a temperature of 1K. The molecular broadening is mainly due to zero-point motion in the T_2 molecule.

contamination larger than 10^{-5} would represent a significant background at the atomic endpoint. Fortunately, the operating conditions for an atomic trap are compatible with very low temperatures ($T < 2$ K) and molecules are untrapped and freeze out.

The basic requirements for an atomic trap as applied to Project 8 are as follows:

- a means for producing atomic tritium,
- cooling to temperatures at which atoms can be trapped magnetically,
- injection into the trap,
- and trapping with a useful lifetime of roughly 10^5 s or greater.

We initially considered a cooling scheme involving a chamber with walls at ~ 150 mK, and the use of ^{4}He or ^{3}He as an exchange gas. Atoms of T injected into a region with a static vapor pressure of He would be cooled collisionally, with the exchange gas carrying heat to the walls. Since neither He isotope has a significant magnetic moment, the He is not trapped, but the T can be. More detailed consideration revealed that the scattering cross section of He on H is anomalously low, which calls for a higher density. Given the dependence of vapor pressure on temperature, even for ^{3}He the resulting temperature is too high for practical magnetic trapping.

We have instead turned to a novel scheme that does not involve an exchange gas. Atomic T produced in a source that could be a hot W cracker or an RF discharge is cooled by accommodation on a cold surface to about 30 K. The atoms then pass through a velocity selector that picks out a slice of the thermal distribution having a width corresponding to approximately 30 mK and a central energy equivalent to a magnetic field of 3 T for low-field-seeking states.

The velocity and state selected beam is prepared in a relatively low field of 0.05 T and enters the magnetic trap by surmounting a wall of 2 T. At the peak field, an RF transition drives the atoms to the high-field seeking state, and they slow further as they enter the central trap volume where the field is 1 T. Finally, circularly polarized radiation drives the atoms irreversibly back to the low-field seeking state, leaving them trapped in the active volume. Fig. 1.16-2 shows the cooling cycle of RF transitions where the central field is 1 T and the axial pinch field is 2 T. Preliminary calculations suggest that the desired density [1] of 10^{12}

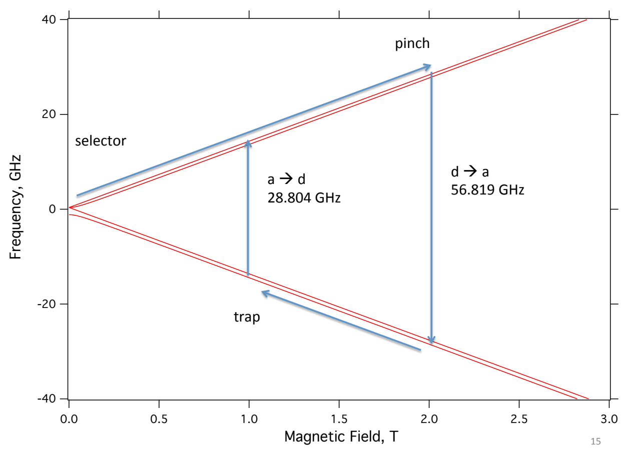

Figure 1.16-2. Breit-Rabi diagram for atomic tritium showing the RF transitions proposed for trapping atoms injected over a magnetic barrier of 2 T into a trap with a central field of 1 T.

cm^{-3} could be reached and maintained. With substantial levels of RF needed to induce the spin flips, a cyclical fill-measure-fill regimen might be called for, but it may be possible to configure the magnetic trap field arrangement to provide enough isolation between the RF drive and the low-noise amplifiers.

SNO

1.17 SNO and the solar-neutrino reaction *hep*

R. G. H. Robertson, N. Tolich, and T. Winchester*

Following more than a half-century of experimental study of the solar neutrino spectrum, all but 2 of the sources of solar neutrinos have been observed. One is the CNO cycle, limited

*Departed August 2016. Presently at Bellevue College, Bellevue, WA.

[1] A. Ashtari Esfahani et al. (the Project 8 Collaboration); J. Phys. G: Nucl. Part. Phys. **44** 054004 (2017).

experimentally now to about 1% of the total solar neutrino flux, and the other is the *hep* reaction,

$$p + ^3\mathrm{He} \quad \rightarrow \quad ^4\mathrm{He} + e^+ + \nu, \tag{1}$$

which produces the most energetic neutrinos in the solar spectrum. Although the predicted rate for this reaction is very low, the neutrino energy places the upper end of the detected spectrum in a region above 15 MeV that is largely free of interfering backgrounds.

The Sudbury Neutrino Observatory (SNO) was an underground, 1 kton heavy water Cherenkov detector in Sudbury, Ontario, Canada, detecting both charged- and neutral-current neutrino-deuteron interactions. The experiment was designed to detect solar neutrinos, and provided the first clear evidence of neutrino oscillations with a measurement of the neutrino flux from the decay of ^{8}B. An initial "box" analysis of SNO data to identify *hep* neutrinos[1] produced two candidate events and an upper limit on the integral *hep* flux of 2.3×10^4 cm^{-2} s^{-1} at 90% CL.

A new analysis[2] makes a number of improvements to increase SNO's sensitivity to *hep* neutrinos. A new event fitter was developed for existing data from SNO that improves both energy and vertex reconstruction. The fitter is used to remove backgrounds that previously limited the fiducial volume, which is increased by 30%. Since the *hep* events have relatively high energies, data not previously used because, for example, a calibration source was present, could be included in the analysis. A modified Wald-Wolfowitz test was employed to increase the amount of live time by 200 days (18%) and show that the additional data is consistent with the previously used data. A Bayesian analysis technique was developed to make full use of the posterior distributions of energy returned by the event fitter. In the first significant detection of *hep* neutrinos, we find (Fig. 1.17-1) the most probable rate of *hep* events is 3.5×10^4 cm^{-2} s^{-1}, which is significantly higher than the theoretical prediction. We also find that the 95% credible region extends from 1.0 to 7.2×10^4 cm^{-2} s^{-1}, therefore excluding a rate of 0 hep events at greater than 95% probability.

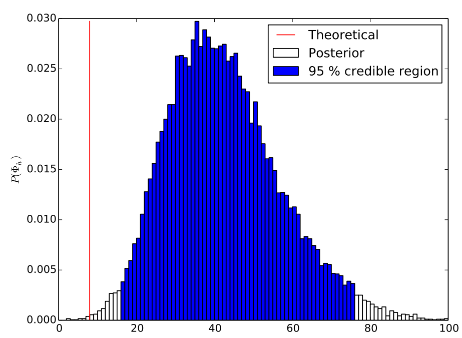

Figure 1.17-1. Posterior distribution for the *hep* flux from the new analysis. The theoretical prediction is given by the red line. The blue region represents the 95% confidence interval which excludes the theoretical prediction.

[1] B. Aharmim et al. (the SNO Collaboration). Astrophys. J. **653**, 1545-1551 (2006); hep-ex/0607010.
[2] T. Winchester, PhD thesis, University of Washington, 2016.

COHERENT

1.18 The COHERENT experiment

A. Cox, C. Cuesta*, J. Detwiler, A. Eberhardt, E. Erkela, Z. Fu, G. Garvey, D. S. Parno†, D. Peterson, T. D. Van Wechel, and A. Zderic

In 2016 we received a UW Royalty Research Fund Award to perform R&D toward fielding an array of NaI(Tl) scintillating detectors at the Spallation Neutron Source (SNS) in Oak Ridge. The SNS produces a pulsed source of stopped pions, which decay to neutrinos with energies reaching tens of MeV. One goal of the experiment would be to measure the coherent elastic neutrino-nucleus scattering (CEνNS) cross section of these neutrinos with the ^{23}Na nucleus, a Standard Model process that has yet to be observed. Another goal would be to perform an improved measurement of the charged-current interaction cross section of neutrinos with ^{127}I. This measurement would test several aspects of nuclear transitions relevant to neutrinoless double-beta decay, such as the potential quenching of g_A. These goals are being pursued in conjunction with the COHERENT Collaboration, who is deploying additional detector targets for the CEνNS search, including CsI(Tl) scintillating crystals, an array of Ge detectors, and a liquid xenon time projection chamber.

CENPA came into possession of a large number of NaI(Tl) crystals that were surplussed from the failed Department of Homeland Security Advanced Spectroscopic Portal (ASP) program. We received 130 crystals of dimension 2" $\times$ 4" $\times$ 16" with photomultiplier tubes (PMTs) attached, giving a total mass of 1.0 tons. Preliminary testing of the crystals at UW and elsewhere shows that they are high quality. The PMTs require high-voltage (HV) power supplies and a voltage divider (PMT base) to operate. We have designed a PMT base that incorporates the socket and HV power supply recovered from the custom bases produced for ASP. A prototype implemented on a perfboard was tested and implemented on printed circuit boards. The design is now being merged with a dual-output amplifier designed at ORNL to achieve sufficient dynamic range to perform both the low-energy CEνNS search and the high-energy CC scattering measurement with the same data run.

Meanwhile, we assisted Duke collaborators with the installation of a prototype 24-crystal array at the SNS (see Fig. 1.18-1). The detectors are held in a compact array surrounded by water shielding to block neutrons from the SNS beam as well as natural gamma radiation in the environment surrounding the detector. The detector has been running since Summer 2016 and data is being shipped via internet to the CENPA mamba cluster for redundant storage and parallel analysis.

*Presently at Centro de Investigaciones Energéticas, Medio Ambientales Y Tecnológicas, Madrid, Spain.
†Presently at Carnegie Mellon University, Pittsburgh, PA.

Figure 1.18-1. UW post-bac researcher Alex Zderic (right) deploying the 24-crystal prototype with Duke colleagues at the SNS in Oak Ridge, TN.

We have also assisted with validation of and upgrades to the neutrino source-simulation code, originally written in GEANT4 by H. Ray and collaborators at the University of Florida. The original estimates for the detector locations in the simulation were improved, and we verified the experimental hall layout using building surveys provided by ORNL. We also began to modify the output data format to improve flexibility, reliability, and readout speed. Separately, we are working on simulations of both large and small (24 crystal) NaI(Tl) arrays to support the analysis of the test deployment.

2 Non-accelerator-based tests of fundamental symmetries

Torsion-balance experiments

2.1 New limits on ultra-light axionic dark matter

E. G. Adelberger, C. A. Hagedorn, and W. A. Terrano*

The success of large scale-detectors in ruling out most of expected WIMP masses, along with the problem that simulations of conventional cold dark matter predict density cusps at the centers of galaxies that disagree with observations, have motivated a new dark-matter paradigm: a coherent field of ultra-light bosonic dark matter (ULBDM) bound in the galaxy[1,2]. Because the axions are bound gravitationally (as is the solar system) they should also have $v/c \approx 10^{-3}$ but, as they are almost dissipationless, the "wind"of presumed axion field can have any direction in the solar system frame. This "wind" acts on an electron at rest in the lab like a kind of "magnetic" field that oscillates at the Compton frequency $f_C = m_a/h$ where m_a is the axion mass and h is Planck's constant; f_C is expected to be coherent for $\sim 10^6$ cycles. In other words, an electron will feel an interaction[1]

$$H_{\text{eff}} = (C_e a_0)/(2F_a)\sin(f_C t/h + \phi)(\boldsymbol{p_a} \cdot \boldsymbol{\sigma_e}) \tag{1}$$

where C_e is the dimensionless axion coupling to electrons, F_a and $\boldsymbol{p}_a$ are the symmetry-breaking scale and momentum of the dark-matter axions in the laboratory frame, and $a_0 = \sqrt{2\rho_{DM}}/m_a$. If the observed dark matter consists entirely of axions then $a_0/m_a \approx 8 \times 10^{-3}$ eV^2, and a signal of 10^{-22} eV (0.1 zeV) would correspond to $F_a/C_e \approx 4 \times 10^{16}$ eV.

Yevgeny Stadnik and Victor Flambaum noted[3] that we could place powerful limits on F_a/C_e by re-analyzing our published rotating-torsion-balance data[4] taken with a pendulum containing 9.8×10^{22} polarized electrons and essentially no external magnetic field. Those data had a DC sensitivity of $\approx 10^{-22}$ eV. We have responded to this suggestion by analyzing a larger data set (used for references[4,5]) that spans 1110 days in 147 data sets containing a total of 12195 measurements. Each measurement typically contained exactly 2 full turntable revolutions and was analyzed as follows. We assumed that the energy of the pendulum in an individual measurement is

$$E = N_e \boldsymbol{\sigma} \cdot \boldsymbol{\beta} \tag{2}$$

where N_e represents the number of polarized electrons in the pendulum, $\boldsymbol{\sigma}$ is the direction of the spin dipole, and $\boldsymbol{\beta}$ is a vector assumed to be approximately fixed in the lab during

*Presently at Technical University of Munich, Germany.

[1] Y. V. Stadnik and V. V. Flambaum Phys. Rev. D **89**, 043522(2014).
[2] P. W. Graham and S. Ragendran, Phys. Rev. D **88**, 035023(2013).
[3] Private communication.
[4] B. R. Heckel, E. G. Adelberger, C. E. Cramer, T. S. Cook and S. Schlamminger, Phys. Rev. D **78**, 092006 (2008).
[5] B. R. Heckel, W. A. Terrano and E. G. Adelberger, Phys. Rev. Lett. **111**, 151802 (2013).

an individual measurement. Each measurement yielded independent determinations of β_N and β_W where N and W are local North and West directions. We suppressed lab-fixed signals by setting to zero the average values of β_N and β_W in each of the 147 data sets. These measurement pairs where then regressed against basis states $eXN\cos\omega_C$, $eXW\cos\omega_C$, $eXN\sin\omega_C$, $eXW\sin\omega_C$, $eYN\cos\omega_C$, $eYW\cos\omega_C$, $eYN\sin\omega_C$ and $eYW\sin\omega_C$, where the first factors transform local to galactic (equatorial X and Y) coordinates and $\omega_C = 2\pi f_C$. The averages of these basis states in each of the 147 data sets were also set to zero. Our initial analysis probed 60,000 f_C values between 1×10^{-8} and 1×10^{-4} Hz. Each value of f_C yielded 4 amplitudes: $a_{X\cos}$, $a_{X\sin}$, $a_{Y\cos}$ and $a_{Y\sin}$. The zeroing process introduced a problem when the sidereal and Compton frequencies were essentially identical because in that case there are only 2 independent amplitudes. For those cases we used a different strategy, making independent 2-parameter analyses for the X and Y directions.

Fig. 2.1-1 shows preliminary distributions of $a_{X\cos}$ and $a_{X\sin}$ for 60000 f_C values between 10^{-8} and 10^{-4} Hz. The region between 11 and 13 μHz was computed using 2-parameter fits as explained above. Fig. 2.1-2 shows the $a_X = \sqrt{|a_{X\cos}|^2 + |a_{X\sin}|^2}$ distribution and the resulting a_X spectral distribution. The results for $\boldsymbol{p_a}$ along Y are very similar those along X. We do not quote results for $\boldsymbol{p_a}$ along Z because those signals do not have sidereal modulation.

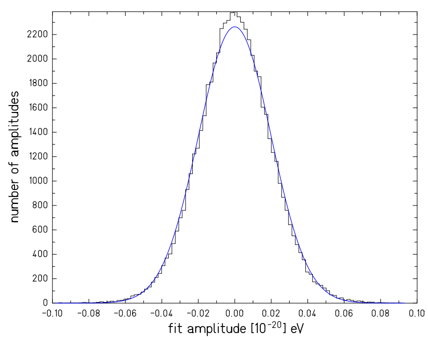

Figure 2.1-1. Preliminary distributions of $a_{X\cos}$ and $a_{X\sin}$ coefficients. The results are quite close to Gaussians with zero mean.

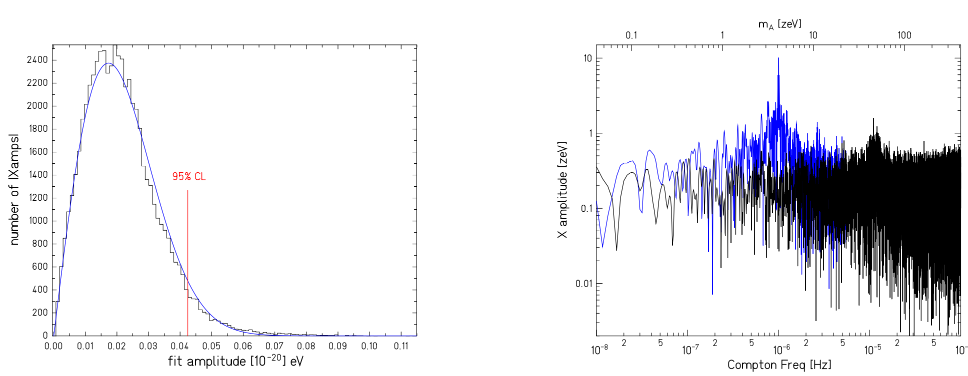

Figure 2.1-2. *Left*: histogram of a_X amplitudes. The results follow the expected Rayleigh distribution. *Right*: preliminary spectral distribution of a_X. The black curve is our data, the blue curve shows the result of adding a synthetic 10 zeV, 1μHz signal to the data. It is resolved by almost 10σ.

2.2 Progress on ground-rotation sensors for LIGO

J. H. Gundlach, C. A. Hagedorn, M. Ross, and K. Venkateswara

The ground-rotation sensors, developed at CENPA, are proving beneficial during the second observation run of the Laser Interferometer Gravitational-Wave Observatory (LIGO). The rotation-sensors improve the low-frequency active seismic isolation system by reducing the tilt/rotation noise in a colocated seismometer, thereby producing a cleaner horizontal ground-translation signal. Under harsh environmental conditions such as high-winds, microseisms and earthquakes, the use of these rotation-sensors for feedforward isolation of the suspended platforms in LIGO was shown to reduce the differential cavity motion, enabling low-noise operation under these conditions. With the installation of these rotation-sensors at the LIGO Hanford Observatory (LHO), the interferometer is proving to be more robust against wind and microseism as compared to the LIGO Livingston Observatory during the second observation run[1].

The first prototype sensor was installed at the X-End-station at LHO in Summer 2014. The sensor measured ground-rotations above 10 mHz with a sensitivity of 0.1 nrad/$\sqrt(Hz)$ allowing high-precision measurements of wind-induced tilt of the ground near the test-mass chambers, and demonstrated efficient tilt-subtraction from a ground seismometer. To benefit the interferometer, an additional rotation-sensor was needed at the Y-End-station in order to reduce the differential motion between the two end-mirrors. In Fall 2015, LIGO Lab tasked our group to build a second rotation-sensor with some improved features, which was delivered and installed in March 2016. Control filters for the feedforward isolation scheme were subsequently developed and improved iteratively. The feedforward system showed a factor of $\sim$ 10 reduction in the differential motion of the arm cavities under wind-speeds exceeding 20 mph.

Fig. 2.2-1 shows an example of the benefit of using these rotation-sensors for seismic isolation. The plot shows x and y-arm optical transmission signals. A large and stable signal indicates that the cavity is locked in feedback near it's operating point. Initially, the x-arm cavity was locked using the rotation-sensors while the y-arm was not using these and was unable to be locked. During the middle section of the plot (-50 s on the x-axis), seismic isolation using the rotation-sensor was turned on and the cavity could be locked shortly thereafter. The rotation-sensors therefore enable noise-free observation during wind speeds exceeding 15 mph, which occurs $\sim$ 15% of the time at LHO.

Last year, we also developed a new compact version of the beam rotation sensor (BRS) with improved readout using two fiber-optic interferometers thus achieving a sensitivity of 10 prad/$\sqrt(Hz)$ at frequencies above 1 Hz. With this improved sensitivity it can measure seismic tilt accurately in the 10-20 Hz range. When located under a LIGO test mass, the tilt signal is proportional to the Newtonian noise from seismic surface waves. The compact-BRS has been deployed at LHO as part of an array of seismic sensors to estimate Newtonian noise on the detector and investigate mitigation schemes. Preliminary results indicate it can be effective in mitigating Newtonian noise by a factor of $\sim$ 5-10.

[1]K. Venkateswara, *et al.* B. Seismol. Soc. Am. **107** 2 (2017) 709-717.

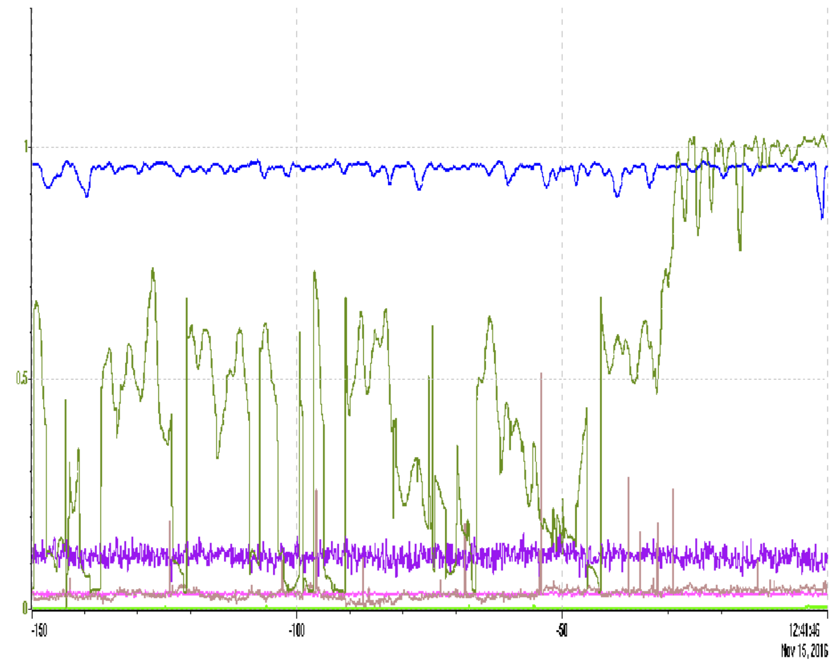

Figure 2.2-1. Plot of the x-arm (blue) and y-arm (green) cavity transmission signals at LHO during wind-speeds of 30-40 mph, which indicate the length stability of the cavity. The x-arm was locked using the rotation-sensor while the y-arm was initally not using it. After the rotation-sensor-seismic feedforward was enabled near $t = -50$ s on the plot, the y-arm cavity was able to be locked stably, demonstrating the benefit of using ground rotation sensors.

2.3 Wedge-pendulum experiment update

E. G. Adelberger, B. R. Heckel, W. J. Kim*, J. G. Lee, and H. E. Swanson

The wedge-pendulum experiment is designed to measure the behavior of the gravitational interaction at short distances[1]. In the past year, several improvements in design and operation have been implemented. The main pursuit has been to achieve a total separation of 50 μm between attractor and detector test masses, while contending with increased seismic noise from a nearby construction project on the UW campus.

Temperature stability of the apparatus has been improved by implementing a digital feedback system with a water-bath chiller. This has decreased temperature fluctuations from 30mK to 10mK, made the system more robust against loss of temperature lock in the room, and improved separation stability from thermal expansion. The attractor turntable motor feedback noise had worsened after several years without maintenance. The full ceramic bearings were replaced, and the shaft coupling softened to minimize torques from slight misalignments. Finally, the vacuum line had been replaced with a larger diameter to improve conductance. Due to the location of the vacuum line, this led to a significant torque on

*Affiliate Assistant Professor, Seattle University, Seattle, WA.

[1]CENPA Annual Report, University of Washington (2016) p. 33.

the apparatus and therefore a tilt when under vacuum ($\sim 100\ \mu$rad), as well as changing tilts from temperature and pressure fluctuations of the room. The vacuum line was partially returned to the smaller diameter line with plans to switch to an ion pump.

The experiment has so far achieved a total separation of about 70 μm: with 10 μm attributable to the thickness of the beryllium-copper electrostatic screen, 25 μm attributable to the attractor-screen separation, and 35 μm of pendulum-screen separation. All separations have been determined through fits of capacitance measurements to newly developed COMSOL models of the true experimental geometry. The attractor-screen separation could potentially see a factor of 2 reduction through careful cleaning. The pendulum-screen separation could potentially be reduced by a factor of 3 with the addition of active seismic isolation[1]. Analysis is currently underway from the preliminary dataset.

2.4 Rotating equivalence-principle test

E. G. Adelberger, J. H. Gundlach, C. A. Hagedorn, E. A. Shaw, H. E. Swanson, and F. Xiong

The equivalence principle (EP), the notion that the gravitational interaction is independent of material composition, is the defining postulate of General Relativity. Any violation of that symmetry, presently tested by our group at the 10^{-13} level, would point the way to new, perhaps unifying, physics.

Continuing our 30+ year program of rotating equivalence-principle tests, we iterated on the instrument in several ways:

Gravity-gradiometer system: Gravity gradients, and any change in gradients over time, are leading systematics for any EP test.

The improved rotating tiltmeter-based gravity gradient monitor system installed last year[2] was put to the test over many months. The variation between sequential measurements reaches the necessary precision of a few percent of the ambient gravity gradient in a day, but the variation over long times remains too large. The system could not identify gravity gradients from nearby earthmoving construction which are easily resolved by our benchmark torsion-balance gravity-gradiometer. Improved thermal shielding, or a different sensor design, may yield sufficient performance.

Bearing pressure variation: After noting a correlation between instrument tilt and variations in the line pressure that feeds the experiment's critical air bearing, we installed a precision pressure gauge. A precision regulator awaits installation the next time we park the turntable.

Bearing tilt feedback: We have largely regained control of the leveling "feetback"

[1] K. Stockton (2017) *Active Vibration Isolation Systems in Torsion Balance experiments* (Master's thesis, University of Washington).

[2] CENPA Annual Report, University of Washington (2016) p. 37.

system, with RMS tilt variation of < 200 nrad on the rotating platform, concentrated in easily-correctable harmonics of the rotation frequency.

Temperature: Temperature variation and temperature gradients are leading systematics for both EP tests and the gravity-gradient monitor. We have implemented a new software feedback system to allow more-precise control over the room temperature, extending previous work[1]. In addition, we tested a commercial high-precision thermistor readout board, which may allow greater numbers of temperature sensors at a reasonable cost.

Turntable: Our FPGA-based turntable controller loop is difficult to modify/audit and uses only fixed-point arithmetic. We successfully locked the turntable loop using a proof-of-concept control loop on a small microcontroller programmable in C, and have recently upgraded the microcontroller to one with a floating-point unit.

2.5 Active vibration-isolation for torsion-balance experiments

J. H. Gundlach, C. A. Hagedorn, J. G. Lee, K. J. S. Stockton, and K. Venkateswara

To partially-mitigate seismic vibration generated by nearby construction on the UW campus, the North Campus Housing project generously co-funded vibration isolation research. Our torsion balances require seismic/tilt stability at frequencies near and below 1 Hz, a challenge for all known commercially-available vibration isolation systems.

In an attempt to isolate our seismically-sensitive submillimeter-gravity experiment (Sec. 2.3), we acquired a Herzan AVI-200M isolator system and characterized its performance in horizontal acceleration, vertical acceleration, tilts, and rotation about the vertical axis. The system delivered its specified performance in vertical and horizontal acceleration, but was too noisy for our requirements in rotation about the vertical.

The 9 Hz vertical "bounce" mode of the torsion balance is our greatest concern, so we focused entirely on vertical motion. After disabling the horizontal isolators and locking the rotation of the isolated platform with flexures, we obtained potentially-useful vertical isolation performance without injecting too much rotation noise. A summary of our results is shown in Fig. 2.5-1.

While the Herzan system was selected in part for its ability to integrate into the submillimeter gravity experiment, installation would involve substantial modification and downtime. With our focus now entirely on vertical motion, we are developing small isolators that can be installed with zero modification to the existing experiment. Complete documentation of the state of the project may be found in Kerkira Stockton's masters thesis[2].

[1] CENPA Annual Report, University of Washington (2012) p. 44.
[2] K. J. S. Stockton, Active Vibration Isolation Systems, Masters Thesis, March 2017.

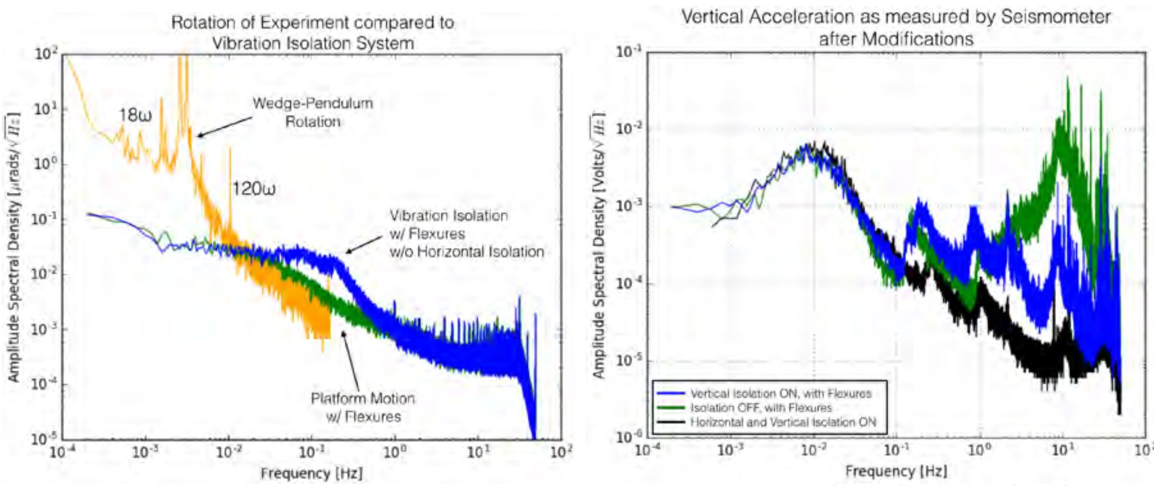

Figure 2.5-1. *Left*: Rotation performance of the modified isolator off (green) and on (blue), compared with the sub-millimeter gravity torsion balance (yellow). The system would not add substantial noise at the critical "120ω" frequency. *Right*: Vertical acceleration of the isolator off (green), and on (blue: modified, black: as delivered)

2.6 A new experimental search for equivalence-principle violating dark matter

E. G. Adelberger J. H. Gundlach, C. A. Hagedorn, J. G. Lee, E. A. Shaw, and K. Venkateswara

A recent theoretical proposal[1] motivates experiments for setting limits on the mass and coupling constants of a Baryon minus Lepton number (B-L) coupled dark matter candidate with $m_{DM} \ll 0.1$ eV. B-L is a conserved quantity in all known interactions and remains so in grand-unified and supersymmetric theories beyond the Standard Model. This makes it a well motivated conserved charge that could have a corresponding massive gauge boson coupled to it. Another advantage of this light dark matter scenario is that it is a potential solution to the core-cusp problem[2]. We can search for a torque signal from this dark matter candidate with a B-L composition dipole pendulum such as the 8-test-body pendulum. The signal from this field-like dark matter would be oscillating at the dark matter compton frequency with a coherent amplitude in an unknown direction in the frame of our solar system. As such, it would introduce a modulation in terrestrial experiments with a period of one sidereal day. Setting new limits requires improvements in thermal noise in the torsion fiber and the angular readout. Additionally, a rotating experiment allows for modulating the signal at a frequency where the torsion balance is optimally sensitive.

Recently, we have developed a technique to fabricate fused silica fibers up to a length of 1 meter and demonstrated quality factors of up to $Q = 500,000$ in the LISA appara-

[1] P. W. Graham, D. E. Kaplan, J. Mardon, S Rajendran, and W. A. Terrano. Phys. Rev. D **93** (2016) 075029.

[2] W. Hu, R. Barkana, and A. Gruzinov. Phys. Rev. Lett. **85** (2000) 1158.

tus[1,2]. Now the LISA apparatus is being used for a B-L dark matter search which we call the Dark-EP experiment. Compared to tungsten fibers with $Q \sim 5000$, the fused silica fibers in the Dark-EP experiment have lower thermal torque noise, $\delta\tau(f) = \sqrt{2k_B T\kappa/(\pi Q f)}$, where k_B is Boltzman's constant, T the fiber temperature, κ the fiber torsion constant, f the frequency, and Q the mechanical quality factor[3]. At room temperature the salient quantity to determine the relative sensitivity of an apparatus is $\sqrt{\kappa/Q}$. For tungsten fibers $\sqrt{\kappa/Q} = \sqrt{2.5\times 10^{-9}/5000}\,\sqrt{\mathrm{Nm}}$ and we achieved $\sqrt{8.1\times 10^{-9}/450000}\sqrt{\mathrm{Nm}}$ with a fused silica fiber and our 8-test-body pendulum. This corresponds to a factor 5 improvement in torque sensitivity and we have shown that we can take advantage of this to set new limits as outlined in Fig. 2.6-1.

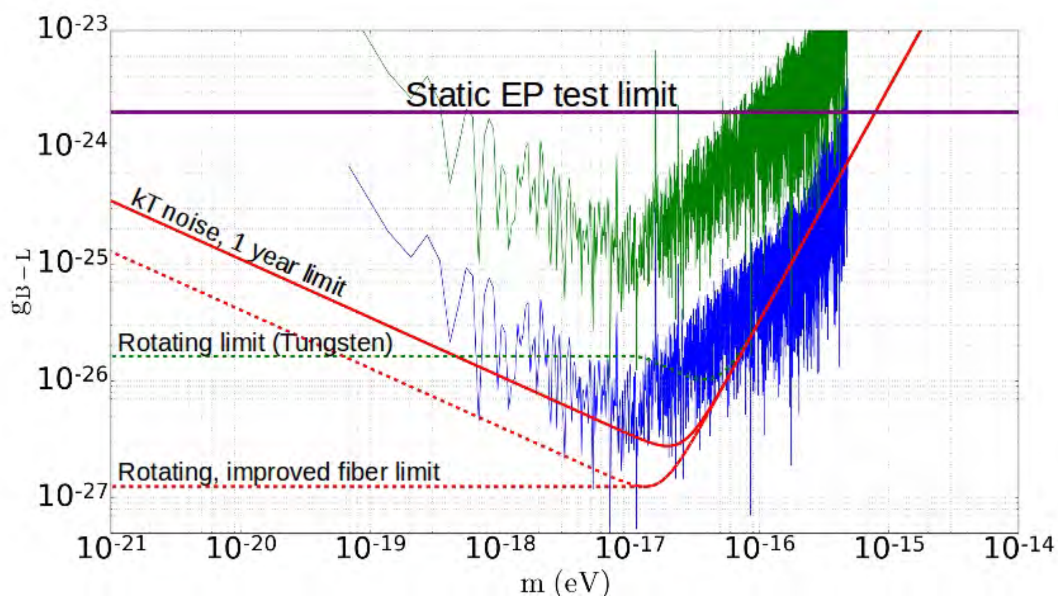

Figure 2.6-1. The Static EP limits are the current best limits set on a B-L coupled particle by our rotating experiment. The green curve is the current statistical noise in the Dark-EP apparatus over the course of one day. The blue curve extrapolates to the limits we could set in 1 year. The kT noise curve is the theoretical limit on the sensitivity of the Dark-EP apparatus. A new rotating limit could be set by running the rotating experiment's turntable at a higher frequency of 3 mHz. A modest improvement in fiber quality could open up the possibility of setting the limits shown in red dashed lines.

[1] CENPA Annual Report, University of Washington (2015) p. 30.

[2] CENPA Annual Report, University of Washington (2016) p. 34.

[3] C. A. Hagedorn, S. Schlamminger, and J. H. Gundlach, Proc. 6th Int. LISA Symp., New York 2006, AIP Conf. Proc. **873** 189-193.

Other tests of fundamental symmetries

2.7 The mercury electric-dipole-moment experiment

Y. Chen, B. Graner, B. Heckel, and E. Lindahl

In 2016, our group reported a new ^{199}Hg electric dipole moment (EDM) result: $d(^{199}\mathrm{Hg}) = +(2.20 \pm 2.75_{stat} \pm 1.48_{syst}) \times 10^{-30} e\,\mathrm{cm}$ which we interpret as a new upper limit of: $|d(^{199}\mathrm{Hg})| < 7.4 \times 10^{-30} e\,\mathrm{cm}$ (95% C.L.). This result represents a factor of 4 reduction of the upper limit on the ^{199}Hg EDM over previous work[1].

The ^{199}Hg EDM apparatus uses UV laser light to polarize and measure the spin precession frequency of ^{199}Hg atoms in a stack of 4 vapor cells, 2 of which (the inner pair) have oppositely directed electric fields. A pump-probe sequence is employed, with the electric fields reversed between each pump-probe cycle. A blind frequency offset is added to the inner cell frequency difference to mask the EDM signal until the analysis of the entire data set is complete. The 2016 experiment used data taken with 6 kV/cm and 10 kV/cm electric fields, magnetic field normal and reversed, and slow and fast electric field ramp rates.

A new systematic error was found in the 2016 experiment: evidence for cell movement due to electric field forces. In the presence of magnetic field gradients, cell movement can lead to an EDM-like systematic error. A new innermost magnetic shield has been installed in the EDM apparatus to reduce the magnetic field gradients. Work is currently underway to make more reproducible the magnetic de-Gauss protocol, to ensure smaller field gradients. With reduced magnetic field gradients, it is our belief that another factor of 3-4 improvement in EDM sensitivity will be achievable in our existing EDM apparatus.

The ^{199}Hg EDM project is primarily supported by NSF Grant 1306743 (PI. Heckel).

[1]B. Graner, *et al.* Phys. Rev. Lett. **116** (2016) 161601.

3 Accelerator-based physics

3.1 The $2_1^+ \rightarrow 3_1^+$ gamma width in ^{22}Na and second-class currents

G. C. Ball*, A. Diaz Varela†, R. Dunlop†, L. Phuthu‡, S. Triambak‡,§ A. García, P. E. Garrett†, D. S. Jamieson†, G. C. Harper, J. N. Orce‡, W. A. Richter‡, D. A. Short, S. P. R. Steininger, C. E. Svensson†, and C. Wrede¶

A measurement of the $\beta-\gamma$ directional coefficient in ^{22}Na beta decay has been used to extract recoil-order form factors.[1] The data indicated the requirement of a significantly large induced-tensor matrix element for the decay, well beyond the calculated first-class contribution. This suggests either second-class currents, which would disagree with other measurements, or a problem with some of the data that were used to arrive at the conclusion.

The conclusion relies heavily on the weak-magnetism form factor for the decay which was determined using an unpublished value of the analog $2_1^+ \rightarrow 3_1^+$ γ branch in ^{22}Na with the further assumption that the transition was purely iso-vector M1. Fig. 3.1-1 shows the decay scheme.

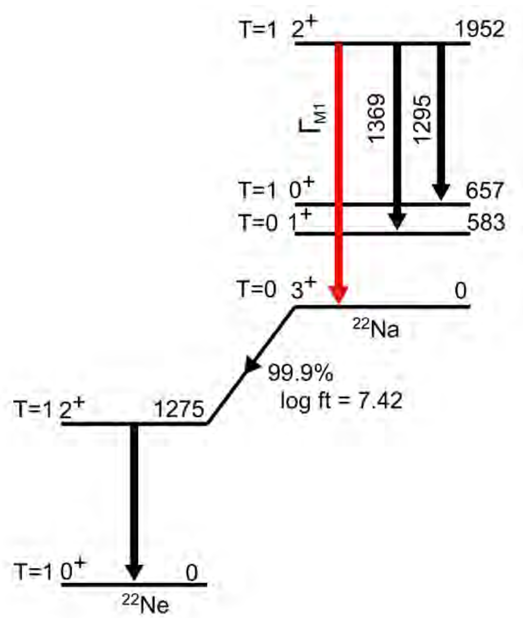

Figure 3.1-1. Decay scheme showing the 2_1^+ state. The branch in question in question is highlighted in red.

*TRIUMF, 4004 Wesbrook Mall, Vancouver, British Columbia, Canada.
†Department of Physics, University of Guelph, Guelph, Ontario, Canada.
‡Department of Physics and Astronomy, University of the Western Cape, South Africa.
§iThemba LABS, Somerset West, South Africa.
¶Department of Physics and Astronomy and National Superconducting Cyclotron Laboratory, Michigan State University, East Lansing, Michigan.

[1] C. J. Bowers et al., Phys. Rev. C **59**, 1113 (1999).

We produced implanted ^{21}Ne targets and used the accelerator in terminal-ion-source mode to feed the 2^+_1 state in ^{22}Na using a p,γ resonance. Selected portions of the gamma spectra that were used to determine the branch are shown in Fig. 3.1-2.

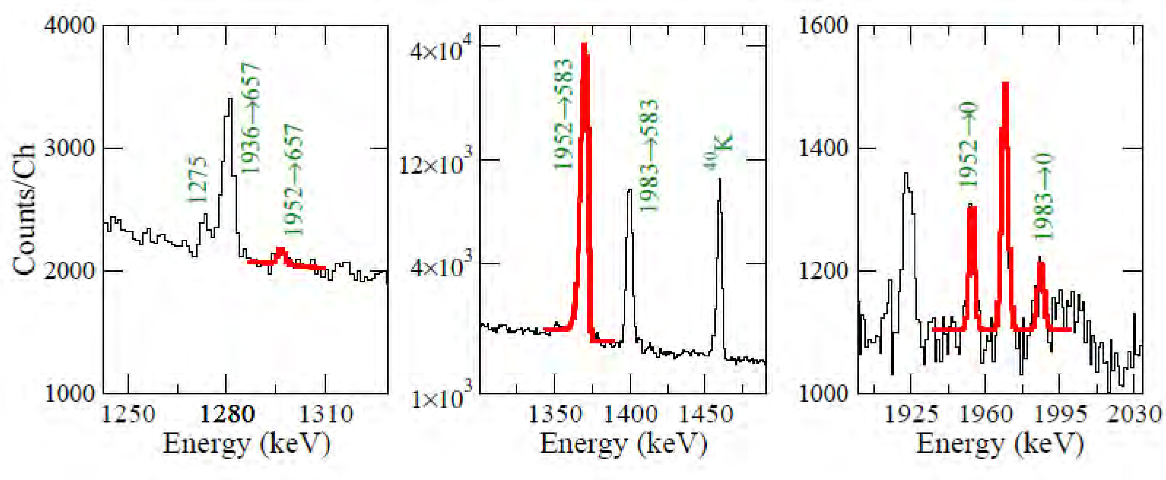

Figure 3.1-2. Selected parts of the gamma spectra that were used to determine the branch.

During last year we finished the data analysis and published our results on the branch[1]. We obtain for the first time an unambiguous determination of the $2^+_1 \rightarrow 3^+_1$ branch in ^{22}Na to be 0.45(8)% compared to the previous unpublished value used before of 0.61(24)%.

Using the Conserved Vector Current (CVC) hypothesis, our measurement determines the weak magnetism form factor for ^{22}Na beta decay to be $|b/Ac_1| = 8.7(1.2)$. Together with the $\beta-\gamma$ angular correlation coefficient, we obtain a large induced-tensor form factor for the decay that is still much larger than the first-class expectation. Two possibilities will be explored in the near future. i) The calculation mentioned above depends on assuming that the sign of the weak-magnetism matrix element with respect to the Gamow-Teller matrix element is given by a shell model calculation. This could be incorrect and we are entreating theory colleagues to take up the challenge. ii) Another possible resolution is that the transition is E2 dominated. In fact, the two levels have been determined to belong to different rotational bands, and this could result in an E2-dominated transition. This issue can be resolved experimentally by measuring the angular distribution and we are working on a proposal to do the measurement at CENPA.

[1]S. Triambak et al., Phys. Rev. C **95** (2017) 035501.

3.2 Overview of the ^{6}He experiments

Y. S. Bagdasarova, K. Bailey*, M. Fertl, X. Fléchard†, A. García, S. Gilligan, M. Guigue‡, M. Imbault§, D. Hertzog, R. Hong*, P. Kammel, K. S. Khaw, A. Knecht¶, A. Leredde*, E. Liénard†, P. Müller*, O. Naviliat-Cuncic‖, T. P. O'Connor*, N. S. Oblath‡ F. Otto, J. Pedersen, R. G. H. Robertson, G. Rybka, G. Savard*, E. Smith, D. Stancil** D. W. Storm, H. E. Swanson, B. A. VanDevender‡, F. Wauters†† and A. R. Young‡‡

We are searching for tensor currents in two different experiments looking at the beta decay of ^{6}He. In an on-going effort we use laser traps to determine the $\beta - \nu$ correlation. A second effort to determine the shape of the spectrum using the CRES technique is developing.

Tensor currents flip chirality and are forbidden in the standard model but predicted by some extensions of it[1]. Fig. 3.2-1 shows limits from several sources. The limits from the LHC obtained by Cirigliano et al. are presently more stringent than those from nuclear beta decays. Shown in red are limits that we could expect from our work, showing that new physics could be discovered in nuclear beta decays.

$\beta - \nu$ correlation from laser trapped ^{6}He

Our present effort aims at determining the $\beta - \nu$ correlation by trapping ^{6}He in a laser Magneto-Optical Trap (MOT). The electron is detected via a combination of a multi-wire proportional chamber and a scintillator. The recoiling Li ions are detected via a focusing electric field that guides them onto a position-sensitive Micro Channel Plate (MCP) detector. By measuring the time of flight and the landing position of the Li ion its momentum can be reconstructed. Together the electron and Li momentum can be used for reconstructing the anti-neutrino momentum.

During the past year we achieved two main goals: 1) a clear understanding of the capability of the MCP detector for determining position of events reaching 8 μm precision, which we published in NIM[2]; and 2) our first physics results, measuring for the first time the charge distribution of Li ions from the decay of metastable ^{6}He[3]. This serves as a solid benchmark for atomic theory calculations that are needed for similar problems. As detailed

*Physics Division, Argonne National Laboratory, Argonne, IL.
†LPC-Caen, ENSICAEN, Université de Caen, Caen, France.
‡Pacific Northwest National Laboratory, Richland, WA.
§Ecole National Superieur d'ingenieurs de Caen, Caen, France.
¶Paul Scherrer Institute, Villigen, Switzerland.
‖Department of Physics and Astronomy and National Superconducting Cyclotron Laboratory, Michigan State University, East Lansing, MI.
**Electrical Engineering Department, North Carolina State University, Raleigh, NC.
††Institut für Kernphysik, Johann-Joachim-Becherweg 45, Johannes Gutenberg-Universität Mainz, Mainz, Germany.
‡‡Physics Department, North Carolina State University, Raleigh, NC.

[1] Cirigliano, Gardner, and Holstein, Prog. Part. Nucl. Phys. **71**, 93 (2013).
[2] R. Hong et al., NIM A **835**, 042 (2016).
[3] R. Hong et al., submitted to PRC.

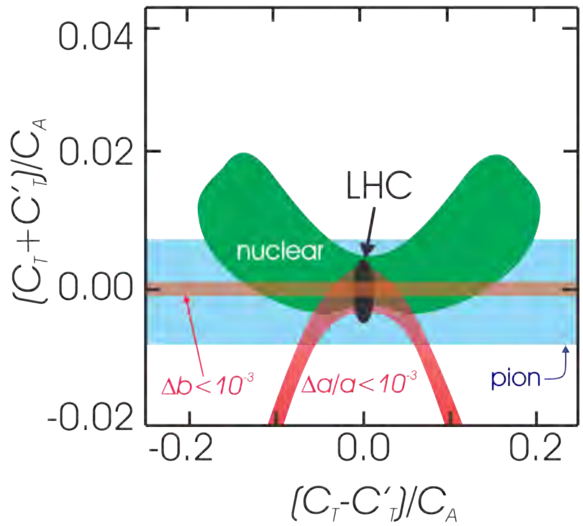

Figure 3.2-1. From Wauters et al., Phys. Rev. C **89**, 025501 (2014): Upper limits (90% C.L.) on tensor currents from several experiments. Green: upper limits from all nuclear beta decays, including neutron decays. Light blue: radiative pion decay. Black ellipse: upper limits extracted by Cirigliano et al. from LHC data [1]. The red-shaded areas indicate the sensitivity one gets from a $\beta-\nu$ correlation experiment with uncertainty $\Delta a/a = 10^{-3}$ and from a spectrum shape determination with uncertainty $\Delta b = 10^{-3}$.

in (Sec. 3.7), we observed some disagreements with a recent calculation, which are now being considered by the atomic theory colleagues. The Li ions' charge distribution is also a factor in the extraction of the $\beta-\nu$ correlation.

With respect to the determination of the $\beta-\nu$ correlation itself, during the last year we have pursued control of several factors that result in systematic errors, such as the stability and the absolute determination of the MOT centroid and shape, the stability of the HV systems, and the detection systems.

We now can get data for a $\sim 1\%$ determination of the $\beta-\nu$ correlation coefficient in less than 3 days of running time, including calibrations. The experiment runs in a stable fashion. The target sensitivity we have with the present setup is 0.5 %.

We expect to finish our systematic analysis and start gathering statistics for the $\beta-\nu$ correlation determination soon.

Shape of the ^{6}He β spectrum using the CRES technique

On a different front, we have assembled a collaboration to extend the use of the CRES technique, developed by the Project 8 collaboration, to determine the shape of the ^{6}He beta spectrum. A proposal was developed analyzing the possibilities of a concrete setup, including Monte Carlo simulations of expected precision and systematic uncertainties. The prospects look very encouraging, showing potential sensitivity better than one order of magnitude beyond the LHC. (Sec. 3.8) contains more details on this part of the program.

3.3 Improvements of the ^{6}He laser-trapping efficiency

Y. S. Bagdasarova, K. Bailey*, X. Fléchard†, A. García, S. Gilligan, R. Hong*, M. Imbault‡, A. Knecht§, A. Leredde*, E. Liénard†, P. Müller*, O. Naviliat-Cuncic¶, T. P. O'Connor*, F. Otto, J. Pedersen, E. Smith, D. W. Storm, H. E. Swanson, and F. Wauters‖

During the past year, several new features have been added to the ^{6}He laser trap setup in order to increase its trapping efficiency and gain a better control and monitoring over its parameters.

A much needed tool, now operational, is the new ^{6}He production monitor with an improved sensitivity while taking data for the $\beta - \nu$ correlation measurement.

Fig. 3.3-1 shows the discharge chamber vacuum system, including the counting volume, where the previous monitoring system is located and used to optimize production. The monitor consists of two sets of thin scintillators coupled to photomultiplier tubes, and the production rate is obtained from the coincidence detection of the beta particles in both detectors. At peak production (2×10^{10} ^{6}He/s), the system at the counting volume measures 1.7 MHz when the beam is diverted to the counting volume. However, when the atomic beam is redirected to the trapping setup for data taking, this rate falls to < 500 Hz and the SNR becomes 1:1, making it difficult to optimize production and diagnose issues while taking data. The new detection setup sits between the turbo-molecular pumps TMP2 and TMP3 in Fig. 3.3-1 and the roughing pump, where the gas is compressed. During data taking, this setup yields a detection rate 100 times lower than the previous one in optimization mode but much higher than the previous in counting mode, with a SNR > 50. The production can thus be monitored continuously and more reliably than before.

The second new feature is the periodic laser switching of MOT2. While taking data, the trapping laser beams can be switched on and off at a 10 kHz rate in order to control the initial atomic state at the moment of the decay. Releasing the atoms for 50 μs does not let them expand enough to impact the measurement. When the laser is on, the atomic cloud is saturated and the atoms are split 50/50 between the metastable state $2^3\mathrm{S}_1$ and the excited state $2^3\mathrm{P}_2$. When the laser is turned off, all the atoms decay back to the metastable state with a lifetime of ~ 98 ns. To validate this method, a pulsed nitrogen laser is used to ionize the trapped atoms from the $2^3\mathrm{P}_2$ state. When the trapping laser is off, no photo-ionization events are detected. This feature has already been used to study the effect of the initial state of the atoms on the shake-off probabilities which are of concern for the precision measurement of $\beta - \nu$ correlation (Sec. 3.7).

*Physics Division, Argonne National Laboratory, Argonne, IL.

†LPC-Caen, ENSICAEN, Université de Caen, Caen, France.

‡Ecole National Superieur d'ingenieurs de Caen, Caen, France.

§Paul Scherrer Institute, Villigen, Switzerland.

¶Department of Physics and Astronomy and National Superconducting Cyclotron Laboratory, Michigan State University, East Lansing, MI.

‖Institut für Kernphysik, Johann-Joachim-Becherweg 45, Johannes Gutenberg-Universität Mainz, Mainz, Germany.

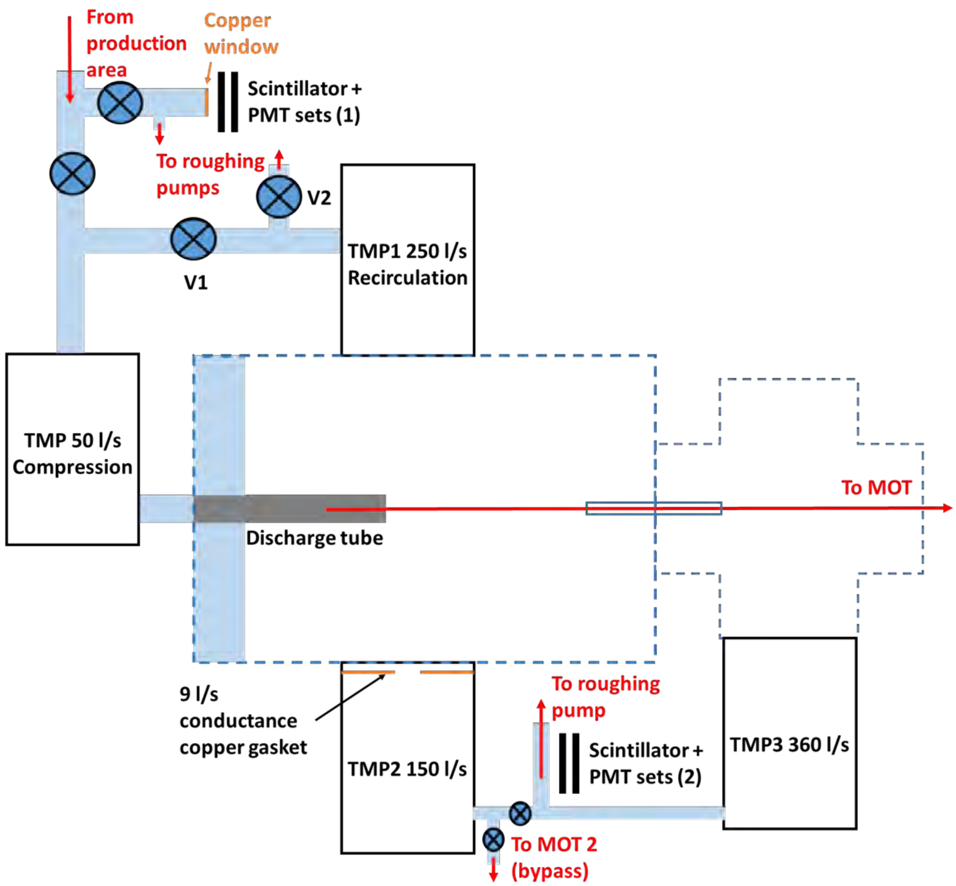

Figure 3.3-1. Sketch of the discharge chamber vacuum system, including the counting volume and the recirculation system. The first production monitor (1) detects the β particles coming from the decays in the counting volume and passing through a thin copper foil. While taking data, the atomic beam is redirected towards the discharge chamber and the counting volume is closed off. The only active pumping in this chamber is provided by TMP2 and TMP3 which compress the gas in the roughing line. The second monitoring system (2) detects the β particles through a non-shielded part of the plastic hose from the roughing line.

In addition, a 2-dimensional optical dipole trap to guide the atoms during their transfer from MOT1 to MOT2 was implemented. This guide beam is a far-detuned intense laser beam aligned along the transfer axis, working on the atomic trapping transition. The red detuning creates an attractive dipole potential centered at the high intensity region of the Gaussian beam. The potential depth goes as the intensity divided by the detuning. On the other hand, photon scattering tends to heat up the atoms but its rate goes as the intensity divided by the detuning squared. Theoretically, it is better to maximize detuning while keeping the depth of the potential large enough with higher intensity. In practice, the laser setup does not have a spare laser diode to generate a flexible detuning. A small fraction of the ^{4}He trapping laser is used to seed a 4 Watt fiber amplifier resulting in a detuning for ^{6}He corresponding approximately to the isotope shift. The effect of the guide beam has been studied using ^{4}He as shown by the figure Fig. 3.3-2. MOT2 trap was turned off and the vacuum was brought to

1×10^{-7} Torr in order to increase the Penning ionization rate due to collision of metastable helium and residual gas molecules. These ions were then collected and detected by the recoil ion momentum spectrometer of the detection setup. On Fig. 3.3-2, the atoms travel from the bottom-right corner of the detector to the top-left corner, creating ions along their path. When the guide beam is off, the transverse distribution of the atomic bunch is wide, as seen on the profile. When the guide beam is on, some of the atoms are kept radially confined along the path of the laser beam. Due to our constraints on detuning, photon scattering is still significant and some of the atoms are heated up and escape the dipole trap, resulting in the broad transverse distribution beneath the sharp pencil beam. After turning on MOT2 and optimizing the parameters of the guide beam, a gain of a factor of 2 has been observed for the MOT-to-MOT transfer.

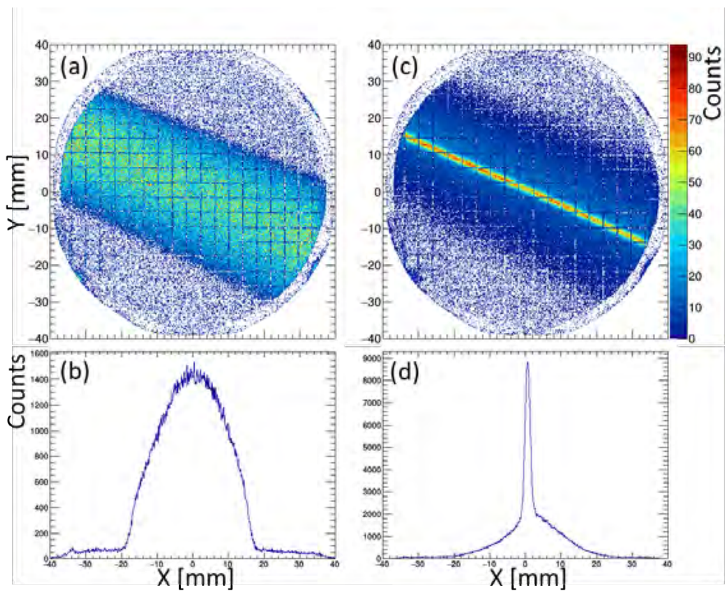

Figure 3.3-2. MCP detector images providing a projection of the atomic bunch coming from MOT1 as it travels in the MOT2 chamber. On the left, the guide beam is off and the bunch of atoms has a wide transverse distribution. The expected Gaussian profile is cut due to an aperture tube sitting at the exit of MOT1 for differential pumping. On the right, the guide beam is on. Some atoms follow the path of the thin laser beam while some escape the trapping potential due to photon scattering.

In June 2016, the effect of the guide beam was confirmed with ^{6}He and a set of data was acquired with a peak detection rate of 6 Hz (β-recoil-ion coincidences). If everything is optimized, the expected rate should be around 8 Hz, which would allow acquiring the statistics needed for the 1% measurement of $a_{\beta\nu}$ in 24 hours. It is also convenient for quickly taking data under different conditions to study systematic effects.

In the future, a dedicated laser diode and a higher power fiber amplifier could be used to create a more efficient guide beam. Currently, the transfer efficiency goes from 10% to 20% when using the guide beam but there should not be any obstacle to getting it close to 100%.

3.4 Image calibrations to determine the stability and systematics of the MOT position

Y. S. Bagdasarova, K. Bailey*, X. Fléchard†, A. García, S. Gilligan, R. Hong*, M. Imbault‡, A. Knecht§, A. Leredde*, E. Liénard†, P. Müller*, O. Naviliat-Cuncic¶, T. P. O'Connor*, F. Otto, J. Pedersen, E. Smith, D. W. Storm, H. E. Swanson, and F. Wauters‖

The uncertainty in the Magneto-Optical Trap (MOT) position and shape are a central concern for the determination of the β-ν correlation. Various calibrations have been devised in order to measure and cross-check the position and shape of the MOT, aiming for 10 μm accuracy[1]. In particular, the TOF measurements of photoionized ^{4}He are a comprehensive check of both MOT properties and the electric field parameters; however, these calibrations require knowing the profiles of the ionizing laser and MOT, and rely on a stable trap. In November 2016, MCP images of Penning ions produced by ^{4}He showed unexplained jumps and drifts in the MOT transverse position up to 100 μm between calibration runs. To diagnose this instability independent of the calibration, we measured the MOT shape and position by imaging the ^{4}He MOT with a new CMOS camera (Fig. 3.4-1).

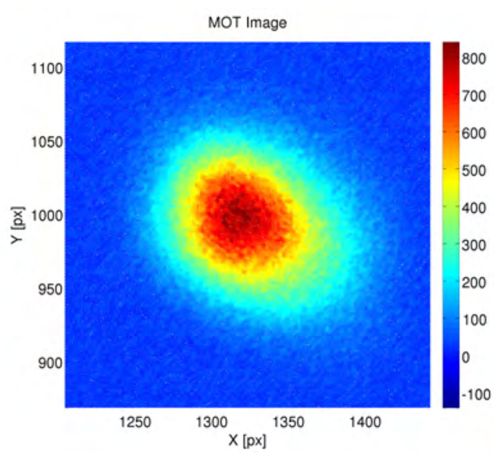

Figure 3.4-1. Processed CMOS camera pixel image of ^{4}He MOT where Y is the chamber vertical direction (Z). The MOT relative vertical position and width are determined in pixels by fitting the image to a 2D Gaussian and then converted to mm using the ruler calibration (Fig. 3.4-2). The MOT width ranges from 300 to 600 μm depending on the laser power and quadrupole field settings (100 px $\approx$ 2.4 mm).

---

*Physics Division, Argonne National Laboratory, Argonne, IL.

†LPC-Caen, ENSICAEN, Université de Caen, Caen, France.

‡Ecole National Superieur d'ingenieurs de Caen, Caen, France.

§Paul Scherrer Institute, Villigen, Switzerland.

¶Department of Physics and Astronomy and National Superconducting Cyclotron Laboratory, Michigan State University, East Lansing, MI.

‖Institut für Kernphysik, Johann-Joachim-Becherweg 45, Johannes Gutenberg-Universität Mainz, Mainz, Germany.

[1]CENPA Annual Report, University of Washington (2016) p. 45.

The CMOS camera focuses at the center of the chamber through a port. To calibrate it, we image a laser-etched ruler grid which rests on the top electrode of the array and extends into the image plane. The image of the ruler is then processed to obtain a linear relation between pixels and mm in the vicinity of the MOT based on microscope measurements of the ruler (see Fig. 3.4-2). To do this, the raw ruler image in pixels is first integrated over a chosen range in X to produce a profile in Y. The position of the grid marks manifest themselves as dips in the profile, which are fit to Lorentzians to obtain the grid mark positions in pixels. The dip positions are in turn fit to the microscope measurements of the grid marks. For now, only the vertical direction, Y, is directly calibrated. The resolution and relative accuracy of the calibration was determined by comparing calibrations of different ruler images at one X position on the ruler. We are able to resolve individual grid line locations on images to within 10 μm, and both the microscope measurments and the camera images show the grid to be linear to within 10 μm. Though the precise resolution of the microscope measurments is unknown, a maximum deviation of 15 μm was observed between the microscope measurements and the camera images. We therefore estimate this to be the relative accuracy of the calibration. The calibration is used with additional routines that process and fit the MOT images (Fig. 3.4-1). These routines were used to analyze trends in the MOT position and width as a function of time, laser power, and magnetic field supply current.

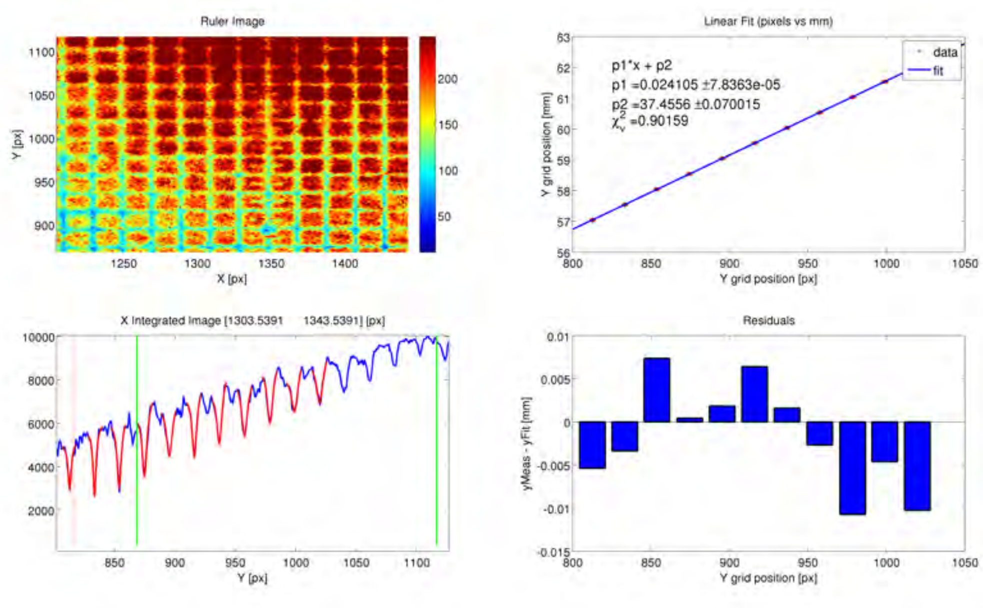

Figure 3.4-2. Calibration of the CMOS camera ruler image. *Top-left:* Ruler image in X and Y pixels for MOT fit region, where Y is the chamber vertical direction (Z). *Bottom-left:* Fit of Y profile dips to obtain grid mark positions in pixels. The red dotted line indicates graphically identified ruler "origin". The green vertical lines correspond to the Y range of the MOT image in Fig. 3.4-1. Dips beyond 1030 pixels were not fit since microscope measurements of those grid marks were not available. *Top-right:* Linear fit of the imaged grid marks to their microscope-measured positions in the MOT region. *Bottom-right:* Residuals of the *top-right* fit in mm.

In January 2017, the camera imaging along with active monitoring of the laser beam power confirmed the instability of the MOT position over time, showing fluctuations as large as 100 μm occurring within 10 minutes (Fig. 3.4-3). Furthermore, it showed that the position tracked linearly with fluctuations in the laser beam power and that the vertical position sensitivity to power fluctuations was large: 30 μm/5%. The dependence of the MOT position on laser beam power arises from a power imbalance between the incident and reflected trapping beams at the MOT position. This imbalance comes from reflective losses on the mirrors but can be compensated by the slight convergence of the beams which concentrates the beam power along its path. If the balance between reflective losses and beam convergence is not perfect at the position of the MOT (as dictated by the magnetic quadrupole field), the MOT will be offset to a degree dependent on the incident power.

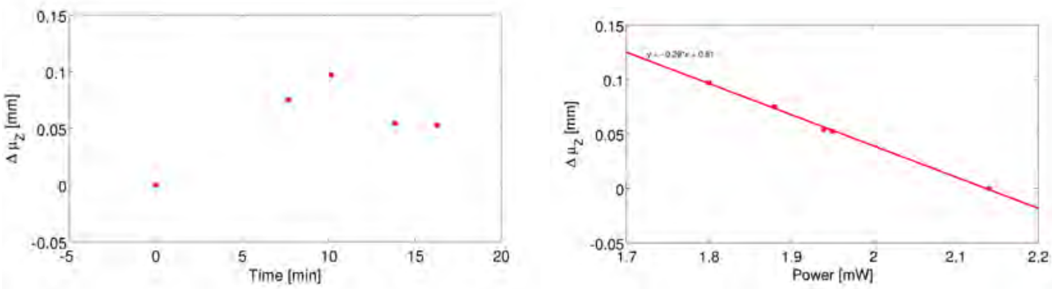

Figure 3.4-3. *Left:* Change in the MOT vertical position over time due to power instability. *Right:* Replotted as a function of monitored laser power. In this setup the measured power was a small fraction of the power diverted from MOT2 via a polarizing beam splitter and is proportional to the delivered power. The dependence of the vertical position on laser power is 30 μm/5%. A 5% change corresponds to about 1 mW of the normally delivered power.

To stabilize the laser power, we now monitor the return beam power with a photodiode and feed the signal into a PID device that controls the amplitude of the RF signal that powers the MOT2 acousto-optic modulator (AOM). The signal amplitude dictates how intense the AOM sound wave is and thus how much of the beam is diffracted into the frequency-shifted sideband used for trapping. Using the PID feedback, the laser power can be controlled to within 0.5% (compared to the 20% fluctuations seen prior).

The dependence of MOT transverse (μ_R) and vertical (μ_Z) position on laser power was measured and optimized as a function of beam focusing, where focusing was adjusted by changing the distance of the focusing lens from the MOT2 fiber output. The measured dependence on power for various lens positions is shown in Fig. 3.4-4. The smallest dependence on the power in Z achieved was 3 ± 5 μm/mW for the 19.5 mm lens position (where 1 mW corresponds to 5% of the nominal laser power). Due to the difference in path lengths and reflective losses between the three beams, only one dimension can be optimized at a time. So although the dependence is diminished for the vertical direction, it ends up larger for the transverse direction. The transverse position dependence on power for the 19.5 mm position was increased to -65 ± 4 μm/mW. For the 1% measurement of a, the transvers MOT position is negligible up to several hundred μm, and unlike for the vertical position, we are able to monitor the X and Y position using the MCP Penning ion image independent of the

TOF spectrum. Furthermore, since the PID limits power instability to less than 100 μW, the corresponding instability in transverse and vertical positions due to power fluctuations is limited to less than 7μm and 1 μm respectively. The MOT width dependence on power does not significantly change with focusing, consistently increasing 10-30 μm/mW for all lens positions measured.

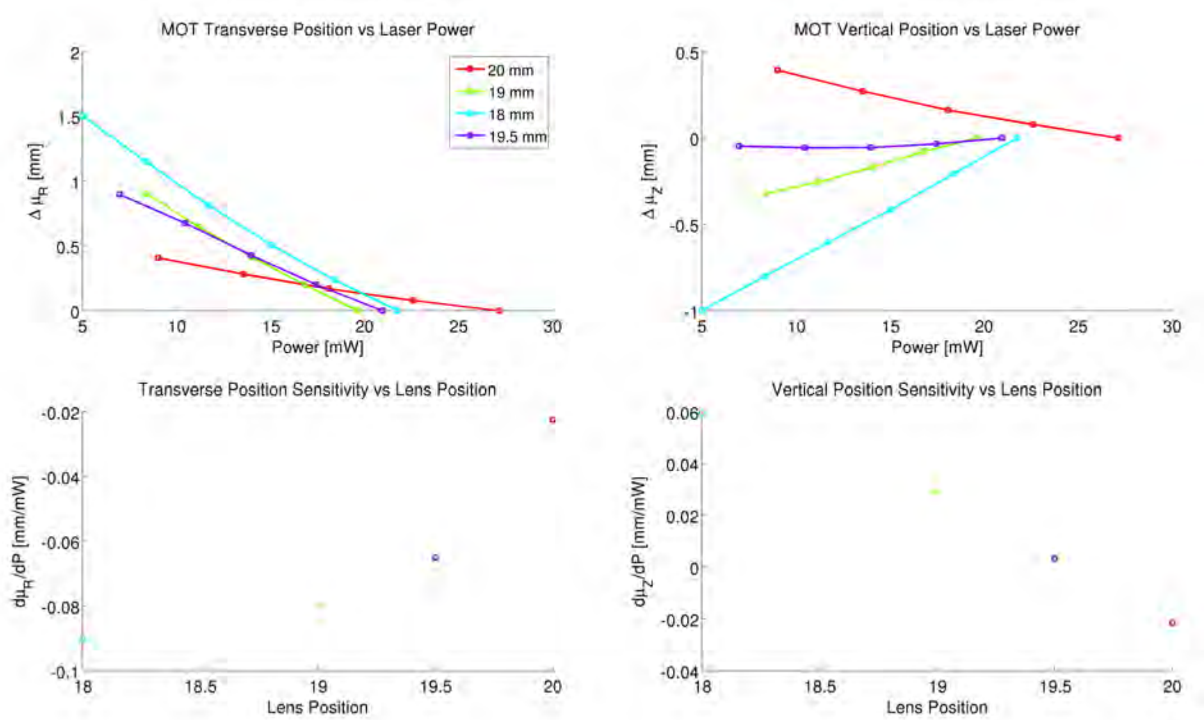

Figure 3.4-4. *Top:* Change in transverse ($\Delta\mu_R$) and vertical ($\Delta\mu_Z$) MOT positions as a function of laser power for different focusing lens distances from the fiber. *Bottom:* Position sensitivity to power with lens position.

The position of the MOT as a function of the Z coil supply current was measured to be 12.5 μm/mA. Synchronous monitoring of the MOT position and the supply current over a period of 14 hours showed drifts in the current below 0.05 mA, contributing to drifts in the vertical position on the sub-μm scale.

Fig. 3.4-5 shows 20 and 40 μm drifts in the transverse and vertical MOT positions over the 14 hour period with the PID power stabalization. The sources of this remaining drift is unknown, but we have ruled out laser power and Z coil supply current instability as dominant sources. This level of stability, accompanied by constant monitoring of the X and Y positions during runs with the MCP Penning ion image, may suffice for the purpose of the ^{4}He photoion TOF calibration and for the measurement of a, provided that we see the same level of stability in the photoion data and the MCP image. The next steps are to confirm this stability *in situ*, with the MCP image and ^{4}He photoion TOF data.

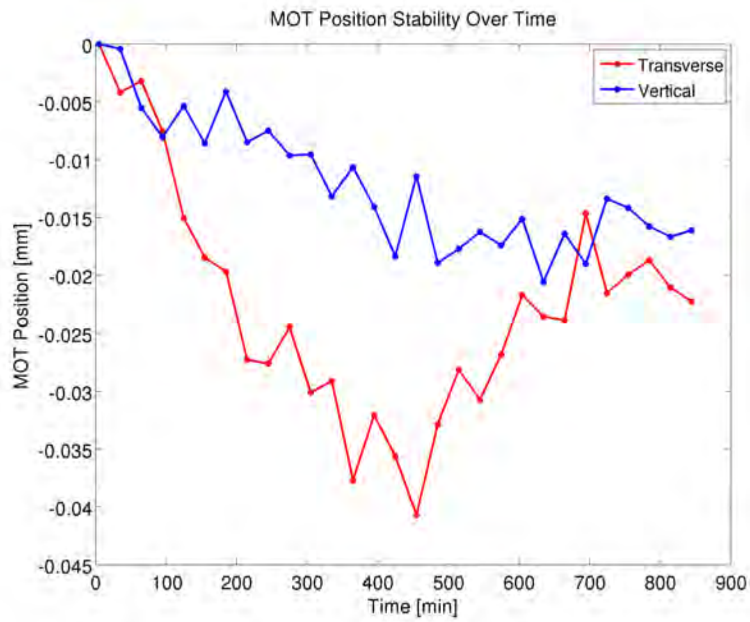

Figure 3.4-5. 14 hour stability of the transverse and vertical MOT positions.

Dependence of the MOT position on laser frequency was also observed. Although the laser frequency is stably locked for a given isotope, the relative offset in frequency for ^{4}He versus ^{6}He may cause differences in position. This remains to be measured.

Finally, determination of the absolute MOT vertical position with respect to the MCP using the CMOS camera image calibration requires accurate measurements of the electrode array geometry. Current methods for determining the geometry via a mechanical inspection[1] limit the accuracy of the position to 60 μm, which systematically shifts a by 0.90% according to MC Simulation studies. The electrode array geometry measurements are also key for an accurate simulation of the electric field. Better determination of the geometry will be a priority in the near future.

[1]CENPA Annual Report, University of Washington (2015) p. 39.

3.5 Position-dependent timing response of the MCP detector

Y. S. Bagdasarova, K. Bailey*, X. Fléchard†, A. García, S. Gilligan, R. Hong*, M. Imbault‡, M. Kossin, A. Knecht§, A. Leredde*, E. Liénard†, P. Müller*, O. Naviliat-Cuncic¶, T. P. O'Connor*, F. Otto, J. Pedersen, E. Smith, D. W. Storm, H. E. Swanson, and F. Wauters‖

The Li-ion kinematics are determined with the help of a time of flight, defined as $TOF \equiv T_{MCP} - T_{PMT} - T_0$, where T_{MCP} and T_{PMT} are the readout times for events that trigger the MCP and the photomultiplier tube (PMT), respectively, and T_0 is a correction for the delays of the detectors, and associated cables and electronics. Currently, two different calibrations[1] are in place to measure T_0: (1) a measurement of the TOF peak for the cascade decay of a ^{207}Bi source and (2) a measurement of the two TOF peaks produced by relativistic beta particles hitting both detectors during the ^{6}He data run. The present accuracy for either method is 200 ps, and we attribute this to the difference in timing response of each detector for a particle type. This timing accuracy is not enough to achieve a 1% measurement of a, so for now we leave T_0 as a floating parameter in the final fit while we try to better characterize the timing response of our detectors.

We observed a relative timing difference as large as 500 ps across the MCP in both the ^{207}Bi timing peak and the diffuse ^{6}He timing peak produced by betas traveling from the MCP to the scintillator (Fig. 3.5-1). There is a single pick up for the back of the MCP whose signal is used to clock T_{MCP}, and we attribute the position-dependence to the different distances signals must travel to reach it, confirming that the trend is consistent with its location on the MCP. To address this, we have begun developing a position-dependent correction to T_{MCP} in the data analysis, based on the analysis of the diffuse ^{6}He data.

For detected betas, the MCP time response is also correlated with MCP charge collection Q_{MCP}, which correlates with the penetration depth of particles within the MCP channel. The betas with higher Q_{MCP} values correspond to interactions that occur close to the surface of the MCP, as for ions. To characterize the MCP response for ions, we choose to look at beta events with $Q^{\beta}_{MCP} > 0.5\langle Q^{ion}_{MCP}\rangle$, where TOF cuts are made to select for ion events or beta events in the diffuse data. Like T_0, the average gain $\langle Q_{MCP}\rangle$ also strongly depends on the MCP position (Fig. 3.5-2). To deal with this in the analysis, the MCP is divided into cells. $\langle Q^{ion}_{MCP}\rangle_i$ is calculated for each cell i, and the cut $Q^{\beta}_{MCP} > 0.5\langle Q^{ion}_{MCP}\rangle_i$ is applied cell by cell. The relative difference in the timing peak for each cell is plotted in (Fig. 3.5-1) and represents the cell-by-cell correction to T_{MCP}.

*Physics Division, Argonne National Laboratory, Argonne, IL.
†LPC-Caen, ENSICAEN, Université de Caen, Caen, France.
‡Ecole National Superieur d'ingenieurs de Caen, Caen, France.
§Paul Scherrer Institute, Villigen, Switzerland.
¶Department of Physics and Astronomy and National Superconducting Cyclotron Laboratory, Michigan State University, East Lansing, MI.
‖Institut für Kernphysik, Johann-Joachim-Becherweg 45, Johannes Gutenberg-Universität Mainz, Germany.

[1] CENPA Annual Report, University of Washington (2016) p. 48.

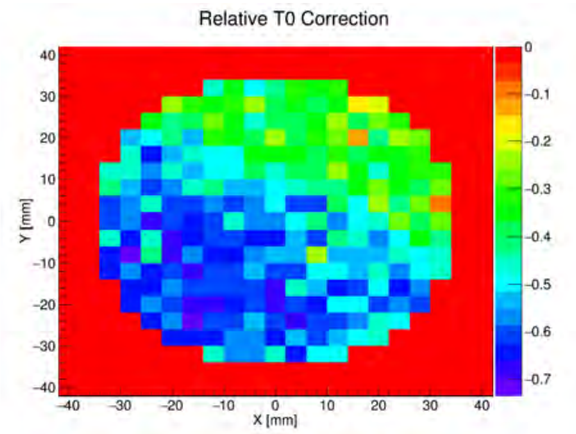

Figure 3.5-1. Colormap of the MCP position-dependent timing response for the diffuse ^{6}He data taken in June. There is a relative timing difference of 500 ps across the detector. The colorbar units are in ns.

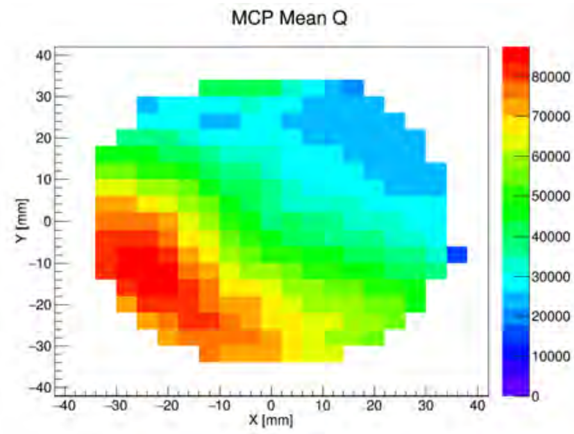

Figure 3.5-2. Average gain of the MCP for ions $< Q^{ion}_{MCP} >$ as a function of MCP position.

The size of each cell is dictated by the statistics of the diffuse data runs. To better characterize the correction and to avoid discretization effects we fit the correction to a polynomial $\Delta T_0(x, y)$.

Care must be taken to not include the beta TOF from the MCP to scintillator in the T_0 correction. The physical TOF correlates with the MCP position and beta energy as well, and accounting for it should reduce the timing spread for each cell and remove the position-dependence due to the distance of travel. The relative timing difference that remains for each cell will be used to obtain the MCP-specific timing correction.

3.6 High-voltage monitoring

Y. S. Bagdasarova, K. Bailey[*], X. Fléchard[†], A. García, S. Gilligan, R. Hong[*], M. Imbault[‡], A. Knecht[§], A. Leredde[*], E. Liénard[†], P. Müller[*], O. Naviliat-Cuncic[¶], T. P. O'Connor[*], F. Otto, J. Pedersen, E. Smith, D. W. Storm, H. E. Swanson, and F. Wauters[‖]

Fig. 3.6-1 shows the high-voltage (HV) electrode system for the second ^{6}He Magneto-Optical Trap (MOT2). It consists of six Spellman MP Series regulating 5-kV supplies which are

[*]Physics Division, Argonne National Laboratory, Argonne, IL.
[†]LPC-Caen, ENSICAEN, Université de Caen, Caen, France.
[‡]Ecole National Superieur d'ingenieurs de Caen, Caen, France.
[§]Paul Scherrer Institute, Villigen, Switzerland.
[¶]Department of Physics and Astronomy and National Superconducting Cyclotron Laboratory, Michigan State University, East Lansing, MI.
[‖]Institut für Kernphysik, Johann-Joachim-Becherweg 45, Johannes Gutenberg-Universität Mainz, Mainz, Germany.

floated and stacked using Ultravolt EFL 30-kV isolators in order to provide upwards of 30 kV on the sixth electrode. The supplies are remotely controlled via the isolators, which limit the accuracy of the high voltage output to 0.2% for each supply. If this uncertainty is systematic across all supplies, it registers as an overall uncertainty in the electric field strength. If this uncertainty differs across supplies, it registers as an uncertainty in the electric field shape. To achieve the desired 1% measurement of a, the uncertainty in the absolute accuracy of the individual supply voltages must be reduced to 0.05%.

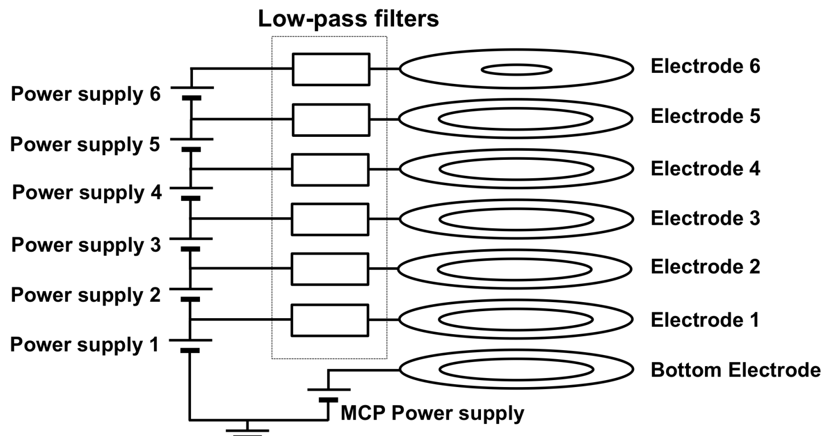

Figure 3.6-1. HV electrode array for the MOT2 chamber, where the decay of ^{6}He atoms are observed.

Last year, we developed and installed a HV monitoring system capable of simultaneously measuring the outputs of all six supplies with respect to ground via six HV dividers (Fig. 3.6-2).[1] Since then, we have been working to improve and optimize the monitoring system to meet our uncertainty requirements. Because the absolute tolerance of the HV dividers themselves are only 1%, they must be individually calibrated against our 0.02% accurate probe to make them feasible as a precision monitoring system. Great care has been taken over the last year to refine portions of our system to improve these calibrations.

After the initial installation period, we began experiencing voltage spikes of up to 60 V across the HV dividers from corona discharge, and eventually ran into sparking from the HV leads of the dividers to their grounded housing. To alleviate these problems, we modified the lid of the housing, increasing the separation between the lid and divider by a factor of 5. Additionally, we applied a commercial Xylene based corona-suppressing varnish to the solder joints of the HV dividers. The sparking has been eliminated, and while the voltage spikes are still present, they've been reduced to 20 V or less. As an added effort to mitigate the effects of these voltage spikes on the calibration, we've developed a rejection algorithm in the analysis stage of our system (Fig. 3.6-3).

For measurements of the system, we initially used a National Instruments ADC to read out the HV dividers, but quickly ran into problems with measurement ghosting in the ADC and an increased noise floor from the nearby power supplies, making the monitoring system

[1] CENPA Annual Report, University of Washington (2016) p. 51.

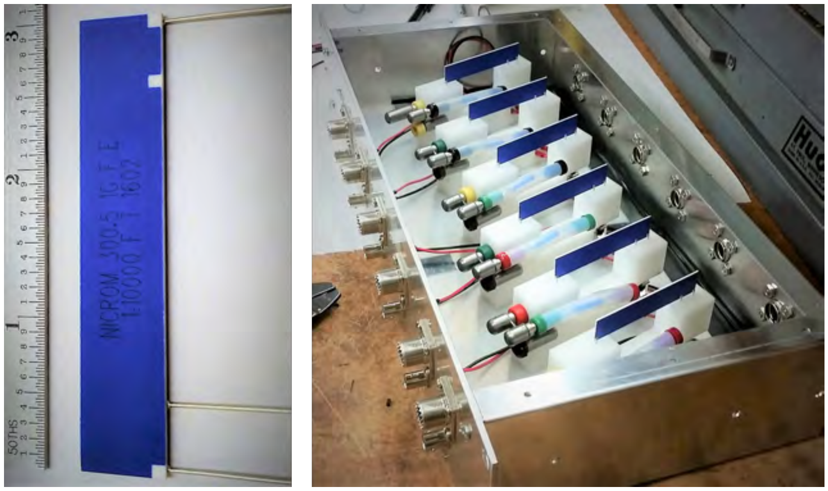

Figure 3.6-2. *Left:* A 1:10,000 high-voltage divider for the HV monitoring system. *Right*: Installation of monitoring system components in low-pass filter box.

unsuitable for our needs. As a solution, our Electronics Shop here at CENPA designed and built a high-speed relay based multiplexer, capable of sequentially multiplexing up to 7 inputs and sending their individual signals to our 6.5 digit multimeter (Fig. 3.6-4). The ghosting has been bypassed, the noise floor has been reduced, and with the use of our multimeter, our resolution has increased as a result.

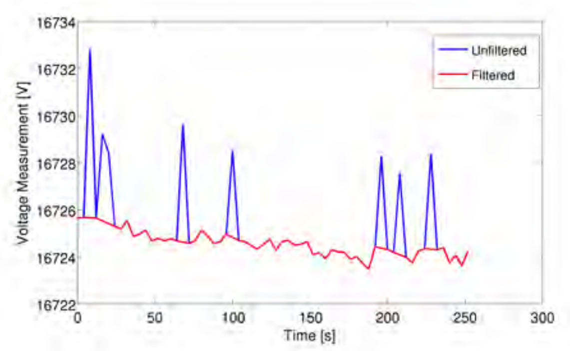

Figure 3.6-3. Plot of the voltage spike rejection algorithm, with unfiltered (rejected) points in blue and filtered points in red.

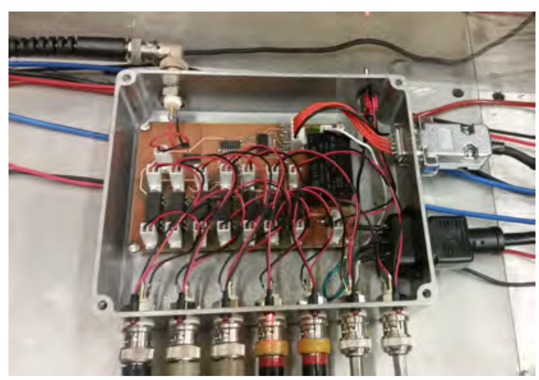

Figure 3.6-4. High-speed multiplexer designed and built at CENPA.

Thus far, our voltage monitoring system has achieved an absolute accuracy uncertainty of 0.2%. We are continuing to make improvements to the system to meet our uncertainty goal of 0.05%, and hope to have it completed within the next few months.

3.7 Recoil-ion charge-state distribution in ^{6}He β-decay

Y. S. Bagdasarova, K. Bailey*, X. Fléchard†, A. García, S. Gilligan, R. Hong*, M. Imbault‡, A. Knecht§, A. Leredde*, E. Liénard†, P. Müller*, O. Naviliat-Cuncic¶, T. P. O'Connor*, F. Otto, J. Pedersen, E. Smith, D. W. Storm, H. E. Swanson and F. Wauters‖

After the nuclear beta decay, with the associated change in nuclear charge, the electrons, initially in ^{6}He orbits, can be considered in linear combinations of ^{6}Li orbits, including the continuum. Thus, the ^{6}Li ions can come with charge states between $q = +1$ to $q = +3$. The decay of ^{6}He, due to the accessible nature of the atomic structure calculations in present days, can be taken as a test of the approximations that are needed for this and for similar problems.

A recent calculation for ^{6}He, taking into account a fairly complete set of atomic wave functions, was performed with predictions on the final state charge distributions.[1]

The issue is of relevance for determining the $\beta - \nu$ correlation because the probability of distributions into the different charge states depends on the recoil energy. In our experiments for determining the $\beta - \nu$ correlation, we do kinematics within an electric field, so our results depend on correctly assessing the recoil-ion energy dependence on the charge. We have consequently spent some effort in testing the calculations. Fig. 3.7-2 shows Monte Carlo simulations assuming that the probability distributions into the three charge states are equal. Fig. 3.7-1 shows data from our experiment.

Our results are shown in Table 3.7-1 and have now been submitted for publication. As can be observed, while we find agreement with the predictions for $q = 2$ we find significant (up to $\sim 19\sigma$) disagreements for the other charge states. This is of some concern and we are in communication with Gordon Drake, who is considering improvements to the calculation.

Ion	Theory[1]	This work
Li^+	88.63(2)	90.5(1)
Li^{2+}	9.5(1)	9.5(1)
Li^{3+}	1.9(1)	≤ 0.01

Table 3.7-1. Comparison of calculated versus measured ^{6}Li ion charge fractions (in %) for ^{6}He decays from $^3S_1$ atomic metastable state.

*Physics Division, Argonne National Laboratory, Argonne, IL.
†LPC-Caen, ENSICAEN, Université de Caen, Caen, France.
‡Ecole National Superieur d'ingenieurs de Caen, Caen, France.
§Paul Scherrer Institute, Villigen, Switzerland.
¶Department of Physics and Astronomy and National Superconducting Cyclotron Laboratory, Michigan State University, East Lansing, MI.
‖Institut für Kernphysik, Johann-Joachim-Becherweg 45, Johannes Gutenberg-Universität Mainz, Mainz, Germany.

[1] E. E. Schulhoff and G. W. F. Drake, Phys. Rev. A **92**, 050701 (2015).

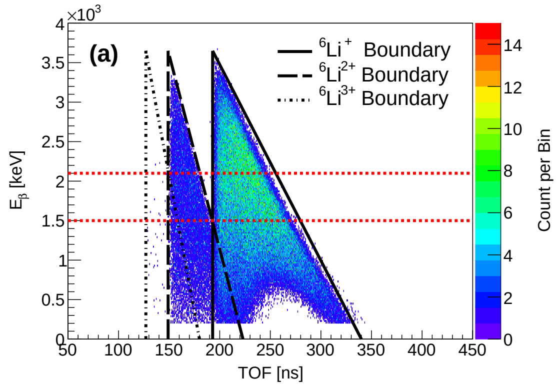

Figure 3.7-1. E_β-vs.-TOF from trapped-^{6}He experimental data. The events observed within the $q = +3$ boundary are expected from background due to non-trapped ^{6}He atoms so we find no net ^{6}Li with $q = +3$.

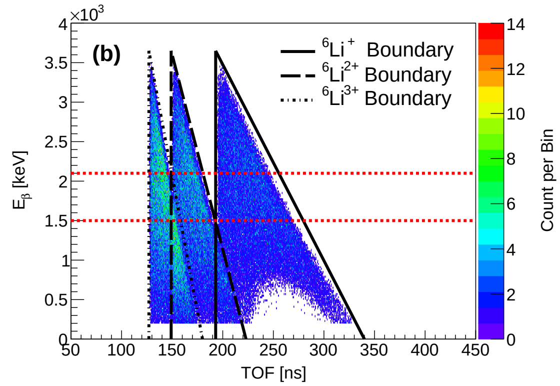

Figure 3.7-2. Monte Carlo calculations of E_β-vs.-TOF. A non-physical scenario of equal fractions on the three different charge states is plotted to visualize the event distribution. The red dashed lines indicate cuts in E_β that allow complete separation between the different charge states.

3.8 Toward measurement of the ^{6}He β-spectrum with Cyclotron Radiation Emission Spectroscopy

M. Fertl, A. García, M. Guigue[*], D. Hertzog, P. Kammel, K. S. Khaw, A. Leredde[†], P. Müller[†], N. S. Oblath[*] R. G. H. Robertson, G. Rybka, G. Savard[†], D. Stancil[‡] H. E. Swanson, B. A. VanDevender[*], and A. R. Young[§]

We have developed an idea to use the Cyclotron Radiation Emission Spectroscopy (CRES) technique of Project 8 to measure the β spectrum from ^{6}He to search for tensor currents.

Briefly, after production the ^{6}He atoms would be sent to a circular RF guide inside a superconducting solenoid, as shown in Fig. 3.8-1. The solenoid can generate highly uniform fields in the range $1-7$ Tesla. Additional non-superconducting coils will be used to produce a magnetic trap for the β's which will produce coherent cyclotron radiation in the guide. Fig. 3.8-2 shows the RF setup which will work in the 18-24 GHz range.

[*]Pacific Northwest National Laboratory, Richland, WA.
[†]Physics Division, Argonne National Laboratory, Argonne, IL.
[‡]Electrical Engineering Department, North Carolina State University, Raleigh, NC.
[§]Physics Department, North Carolina State University, Raleigh, NC.

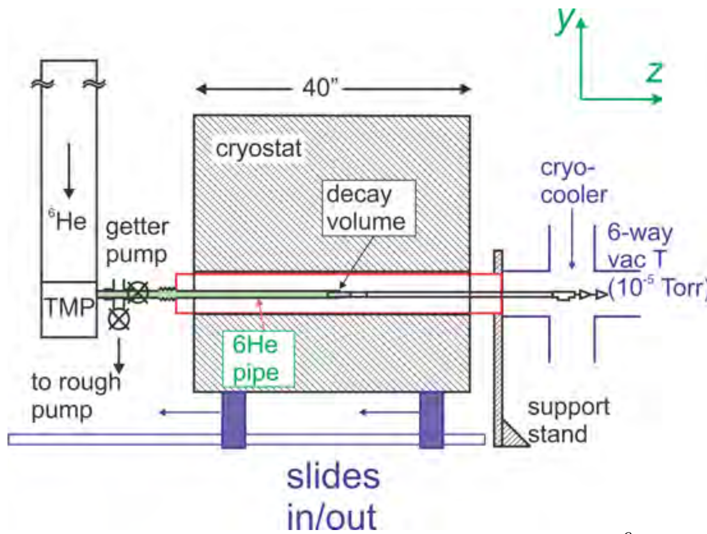

Figure 3.8-1. Sketch of setup for detecting cyclotron radiation from ^{6}He. The ^{6}He atoms are sent towards a turbo-molecular pump which compresses the gas into a "^{6}He pipe". The latter connects to the circular RF guide located inside the bore of a superconducting magnet. The decaying volume will be separated from the rest of the RF system by kapton windows.

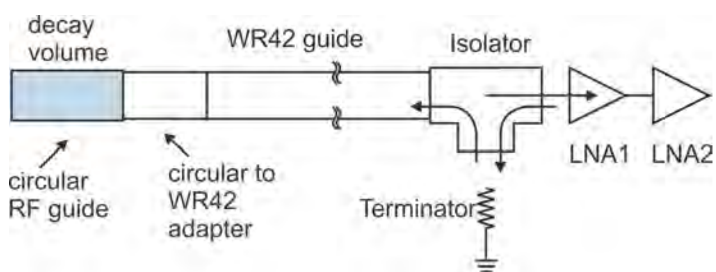

Figure 3.8-2. RF components: the circular guide will connect to a WR42 guide connecting to low-noise amplifiers (LNA). The isolator between the WR42 guide and LNA1 is used to minimize RF reflection.

Fig. 3.8-3 shows Monte Carlo simulations indicating the different parts of the spectrum that would be measured for different magnetic field intensities. Fig. 3.8-4 shows the extracted values of b at each field value independent of the other points. Further normalizing data taken at different fields by using a stable scintillator at the position indicated as "getter pump" in Fig. 3.8-1 will further increase precision.

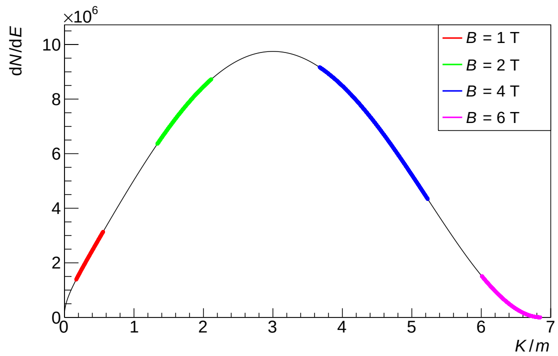

Figure 3.8-3. Monte Carlo simulation of beta spectra versus kinetic energy (in units of m) in 1 keV bins showing data points within the 18-24 GHz frequency window. The simulated data are shown for $B = 1$ (red), 2 (green), 4 (blue), 6 (magenta) T. The total number of events in the whole beta spectrum is 2×10^{10} for this simulation.

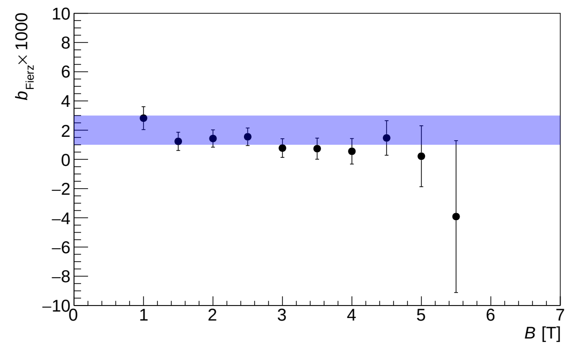

Figure 3.8-4. Extracted b_{Fierz} from the simulated data shown at left. In the simulation we assumed $b_{\mathrm{Fierz}} = 0.002$. The shaded area indicates the $\pm 10^{-3}$ region.

Our proposal is to explore this method with neutral ^{6}He diffused through the decaying volume to make a proof of principle of the basic method. Later we would move to an ion-trap system that will allow minimizing systematic uncertainties. A summary of the main systematic uncertainties found in the study for the two setups are shown in Table 3.8-1.

	No trap	Ion trap
Magnetic field uncertainties	10^{-4}	$< 10^{-4}$
Wall effect uncertainties	10^{-3}	0
RF pickup uncertainties	10^{-4}	10^{-5}
Misidentification of events	10^{-4}	5×10^{-5}

Table 3.8-1. Summary of expected systematic uncertainties on b. For comparison, the best limits on b, from LHC data, are $b < 5 \times 10^{-3}$.

4 Precision muon physics

4.1 Overview of the muon physics program

M. Fertl, A. T. Fienberg, A. García, N. S. Froemming, J. Hempstead, D. W. Hertzog, R. Hong*, P. Kammel, J. Kaspar, K. S. Khaw, B. K. H. MacCoy, E. Muldoon, M. H. Murray, R. E. Osofsky, D. J. Prindle, R. A. Ryan, D. J. Salvat, M. W. Smith, and H. E. Swanson,

The Precision Muon Group is involved in fundamental experiments that determine Standard-Model parameters, low-energy effective-field-theory constants, or provide sensitive tests for new physics. With strong CENPA support, the group has carried out a significant number of hardware development projects and has led several important data-taking campaigns. During this Annual Report period, we completed the data-taking phase of the MuSun experiment (P. Kammel, Co-Spokesperson) at Paul Scherrer Institute. We completed our third Test Beam Experiment (J. Kaspar, Spokesperson) at SLAC to make final tests of the complete precession frequency instrumentation being built for the Muon $g-2$ experiment at Fermilab. Our Precision Magnetic Field group (Deputy Team Leader E. Swanson) completed the shimming of the superconducting storage ring magnetic field, with great success. Finally, the many tens of dozens of components being prepared for the commissioning of the Muon $g-2$ experiment (D. Hertzog, Co-Spokesperson) as a whole are nearly all installed with beam commissioning still on track to start in June 2017. The era of data taking here is nearly upon us. The UW group has 8 Ph.D. students on these two experiments at present.

With the final run in Fall 2016 of the MuSun experiment, we accomplished our goal of acquiring the statistics needed for a precision measurement of the μd capture rate. The very challenging analysis that lies ahead will occupy our UW group throughout the next year and longer. MuSun graduate student Murray defended his thesis, which was devoted to developing the delicate correction mathematics necessary to correct the data for the perturbation from certain muon catalyzed fusion events. Graduate students Ryan and Muldoon are leading the high-statistics data set evaluations from more recent running years, and Research Associate Salvat is leading many of the systematic error studies. Data analyst Prindle has been leading the detailed Monte Carlo simulation effort.

The $g-2$ Experiment is about 95% complete at the time of this writing. Over the past year, the Magnetic Field Team within the Collaboration completed an iterative and exhaustive process to shim the magnetic field to a high degree of uniformity. Their efforts – locally led by Swanson, Smith, Osofsky, and Fertl – resulted in a 3-fold improvement compared to the best result achieved at BNL for E821. The UW team has since installed all of the locally built fixed NMR probes and instrumented them with locally built electronics. The Field DAQ was developed by UW graduate student Smith, who will graduate in the next few months. Fertl and graduate student Osofsky built a device to measure the radial magnetic fields and they carried out the measurements, obtaining somewhat surprising results. Graduate student Froemming has continued to lead in the GEANT-based simulation effort of the muon injection

*Presently at Argonne National Laboratory, Lemont, IL.

and storage devices, leading to predictable tuning settings that will soon be tested against beam. On the detector side, we completed testing, fabrication, and assembly of the 1296 PbF2 crystal / SiPM detector combinations and we installed them into their custom houses (grad student Hempstead, tech Huehn). The completed calorimeter worked flawlessly during a 3-week test at SLAC. We are engaged in the analysis of these data and drafting a paper. We also published a comprehensive paper on our SiPM electronics development, including key calorimeter performance tests [1]. Kaspar has been named the overall Detector Coordinator for $g-2$, which entails oversight of not only the UW systems, but also the electronics, DAQ, calibration, tracker, and in-beam instrumentation. Research Associate Khaw and graduate student Fienberg have led the software analysis effort from raw unpacking, through physics object creation, to online data monitoring, and finally to offline full analysis. Kammel, and new graduate student MacCoy, have been designing the new IBMS (Inflector Beam Monitoring System) scintillating fiber hodoscopes to be mounted in front of, and inside, the narrow muon entrance corridor.

Highlights of our research program and details on the specific technical contributions are described in the series of reports that follow this introduction

[1] J. Kaspar *et al.*, "Design and performance of SiPM-based readout of PbF_2 crystals for high-rate, precision timing applications," JINST **12**, no. 1, (2017) P01009.

MuSun

4.2 Muon capture on deuterium, the MuSun experiment: Overview

D. W. Hertzog, P. Kammel, E. Muldoon, M. H. Murray, D. J. Prindle, R. A. Ryan and D. J. Salvat

The goal of the MuSun experiment is a 1.5% precision measurement of the rate of the weak semi-leptonic process

$$\mu + d \rightarrow n + n + \nu. \tag{1}$$

This process can be precisely calculated in the standard model, apart from a poorly known low-energy constant (LEC) involved in modern, QCD-based, effective field theory (EFT) calculations of weak nuclear reactions. MuSun plans to measure this LEC with 5 times better precision than presently available from the two-nucleon system. This LEC is an important ingredient in developing an EFT-based theory of nuclear forces and is needed for calculating more complicated weak nuclear processes of topical interest, like double beta-decay rates. Regarding the family of two-nucleon weak-interaction processes, the determination of this LEC in muon capture will provide the required input for model-independent calculations of astrophysical processes of fundamental importance, like pp fusion or νd scattering, whose rates have never been measured directly. For a more detailed discussion of the the physics aspects of this field we refer to review[1]. More recent theoretical work includes the first calculations of the muon capture rate for process (1) within a self-consistent chiral perturbation theory framework[2] and a pioneering lattice QCD calculation[3] of the relevant LEC.

MuSun developed a novel strategy to measure Λ_d, the capture rate from the doublet hyperfine state of the muonic deuterium atom in its 1S ground state. Muons are stopped in an active target, a time projection chamber (TPC) filled with deuterium gas and the disappearance rate λ_- of negative muons in the target is determined, by observing the electrons from muon decay. The capture rate is derived from the difference $\Lambda_d \approx \lambda_- - \lambda_+$, where λ_+ is the precisely known positive muon decay rate. In a simplified overview (see Fig. 1), the detector consists of muon detectors (muSC, muSCA, TPC), electron detectors (ePC1/2, eSC) and neutron detectors (not shown). The experiment is performed in an international collaboration at the Paul Scherrer Institute (PSI), Switzerland, which provides the world's highest intensity/highest quality muon beams at low energy. Kammel serves as a co-spokesperson of the collaboration.

Experimental challenges were numerous, as this program attempts to improve the measurement Λ_d by about an order of magnitude beyond earlier experiments. A key aspect was the development of the cryogenic high-density TPC operating with ultra-pure deuterium, which needed an extensive development phase, followed by significant upgrades to attain reliable operation over long running periods and excellent energy resolution.

[1] Kammel, P. and Kubodera, K. *Annu. Rev. Nucl. Part. Sci.* **60**, 327-353 (2010).
[2] Marcucci, L. E. *et al.*, Physical Review Letters **108**, 052502 (2012).
[3] Savage, M. J. *et al.*, arXiv preprint arXiv:1610.04545 (2016).

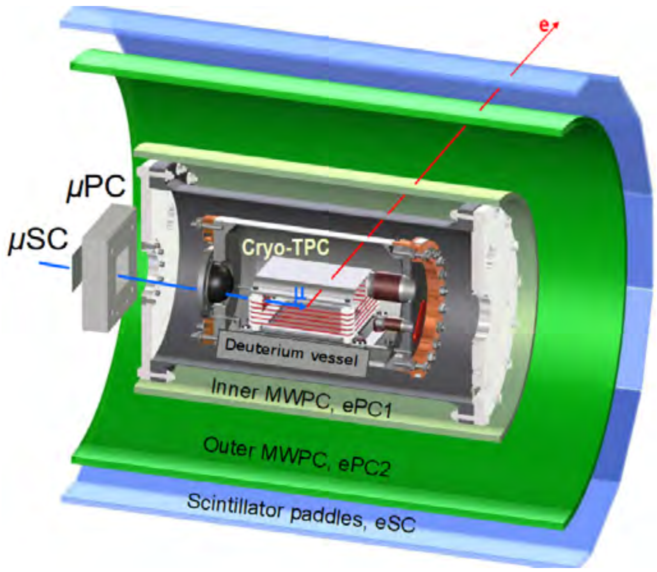

Figure 1: MuSun detector model. Muons pass through entrance detectors to stop in a deuterium target TPC. The decay electron is detected in two cylindrical wire chambers (green) and a 16-fold segmented scintillator array.

Data set	μ^-	μ^+
R2011	4.5×10^9	0.5×10^9
R2014	6×10^9	1.0×10^9
R2015	7×10^9	1.0×10^9

Table 4.2-1. Muon decay events collected in each production dataset.

The data taking phase of MuSun was completed in 2016. The experiment is still fully assembled at PSI and will remain so, until the first physics analysis is complete. Let us briefly recall the main steps towards achieving this challenging experimental goal. A first high statistics collection took place in 2011 (run R2011). Subsequently, the experiment had to be relocated into a different dedicated area. This allowed much better access and stability of the complex apparatus, but also cost more than a year in installation and commissioning of the new beam line. This time period was used to build a new TPC and implement new cryogenic preamplifiers, both designed at UW. Other systems, like the external monitoring of the gas purity were also improved and large neutron detectors installed in 2015. These improvements led to the highly successful production runs R2014 and R2015. A short run in 2016 was hampered by accelerator problems at PSI, but still provided useful information about important systematic issues. The statistics of fully reconstructed events used for the final lifetime histograms are shown in Table 4.2-1. Smaller data sets with positive muons were collected for systematic studies.

MuSun needs to measure Λ_d with an uncertainty $\delta\Lambda_d = 6$ Hz. The capture rate is derived from the difference between negative and positive muon decay rate, with the latter well-known from MuLan[1]. Thus the uncertainty in $\delta\Lambda_d$ is dominated by the MuSun measurement of λ_- in deuterium. If we assume equal statistical and systematic contributions to the final result, the statistics requirement for the number of fully reconstructed $\mu - e$ decays amounts to $\approx 1.2 \times 10^{10}$ events. The experiment was not yet fully optimized for R2011, but this run was instrumental for developing the strategy for constraining leading uncertainties in MuSun and informing the necessary upgrades. These were implemented for R2014 and R2015, and we obtain an estimated number of 1.3×10^{10} events for the high-quality production data. The statistics quoted come from preliminary analyses. We still have to establish the final analysis cuts which might result in some losses. Nevertheless, we are optimistic that the collected statistics will realize the design goal of our experiment. Thus, the priority in the coming year will be on data analysis towards a first physics result, which includes the full evaluation of data consistency, systematic uncertainties, as well as statistics after all cuts.

4.3 Correcting for Muon-Catalyzed Fusion in the TPC

D. W. Hertzog, P. Kammel, E. T. Muldoon, M. H. Murray, D. J. Prindle, R. A. Ryan, and D. J. Salvat

The Ph.D. dissertation of M. H. Murray (March 2017) describes a correction for a systematic error in the MuSun lifetime measurement related to muon-catalyzed fusion (MCF) events in the TPC, using the 2011 commissioning dataset. Approximately 6% of the time, muons form $d\mu d$ molecules in the TPC. The small size of these muonic molecules reduces the Coulomb barrier between the constituent deuterium nuclei, and fusion to either p-t or n-^{3}He rapidly occurs. Events with MCF have a decay time that is on average later than events without MCF; therefore, analysis cuts with an acceptance that differs between MCF and non-MCF events will distort the measured disappearance rate. In particular, the tracking algorithm used to determine the muon stop position in the TPC is affected by MCF, and the subsequent fiducial volume cut can accept or reject an excess of these events. Through analysis of data and Monte Carlo, we have identified the event topology that gives the most significant contribution to this effect: fusions with p-t in the final state, with proton tracks that cross the boundaries of the TPC pads along the longitudinal (z) direction.

We have devised a method for quantifying and correcting for this effect. The correction $\Delta\Lambda_d$ can be expresed as

$$\Delta\Lambda_d = k\frac{M}{N} \tag{1}$$

with N the known total number of muon stops in the TPC, M the number of excess accepted stops with p-t fusion, and k a constant of proportionality which must be determined by the data. We quantify the correction by using a tracking algorithm subject to MCF-related tracking errors that can be modeled analytically. The analytical model predicts the probability of incorrectly assigning the muon stop position versus the true muon position z, and we find it to be in good agreement with Monte Carlo predictions.

[1]Tishchenko, V. et al. *Phys. Rev.* **D87**(5), 052003 (2013).

To make this correction, we must estimate the distribution of muon stops within each of the coarsely-grained anode pads. To do so, the spatial distribution of stops versus z anode pad is fit to a gaussian. Being derived from the data, this observed distribution is affected by the errors in TPC tracking; using the probability model, the true underlying distribution of stops can be deconvolved, allowing us to determine the excess number of fusion events accepted or rejected by the fiducial volume cuts, M.

Finally, to determine the constant of proportionality k, the fiducial volume is divided into sub-volumes along z and the disappearance rate from each sub-volume is determined from the electron time distributions. This amplifies the effect of fusion interference, and by repeating the above analysis within each sub-volume we can compare excess fusion events M/N with measured disappearance rates, using a linear fit to determine k. This is shown in Fig. 4.3-1.

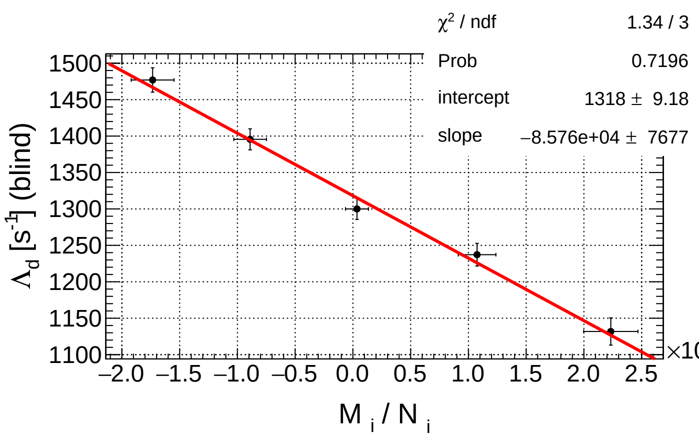

Figure 4.3-1. The observed disappearance rate from muon stops in each TPC sub-volume versus the calculated fraction of excess fusion events in each sub-volume. The linear fit determines k. The low χ^2 value is due to the conservative estimation of uncertainties in M/N.

This analysis leads to a correction $\Delta\Lambda_d = 2.0 \pm 1.4$ s^{-1} for the 2011 commissioning data for MuSun. This correction depends upon the exact muon stop distribution for the given dataset, and must be re-evaluated for the 2014 and 2015 production datasets; however, it shows that the fusion interference effect can be accounted for within our error budget of ~ 6 s^{-1}. The uncertainty can potentially be reduced further by utilizing more sophisticated energy cuts within the TPC, and by performing more detailed studies of the continuous distribution of muon stops in the TPC (Sec. 4.5). These improvements will be explored in forthcoming analyses of the production data.

4.4 Background subtraction techniques developed for analysis of R2014 dataset

D. W. Hertzog, P. Kammel, E. Muldoon, M. H. Murray, D. J. Prindle, R. A. Ryan, and D. J. Salvat

The data collected in the R2014 production run accounts for half of the full statistics of the MuSun experiment. A first full analysis of this dataset in 2016 revealed a large time dependent beam electron background caused by the fast electric kicker in the beam line. The kicker is operated in a muon-on-request mode to reduce muon pileup events, deflecting the incident beam once a muon enters the detector via a pair of deflection plates. There is an 800 ns delay for the plates to charge once the muon is observed, due to switching times and signal cable length, leading to a shift in the observed beam electron background rate.

A system to periodically trigger detectors in the absence of a muon was set up during portions of the R2014 data collection to measure the underlying accidental background. A change in the background rate after the 800 ns activation window of the kicker can be seen in Fig. 4.4-1.

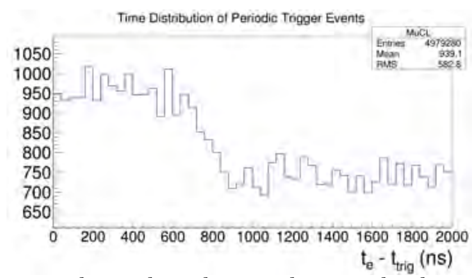

Figure 4.4-1. Underlying time dependent beam electron background measured with the periodic trigger in the absence of a muon. Note the change in rate before and after activation of the kicker at 800 ns.

For the periods where this periodic trigger was running, the independent measure of the beam electron time distribution can be used for a background subtraction. However, because the background is sensitive to changes in beam tune, another approach must be used for the data collection spans where the periodic trigger was not implemented. A technique has been developed, which utilizes event electron multiplicity to suppress either the electron background or suppress the decay distribution in order to resolve the underlying accidental distribution.

The overall time distribution can be written as a sum of the muon decay distribution and the kicker induced time dependent background,

$$e_{all}(t) = \epsilon\lambda e^{-\lambda t} + R_B(t) \equiv e(t) + R_B(t) \qquad (1)$$

where λ denotes the muon decay rate, ϵ is the electron detector efficiency, and $R_B(t)$ is the time dependent electron background rate.

If events with a single electron are selected, the decay component gets multiplied by the probability that an accidental was not detected, $(1 - P_a)$, and the accidental term by the probability that the decay electron was not detected, $(1 - \epsilon)$.

$$e_1(t) = e(t) \cdot (1 - P_a) + R_B(t) \cdot (1 - \epsilon) \tag{2}$$

With the small background rate, $R_B \sim 600\ Hz$, and high detector efficiency, $\epsilon > 70\%$, the decay term is practically unchanged, while the accidental background is suppressed, as seen in the green curve in Fig. 4.4-2.

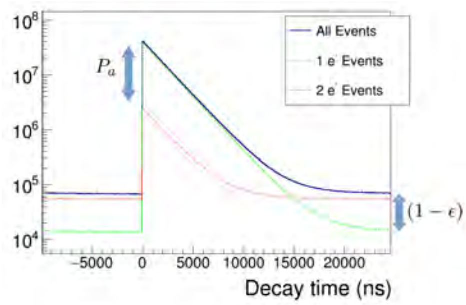

Figure 4.4-2. Time distributions of electron detection relative to the muon arrival with various electron multiplicities. All electron events are shown in blue. Events which contained only a single electron within the muon event window (green) show a suppressed background component. Conversely, events with two electrons in a given event window (red) suppress the decay component to better resolve the underlying time dependent background term.

Conversely, by requiring two electrons in the event window, the decay component is multiplied by the probability that an accidental was detected, and the background term by the probability that the decay electron was observed.

$$e_2(t) = e(t) \cdot P_a + R_B(t) \cdot \epsilon \tag{3}$$

In this case, the decay term is suppressed relative to the accidental term, as shown by the red curve in Fig. 4.4-2.

The single (e_1) and multiple (e_2) events are statistically independent, such that the e_2 histogram can be used to subtract the electron background from the e_1 lifetime. Working under the assumption that the accidental rate is equivalent between the two event selections, the e_2 background is scaled to the e_1 background at late times, then subtracted. This effectively removes the time dependent background, at the cost of a 10% reduction in statistics due to the remaining decay component in the e_2 distribution which is subtracted off. Lifetime fit results before and after this subtraction and the fit residuals for five independent subsets of the R2014 data can be seen in Fig. 4.4-3. The upper left corner shows the $400s^{-1}$ variation in the fitted rate without background subtraction in black. The large improvement in dataset consistency with the application of the background subtraction technique is shown in red. The 800ns step is seen clearly in the fit residuals (upper right), and this effect is suppressed once the background subtraction is applied (lower right). The remaining trend in the early fit residuals is due to fusion interference effects. A comparison of the fitted parameters and fit residuals for the datasets with the muon clock data show consistency between the muon clock and electron multiplicity subtraction methods.

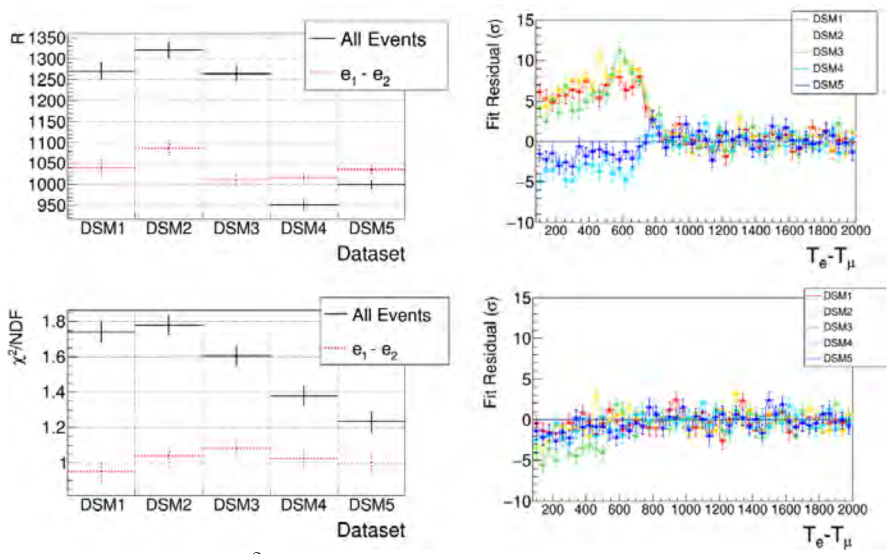

Figure 4.4-3. The rate and χ^2 values for lifetime fits using an exponential with constant background term before (black) and after (red) the background subtraction technique is applied to remove the time dependent background induced by the electronic kicker. Early fit residuals on the right show the suppression of the step at 800ns after background subtraction has been applied.

4.5 MuSun systematic effects run campaign

D. W. Hertzog, P. Kammel, E. T. Muldoon, M. H. Murray, D. J. Prindle, R. A. Ryan, and D. J. Salvat

During a four week beam-time period at PSI in the fall of 2016, we used specialized experimental configurations to study the most critical systematic effects for the MuSun experiment. In particular, we

- ran the experiment in a production-like mode, injecting known amounts of chemical impurities (most notably N_2) to observe the resulting signals in the gas chromatograph and in the TPC.
- implemented additional detectors with optimal sensitivity to beam-related backgrounds (Sec. 4.4) in order to characterize the spatial distribution, time-dependence, and detector response of these backgrounds.
- removed the TPC from the apparatus and replaced it with foils composed of the various materials used in the experiment in order to estimate the neutron yield from muon stops in these materials; this is needed for the analysis of muons stopping in wall materials (Sec. 4.6).

- performed fine scans of the beam momentum to determine the shape of the distribution of stopped muons; the fusion interference analysis (Sec. 4.3) depends upon the shape of this distribution, and improved knowledge could reduce the fusion interference uncertainty by approximately two-fold.

Here we focus on the first two of these studies.

The presence of nitrogen impurities in the TPC causes a systematic effect: muons from μ-d atoms can transfer to nitrogen to become μ-N, where the muon undergoes nuclear capture at a rate $\sim$ 150 times faster than on the deuteron, systematically increasing the observed disappearance rate in the experiment. The subsequent recoil energy of the daughter nucleus from nuclear capture on nitrogen deposits a signal in the TPC, and with proper cuts we can identify an excess of events with delayed, low energy pulses which should be proportional to the impurity concentration. This is a powerful *in situ* check of the standard chromatography method used to assess TPC purity. Further, we can inject known amounts of chemical impurities using mass-flow controllers and calibrate the signals from these measurements. Some results from this calibration procedure during the 2016 campaign are shown in Fig. 4.5-1. Ultimately, these impurity capture signals will be compared with the highly-sensitive *ex situ* chromatography method to assure that the latter accurately measures impurities originating from the TPC at the required level of 1 ppb.

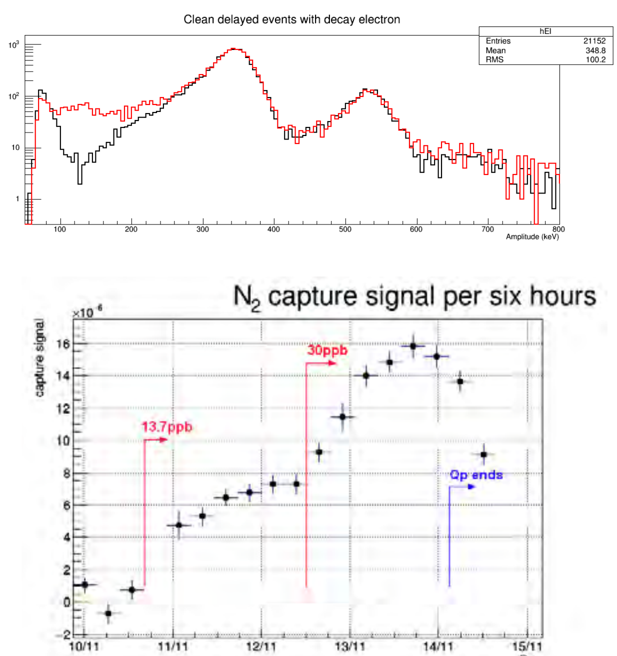

Figure 4.5-1. *Top*: The recoil energy from delayed events in the TPC. The events in black require an event in the electron detectors (suppressing the impurity signal) while the events in red veto electrons (enhancing the signal). The excess events in the $\sim$ 100 to 200 keV range from the latter is taken as the impurity signal. *Bottom*: The impurity signal versus time after injection of N_2. The signal increases and saturates after injection (red lines); eventually, the flow rate Q_P of impurities ceases (blue lines), and the active filtration causes the signal to diminish with time.

Background subtraction techniques (Sec. 4.4) are needed to correct for the kicker-related background. During the 2016 run campaign, we optimized the experimental configuration to maximize our sensitivity to background events in order to carefully study the source of these backgrounds. A Pb foil was used to stop muons just after the entrance scintillator, and an additional 4 mm plastic scintillator and thin silicon detector were installed after the existing muon entrance detectors. The Pb foil suppressed the usually dominant signal from decay electrons, while permitting the transmission of beam electrons; the additional detectors were used to tag the electrons in coincidence with the MuSun electron detector array, enhancing our background sensitivity. From these studies, we have confirmed that the activation of the kicker broadens the spatial distribution of the electrons in the beam, changing their propensity to scatter off of the TPC vacuum vessel and other materials in the experiment and into the electron detectors. This ultimately leads to a change in rate before or after the activation of the kicker, giving us confidence that our current analysis can correct for this effect.

4.6 Constraining stops in TPC wall materials via neutron detection

D. W. Herzog, P. Kammel, E. T. Muldoon, M. H. Murray, D. J. Prindle, R. A. Ryan, and D. J. Salvat

In the MuSun experiment, it is critical to reject events which do not stop in the D_2 gas, because captures in other materials have different disappearance rates and distort the measured decay spectrum. Our error budget of 2 s^{-1} for the muon lifetime can be produced by muon stopping fractions of only 1×10^{-4} in iron or as low as 3×10^{-5} in silicon. The MuSun experiment eliminates muon stops in the beam pipe or pressure vessel using a time projection chamber to select only muons that stop in a central fiducial volume. Since the reconstructed stop positions are not always accurate, we must still consider the possibility of muons which stop in the walls of the TPC itself, while appearing to stop in the fiducial volume. We need an independent method of measuring the frequency of these wall stops, which will allow us to estimate the systematic error from these events and optimize the fiducial volume.

The TPC is mostly constructed of high-Z materials such as silver, which requires a significantly larger stopping fraction of 1.4×10^{-3} to produce a 2 s^{-1} lifetime shift. The high capture rate in these materials is more easily distinguished from the expected slow decay in deuterium. In the vertical (Y) direction the TPC volume is bounded by solid electrodes, making the top and bottom of the TPC the primary source of wall stops. The Y stop position can also be precisely calculated from the drift time, making the Y axis ideal for measuring the effects of wall stops in a fine-grained way.

To investigate wall stops, eight liquid scintillator neutron detectors are mounted around the target, positioned behind the electron timing scintillators to allow for charged particle rejection. In addition, γ-ray events are rejected with pulse-shape discrimination (PSD) based on the length of the pulse tail. After these cuts, we must account for other sources of neutrons and other backgrounds. Most neutrons are generated by n-^{3}He fusion events rather than muon capture, so these fusion neutrons must be discriminated. Fusion events are typically accompanied by a delayed electron from the subsequent decay of the muon, while capture events consume the muon and thus have no decay electron. Fusion products also cause additional energy deposition in the TPC that is not present for non-fusion events. Therefore, the combination of an electron requirement with a TPC energy cut can effectively eliminate most fusion events.

Once the fusion neutrons are rejected, neutrons from muon capture in the D_2 gas must be distinguished from muon capture in wall materials. The only difference between the two is their time distribution, so we look for a fast exponential decay on top of the expected slow decay. These time distributions are also subject to accidental backgrounds, which are believed to be due to unrelated muon captures in the walls. The MuSun experiment uses pileup protection to ensure only one muon is present in the detector, but some additional muons still enter due to the entrance detector inefficiency. This background is affected by the kicker, producing a time-dependent background with a step at 800 ns. We can model this background using the measured time dependence of the entrance detectors convolved with an exponential decay to approximate wall captures. Combined with an additional constant background term to account for completely uncorrelated events such as cosmics, we find reasonable agreement with the data.

After the above cuts and background subtraction procedure, the remaining excess events are interpreted as wall captures. Repeating this procedure with various TPC stop position cuts and normalizing to the number of incident muons produces a map of the wall stop fraction versus position in the TPC. The overall scale of this fraction depends upon the detector efficiency, and this scale is set by adjusting the frequency of D_2 capture events to the expected theoretical value. This analysis assumes equal neutron yield from captures in D_2 and wall materials, which will be checked using data from the 2016 systematics run campaign (Sec. 4.5).

The resulting wall stop fraction is plotted versus reconstructed Y position in Fig. 4.6-1. Note that the fraction approaches a constant, non-zero value towards the center of the TPC, where we expect the fraction to vanish. This is most likely caused by either a small remaining admixture of fusion events or by decreased pileup protection efficiency during the entrance detector dead time, both of which could be misidentified as additional wall stops. We are working on measuring these effects, but in the meantime we can treat this as an empirical probability of false positives. To account for these extra neutrons, we define a central golden volume ($25\text{mm} < Y < 46\text{mm}$) and assert that the wall stop contribution must be negligible within this range. Subtracting away the average yield of the golden volume produces the red points. The estimated fraction of wall stops in the fiducial volume is $(8.7 \pm 0.3) \times 10^{-5}$ before the subtraction and $(6.2 \pm 6.5) \times 10^{-6}$ afterwards. Recalling that for silver our error budget allows for a stopping fraction of up to 1.4×10^{-3}, we seem to be well within our desired range and may be able to safely expand the fiducial volume.

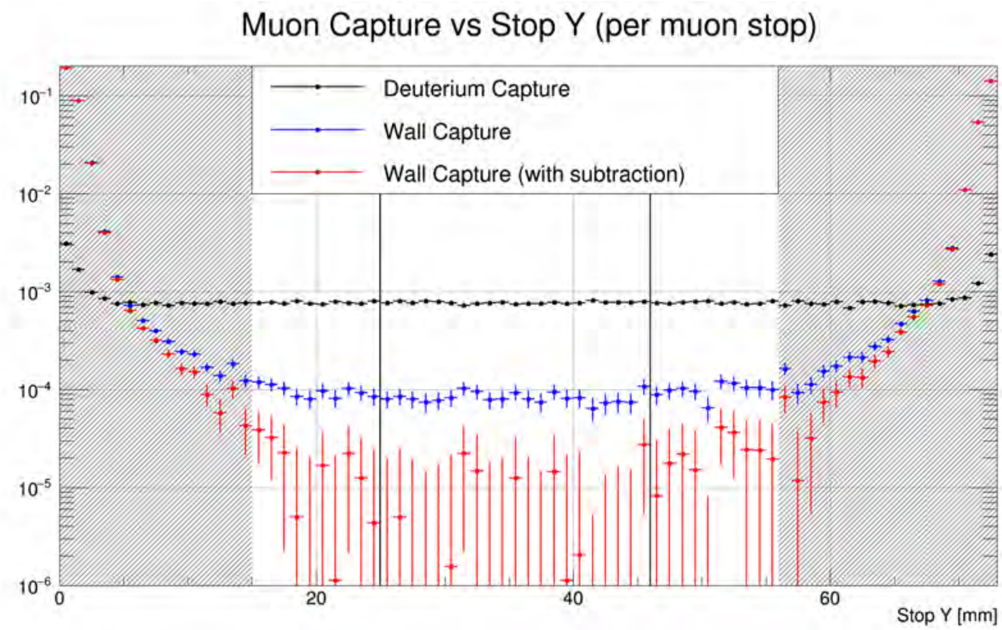

Figure 4.6-1. Estimated capture probabilities vs reconstructed Y stop. The shaded regions are outside the fiducial volume, while the vertical lines indicate the golden volume. The red points have been adjusted such that the average yield in the golden volume is 0, resulting in a yield of $(6.2 \pm 6.5) \times 10^{-6}$ for the fiducial volume as a whole – well within our uncertainty goal.

4.7 Monte Carlo framework and studies

D. W. Hertzog, P. Kammel, E. T. Muldoon, M. H. Murray, D. Prindle, R. A. Ryan, and D. J. Salvat

The MuSun Monte Carlo[1] simulates the TPC in detail, including pad-by-pad gain variations and thresholds; all the other detector elements have an essentially ideal response. The primary focus of our Monte Carlo studies has been to study fusion and electron interference effects, relying upon the detailed simulation of the TPC. Most notably, moderate-sized ($\sim 10^9$) Monte Carlo samples simulating the 2011 data have been essential in developing tracking algorithms in the TPC[2].

In 2016 we generated a large-scale Monte Carlo dataset simulating the 2014 and 2015 production data conditions, including lower electronic noise in the TPC and muon beam parameters tuned to match the μ^- stop distributions from the data. This also includes a model of electron-ion recombination in the TPC gas that reduces the observed energy of the highly-ionizing ^{3}He from fusion. This Monte Carlo dataset has 5×10^9 μ^- stops in the TPC fiducial volume with coincidences in the electron detectors, comparable to the statistics of

[1]CENPA Annual Report, University of Washington (2014) p. 91.
[2]CENPA Annual Report, University of Washington (2015) p. 89.

the 2014 or 2015 production run. This used approximately 30% of our 2016 annual allocation on the Stampede cluster, occupying 175 TB of disk space.

An example of the statistical power is given in figure Fig. 4.7-1. This shows the fitted μ^- capture rate on deuterium as a function of the starting time of the fit for two different TPC tracking algorithms. The statistical uncertainty for early times is better than $\pm 10\mathrm{s}^{-1}$, comparable to our experimental goal of 6 s^{-1}. The variation of the fitted capture rate as a function of the start time is within the expected statistical variation.

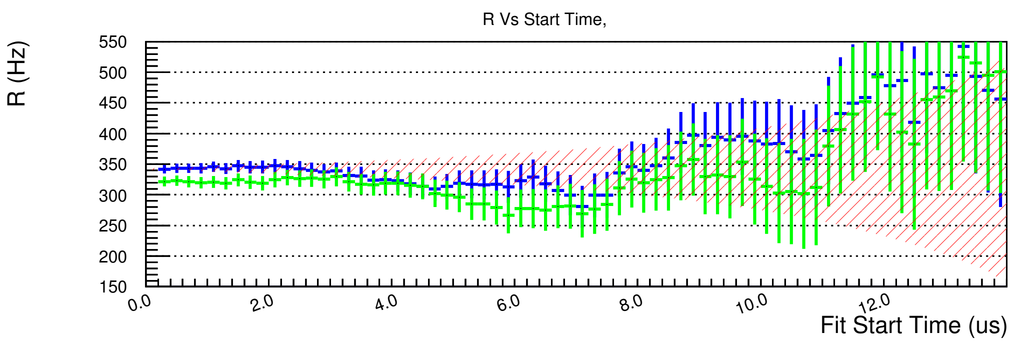

Figure 4.7-1. Start time scan for the upstream (*blue*) and pdir (*green*) trackers.

We are currently examining the Monte Carlo dataset for systematic effects only resolved with high statistics. The discrepancy between the two trackers for early start times is likely due to fusion interference, and this is currently being investigated. Further, we have identified significant background in the electron detector due to recoil energy in the electron scintillators from fusion neutrons. While these are likely to be below the experimental thresholds, the Monte Carlo information will allow us to study this effect in detail.

g-2

4.8 Overview of the $g-2$ experiment

M. Fertl, A. T. Fienberg, A. García, N. S. Froemming, J. Hempstead, D. W. Hertzog, P. Kammel, J. Kaspar, K. S. Khaw, B. K. H. MacCoy, R. E. Osofsky, M. W. Smith, and H. E. Swanson

Context

Muon $g-2$ is a special quantity because it can be both measured and predicted to sub-ppm precision, enabling the so-called $g-2$ test for new physics defined by $a_\mu^{\rm New} \equiv a_\mu^{\rm Exp} - a_\mu^{\rm SM}$. As a flavor- and CP-conserving, chirality-flipping, and loop-induced quantity, a_μ is especially sensitive to new physics contributions[1,2]. We update the $g-2$ test compared to our previous Annual Reports owing to a new evaluation of hadronic vacuum polarization (HVP) that takes into account the more recent updates of cross sections from experiments. Davier's accounting[3] gives

$$\Delta a_\mu^{\rm New} = [274 \pm 76] \times 10^{-11} \quad 3.6\,\sigma. \tag{1}$$

The persistent discrepancy between experiment and theory continues to fuel speculative models that include supersymmetry (SUSY), Dark Photons and beyond, even though many of these theories are being constrained now from low-energy measurements and LHC results. Our UW group is helping to lead a next-generation $g-2$ experiment (E989) at Fermilab which aims to improve the BNL E821 final result[4] by a factor of 4, thereby reaching a relative precision of 140 ppb on a_μ. In the 13 years that have passed since the BNL final result was published, the Standard Model (SM) uncertainty has been reduced by a factor of 2. Anticipated theory improvements on the timescale of E989 data taking aim to reach the uncertainty goal of the experiment; see Fig. 4.8-1.

The SM terms are usually listed in five categories:

$$a_\mu^{\rm SM} = a_\mu^{\rm QED} + a_\mu^{\rm Weak} + a_\mu^{\rm HVP} + a_\mu^{\rm Had-HO} + a_\mu^{\rm HLbL}. \tag{2}$$

The QED, Weak, and hadronic higher-order (Had-HO) terms have negligible uncertainties. The HVP precision continues to improve; it can be determined from experiment through a dispersion relation that amounts to an energy-weighted integral of $e^+e^- \to hadron$ total cross sections. The hadronic light-by-light (HLbL) effect has been evaluated using models and the quoted uncertainty of 26×10^{-11} is only a consensus estimate reached by comparing a variety of models; it is not a well-defined uncertainty. What is promising is the rapid progress

[1] A. Czarnecki and W. J. Marciano, "The Muon anomalous magnetic moment: A Harbinger for new physics," Phys. Rev. D **64**, 013014 (2001).

[2] D. Stockinger, "The Muon Magnetic Moment and Supersymmetry," J. Phys. G **34**, R45 (2007).

[3] M. Davier, "Update of the Hadronic Vacuum Polarisation Contribution to the muon g-2," arXiv:1612.02743 (2016).

[4] Muon g-2 Collaboration: G.W. Bennett *et al.*, Phys. Rev. D **73** 072003, (2006).

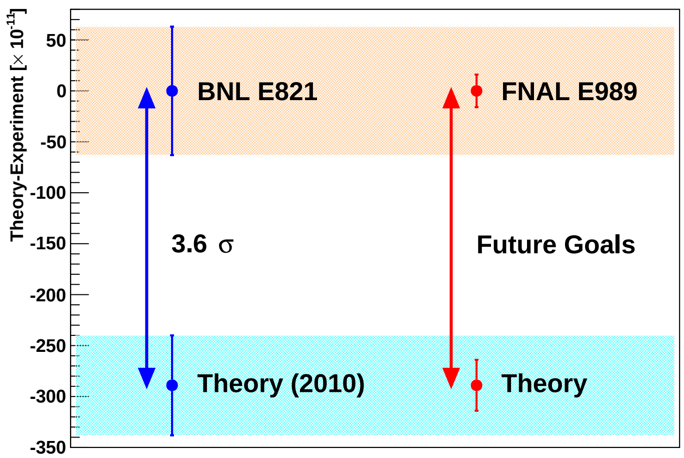

Figure 4.8-1. Comparison of Experiment to Theory at present and what might be expected on completion of Fermilab E989 and by a twofold reduction in the theory uncertainty.

being made to calculate the HLbL contribution to high precision using the lattice. In 2016, the group of Blum *et al.*[1] have completed a calculation of HLbL with realistic inputs (quark masses, appropriate lattice sizes). They evaluated all connected and leading disconnected diagrams and obtained a statistical uncertainty of 13.5×10^{-11}, a remarkable accomplishment. Systematic studies are required before their central value and final uncertainty can be included in the overall SM evaluation.

Experiment and Collaboration

The muon anomaly is proportional to the ratio ω_a/ω_p, where ω_a is the anomalous precession frequency of the muon spin in a magnetic field and ω_p is a measure of that average magnetic field carried out using proton nuclear magnetic resonance (NMR). Both frequency measurements must control systematic uncertainties to 70 ppb. The statistics required to determine ω_a exceed those at Brookhaven by a factor of 20. Our UW group is involved in both the ω_a and the ω_p measurements. We are designing and building a significant array of hardware tools in both cases. Additionally, we have been modeling the optimization of muon storage in the ring, including tuning strategies of the superconducting inflector and the kicker field strengths, and the quadrupole and collimator geometries. A set of entrance imaging counters is also being designed to aid in the tuning phase. Over the past year, we have devoted considerable effort to being ready for data analysis, through accurate simulations that produce online-equivalent datasets to all of the unpacking, physics object interpretation, online monitoring, and offline evaluation steps. The E989 Collaboration has 35 institutions and > 160 collaborators from 8 countries. D. Hertzog remains Co-Spokesperson. J. Kaspar has been

[1] T. Blum, N. Christ, M. Hayakawa, T. Izubuchi, L. Jin, C. Jung and C. Lehner, "Connected and Leading Disconnected Hadronic Light-by-Light Contribution to the Muon Anomalous Magnetic Moment with a Physical Pion Mass," Phys. Rev. Lett. **118**, no. 2, 022005 (2017).

named Detector Coordinator. E. Swanson is Deputy Field Team Leader. K.S. Khaw is the Level-0 Calorimeter Analysis manager; A. Fienberg is the Data Quality Monitor manager. The UW group has 7 Ph.D. students on the experiment, with the first two theses expected in the next 12 month period. The nearly complete collaboration construction work has evolved into a coordinated commissioning period. The technical groups are generically named: Beam, Ring, Field, Detector, Simulation, and Offline.

The Beam delivery design involves in order the Booster, Recycler, Transfer Lines, Target Station, Decay Beamline, Delivery Ring (DR), and final M4/M5 beamline. This suite is necessary to create and deliver a bunched, 3.1 GeV/c polarized muon beam, which is purified of background pions and protons by running the bunch around the DR for several turns prior to injection in our storage ring. This effort is led by Fermilab accelerator physicists with collaboration members providing some of the modeling. The installation of the new beamlines is complete and commissioning is scheduled to begin in April. We are expecting the first beam bunches to arrive at the storage ring entrance in early June. However, this beam will *not* yet go around the DR, which is not ready. Consequently, protons will not be removed and some fraction of pions will remain. Nevertheless, we have developed a plan to commission the experiment and test the equipment prior to the 2017 Shutdown period. Commissioning of the DR and physics production data taking will begin in FY2018.

The Ring team is responsible for building and operating the storage ring. They also provide the inflector, quadrupoles, collimator, and kicker subsystems. The team carries out simulations of muon storage and evaluates beam dynamic systematic uncertainties. UW student Froemming's exquisitely detailed Geant4-model of the storage ring and its components have led to modifications of the E821 Q1 outer electrostatic quadrupole plate material and support system and to the optimization of new asymmetric collimators, and it has provided the needed simulation justification to warrant construction of a new open-ended inflector magnet. The quad and collimator changes have now been implemented and the project continues to try to provide some contingency funds for construction of a new inflector. The Beam team has produced complete end-to-end models resulting in large files of simulated muons with all phase space and spin variables well defined. These "muons" are used as input to Froemming's Ring transmission and storage simulation. His thesis will be based on using this tool to help optimize the muon storage fraction. The model will guide the commissioning effort this spring. As realized in our completed beam injection studies, a set of imaging detectors along the magnetic field-free corridor – from the last beamline quadrupoles to the inside of the storge ring – will greatly aid the beam tuning process. P. Kammel has designed a detector system using SiPM technology with thin scintillating fibers. We are presently building the first full-scale model with intent to install it prior to the spring commissioning run.

The Field team completed shimming the magnet to ultra-high uniformity by November, 2016. The magnet was then warmed up for a critical repair of a small vacuum leak and for the removal of three plates of charcoal that had crumbled, losing contact with the cold reservoir, and causing vacuum "burps" that have prevented 24 h operation field. E. Swanson developed the theory that the charcoal panels – installed when the magnet was built about 20 years ago – probably had fallen off their panels. Investigative work by the technical team discovered that indeed this was the case and successful storage ring "surgery" resulted in the complete removal of the charcoal. The magnet is being recommissioned now. The Team next will tune the final elements, a set of trim coils that are used to reduce the amplitudes of some small remaining multipole components. Owing to the challenge in E989 of a better understood field, Fertl and Osofsky designed a radial field measuring cart and managed to map the radial components of the field in many places around the azimuth. As documented in their article, the results were somewhat surprising. Over the past year, the field data taking and much of the critical analysis and modeling of the "next iteration" procedures was carried out by UW grad student Smith. He will complete his thesis on this topic in summer, 2017.

The Detector Team provides the instrumentation to monitor the stored muon distribution and to measure the decay positrons from which the characteristic precession signal histograms are built. The UW group led a six-university consortium proposal to NSF to secure funding for the precession frequency measurement; this work is essentially complete. At UW, we are responsible for the electromagnetic calorimeter system, which consists of 24 stations, each having arrays of 54 PbF_2 crystals with large-area SiPM readouts. The electronics, testing, and mechanical supports are all developed and built at CENPA. All 1300 crystals and nearly 1400 SiPM boards have been individually evaluated in two custom QC stations we built. Next, each crystal was glued to a corresponding SiPM and packaged according to its precisely measured transverse dimensions so that well-fitted groups of 54 crystals could fit into a coherent whole. The mechanical efforts included design and construction of 24 Calo Houses that feature a cooling and exhaust channel to maintain stable temperatures across all columns of SiPMs. The houses hold a stack of breakout boards that distribute the needed low voltage and communications to run the PCBs and the bias voltage required to operate the SiPMs above Geiger threshold. The Houses were stuffed with crystals and cabling – a significant effort occupying some months – at Fermilab in the D0 Assembly Building. A set of Calo Chariots was also designed and built. The Chariots hold all the support and readout electronics – uTCA crates with Cornell digitizers, BeagleBone control boards, BK Power Supplies, Internet router, JMU Power Distribution units. Their diving board platform supports the Calo Houses. J. Kaspar, together with CENPA technical staff Van Wechel, Peterson, and Amsbaugh, were responsible for realizing this system; see article by Kaspar. A completed final Calo House with complementary contributions from the laser-based calibration system, the high-speed digitizers, the fast DAQ, have all been integrated and tested during a 3-week SLAC run in June 2016; see article by Khaw.

New this year has been a major effort by graduate student Fienberg and postdoc Khaw on many aspect of the data analysis pathway, from interpretation of the raw data into fit pulses with calibrated times and energies, to clustering, to reconstruction of histograms. They have built both online tools and offline framework-based protocols and have led Workshops to train others. It is fair to say that the rapid interpretation of any data we will acquire during commissioning will only be possible owing to their work. The effort started during the SLAC run where their online, and fast offline, analysis provided nearly immediate feedback on the detector performance. See articles by Fienberg and Khaw which emphasize various aspects of these efforts.

4.9 Calorimeter status and SLAC run

J. F. Amsbaugh, A. Fienberg, J. Hempstead, D. W. Hertzog, M. Huehn, J. Kaspar, K. S. Khaw, D. A. Peterson, and T. D. Van Wechel,

After a stored muon decays into a positron and neutrinos, the positron has insufficient energy to remain on the magic orbit in the ring. It will curl inward and hit a calorimeter sitting in the scallop of a vacuum chamber in the opening of the C-shaped magnet. Twenty-four calorimeter stations are positioned along the inside storage-ring radius at discrete locations. The calorimeters are highly segmented arrays of lead-fluoride (PbF_2) crystals, which are pure Cherenkov radiators, read out by large area silicon photomultipliers (SiPM). Systematic uncertainties related to particle pileup played a major role in the previous experiment. The new calorimeter design addresses the pileup challenges by segmenting each calorimeter into 54 independent PbF_2 crystals, to mitigate spatial pileup, and by using a Cherenkov absorber coupled to fast SiPMs with a PMT-like pulse shape (FWHM < 10 nsec), to handle particles hitting the same spot on a calorimeter as close in time as 3 nsec. Non-magnetic SiPMs successfully run in, and at the same time do not disturb, the highly uniform 1.45 T magnetic field of the storage ring.

This year we finished the quality control program of all 1300 PbF_2 crystals, including a meticulous set of quality control measurements related to optical transmission and physical dimensions. Crystals corresponding to an individual calorimeter station were arranged in 6×9 arrays. A sorting program was used to associate crystals to specific calorimeters based on their common transverse dimensions. Further, we finished quality control and assembly of custom made SiPM boards, based on the concept of a multi-staged transimpedance amplifier. Finally, we finished gluing SiPM boards to PbF_2 crystals using a high index-of-refraction optical epoxy having good optical transmission above 300 nm.

In June 2016, we evaluated the first production calorimeter at SLAC. It was our third test run there. The test was performed using $2.0-4.5$ GeV electrons at End Station A. The SiPMs were gain matched using a laser-based calibration system, which also provided a stabilization procedure that allowed gain correction to a level of 10^4 per hour. In the course of the three week run, we demonstrated the timing resolution of the calorimeter of $\sim$20 ps, exercised the timing and synchronization algorithms, verified the energy resolution meeting our specs, and performed careful scans of the beam hit positions and impact angles to improve our understanding of the EM shower propagation and Cherenkov photon transportation in lead fluoride. The SLAC accelerator is capable of delivering double-bunches of electrons with the buckets separated by a couple nanoseconds, which were used to demonstrate our ability to separate pile-up when particles hit the same part of the calorimeter close in time.

Following the successful test run, we published a JINST paper covering the development of the SiPM board[1] using some data collected at SLAC. In the paper, we have described our custom amplifier board that supports a large-area, 16-channel SiPM from Hamamatsu. While the design was driven by the end-use calorimetry requirement for the new $g-2$ experiment at

[1] J. Kaspar *et al.*, "Design and performance of SiPM-based readout of PbF2 crystals for high-rate, precision timing applications," JINST **12** (2017) no.01, P01009.

Fermilab, the desired performance characteristics are relatively common in many nuclear and particle physics applications. They include: operation in high magnetic fields, good (near) linear response for pulses of hundreds to thousands of photo-electrons, operation at MHz rates, short-duration "PMT-like" pulse shapes, and a high degree of gain stability. The final design PCB, together with careful attention to the external bias supply, achieves these goals. Notably, we measure $\sim$5 ns pulse widths and achieve $\sim$20 ps time resolution. For ease-of-use, the PCB also includes a variable gain amplifier, an on-board temperature readout, and a built-in EEPROM for identification of the unit and storage of gain settings. The low voltage, bias voltage, and communication lines are all conveyed using commercial HDMI cables. The differential signal output is conveyed by a custom Samtec cable. The PCB components and the cabling are all non-magnetic.

The Muon $g-2$ experiment is scheduled to start taking commissioning data in late Spring 2017, and begin physics running shortly after the 2017 summer shutdown. We shipped the detectors components we had been preparing at the University of Washington to Fermilab in late summer 2016. These include the chariots rolling on a pair of leveled steel plates, power distribution units, bias voltage power supplies, slow control system, air-cooling system, calorimeter enclosures, and electronics boards. A group of UW students and a lab technician assembled the shipped parts into the functioning detectors and burned them in at the assembly area using a laser system. At the time of writing this report, the assembled calorimeters are being moved into the ring, installed in the scallops of vacuum chambers, and laser fibers are being connected to the diffuser panels in the calorimeter enclosures, see Fig. 4.9. The commissioning of the detector will start in April 2017 and result in an engineering run in June.

Figure 4.9-1. Photo of the Muon Storage Ring in April, 2017. Much of the overall installation is complete. The UW calorimeters are being installed in the discrete locations provided by the scalloped vacuum chambers. Each calorimeter rides on a chariot that houses the supportive electronics, power supplies, and cooling.

4.10 Building a calorimeter

J. Hempstead, D. W. Hertzog, M. Huehn, J. Kaspar and K. S. Khaw

Central to the measurement of ω_a are the twenty-four calorimeters stationed around the magnetic storage ring. Each calorimeter sits on the diving board of its associated chariot, which also holds all the the electronics necessary to operate the calorimeter.

The basic structure of the calorimeter is an aluminum box into which the 54 lead fluoride (PbF_2) crystals, with attached SiPMs, are stacked. A duct system is installed to facilitate airflow to the SiPMs. Attached to the front of the box is the calibration box provided by our Italian collaborators. The calibration box diffuses light from an external laser to 54 individual fibers. Prisms positioned in front of each PbF_2 crystal redirect the laser light from the fibers into the crystals, toward the SiPMs.

The PbF_2 crystals are stacked starting at the side of the calorimeter destined to be further away from the storage ring. Crystals are stacked according to a map for every calorimeter previously made. The map was made to optimize the way the crystals fit together by using measurements of the individual crystals' dimensions. The first crystal in the row is pushed so that its longest side is flush with an internal wall, and the SiPM is opposite the calibration box. A plunger and spring pushes on the heat sink of the SiPM to hold the crystal in place against the front panel of the calibration box. Successive crystals are pushed flush with the previously placed crystal before the plunger is engaged. Once one row of crystals is finished, the next row is started on top of it. Around the heat sinks is a baffle to direct the airflow from the duct. During the stacking process, the crystals are wrapped in black Tedlar. To minimize the space required for the wrapping, a scheme was created to isolate every crystal while using the least amount of paper. The scheme, as seen in Fig. 4.10-1, uses alternating up- and downturned U-shaped pieces. On the sides, bottom, and after every second row are larger sheets of Tedlar. Between the crystals and the front panel is placed a plastic sheet with holes cut out for the laser light.

HDMI cables are used to provide bias voltage and slow-control communication for the SiPMs. Each SiPM is attached via an HDMI cable to one of four breakout boards stacked on top of the internal duct work. Because of their close proximity to the magnetic storage region, the HDMI cables need to be non-magnetic. Scarce commercial availability necessitated a process to remove the slightly magnetic sleeves on the ends of the HDMI cables ourselves. The metal is pried off and Kapton tape is wrapped around the now bare end to ensure a snug fit. After this process, the cables are checked to make certain all of the connections still work.

Two lengths of HDMI cables are used: 2 feet and 3 feet. The shorter cables are used for the breakout board positions closest to the crystals. Cables are labeled on the end plugged into the breakout board corresponding to their crystals' positions. None of the HDMI cables are plugged in until after all 54 crystals are stacked. Then, the cables going to the lowest breakout board are plugged in first so that space within the box can be utilized efficiently. The SiPM to breakout board location matching is standardized between calorimeters based on SiPM location within the calorimeter.

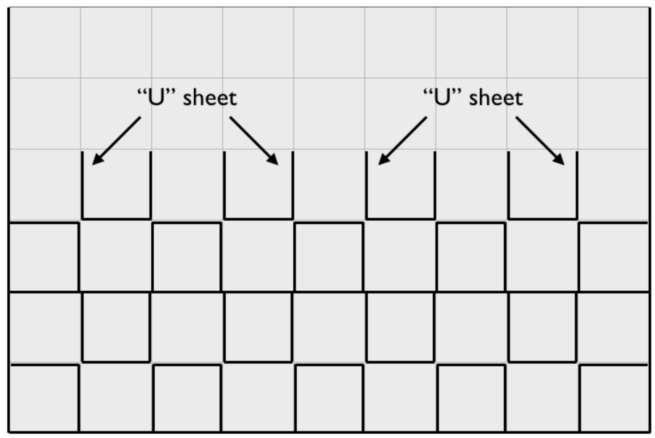

Figure 4.10-1. The wrapping scheme for the 54 PbF_2 crystals is shown. The darkened borders are where pieces of Tedlar are placed. The same scheme continues for the upper two rows of crystals with a final large piece of Tedlar to be placed above the top-most row.

After the HDMI cables are all attached, the signal cables for each SiPM need to be attached. Eleven custom Samtec cables are used, each with 5 separate connections. The pins for each connection were too loose initially, so they are manually tightened. Using a pair of tweezers, the cables are pushed onto the pins located on the SiPMs. The best cables, as determined by quality control measurements, are used for the columns of crystals closest to the beam while the less ideal cables are relegated to the opposite side. Once all the signal cables are in place, the calorimeter is complete and ready for testing (see Fig. 4.10-2). All calorimeters will be completed by mid-April 2017.

4.11 Nearline and offline data-analysis framework

A. T. Fienberg, D. W. Hertzog, J. Kaspar, and K. S. Khaw

The Muon g-2 offline reconstruction and analysis framework has evolved substantially since the last annual report, and the current data flow is depicted in Fig. 4.11-1. The data digitization and reconstruction chain for the simulated data was tested and improved using a simulated dataset from a mock data challenge. The unpacking and reconstruction chain for the experimental data was tested and improved based on the experience at the SLAC test beam in summer 2016. Data unpacking involves parsing binary raw data and converting them into human readable structures before passing them to the data reconstruction stages such as pulse fitting. User analyses are then performed on the reconstructed objects like the clusters.

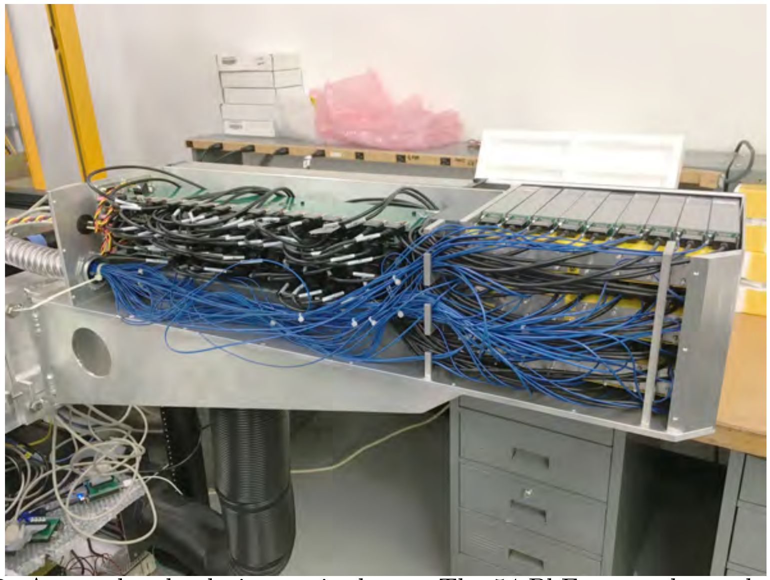

Figure 4.10-2. A completed calorimeter is shown. The 54 PbF_2 crystals can be seen in the right side of the picture. Before closing the calorimeter box, another piece of black Tedlar will be placed on top of these crystals. Attached to each is a green SiPM board. The green breakout boards can be seen to the left of the crystals, connected to the individual SiPMs by black HDMI cables. The blue cables are the custom Samtec signal cables.

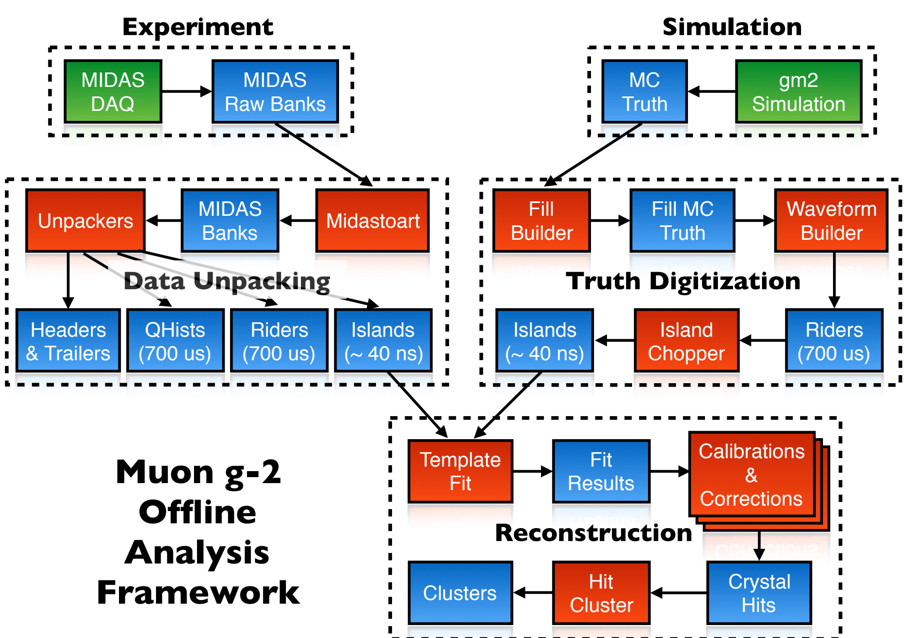

Figure 4.11-1. Muon $g-2$ offline analysis framework. Full chains for the simulated (data unpacking and reconstruction) and experiment (truth digitization and reconstruction) data were tested and improved this year.

The difference between simulated and experimental data in the reconstruction stage is that, in the simulation, all the PbF_2 crystals and the silicon photomultipliers (SiPMs) are assumed to be identical (e.g. light yields of the crystals and gains of the SiPMs are the same). Quality control of the crystals and the SiPMs have indicated that they could differ by about 20% regarding light transmission and breakdown voltage. Hence in practice, additional steps have to be taken to equalize them as much as possible. A photon calibration procedure using a neutral-density filter wheel is used to extract the photon calibration constant, and a laser monitoring system is used to monitor the SiPM gain fluctuation. Additional corrections involve monitoring the laser fluctuation using pin diodes and PMTs. All these calibration and correction constants are applied to the fitted energy in sequence, and the final number is a proxy for the particle energy.

Two important features we have implemented recently into the offline framework are the MIDAS online database (ODB) parser and the database access. The ODB is written into the raw Midas file and includes all the run information needed for data reconstruction. A dedicated ODB parser based on the boost library is implemented to extract information like the channel to crystal number mapping and the number of enabled digitizer channels. Calibration and correction constants extracted by *art* modules[1] were written into a text file during the SLAC test beam. To ensure the accessibility of the constants, we store them in the $g - 2$ local and FNAL central databases by implementing a dedicated database service that can talk to both databases using libraries like *pqxx* (postgres C++ API) and *boost::asio* (url request library).

In addition to the features mentioned above, we have also utilized the multi-threading library - Intel Threading Building Blocks (TBB) to parallelize data processing within an art module. This parallelization is possible because our data products are in a nested structure and data from each calorimeter are in principle independent. We have implemented such parallelization in the unpacking and the reconstruction stages. Initial tests have indicated that a processing rate of $8 - 10$ Hz is achievable using a 16-core CPU machine. Such a speed up in the data processing enabled us to develop a fast turnaround framework called *nearline*, and this will be the near-to-live data cruncher for the commissioning of the Muon g-2 experiment in June 2017.

To complete the story, an overview of the experimental data flow is sketched in Fig. 4.11-2. It shows how the nearline and the offline framework are connected to the other parts of the experiment. All the raw data will be stored in the tape storage area as well as the output *art* and ROOT files from the offline analysis framework. These files are cataloged using the SAM metadata management system provided by Fermilab. Information like run condition or run type are stored in the SAM database.

[1]The *art* framework is an application used to build scientific programs by loading science algorithms, provided as plug-in modules; each experiment or user group may write and manage its own modules.

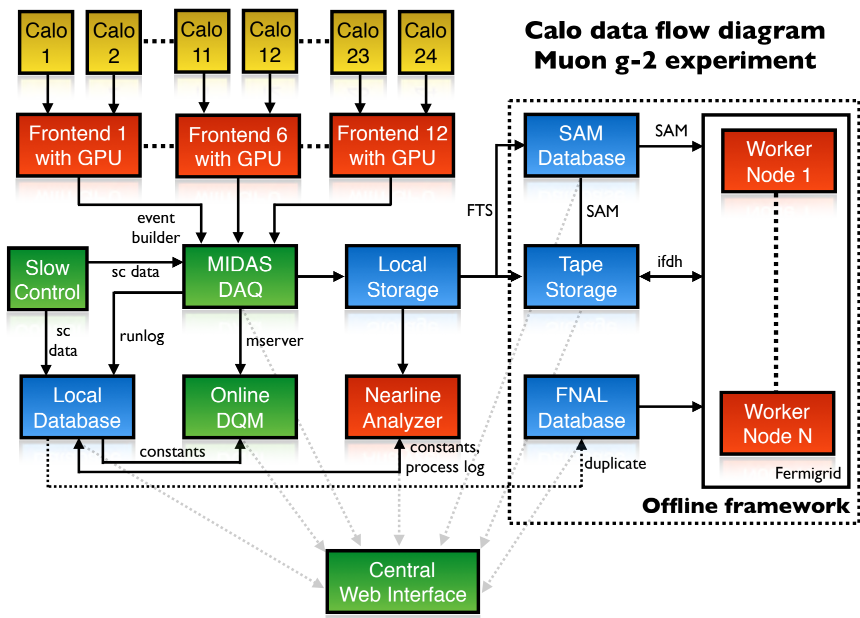

Figure 4.11-2. Muon $g-2$ experimental data production work flow for the calorimetry data. Nearline framework has access to the most recent data files in the local storage and the information in the local database. Offline framework has to wait for the Fermilab's File Transfer Service (FTS) to complete the file transfer to the tape storage, before any offline analysis can be performed.

Finally, for the offline production, a web interface named POMS, which was initially developed by a Fermilab offline production team, is used. Preliminary production tests for the simulation were successful, and the production of experimental data will be performed soon.

4.12 Data quality monitoring

A. T. Fienberg

Data quality monitoring (DQM), also called online data monitoring, is the real time analysis and visualization of data as it is being collected. Such analysis spans the range from low level data integrity checks such as checksum validations to the creation of high level, reconstructed physics objects. DQM is essential at any point during the experiment's data taking to ensure rapid identification and diagnosis of issues, but it is especially critical during commissioning. Efficient use of the beam time prior to the 2017 shutdown will require immediate feedback from all detectors and instruments; this feedback will come from the DQM.

During the 2016 calorimeter test beam experiment, a need was identified for a modular, expandable, and scalable DQM system. Initial approaches encountered performance issues when monitoring data from a single calorimeter. The $g-2$ experiment's configuration will have 24 calorimeters as well as a number of other detectors. Additionally, if built using a different system from the offline reconstruction, an immense duplication of effort will result as unpackers, analysis routines, and reconstruction algorithms would be built and maintained both for the DQM system and the offline system. After the completion of the test beam run, a DQM system was developed that addresses these concerns.

The natural solution to the redundancy problem is to build the DQM using the same framework, *art*, that is used for the offline reconstruction and data analysis. The $g-2$ experiment uses MIDAS for data acquisition. As of last summer, the midastoart module, which translates data from the MIDAS format into *art* data products, had already been written, and so had unpackers for much of our raw data. All reconstruction code has been and will continue to be implemented as *art* modules. midastoart was built originally to operate on MIDAS data files, but a modification enabled it to be configured to read MIDAS events live through a TCP socket from a running experiment. After this modification, all previously written and future *art* modules could be run online with no changes to the code.

The *art* framework works well for online event processing, but it is less convenient for producing interactive, live-updating graphs: more tools are needed to complete a full DQM system. The $g-2$ DQM team elected to create a web-based interface to display graphs and other information. There is a wealth of open source software available for creating realtime web-based applications, and web pages are easily accessed remotely. The web-based interface consists of http servers built with node.js that receive live data streams from a running *art* job through TCP connections. The TCP connections are implemented using the ZeroMQ messaging library. These servers aggregate and cache the data necessary to make graphs such as histograms and trend plots. These data are sent to clients on demand using the Socket.IO JavaScript library. Plots are rendered in the browser. Plotly is currently used for most graphs, but the system described here does not prescribe any particular client side plotting library.

This system scales well to the full $g-2$ configuration. Many node.js servers are deployed, each responsible for a different subsystem. Each server can be run independently or in concert with the others, and they can be run on as many different PCs as necessary (although, in practice, one has seemed sufficient). A reverse proxy is the point of access for users; the number and existence of the multiple servers is hidden. Further, MIDAS allows us to connect multiple *art* jobs to the same experiment. The offline reconstruction chain is already highly multithreaded, though, so splitting the *art* job into multiple processes has not been necessary. By outsourcing graphing to the clients' browsers, the *art* jobs and node.js servers avoid spending any computational resources on rendering images. The architecture is displayed graphically in Fig. 4.12-1.

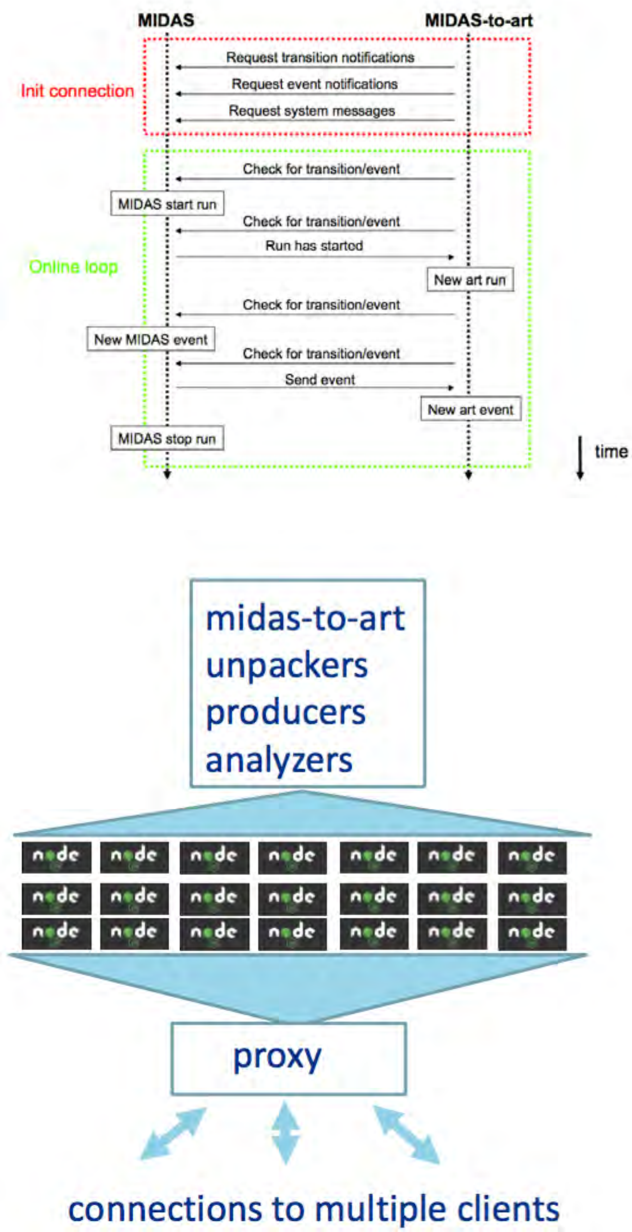

Figure 4.12-1. *Top*: The operation of midastoart in online mode. *Bottom*: The architecture of the DQM system.

The new DQM has already proven its worth in a number of test stands and detector construction stations, including DAQ test stands, the calorimeter commissioning station, and the cosmic test stand used for testing the $g-2$ trackers. It has proven to be robust and reliable, and identified a number of calorimeter construction errors that were relatively easily fixed on the spot at the commissioning station, but would have been much more troublesome if missed until later. DQM modules using the framework described currently exist for the tracker, fixed probes system, NMR trolley system, and calorimeter. Many other subsystems as well are planning to develop DQM modules using this system in the coming months. Some example displays from the calorimeter DQM system are shown in Fig. 4.12-2. An example from the fixed probe DQM system, built using the same framework, is shown in Fig. 4.19-4.

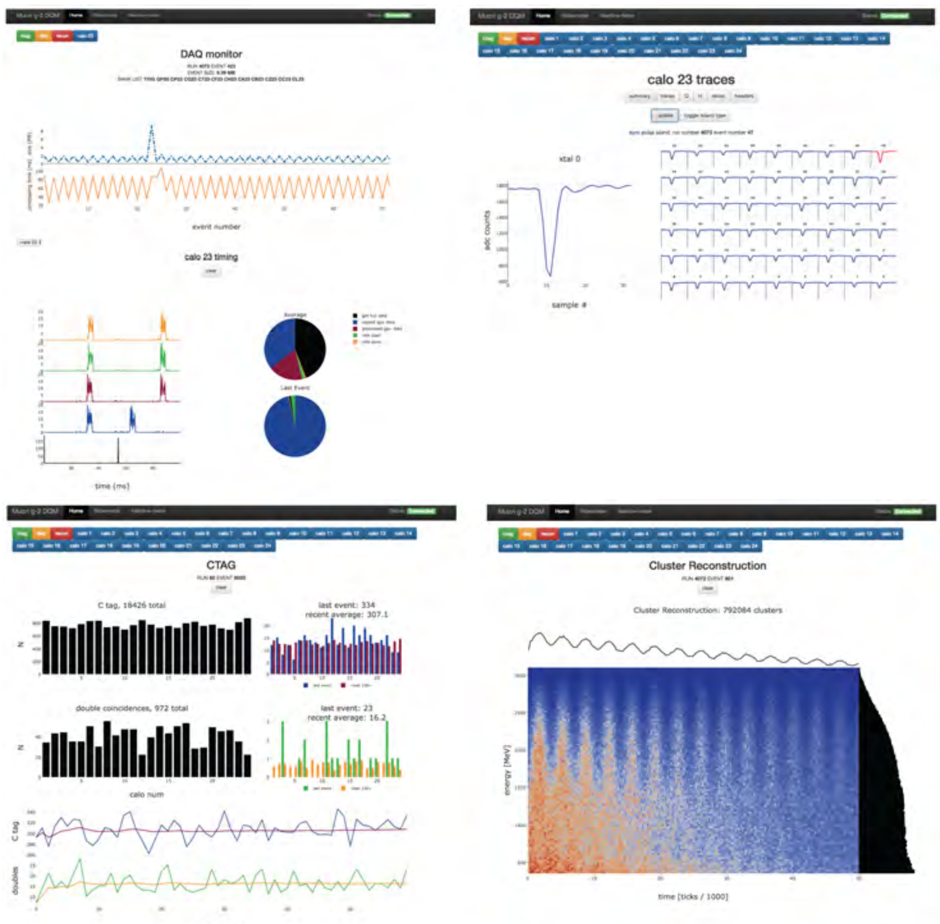

Figure 4.12-2. Examples from the calorimeter DQM. *Top Left*: DAQ diagnostic information, such as event size and processing time. *Top Right*: SiPM traces from a single calorimeter. *Bottom Left*: CTAG display. CTAG is a value counting the number of high energy decay events reconstructed in the $g-2$ ring after a certain time, a value proportional to the number of stored muons. *Bottom Right*: A 2-dimensional reconstructed positron decay distribution as a function of time and energy.

4.13 Calorimeter algorithms

A. T. Fienberg, D. W. Hertzog, J. Kaspar, and K. S. Khaw

The offline reconstruction chain introduced in (Sec. 4.11) has pulse fitting and clustering as its primary components. Pulse fitting is the process by which digitized pulses from calorimeter segments are summarized with times and energies, and clustering combines calibrated times and energies from the pulse fitter into cluster times and energies. Ideally, a cluster time and energy corresponds to the time and energy of a decay positron impact.

The baseline algorithm used for pulse fitting is called template fitting. A template is an empirical function of time describing the shape of a digitized SiPM pulse. There are slight pulse shape differences between SiPMs, so each one requires its own template. Template building is the process of generating these templates from a set of digitized waveforms and consists of the following steps:

1. Sort waveforms based on phase (where the peak falls between digitizer samples). This is determined from three samples, the peak sample and its neighbors.

2. Normalize each pulse by area.

3. Average pulses with the same phase

4. Recombine average pulses, offset appropriately based on their phases.

5. Interpolate these finely binned samples with a cubic spline to obtain a smooth template.

An example template is shown in Fig. 4.13-1.

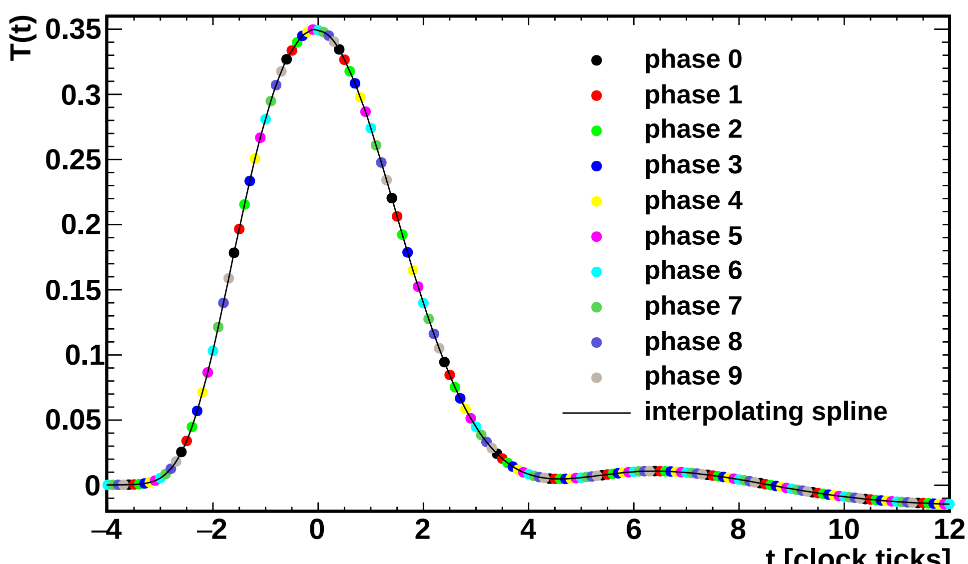

Figure 4.13-1. A pulse template built using the procedure described in the text. A unique pulse template must be built for each SiPM.

Templates are used to fit digitizer pulses with a standard χ^2 minimization, although there is a custom implementation optimized for the $g-2$ application using the eigen C++ linear algebra library. Digitized waveforms are passed to the fitter in short chunks called "islands." An island is a small number of contiguous samples, usually about 40, taken from all calorimeter segments by the DAQ when any segment goes over a configured threshold. These islands could have any number of pulses on them, including zero if noise triggered the island to be saved. The template fitting method generalizes nicely to an arbitrary number of pulses in a waveform, as one can add as many copies of the template as necessary placed at different times. For N pulses, there are $2N + 1$ parameters: one baseline, and a time and energy for each pulse. This technique is demonstrated to provide a 30 ps timing resolution for 1 GeV pulses and to have 100% separation efficiency for consecutive pulses more than 4 ns apart. The template fitting procedure processes approximately 100,000 pulses per second per CPU. An example template fit to a double pulse is shown in Fig. 4.13-2.

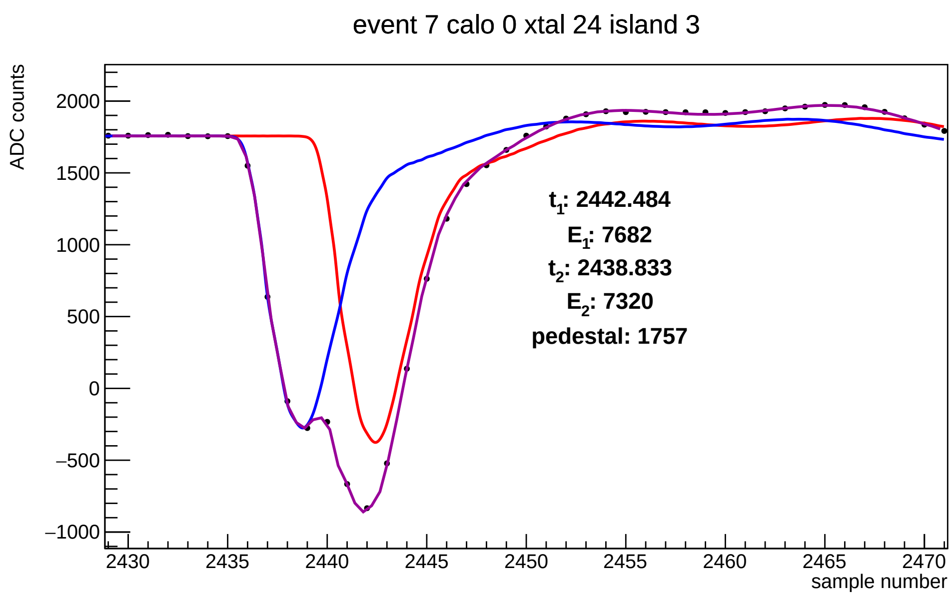

Figure 4.13-2. A template fit to two 3 GeV electrons from the SLAC accelerator. The time separation is about 4.5 ns. The digitizer sampling rate is 800 MHz.

Sets of calibrated fit result energies and times, called crystal hits, must be grouped by the clustering procedure in order to reconstruct decay positrons. The number of fitted pulses will differ between segments, so each segment will have an arbitrary number of crystal hits. The current clustering algorithm breaks into two independent steps: time partitioning and spatial separation. Time partitioning finds sets of crystal hits in an island that are grouped in time, typically all within about 2 ns. Each of these groups is sent to the spatial separation algorithm, which looks for sets of hits that are grouped spatially in the calorimeter. Finally, the energies of crystal hits in these final groups are added together and recorded as a cluster energy. The best way to find a cluster time is currently under investigation, with possibilities including an energy weighted time of all crystal hits in a cluster group and taking the time of the crystal hit with the maximum energy deposition. The difference in cluster time between these techniques is quite small, on the order of a hundred picoseconds. Nevertheless, it may have systematic error implications.

A position reconstruction algorithm is applied at the clustering stage. The most accurate technique tested so far is a logarithmic weighting technique, where $x_{reco} = \sum(w_i x_i)/\sum(w_i)$, where $w_i = max(0, w_0 + E_i/E_{sum})$. w_0 is a free parameter of this technique, and the optimum w_0 value for our calorimeter was determined to be about 4.0. This position reconstruction algorithm provides 2 mm position resolution for 2 GeV positron impacts. A good position reconstruction algorithm should as much as possible have no bias and a resolution independent of impact position. This position reconstruction algorithm was tested on real data at SLAC this past summer, and the results are shown in Fig. 4.13-3.

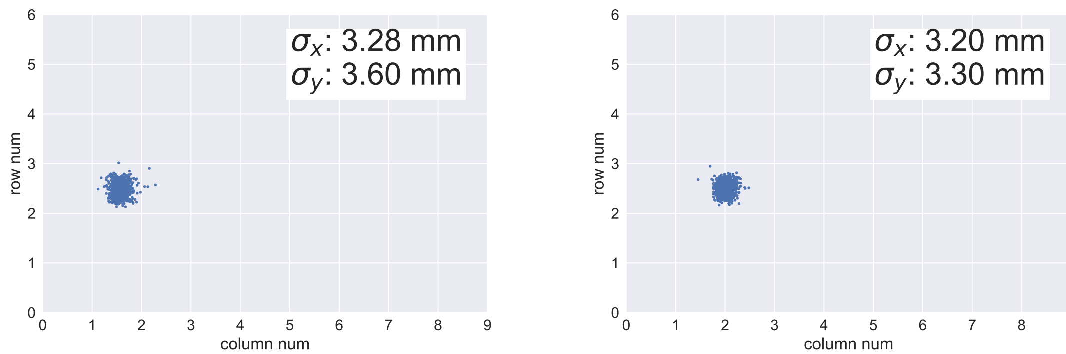

Figure 4.13-3. *Left*: Reconstructed positions when the beam was aimed at the center of a crystal. *Right*: Reconstructed positions when the beam was aimed at the crack between two crystals. The reconstructed beam width in x is mostly unchanged in these two cases. The y width shows a difference in the two cases, but this could be explained by calibration errors and the difference is less than that obtained with other methods. The width in these graphs includes both the resolution of the calorimeter and the width of the beam itself.

As described in (Sec. 4.14), the full reconstruction chain was exercised during the SLAC test beam run last summer. All components are functioning, and the $g-2$ calorimeter offline chain is fully ready to transform raw data into reconstructed decay positrons as soon as our first beam data arrives.

4.14 Highlights of the SLAC 2016 data analysis

A. T. Fienberg, J. Hempstead, D. W. Hertzog, J. Kaspar, and K. S. Khaw

In June of 2016, the Muon g-2 ω_a team completed another Test Beam Experiment at SLAC to make a final evaluation of the full instrumentation for measuring the ω_a for the Muon g-2 experiment at Fermilab. The performance was evaluated using an electron beam at the End Station Test Beams (ESTB) and the tested system includes a PbF_2 calorimeter, 800 MSPS custom waveform digitizers, hybrid CPU-GPU DAQ system, MIDAS-based data acquisition system and event builder and *art*-based offline data analysis framework.

As explained in the previous section, the offline analysis framework starts by unpacking raw DAQ data into data products with structure. The one that is relevant for the analysis is called the island - a short waveform digitizer trace around the samples above a threshold. This island is then fitted using a template waveform (Fig. 4.13-1) to extract the pulse integral.

This pulse integral is then converted to number of photo-electrons using a calibration constant (SiPM gain), derived through a laser calibration[1] method. The effective number of photo-electrons serves as a proxy for energy deposited into a crystal. Finally a clustering algorithm is applied to these crystals to create a cluster that serves as the proxy for an electron impact.

To ensure a uniform response across the calorimeter, the SiPM gains must be as uniform as possible. They depend mainly on the over-voltage[2] and the ambient temperature. A systematic procedure has to be followed in order to achieve this uniformity.

- First, the SiPMs are grouped into a calorimeter with as small as possible the variance in breakdown voltages (provided by the manufacturer Hamamatsu).

- Then, to correct for the temperature gradient across the calorimeter crystals (about 5°C from the left to the right column), the SiPMs are separated into four groups based on their position within the calorimeter, and each of these groups is connected to an independent bias supply.

- Additionally, each SiPM amplifier board contains a programmable gain amplifier (PGA) with amplitude amplification adjustable over the range 2-20.

The gain equalization process is then iterative and consists of alternating laser calibrations and adjustments to the gains and bias voltages. After several iterations, equalization on the level of 8% in RMS was achieved and is shown in Fig. 4.14-1. Further improvement is very challenging due to the limited number of bias supplies (4 bias supplies to drive 54 SiPMs) and the limited gain steps (80 steps from a gain of 2 to 20). Laser calibrations were performed on average every three hours to monitor stability.

[1] Laser calibration method utilizes photo-statistics to extract the number of photo-electrons/pulse-integral by varying the laser intensity through a neutral density (ND) filter wheel.

[2] Over-voltage, $V_{ov} = V_{ap} - V_{bd}$, where V_{ap} is the applied voltage and V_{bd} is the breakdown voltage, an intrinsic properties of the SiPM.

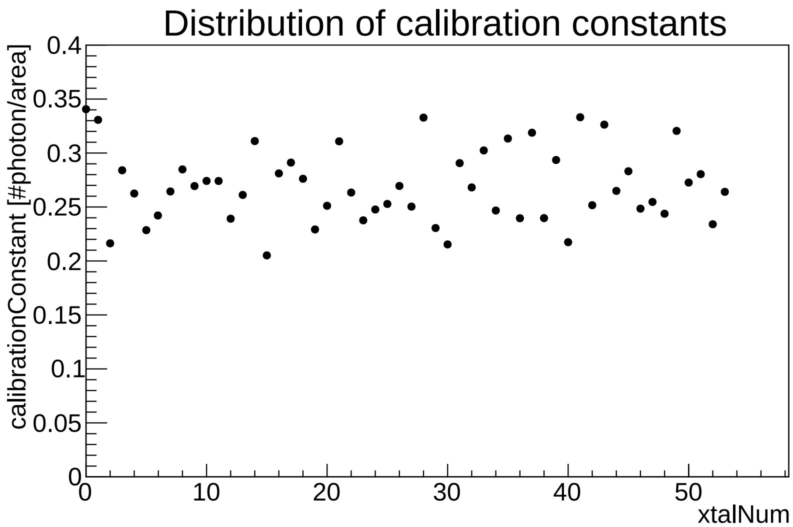

Figure 4.14-1. Distribution of 54 photon calibration (SiPM gain) constants.

The SiPM gains that were extracted using the laser calibration procedure above are valid for any subsequent runs if there is no drift as a function of time. To account for any drift in the gain, the SiPM's laser response is monitored as a function of time. The laser's intensity fluctuation is also measured using pin diodes to serve as a normalization factor. These two corrections are applied to the extracted number of photo-electrons and the resulting stability is shown in Fig. 4.14-2.

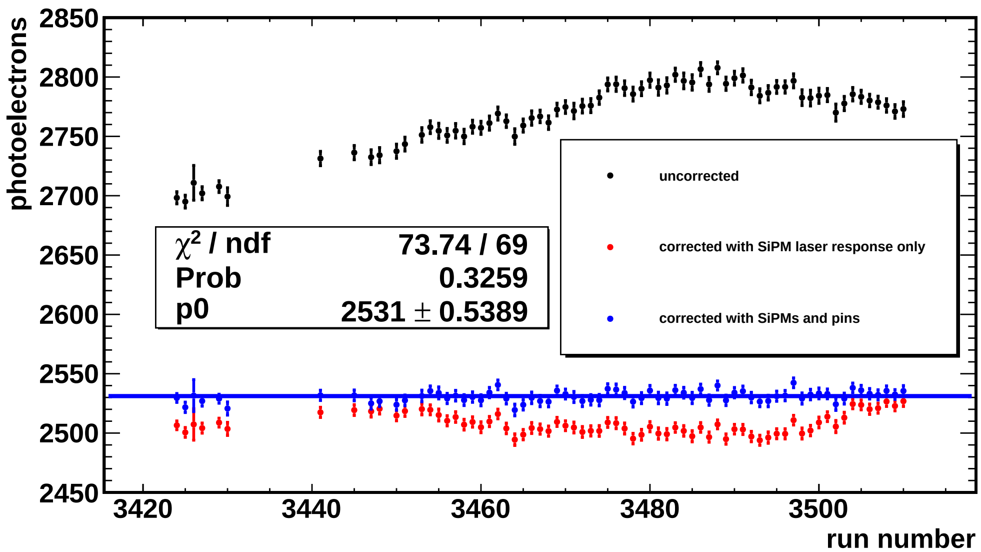

Figure 4.14-2. Stability of the SiPM's beam response as a function of run (a run is 15-20 minutes).

The gain equalization and drift correction procedures described above do not take into account any possible variance in light yield, light transmission efficiency[1], optical coupling between the crystal and the SiPM and so on between the crystals. To study the uniformity of the energy response of the calorimeter taking these effects into account, we aimed the electron beam at the center of each crystal and measured the energy distribution. The result is summarized in Fig. 4.14-3. A uniformity of 10% is within our expectation as we could only achieve an 8% level equalization for the SiPM gain as mentioned two paragraphs before. The remaining 6% deviation can be attributed to the effects described above.

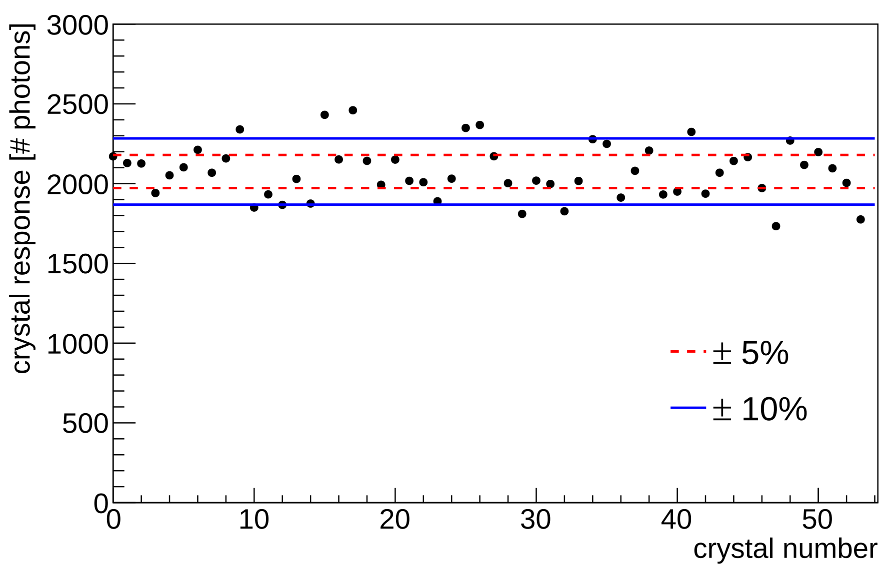

Figure 4.14-3. Distribution of the energy response of the 54 PbF_2 crystals and SiPMs.

To extract the energy resolution at various beam energies, we fit the reconstructed energy spectrum at 3 to 5 GeV with a Gaussian function. The energy resolution we measured, as shown in Fig. 4.14-4 (left), is 2.7% at 3 GeV, which surpasses the required 5% at 2 GeV specified in our TDR. We have also tested the linearity of the calorimeter by varying electron beam energy from 2.5 GeV to 5 GeV. Our calorimeter exhibited a very good linearity in this energy range as indicated in Fig. 4.14-4 (right).

[1]Quality control measurements of PbF_2 transmission indicated a 4% standard deviation.

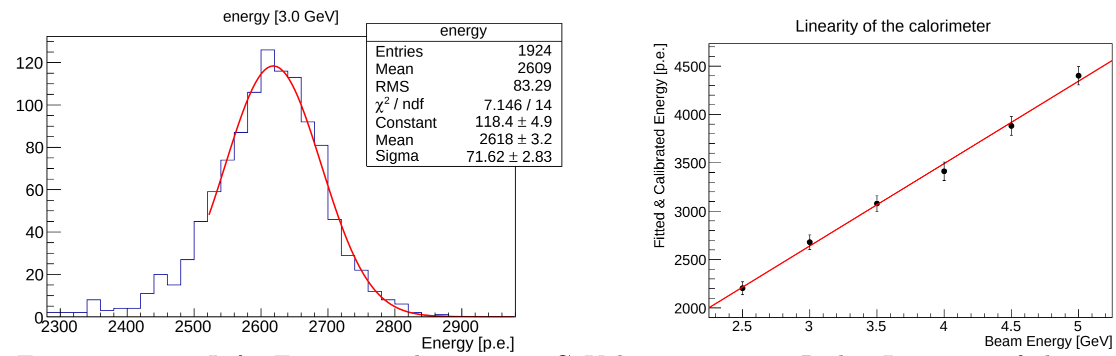

Figure 4.14-4. *Left*: Energy resolution at 3-GeV beam energy. *Right*: Linearity of the calorimeter.

There are two timing resolution plots of interest that can be extracted from the sync laser pulse measurements. The first one is the time difference between different channels (i and j) of the same laser shot and it is given by $\Delta t_1 = t_{\mathrm{laser},i} - t_{\mathrm{laser},j}$. The second one is the time difference between pulse a and pulse b of the same channel i, $\Delta t_2 = t_{\mathrm{laser,a},i} - t_{\mathrm{laser,b},i}$. We plot the time difference between different channel of the same laser shot Δt_1 in Fig. 4.14-5 (left). The time resolution is about 25 ps, surpassing the specification in our TDR[1]. The timing resolution between consecutive laser shots is about 300 ps and is shown in Fig. 4.14-5 (right).

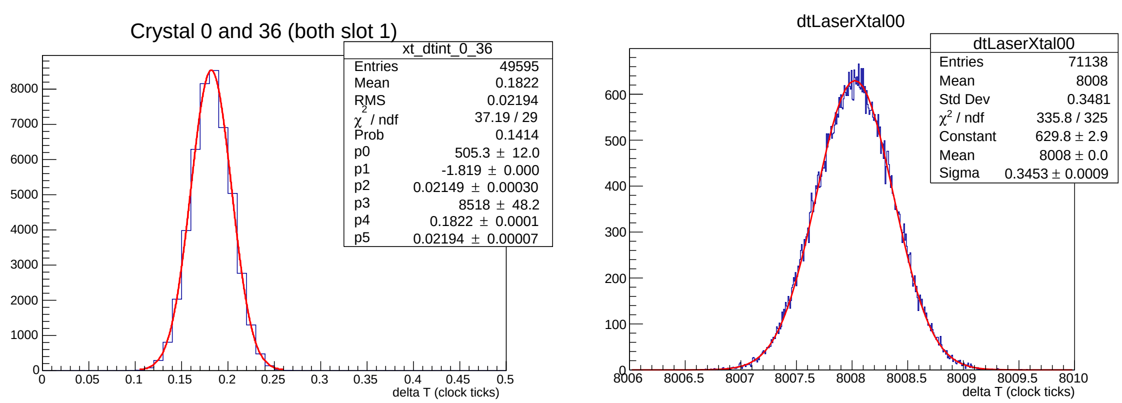

Figure 4.14-5. *Left*: The timing resolution between two channels for the same laser shot ($\approx$ 25 ps) and *Right*: the timing resolution between two laser shots in the same channel ($\approx$ 300 ps).

Described above are core analysis results related to the performance of the ω_a measurement system. Several analyses like angle reconstruction using relative energy and timing information, understanding of the electromagnetic shower propagation and the Cerenkov light transportation in our PbF_2 crystals are ongoing.

[1]The time resolution requirement outlined in the Muon g-2 TDR is 100 ps for a positron with energy above 100 MeV.

4.15 Muon beam injection and storage studies

N. S. Froemming, D. W. Hertzog, J. Kaspar, and K. S. Khaw

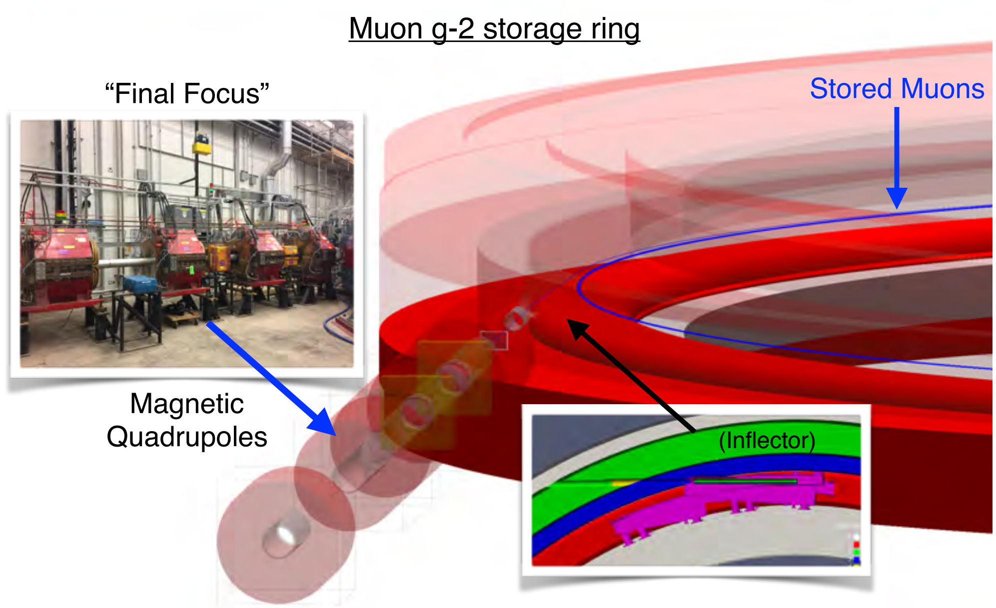

Figure 4.15-1. Simplified example of a muon-storage-ring simulation. This particular simulation features a novel implementation of electromagnetic fields (not shown) as well as the "final focus," a set of four magnetic quadrupoles just upstream of the muon storage ring that will help optimize the injection tune of the incident muon beam.

When muons are injected into the $g-2$ storage ring, approximately 97% will be lost almost immediately. Most of these losses ($\sim 90\%$) arise from a momentum mismatch between the muon beam delivered by Fermilab and the storage ring originally designed and built at Brookhaven National Laboratory.[1] For the remaining few percent of storable muons, the largest contributors to injection losses are (1) upstream beam parameters and injection tune; (2) scraping, multiple scattering, and energy loss in the beam channel; and (3) inefficiencies in "kicking" the muon beam onto the proper storage-ring orbit once the beam has entered the ring. Optimizing these injection parameters is key for capturing as many muons in the storage ring as possible and ensuring the experiment is completed on the required time scale with the required statistics. Simulations have played a key role in facilitating understanding and guiding experimental design, and UW simulations in particular have influenced almost every aspect of injection in a positive way. One such example is shown in Fig. 4.15-1.

[1]The same magnetic storage ring used at BNL, with many upgrades and improvements, will also be used at Fermilab.

4.16 Inflector beam monitoring system

J. F. Amsbaugh, W. A. Collins*, N. S. Froemming, D. W. Hertzog, P. Kammel, B. K. H. MacCoy, D. A. Peterson, M. W. Smith, and T. D. Van Wechel

The muon injection into the $g-2$ storage ring is one of the most critical and complex elements in the muon delivery concept. The challenges are extensively described in the Muon $g-2$ TDR. The entering muon beam has to pass through strong fringe fields and the narrow inflector apertures (18 mm(W) $\times$ 56 mm(H)), which results in a mismatch between transmitted beam phase space and the ring acceptance. Extensive simulations were performed to study the impact of this beam section on the muon storage fraction and betatron oscillation amplitudes in the $g-2$ ring.

The Inflector Beam Monitoring System (IBMS) is being designed and constructed at CENPA; it is the primary diagnostic tool to develop and verify the beam optics tune in the muon injection section. It is also foreseen as a continuous monitor of the beam properties, relevant for detecting systematic problems.

The locations of the IBMS detectors and the expected beam profiles are shown in Fig. 4.16-1. Detectors 1 and 2 will be made of two planes of 16 scintillating fibers each, oriented in

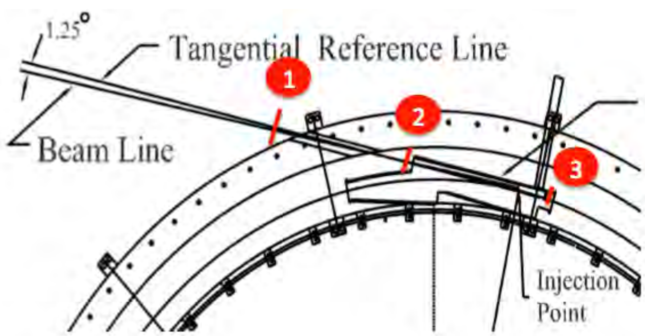

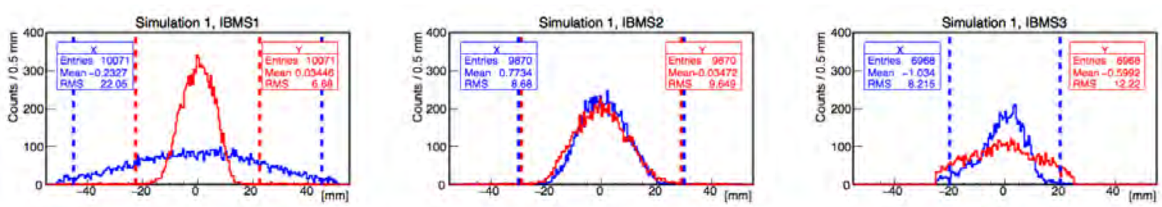

Figure 4.16-1. *Top*: The three IBMS detectors monitor the critical passage of the beam from entrance into the yoke until injection into the ring. *Bottom*: Beam profiles at the detector locations in x (radial) and y (vertical). The plot y-axis represents muon hits per fiber at candidate fiber locations, calculated for 10,000 incident muons (expected rate is 70 times higher at 700,000 muons per pulse). The dashed lines indicate bounds of the IBMS active area. IBMS 3 reads only the x (radial) beam profile, so the corresponding plot shows only x bounds (blue dashed lines).

*Undergraduate taking research credit. Presently at Skidmore College, Saratoga Springs, NY.

the horizontal and vertical directions. Simulations show that only vertical fibers are needed for detector 3. Each 0.5 mm diameter, double-cladded fiber (SCSF-78 from Kuraray) will be read out by silicon photomultipliers from Hamamatsu. These 1 mm^2 area devices were selected for their large dynamic range (10,000 pixels) and fast recovery time. All fiber signals will be digitized with a CAEN V1742 Switched-Capacitor Digitizer.

During the last year the project realized the following important steps:

Prototype detector and readout electronics built and characterized. The prototype detector was 100 mm long, with an aluminum and a lucite end, where the fibers were glued in. This detector can be seen in Fig. 4.16-2 *right* along with the final 32-fiber IBMS 2 detector on the *left*. Three fiber pairs were mounted: 0.5 mm diameter round Kuraray, 1 mm diameter round Kuraray, and 0.5 mm square Bicron. A two-channel readout board was designed. Extensive studies of the light output and homogeneity of scintillation light excited by a beta-source were performed by Kammel and PhD student Froemming, and determined that the 0.5 mm fiber was the optimal choice regarding low mass and sufficient signal.

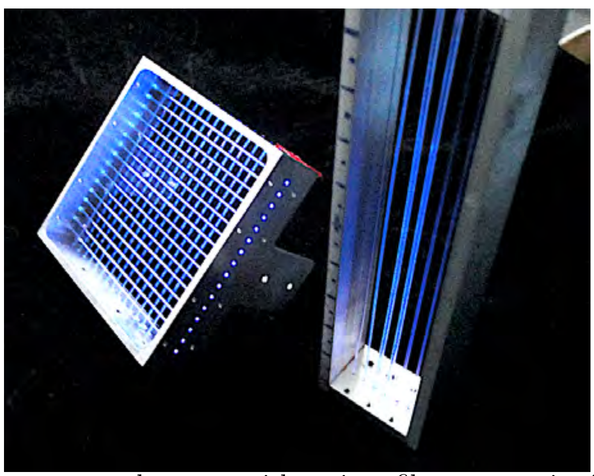

Figure 4.16-2. *Right*: prototype detectors with various fiber geometries from different vendors. *Left*: final IBMS 2 detector, with the selected 0.5 mm round fibers from Kuraray, built by REU student Collins.

IBMS 2 transport rail system constructed and deployed into $g-2$ magnet. IBMS 2 needs to be moved 2.3 m into the yoke of the $g-2$ ring to its measuring position right before the inflector. A rail system, flexible enough to overcome misalignments in the beam entrance pipe, was constructed and successfully deployed at Fermilab. The challenging travel of the final detector system deep into the narrow beam pipe is being developed with a mock-up system at UW. The various stages of the project are shown in Fig. 4.16-3.

High density amplifier prototype characterized and final readout board constructed. The SiPM amplifier has to fulfill demanding constraints. In particular for IBMS 2, the available space is extremely limited. The particles per pulse will vary significantly between fibers and during the commissioning period. Pixel saturation, resulting from the limited number of pixels per SiPM, will be minimized by inserting neutral density filters. The final amplifier is based on low-noise, programmable gain amplifiers followed by line

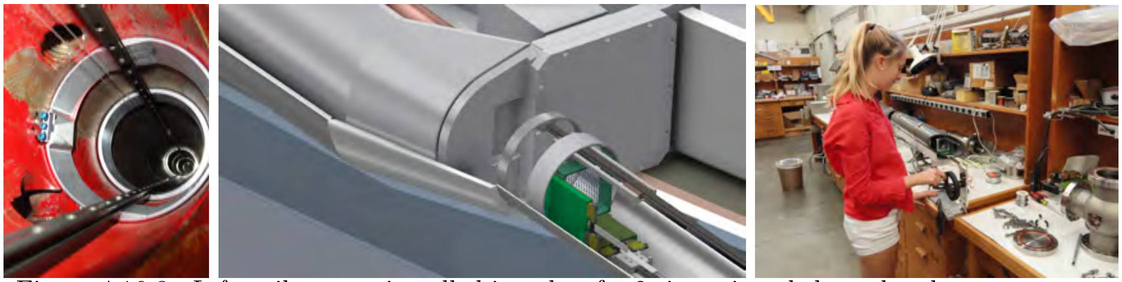

Figure 4.16-3. *Left*: rail system installed in yoke of g-2 ring, viewed through yoke entrance. *Center*: CAD model of rail system guiding IBMS 2 into the yoke. *Right*: REU student Collins practices inserting IBMS 2 with the mock-up rail system.

drivers to transport the analog signals via micro-coax cables to the receiving waveform digitizers. While a vast amount of literature about fast pulse applications with SiPMs exists, information about recording extended pulses, like the 120 ns long $g-2$ beam spill, is scarce. Dedicated studies were required and performed by PhD student MacCoy and Kammel to maintain high voltage stability and sufficient dynamic range under these challenging conditions. Fig. 4.16-4 shows the series of boards leading to the final design (right). The final 16-channel board fits onto the final IBMS 2 detector (Fig. 4.16-2), with one board reading out each 16-fiber axis of the 32-fiber detector.

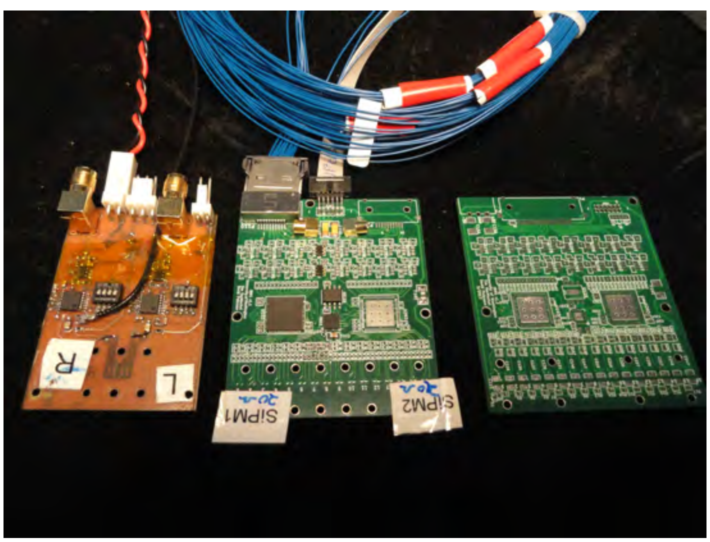

Figure 4.16-4. *Left*: early two-channel readout board prototype. center: 16-channel readout board prototype used for stability and dynamic range studies. *Right*: final 16-channel readout board.

In early 2017, $g-2$ project funding was realized for the commercial readout electronics located in two VME crates inside and outside of the ring. The DAQ and analysis software for detector quality control and beam monitoring is currently under development. PhD student MacCoy is developing a laser calibration system and contributing to the design of IBMS 3, which will be situated inside the $g-2$ ring vacuum close to the circulating muon beam and will be constructed from selected non-magnetic materials.

4.17 Magnetic field overview - the shimming story

M. Fertl, A. Garcia, R. Ortez*, R. Osofsky, M. Smith, and H. E. Swanson

Our goal for the new g-2 experiment is to achieve an uncertainty in the average muon weighted field value of 70 parts per billion (ppb). Pulsed proton NMR typically achieves resolutions of 10 ppb, well below this goal. During a run, field measurements consist of two parts: 1) a matrix of NMR probes is pulled through the muon storage region (the so-called trolley) every few days measuring the spatial distribution of the field and 2) groups of stationary probes installed above and below the storage volume (fixed probes) every five degrees around the ring continuously track the time behavior of the field between trolley runs acting as a proxy for the volume field. Shimming is the process for achieving a homogeneous field in the storage ring which allows our measurement scheme to faithfully represent the field.

The UW field team spent the better part of 2016 at Fermilab completing the shimming project. The previous annual report[1] describes measurement techniques and tools created for the shimming process. Field measurements were made with a matrix of 25 NMR probes mounted on a platform that rolled along the lower pole surface. The first phase, which was underway at the time of writing that report, was to make the physical upper to lower pole gap as uniform as possible around the ring. Pole tilts and gap discontinuities at pole edges were measured using a UW built electrolytic bubble level with microradian precision. These data and measurements of the pole gap were fit to a globally flat surface model and residuals specified changes to heights of the pole's mounting feet. The ring has 72 poles with as many as 10 mounting feet per pole that required adjustments. In a typical sequence 3 adjacent poles were removed in the morning followed by the work party removing the feet and finding the closest combination of shims to match the specified heights. This is shown in Fig. 4.17-1 where bottom pole pieces needed to be flipped to access the mounting feet. After re-installing the shimmed feet, poles were put back in place and re-aligned. Subsequent field measurements monitored our overall progress and alerted us when mistakes were made.

Figure 4.17-1. *Left panel*: Fermilab technicians flipping a bottom pole to expose mounting feet for adjustments. *Right panel*: UW student Rachel Osofsky searches with a micrometer for the right combination of shim material to match the thicknesses specified by the computer code, UW student Mathias Smith re-installs feet on the pole piece and UW graduate Brendan Kiburg records the changes.

*Presently at UCSB, Santa Barbra, CA.

[1]CENPA Annual Report, University of Washington (2016) p. 76.

This iterative process continued until May 2016. We had reached the point of diminishing returns and any further changes in the height of the feet were within the measurement errors of the shims. With the magnet gap now largely constant around the ring we started the second phase of magnetic field shimming. In this phase the primary components are field measurements and the shimming tool kit included in the design of the magnet. Fig. 4.17-2 shows a radial slice through the storage ring including these tools. The magnetic circuit consists of inner and outer coils, flux return yokes, upper and lower poles and shimming elements Top Hats and Wedges. 12 yoke sections make up the entire storage ring. Top Hats are slabs of iron mounted above and below the yokes with variable thickness spacers. Changing the thickness affects the field in the gap over the length scale of a yoke or 30° in azimuth. Wedges located in the space between poles and yokes compensate for the C-shaped flux return and can be moved radially to vary the field in the pole's gap with length scale 10° in azimuth. Interestingly, we ended up making upper and lower poles not quite parallel to correct wedge angles and better compensate for the asymmetry of the yoke.

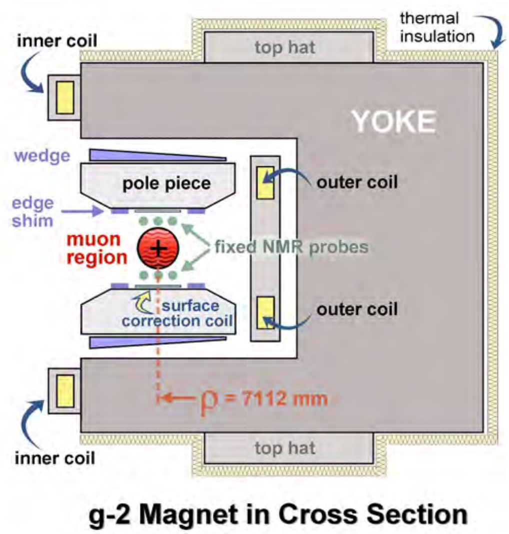

Figure 4.17-2. A cross sectional view of the storage ring magnet showing poles, the muon storage volume and shimming tools. Wedge shaped iron pieces in the spaces between poles and yoke compensate for the asymmetry in the C shaped yoke and they can be moved in and out to vary the field strength in the gap defined by the particular pole. There are 12 of these per pole and their influence on the field has the same azimuthal extent as the pole itself, 10°. Top hats also affect the field in the gap. They are spaced above and below the yoke iron with non-ferrous spacers. The effective permeability of the flux return is varied by changing spacer thicknesses. These have an azimuthal extent of 30°. Additional shims shown mounted in the gap directly on pole surfaces correct higher order effects.

Each representative element was calibrated by comparing field maps before and after positions of these elements were changed by a known amount. Using difference maps as templates, a computer code optimized positions of all the elements. This took until July 2016, iterating between making field maps and adjusting the 48 top hats and 864 wedges. Fermilab personnel moved top hats which required the use of the crane. Wedge adjustments were made by the Field Team and often involved the help of graduate students and postdocs from other teams in the project. Mapping the field took upwards of three hours for each trip around the entire ring.

Remaining field variations had length scales shorter than the poles and it became clear these could not be further reduced with the built in shimming tools. Following the example of the BNL team we developed an additional tool for the kit and embarked on a third shimming phase. Strips of thin iron foils added to pole surfaces increase the field in the gap with length scales of order of the strip widths. In the 1.45 T field of the magnet these strips are saturated and their effect on the field can be modeled as a collection of dipoles of this saturation strength. Using this model a computer code calculates the mass of iron required to fill in low field regions of the field map. In our implementation foil locations are fixed in azimuth and their widths varied to achieve the specified mass.

For a proof of principle a small number of these foils were cut out by hand. Each batch of foil material had to be checked for consistency in permeability through field measurements. All remaining strips were cut from roles of calibrated 1 mil shim stock using the laser cutter at CENPA. Fig. 4.17-3 shows a recent graduate Ronaldo Ortez spending his summer operating the laser cutter. Thickness non-uniformity of the foil material required us to weigh each foil and select foils based on their actual masses. This was done back at Fermilab by a small army of students and summer interns. We ended up producing about 10,000 iron foil strips.

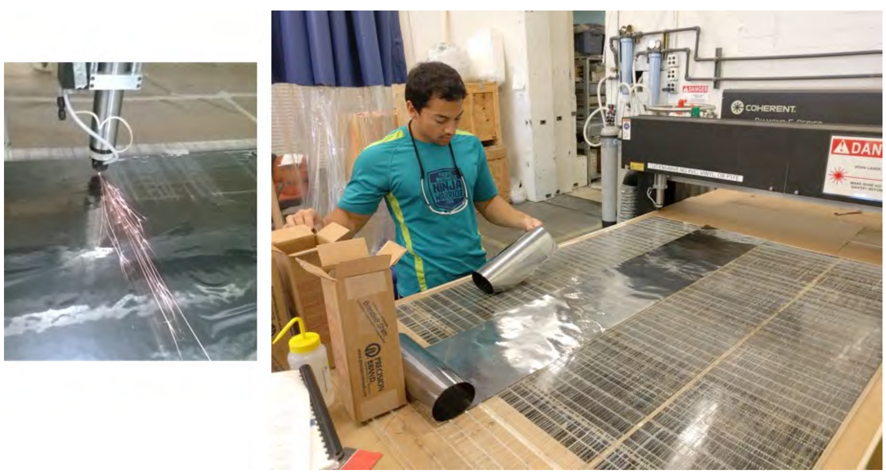

Figure 4.17-3. *Left panel*: the laser cutter in action. *Right panel*: UW student Ronaldo Ortez setting up the laser cutter at CENPA to cut iron foils used in shimming the magnet. About 10,000 individual foils were produced.

Foils were laminated with double sided tape on G-10 sheets cut to the size of the poles. Templates with radial lines spaced every 3 cm were placed under the G-10 and were visible through the G-10 material as an aid in positioning the strips. Fig. 4.17-4 shows a completed lamination. Three independent strips were placed along each radial line with widths chosen to cancel field variations across the storage volume. Fixed probes that monitor the field are adversely affected by field gradients produced by these stripes. In regions that are in close proximity to a group of probes we placed a section with thinner strips oriented in the orthogonal direction. They preserved the same average mass density and reduced the problematic gradients. These regions appear as having different shadings just above the yellow stanchions.

Figure 4.17-4. Foils are attached to G-10 sheets with double sided tape. Foil locations are uniformly distributed around the circumference and a computer code specifies the mass at each location to fill in low regions in the field map. The approximately square homogeneous sections near the center (above the two yellow stanchions) have smaller field gradients to accommodate nearby fixed probes. These sheets are then epoxied to the pole pieces. The photo was taken inside the muon storage ring.

Proper alignment of these laminations in the storage ring is critical for their purpose of filling in the field valleys. The azimuth angle coordinate of the field map is given relative to a fixed location on the measurement trolley, not to active volumes in the NMR probes. While this offset is generally known its uncertainty exceeds the alignment precision needed. Actual clocking of the laminations was data driven making use of field measurements and features they were made to suppress. By September lamination production was complete and the 72 G-10 boards were epoxied to the pole surfaces, foil side towards the poles. We made a few more tweaks of wedges and Top Hats to compensate for the additional iron in the foils but for the most part this marked the end of the mechanical shimming program. It had been about a year ago when we started with peak to peak field variations of 1400 ppm. During this time the ring's field was mapped in excess of 50 times and in addition we determined the longitudinal and radial components of the field at many azimuthal positions with Hall probe elements. The NMR measurement system has no directional sensitivity.

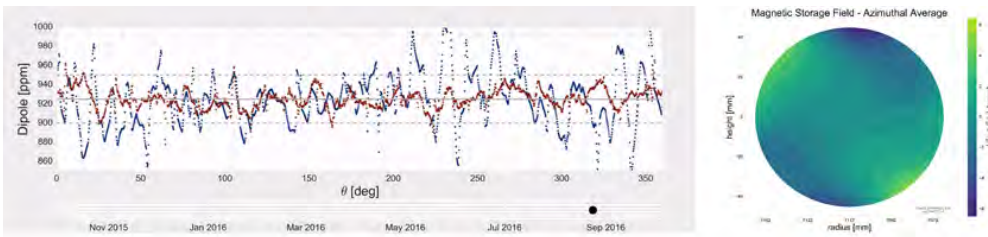

Dipole Field	RMS (ppm)	p-p (ppm)
FNAL (After Shimming)	10	75
BNL (Typical scan)	30	230

Figure 4.17-5. *Upper left panel*: Dipole field variations as a function of ring azimuth. Red shows the field at the end of shimming. The blue curve is a typical scan from the Brookhaven National Laboratory (BNL) g-2 experiment. *Upper right panel*: The transverse variation of the field in the storage ring volume averaged over azimuth. *Bottom panel*: A numerical comparison of our shimming result with the BNL field.

Our final field map is given by the red curve in the upper left plot of Fig. 4.17-5. The blue curve by contrast shows a typical scan from the BNL g-2 measurement. The table gives a comparison of the peak to peak and RMS values for these two plots. By both measures magnetic field variations in the Fermilab ring are reduced by a factor of three when compared to the BNL ring. The upper right panel shows transverse variations in the field averaged over the ring circumference. The pattern is dominated by the sextupole moment of the field distribution. At the begining of this article we gave our systematic error goal as 70 ppb, a two-fold improvement over BNL's estimate. Much of this reduction comes from alignment efforts to improve position uncertainty in field measurements. The improved homogeneity of the field reduces sensitivity to these position errors as well as to uncertainties in muon trajectories.

4.18 NMR hardware

M. Fertl, A. Garcia, R. Ortez, R. Osofsky, M. Smith, and H. E. Swanson

The 1.45 T precision magnetic field in the muon storage ring is measured using pulsed nuclear magnetic resonance (pNMR) magnetometers. Each magnetometer consists of a so-called pNMR probe (the sensitive part of the magnetometer) combined with a pulse and frequency mixing unit. In 2016 the CENPA team finished the production of more than 450 pNMR probes. All probes passed a careful Q&A test before they were delivered to the experimental site at Fermi National Accelerator Laboratory and to the test magnet setup at Argonne National Laboratory. A subset of 28 pNMR probes was installed on a shimming cart in 2015 and used to perform the passive shimming of the magnetic field, which continued into 2016. In preparation for the vacuum chamber installation a subset of 378 pNMR probes was installed into dedicated grooves machined into the outside of the vacuum chambers walls.

Figure 4.18-1. Erik Swanson completing initial installation tests of the pNMR probes in the walls of the vacuum chambers of the muon $g-2$ storage ring.

The physical installation with hot glue in the vacuum chamber grooves was initially tested at UW. In Fig. 4.18-1 the installation procedure of a single pNMR probe on the bottom side of the vacuum chamber is shown. Each pNMR probe was fixed in its dedicated groove using hot glue and its position was recorded in the pNMR probe database.

In order to excite the free induction decay (FID) signal, which encodes the magnetic field information, a strong radio-frequency (RF) pulse ($\approx 10\,\mathrm{W}$, ≈ 7 ¯s, 61.74 MHz) is gated into the probe head and the resulting weak FID signal is digitized after initial pre-amplification and mixing with a reference frequency. The CENPA electronics shop designed a combined pulser/mixing module from state of the art solid state electronic components to replace the hardware used in the BNL E821 experiment. The new design allows to control the excitation pulse start time and pulse length with signals generated with a field programmable gate array (FPGA). This allows us to optimize the amplitude of the FID signal obtained from each individual probe head. The time structure of the experiment allows for a highly multiplexed excite-and-probe cycle across all the pNMR probes and therefore each pulser/mixing unit is combined with a 24 channel switch board in a single enclosure. Twenty of these combined units have been built at CENPA during summer 2016. One pNMR multiplexer unit typically has a pair of 20 pNMR probes connected with the remaining channels serving as spare during the experimental runs.

After the installation of the vacuum chambers in the gap of the superferric storage ring the pNMR pulser/mixer units were installed on top of the magnet yoke in February 2017. After this, the individual pNMR probes have been connected and their cables have been

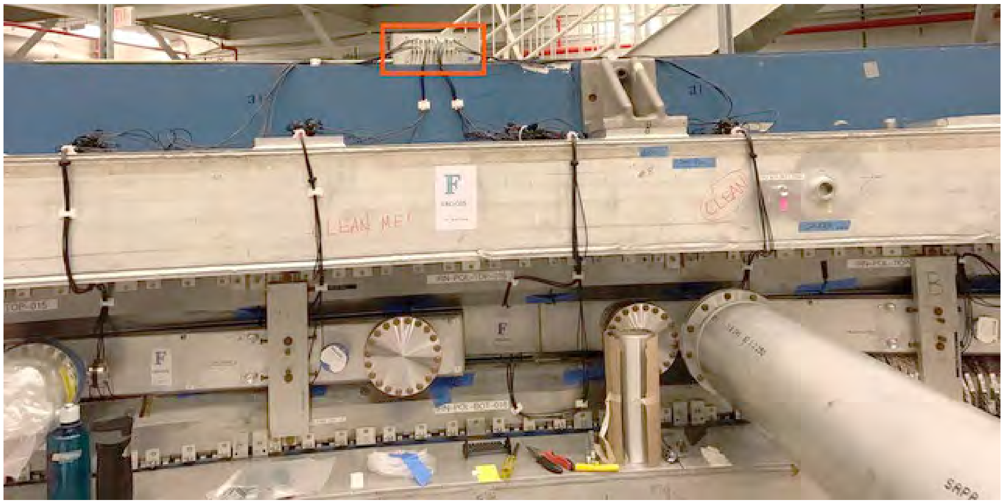

Figure 4.18-2. Installation of a multiplexer unit on top of the storage ring magnet. Each pulser/mixing unit controls about 20 pNMR probes in an arc-like subsection of the storage ring. The multiplexer unit is highlighted in the red rectangle.

carefully routed in order not to interfere with other experimental subsystems. The picture of the first completely installed pulser unit is shown in Fig. 4.18-2.

In February 2017 all the RF signal cables were routed to the central digitizer station in the center of the storage ring. This will allow us to finish the commissioning of the pNMR probe hardware as soon as the magnetic field in the storage ring is ramped up again in March 2017. A detailed discussion of the field data acquisition is given in 4.19.

In addition, the UW team finished the production of two sets of twenty pNMR probes for the remotely controlled field mapper ("trolley") that scans the magnetic field in between muon operation periods. The two subsets have a different spatial extent of their magnetic field sensitive region, which can be used to perform detailed systematic studies of the magnetic field value measured with the trolley. Seventeen of these probes were installed in the trolley at ANL during its final assembly in March 2017.

4.19 Magnetic field data acquisition and analysis

M. Fertl, A. Garcia, R. Ortez, R. Osofsky, M. Smith, and H. E. Swanson

The Muon $g-2$ Experiment at Fermilab derives two quantities through steadfast data acquisition and rigorous analysis, one of which represents the magnetic field experienced by the muons. The machinery for measuring the magnetic field is set to come online soon. The core field measurements are taken by a 17-probe matrix on a mobile trolley which allows construction of a 2D map of the field in the region occupied by muons, and fixed NMR probes around the storage ring which measure drift. The crux of the technique is illustrated in Fig. 4.19-1. The 2D field map and the fixed probe interpolation correction are used in conjunction to produce the field team deliverable, the magnetic storage field as a function of time and space.

$$\vec{B}(\vec{x},t) = \vec{B}_0(\vec{f}_{trolley}, t_0) + \delta\vec{B}(\vec{f}_{fixed}, t) \tag{1}$$

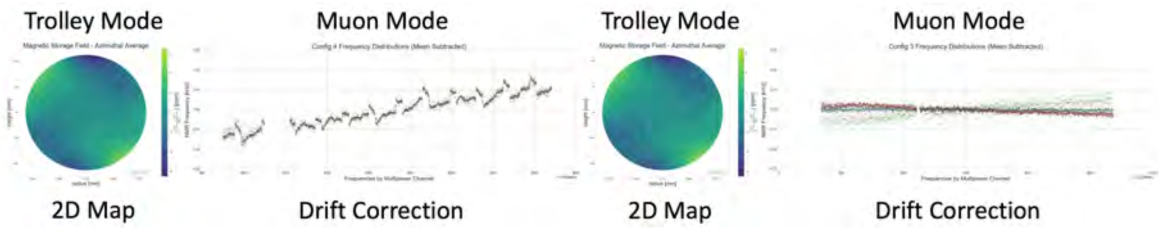

Figure 4.19-1. The basic scheme behind the $g-2$ magnetic field mapping technique is illustrated here using plots and data from the rough shimming stages of the field evolution. The "Trolley Mode" plots depict the 2D field map azimuthally averaged over the toroidal muon storage volume, and the "Muon Mode" plots represent fixed NMR probe frequencies drifting over time. Each mode will recur many times in lockstep. Each "Muon Mode" drift is used to interpolate between adjacent "Trolley Mode" 2D field maps.

In addition to the core components, there are additional essential elements to convert the measurements into an absolute field value. Other systems include the power supply feedback system which corrects the average field drift, the surface current coils which correct the average field asymmetries, and the fluxgate system to monitor potential fast transients in the field values.

The subsystems of the $g-2$ field data acquisition (DAQ) system communicate with independent hardware systems through a combination of custom code written by the field team and libraries provided for the hardware, see Fig. 4.19-2. The trolley subsystem loads in a movement plan for the Galil motion controller, then, constantly reads back position information and NMR waveforms throughout the trolley run. The fixed probe subsystem consists of 378 NMR probes (see layout in figure Fig. 4.19-3) which are divided amongst 20 pulser/mixer module sets. The DAQ must handle selecting the proper multiplexer channel, triggering NMR pulsers over VME, then, subsequently reading out and mapping the NMR waveforms to the fixed probe data structure. As far as other systems, a Yokogawa power supply provides feedback for the main current by setting the average magnetic field over USB by both setting and getting current values. The fluxgate system pushes data through a National Instruments C-library, a Meinberg GPS clock reads out over a Linux system driver, and the surface coil system sets and reads current values by communicating with several satellite Linux systems over ZeroMQ sockets (TCP).

The design of the DAQ system aims to utilize the power of several existing frameworks and add new code in a flexible, reusable way. The standard data pipeline for $g-2$ runs through the following: MIDAS framework to interface with hardware and aggregate data, midas-to-art unpacker modules to convert the MIDAS files into the event based, Fermilab supported, art analysis framework, midas-to-art modules for online data-quality monitors (DQM), and art-analysis modules. The field DAQ follows the standard pipeline with some nuance. The field DAQ team elected to abstract hardware communication into a reusable

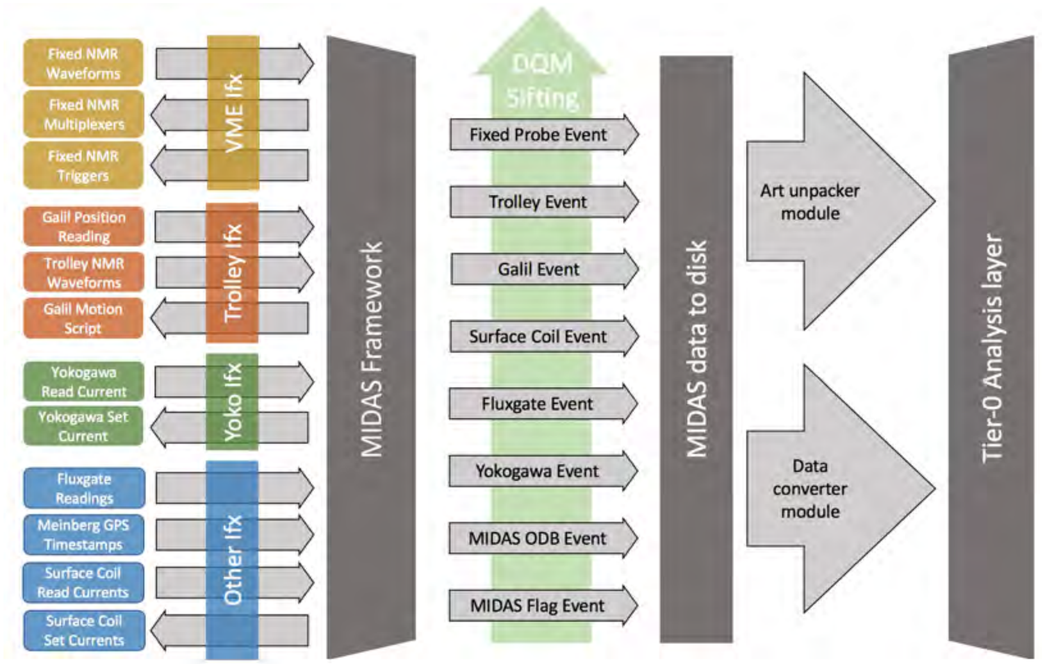

Figure 4.19-2. An outline of the field DAQ components with arrows to indicate communication and data transfer. Paths start on the left with the hardware components as software blocks. The gray arrows depict the direction of data flow and overlaid colored boxes indicate which interface (ifx) library handles the communication. At the MIDAS framework level all front-ends send data events to be written to a MIDAS file on disk. This is also the point where the data quality monitor system sifts off events to monitor data quality. The events in the MIDAS file can be unpacked by art modules into art files or secondary data formats for further analysis.

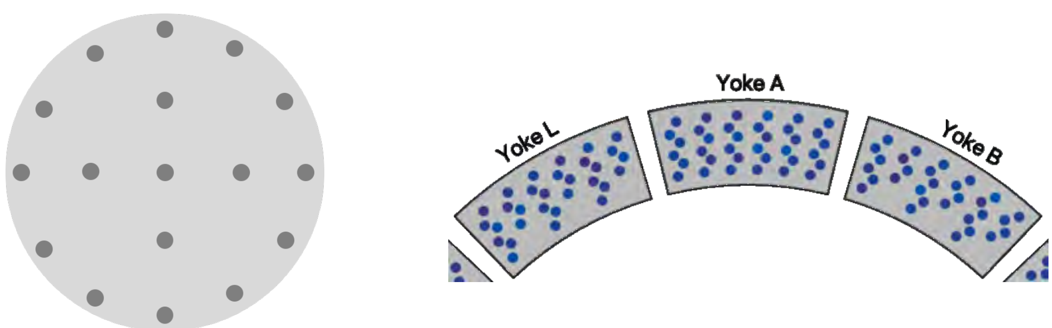

Figure 4.19-3. *Left*: Probe matrix from the NMR trolley which maps the 2D magnetic field around the storage ring. *Right*: Overhead view of several of the 12 ring sections highlighting the relative locations of the fixed NMR probes with top and bottom slightly offset in radius and azimuth. The color of the probes on the yoke sections indicates signal health, ranging from red to blue.

interface layer. The team also implemented direct propagation for a non-data MIDAS event which carries flags set by the front-ends and MIDAS itself. The full pipeline is displayed in diagram form in Fig. 4.19-2.

Online monitoring fulfills an essential role in any DAQ system. The experiment will be run by shifters, most of whom were not involved in writing elements of the DAQ. They must be able to monitor the viability of the data and take actions when necessary. For this purpose the DAQ team produced a data quality monitor (DQM) framework built on top of ZeroMQ socket messaging and web technology like nodejs, plotly, and socketio. The gist of the system is that a midas-to-art module hooks into the MIDAS data stream by selectively picking off events without blocking the main MIDAS functionality. The module then parses the MIDAS data and packs it into several data messages to be picked up by the DQM server which runs locally (likely the same machine). The server written in nodejs then, using socketio, ships data and visualization code to clients, which can be accessed from anywhere. The field team displays use bulma.css for visual styling, plotly.js for creating interactive plots, and d3.js for utility graphics. See an example of a client-side display in Fig. 4.19-4.

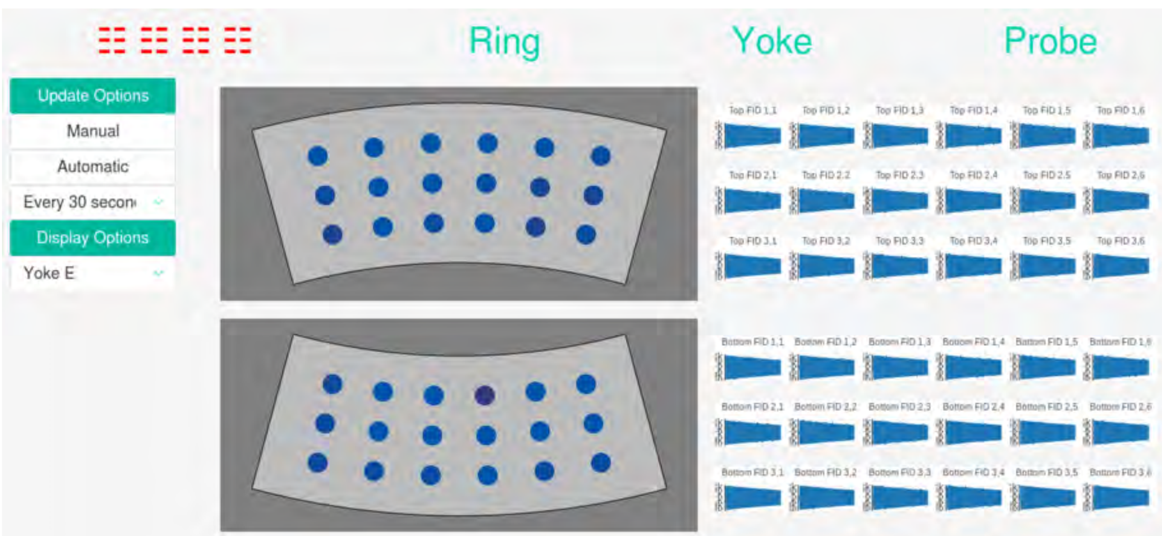

Figure 4.19-4. A prototype display showing the relative health of NMR probes and waveform plots of the NMR signals for a specific yoke to further diagnose problems with the hardware on the righthand side.

With all components working in concert, the field DAQ delivers data ripe for analysis. The analysis stage has only begun to pick up steam as the development stage matures, but the future holds many systematic and statistical studies. The DAQ system has been composed to hand off data in both the collaboration standard art framework and other formats such as ROOT or CSV. While all core components of the analysis will be implemented in art, the secondary data stream still allows a busy researcher with no time to master the overhead of the art framework to make plots using their familiar tools. Many pieces of the analysis, such as frequency extraction from NMR signals and position extraction from trolley data, have been implemented already. The full field analysis will not really come to fruition until the field systems have been commissioned and the analysis inclined members of the field team have real data. The team looks forward to a fun period of analysis developments in the coming year.

4.20 Radial and longitudinal field measurements in the $g-2$ storage ring magnet

M. Fertl, A. Garcia, R. Osofsky, M. Smith, and H. E. Swanson

The magnetic field in the $g-2$ storage ring influences the motion of muons in the ring. Non-vertical magnetic field components cause the muons to stray from their ideal orbits and swim vertically and radially as they move azimuthally around the ring. An average radial or longitudinal field can be compensated for using surface correction coils on the pole surfaces, but in order to determine the amount of compensation necessary, the radial and longitudinal fields around the ring needed to be measured.

The field in the storage ring is mapped using pulsed nuclear magnetic resonance (pNMR) probes. While the pNMR probes provide an accurate description of the main, vertical field, they are sensitive only to field magnitude, not field direction, and can not be used to measure the small radial and longitudinal field components. These fields were instead measured using a Hall probe, sensitive to both magnetic field magnitude and direction.

In general, the voltage across a Hall probe contains contributions from 3 sources, namely the normal Hall effect, the planar Hall effect, and an Ohmic offset voltage, and is given by

$$V = k_1 B_\perp I + k_2 \vec{B}_{||}^2 I \sin(2\psi) + V_0 \tag{1}$$

where k_1 and k_2 are the normal and planar Hall coefficients, I is the current across the Hall probe, $B_\perp$ and $\vec{B}_{||}$ are the magnetic field components perpendicular and parallel to the Hall probe active region, ψ is the angle between the Hall probe current and the in-plane component of the magnetic field, and V_0 is the Ohmic offset voltage.

For a radial or longitudinal field measurement, it is only the normal Hall component that we are interested in. The Ohmic offset contribution can be subtracted away by rotating the Hall probe by 180° about the vertical axis and taking half of the difference of the 2 measurements. To minimize the planar Hall contribution, Hall probes with an ultra-low planar Hall coefficient were used. The contribution was measured by taking a series of field measurements at one azimuthal location as a function of rotation angle about the Hall probe normal vector (as a function of ψ) and it was determined that the planar Hall contribution was negligibly small.

In designing a measurement apparatus, we needed to consider that the precision of the measurements would be directly influenced by our ability to reposition the Hall probe after a rotation. We designed an apparatus that allowed for easy positioning in four orientations, two for radial field measurements and two for longitudinal field measurements. Additional rotation about either of the other two axes when executing the 180° rotation about the vertical axis leads to a contribution to the small field measurement from the dipole field. This source of error was minimized through the use of electrolytic tilt sensors mounted, in both the radial and azimuthal directions, to the Hall probe platform. Using finely threaded adjustment screws, the platform was adjusted after each rotation until the tilt sensors read within 5μrad of their values pre-rotation. The measurement platform, which also allows for radial and vertical positioning of the Hall probe, is shown in Fig. 4.20-1.

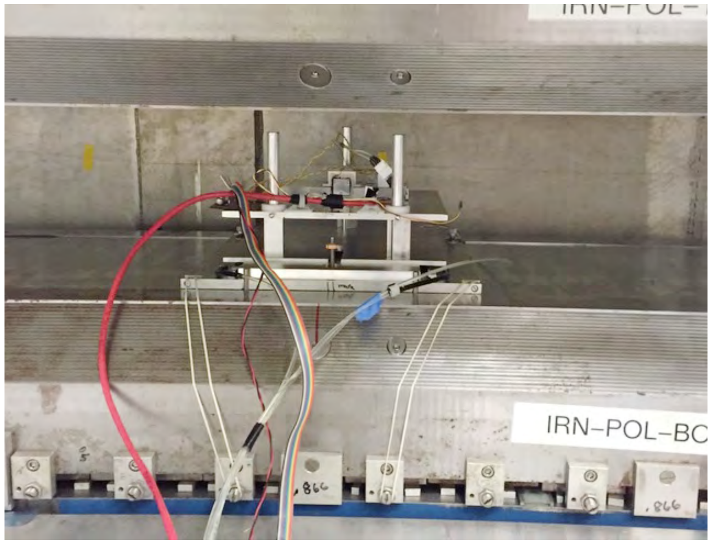

Figure 4.20-1. The radial and longitudinal field measurement platform. The platform allows for both normal and rotated measurements with the Hall probe and holds 2 electrolytic tilt sensors used to monitor the platform tilt before and after a rotation. The platform tilt can be adjusted using 3 finely threaded adjustment screws. The Hall probe height can be adjusted using vertical spacers while its radial position can be adjusted by sliding the middle platform along rails.

Using this platform, radial field measurements were taken at over 150 azimuthal locations, and longitudinal measurements at over 100 azimuthal locations, around the ring, shown in Fig. 4.20-2. At the end of passive shimming, the average measured radial field was 68.5(68.9) parts per million (ppm) of the dipole field and the average measured longitudinal field was 0.14(35.8) ppm. Active shimming, in the form of surface correction coils to be commissioned in March 2017, will be used to mitigate this average radial field. The effects of the random fluctuations around the average value can not be corrected for, however their effects are minimal.

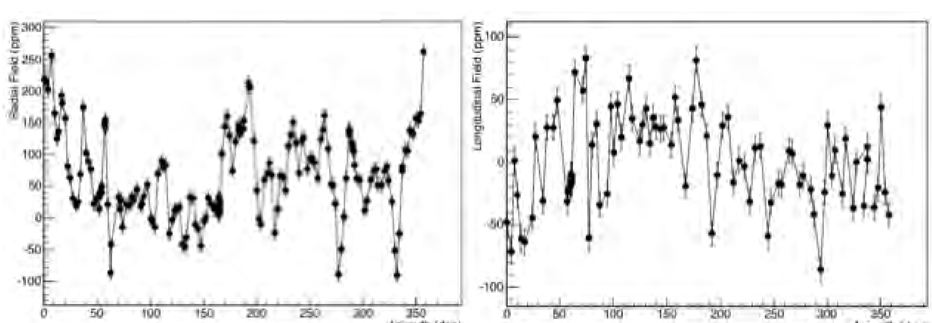

Figure 4.20-2. We measured the radial and longitudinal field components at over 100 azimuthal locations around the storage ring after the completion of passive shimming. The average measured radial field was 68.5ppm and the average measured longitudinal field was 0.14ppm.

5 Axion searches

ADMX (Axion Dark Matter eXperiment)[1]

5.1 Overview of ADMX

C. Boutan*, N. Crisosto, N. Du, N. Force, R. Khatiwada, E. Lentz, H. LeTourneau†, A. Malagon‡, R. S. Ottens, L. J. Rosenberg, G. Rybka, J. V. Sloan§, D. Stromecki, and D. I. Will

The Axion Dark Matter eXperiment (ADMX) is a search for galactic dark matter axions whose detection apparatus is an implementation of Pierre Sikivie's axion haloscope[2]. The ADMX collaboration has operated a series of axion searches since the mid-1990s. The experiment has been located at CENPA since 2010. Following a data run in 2013-2014, ADMX has been undergoing a series of upgrades, most notably the addition of a dilution refrigerator, to enter phase "Gen 2." At the time of writing, March 2017, the dilution refrigerator has been installed in the experimental insert and the upgrades have been completed on the ADMX insert. ADMX is currently in a data taking run and the anticipates an unprecendented level of sensitivity to QCD axions.

The axion first emerged in the late 1970s as a consequence of a solution to the "strong CP problem." The strong CP problem can be concisely stated as: An exceedingly fine, arguably unnatural, tuning of the Standard Model is required to account for the conservation of the discrete symmetries P (parity) and CP (charge conjugation times parity) within quantum chromodynamics (QCD). The amount of CP violation in QCD is encoded in a phase θ which appears in the QCD Lagrangian. When θ differs from zero, QCD violates P and CP. Since the strong interactions appear to be P- and CP-symmetric in the laboratory, θ must be very small, namely, the upper limit on the neutron electric-dipole moment requires $|\theta| < 10^{-10}$. However, in the Standard Model, P- and CP-violation by the weak interactions feeds into the strong interactions so that the expected value of θ is of order unity. Peccei and Quinn proposed a solution to this problem in which the Standard Model is modified so that θ becomes a dynamical field and relaxes to zero, thus conserving CP in a natural way[3]. The theory's underlying broken continuous symmetry dictates existence of a particle: the axion. The axion is the quantum of oscillation of the θ field and has zero spin, zero electric charge, and negative intrinsic parity. So, like the neutral pion, the axion can decay into two photons. Soon after the initial proposal of the axion, it was realized within a certain range of possible

*Presently at Pacific Northwest National Labs in Richland, WA.
†Presently at University of Washington for Master's Degree in Seattle, WA.
‡Presently at Climate Corp in Seattle, WA.
§Presently at North Seattle College in Seattle, WA.

[1]ADMX is supported by the DOE Office of High-Energy Physics and makes use of CENPA resources by recharge to the cost center.

[2]P. Sikivie, Phys. Rev. Lett. **51**, 1415 (1983).

[3]R. D. Peccei and H. R. Quinn Phys. Rev. Lett. **38**, 1440 (1977).

masses the axion is ideal dark matter candidate. Experiments and astronomical observations have since constrained the axion's mass to within a range in which the axion contributes a significant portion of dark matter; this mass range corresponds to microwave photons.

ADMX operates by stimulating the conversion of local dark matter axions into photons via Primakoff conversion and detecting the resulting photons. The experiment consists of a large tunable microwave cavity, shown in figure Fig. 5.1-1(*Right*), immersed in a static magnetic field. The resonance of the cavity further enhances the conversion, and the resonance is tuned to search for axions of varying mass. An RF receiver records the power spectrum of the cavity for each tuning configuration as ADMX scans in frequency. However, despite the prodigious predicted local density of dark matter axions (approximately 10^{14}/cc), the expected electromagnetic signal is extraordinarily weak, around 10^{-22} W in the ADMX apparatus. Our present ADMX collaboration (University of Washington, LLNL, University of Florida, University of Sheffield, NRAO University of California Berkeley, PNNL, LANL, FNAL, and WU), shown in figure Fig. 5.1-2, has constructed and is operating the first, and presently only, experiment sensitive to plausible dark matter axions.

ADMX is essentially an extraordinarily low-noise radio receiver with a tunable RF cavity forming a tuned resonance circuit. A short electric-field probe couples power from the cavity into a cryogenic amplifier which is cooled to near the cavity temperature.

The dominant background in ADMX comes from thermal noise; the system noise temperature is the noise temperature of the amplifier plus the cavity physical temperature. The motivation for lowering the system noise temperature is clear: (i) for a given axion-photon coupling, the frequency scan rate decreases as the square of the system temperature and (ii) for a given scan rate, the power sensitivity increases as the system temperature drops. ADMX reduces its thermal noise by using low noise first stage amplifiers and cooling the cavity. ADMX collaboration members developed SQUID amplifiers in the $100 - 1000$ MHz range specifically for ADMX; this development allowed more than an order-of-magnitude reduction in system noise temperature.

The previous version of ADMX, ADMX Phase 1, was located at LLNL and operated from 2002-2009. The Phase 1 apparatus was fitted with superconducting quantum interference device (SQUID) amplifiers and operated at about 2 K physical temperature via a pumped ^{4}He system. ADMX Phase 1 completed a scan of the $1.9 - 3.5$ μeV axion-mass range and the results for conservative estimates of dark matter density were published[1]. After further analysis the ADMX collaboration published a search for axions assuming non-virialized dark matter distribution within our galaxy[2].

[1] S.Asztalos *et al.*, Phys. Rev. Lett. **104**, 041301 (2010).
[2] J. Hoskins *et al.*, Phys. Rev. D **84**, 121302 (2011).

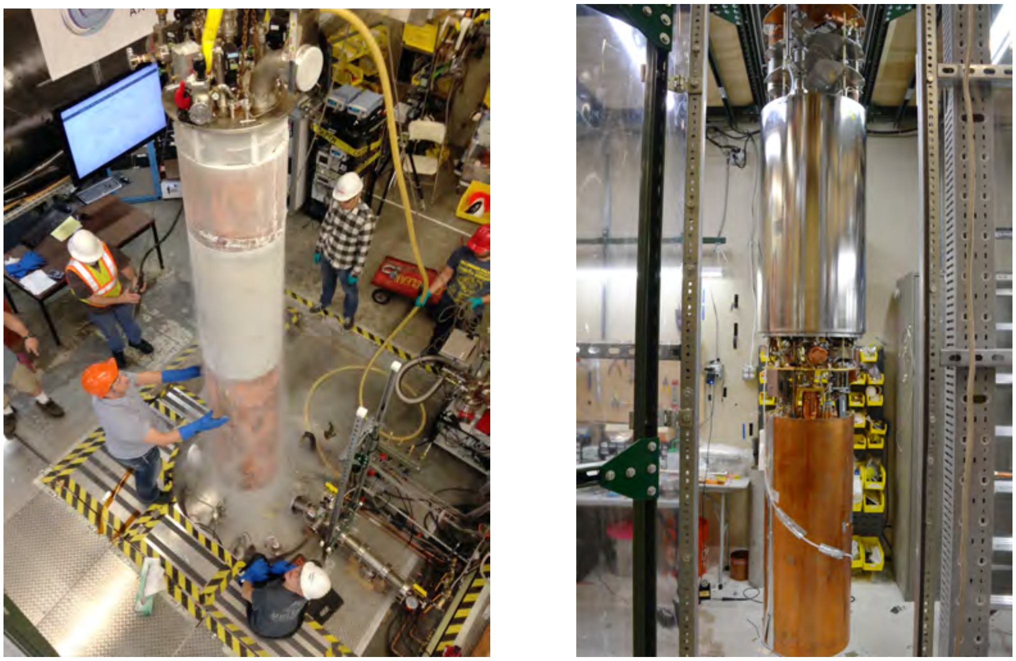

Figure 5.1-1. *Left:* Removal of the ADMX insert after a successful commissioning run *Right:* ADMX insert in the cleanroom

Starting in 2010, ADMX was entirely redesigned and rebuilt at CENPA. The 2013-2014 data runs of ADMX (hereforth referred to as "Phase 2a") were the first data collected by ADMX at CENPA. Throughout the 2014 data runs ADMX employed a pumped ^{4}He system achieving physical temperatures of about 1.2 K and SQUID amplification. The success of Phase 2a demonstrated full functionality of the new ADMX design and success of the closed loop helium liquefaction system in maintaining ADMX operations through order-months extended data runs. Additionally, Phase 2a was the first time an axion haloscope has taken data through two independent receiver chains simultaneously and the first time a nonfundamental cavity mode achieved sensitivity to plausible QCD axions. New axion exclusion limits were set in two frequency regimes: $600 - 720$ MHz (corresponding to the "TM010" mode) and $1050 - 1400$ MHz ("TM020" mode), with benchmark QCD axion sensitivity in select frequency ranges.

ADMX was selected as a flagship DOE "Gen 2" dark matter experiment in fall 2014 and began a period of design, build, and upgrade. Among the major upgrades are: the installation of a dilution refrigerator and supporting plumbing and infrastructure, a smaller cavity that will take data in parallel with the main cavity (named "Sidecar"), a redesigned RF system including Josephson Parametric Amplifier and SQUID amplifiers, and substantial redesign of the thermal linkages and connections in the experiment to achieve lowest possible operating temperature.

ADMX Gen 2 began its commissioning run in summer 2016 with the first test of the integration with a dilution refrigerator designed and built by Janis Cryogenics. The integration with the dilution refrigerator was a success, allowing the ADMX cavity to reach a temperature of 200 mK. In addition, the main ADMX experiment collected axion search data around 696.6MHz. ADMX Gen 2 completed it's commisioning run on October 2016, at which point the insert was removed from the magnet, shown in figure Fig. 5.1-1(*Left*), for maintenance. In addition to the main experiment, a smaller 4-6 GHz cavity, called "Sidecar", is mounted on top of the main cavity and shares mechanical supports and cryogenics with the main experiment. Sidecar has its own receiver chain and is tuned by piezoelectric motors. Sidecar is a pathfinder for future high frequency ADMX cavities. Its implementation of piezoelectric motors is a first for axion search experiments and allowed for much finer tuning of the cavities' resonant frequency, a important factor in higher frequency axion searches. Graduate student Christian Boutan designed and operated Sidecar, and attained a doctorate with a thesis based off the analysis from the Sidecar axion search data around 5 GHz.

ADMX Gen 2 began its first data taking run in January 2017 with plans to explore a $650 - 680$ MHz range. The ADMX main cavity is currently operating at 150 mK in a 6.7T magnetic field. The low temperature in combination with the high magnetic field will allow ADMX to achieve unprecedented level of sensitivity to QCD axions and we anticipate a high-profile paper to be published on the results from this run.

Figure 5.1-2. Select members of the ADMX collaboration, 15 January 2016.

5.2 Higher Frequency Axion Searches with Sidecar

C. Boutan*, N. Du, L. J. Rosenberg, and G. Rybka

The main ADMX cavity is designed to search for axions between 500 and 2500 MHz. In the event that the main cavity rules out axions in that frequency range, new technologies will be required to probe for higher mass axions. ADMX Sidecar, the thesis project of Christian Boutan, is a higher frequency pathfinder experiment that uses a miniature resonant cavity to search for axions in the 3.5 to 6 GHz frequency range. In summer 2016, Sidecar was positioned on top of the main ADMX cavity (see Fig. 5.2-1). This position allows Sidecar to share the magnetic field and cryogenics of the main experiment, while otherwise being a stand-alone experiment with its own data acquisition system and electronics[1].

The main ADMX cavity is tuned using a series of gear boxes and fiberglass shafts to rotate two tuning rods in the main cavity. Higher frequency experiments, which will utilize smaller cavities and multiple cavity arrays, will require much higher precision tuning. Sidecar is tuned and coupled using two cryo-compatible Attocube piezoelectric motors to adjust a tuning rod and antenna.

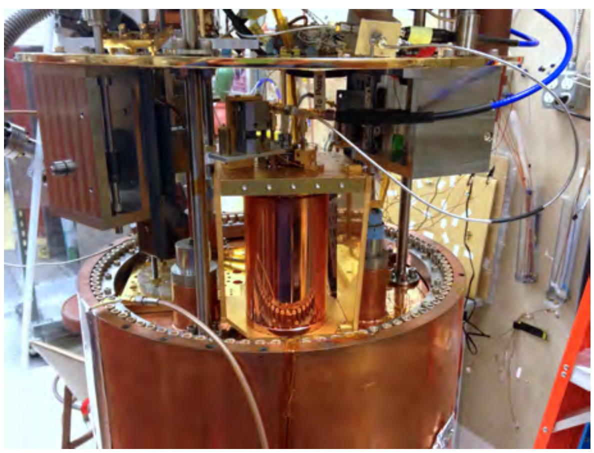

Figure 5.2-1. Sidecar cavity. Two piezoelectric actuators are visible on top of the cavity's gold-plated mechanical support. Actuators are used for tuning the cavity via rotary motion of the Sidecar tuning rod and coupling to the cavity via linear motion of an antenna.

The first data-taking run with Sidecar was in summer 2016, where we searched for axions around 5 GHz in a 0.8-T field at 7 K. From this run, new limits on the axion mass and coupling were achieved, as shown in Fig. 5.2-2. Graduate student Christian Boutan designed and operated Sidecar and produced a Ph.D. thesis from the analysis of the Sidecar axion search data. Sidecar is currently in a second data taking run, searching for axions using the higher-order TM020 mode around 7 GHz. Repositioning the Sidecar cavity into the center of the magnet to increase the field strength, and implementation of quantum-limited amplifiers

*Presently at Pacific Northwest National Labs in Richland, WA

[1] C. Boutan, *A Piezoelectrically Tuned RF-Cavity Search for Dark Matter Axions.* Ph.D. thesis (2017).

to lower the noise floor, could increase the sensitivity of Sidecar to axion coupling by a factor of 60.

The successful integration of piezoelectric tuning at higher frequencies demonstrated by Sidecar will be incorporated into the larger multicavity system in the main ADMX experiment. This system will incorporate an array of Sidecar-like cavities to search for higher mass QCD axions.

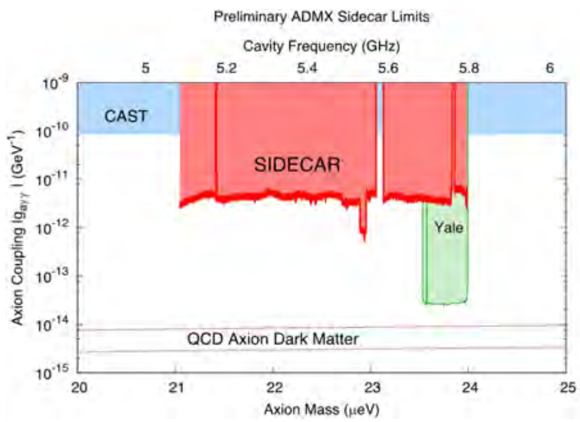

Figure 5.2-2. Preliminary limits on the axion coupling in the 21-24 μeV range, set by Sidecar for higher frequency axions from the summer 2016 data run (Boutan thesis). Data was taken over a 2 month period from August to September 2016 in a 0.8-T field at 7 K. At the end of the run, the magnetic field was ramped up to 2.7 T and a more sensitive search was done at 23μeV. Also included are limits on axion coupling and mass set by axion dark matter searches performed by Yale and the Cern Axion Solar Telescope (CAST).

5.3 Signal Models for Axion Cavity Searches

N. Du, E. Lentz, T. R. Quinn*, L. J. Rosenberg, and M. J. Tremmel*

Current signal estimates for direct axion dark matter detection have relied on the isothermal sphere halo model of dark matter distribution in our galaxy for the past several decades. This models dark matter halos as a thermalized, pressureless, self-gravitating sphere of particles[1]. The resulting velocity distribution is given by a Maxwell-Boltzmann distribution

$$f_{\vec{v}} \ \propto \ e^{-\vec{v}\cdot\vec{v}/2\sigma_v^2} \tag{1}$$

where $\sigma_v = \sqrt{2}v_c$ and v_c is the circular speed[2]. The frequency ν of an axion decay is determined by its total energy, which is dominated by the axion rest mass m_a but also depends upon its speed

$$\hbar\nu = m_a c^2 + m_a v^2/2. \tag{2}$$

*Department of Astronomy, University of Washington, Seattle, WA.

[1]S.Asztalos *et al.*, Phys. Rev. Lett. **104**, 041301 (2010).
[2]J Binney *et al* Princeton Univ. Press, ISBN-13:978-0-691-13026-2.

Therefore, the local distribution of axion velocities must be understood to interpret a signal in ADMX.

While this model can predict the broad signal structure, it is incapable of describing fine structures that arise from a halo's infall history or the influences of baryonic matter on the halo's structure. The ADMX experiment has a frequency resolution of a part in 10^9 or better, allowing it to resolve fine structure in the axion signal distribution. The goal of this project is to develop an improved signal model for axion cavity searches in order to make use of the high resolution allowed by modern axion detectors.

The Romulus25 N-Body+Smoothed Hydrodynamics simulation is a state-of-the-art simulation tool developed by the UW N-Body shop[1]. Romulus25 simulates a 25 Mpc periodic cosmological box filled with dark matter particles, evolving gas and star particles and supermassive black holes. Dark matter and gas particle masses of $3.39 * 10^5$ and $2.12 * 10^5$ solar masses are used, respectively. Romulus25 produces approximately 30 Milky-Way mass halos. From these candidate halos, we impose additional requirements on the virial radius and virial mass to identify galaxies most similar to the Milky Way. These halos are then analyzed to extract the velocity distributions, as well as other quantities relevant for understanding the dark matter signal.

In the galactic frame, both the speed and energy spectra were found to be consistent with the isothermal sphere model[2]. However, as shown in figure Fig. 5.3-1, there was a significant departure in the energy spectrum from the isothermal sphere model in the laboratory frame[3]. The proposed signal shape keeps a Maxwell-Boltzmann like form

$$f_\nu \;\propto\; (\frac{(\nu-\nu_0)h}{m_a T})^\alpha e^{-(\frac{(\nu-\nu_0)h}{m_a T})^\beta}. \tag{3}$$

where ν_0 is the frequency associated with the resst mass energy, m_a is the axion mass, and α, β and T are fitted dimensionless parameters with values of 0.36, 1.39 and $4.7 * 10^{-7}$, respectively. The energy spectra observed from the simulation are 1.8 times narrower than the isothermal sphere distribution. This narrowing of the signal shape would improve the sensitivity of ADMX by $\sqrt{1.8}$.

We are continuing the development of improved axion signals for ADMX. In particular, Ph.D. student Erik Lentz is actively working on explaining the underlying dynamics of the signal shape and implementing a filter in the axion data to improve the sensitivity of the ADMX experiment.

[1] M. Tremmel *et al.*, arXiv:160702151T(2016).
[2] J.D. Sloane *et al.* Astrophys. J. **831** 93S (2016).
[3] E. Lentz *et al.*, arXiv:1703.06937(2016).

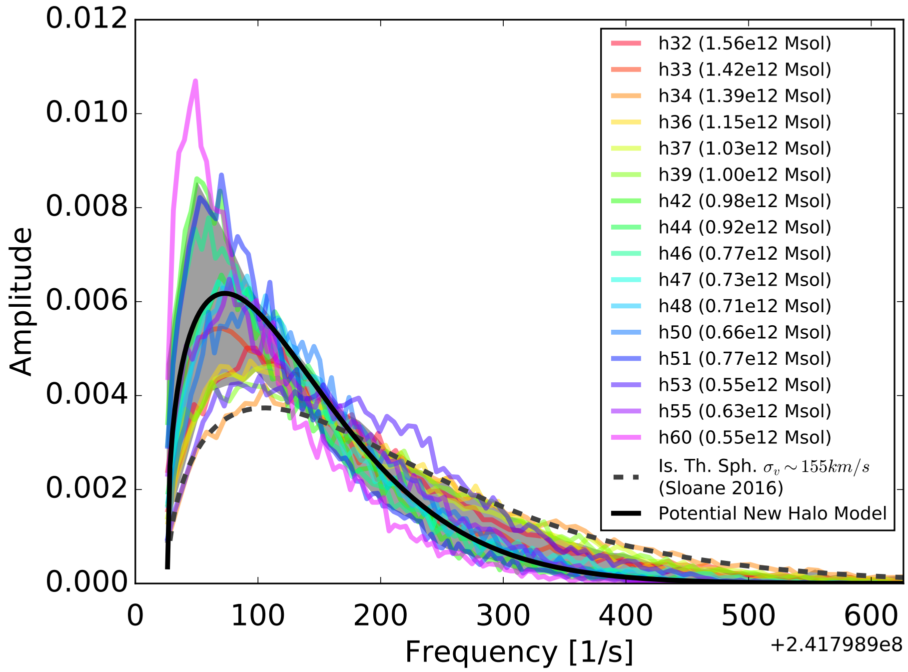

Figure 5.3-1. Frequency spectra of Milky Way-like halos from Romulus25. The dotted black line represents the frequency spectrum derived from the isothermal sphere model, and the solid black line represents a fit to proposed new halo model.

6 Education

6.1 Use of CENPA facilities in education and course work at UW

E. B. Smith

CENPA continues to maintain a prominent role in broad scope, practical, hands-on training for both undergraduate and graduate students at the University of Washington. One of the most significant and unique advantages that our students enjoy is direct participation in ongoing research and engineering, resulting in contributions both locally and at our off-site collaborations. This extensive training through participation occurs in our experimental laboratories, electroinics shop, student shop, and chemistry laboratories. It is complimented by laboratory safety training (Sec. 7.8).

We have continued to maintain a presence in the UW curriculum since 2011, and currently offer an accelerator-based laboratory course in nuclear physics titled "Nuclear Physics: Sources, Detectors, and Safety", Phys 575/576 (Sec. 6.3).

6.2 Student training

J. F. Amsbaugh, G. T. Holman, D. R. Hyde, J. R. Pedersen, D. A. Peterson, E. B. Smith, T. D. Van Wechel, and D. I. Will

CENPA faculty, engineering staff, and technical staff provide students with training in our shops, chemistry laboratories, and experimental laboratories that comprise the overall facility. Students also receive specific training in laboratory safety, which includes requiring students to complete UW provided in-person and online classes.

Our electronics shop is available for use by the students (Sec. 7.4) where they can learn electronic design and assembly. Two electronics shop staff members are available to provide instruction in soldering, wiring, and the use of basic electrical and electronic components. Assistance in the use of Electronic Design Automation (EDA) software for producing prototype printed circuit boards (PCB) is also provided (Fig. 6.2-1). Training in the use of a UV ProtoLaser (purchased with UW Student Technology Fee (STF) funds) is given to any UW individuals wanting to fabricate prototype PCB for research projects.

The CENPA student shop (Sec. 7.5) trains all users in machine tool operation and safety. A staff instrument maker, dedicated to the student shop, instructs faculty, staff, and students on a continuing basis. These individuals learn how to safely operate a variety of machines including lathes, milling machines, drill presses, saws, grinders, metal shears and breaker, hand tools, and power tools. Some are even trained to use an oxygen/acetylene cutting torch. Additionally, instruction is given on use of the student-shop NC 2-Axis TRAK milling machine, newly acquired Track DPM2 3-axis CNC Milling Machine, and KERN HSE large

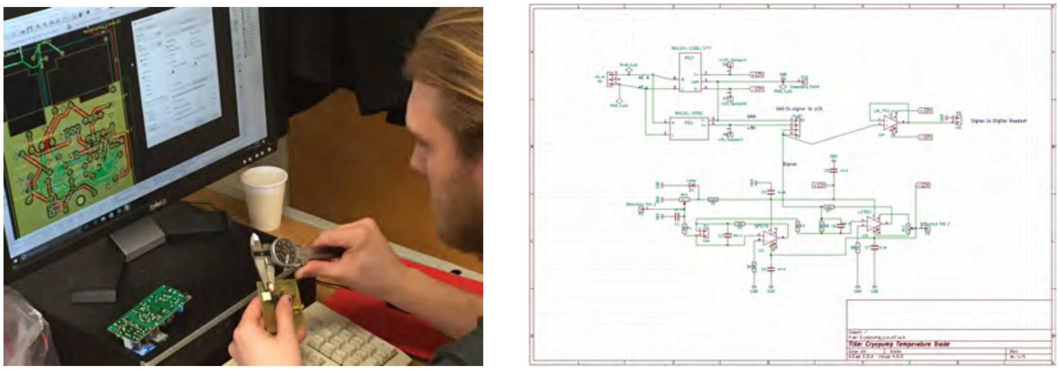

Figure 6.2-1. Undergraduate student Joshua Oppor using EDA software (*left*) to design diode sensor circuit (*right*) and layout for a temperature measurement PCB, prototyped with UV ProtoLaser, for use with a vacuum cryopump.

format laser cutter system, all three of which provide computer controlled fabrication of complicated parts for research projects.

Training in the safe use of chemicals utilized throughout CENPA, and their proper disposal, is provided by staff engineers and complimented by required UW online training (Sec. 7.8). Three chemistry laboratories, each containing multiple fume hoods, are available.

CENPA faculty and staff provide hands-on student instruction (Fig. 6.2-2) in an array of laboratory technical skills & safety on topics ranging from electrical power, compressed gases, cryogenic liquids (He & N_2) (liquefaction, dispensing, delivery, transport), lifting and hoisting, vacuum technology, high voltages, high currents, high magnetic fields, radiation, and radioactive sources. Completion of available UW online safety training is also required (Fig. 6.2-3).

Figure 6.2-2. Undergraduate student Brett Hamre replacing a thermal switch on a high current magnet power supply shunt.

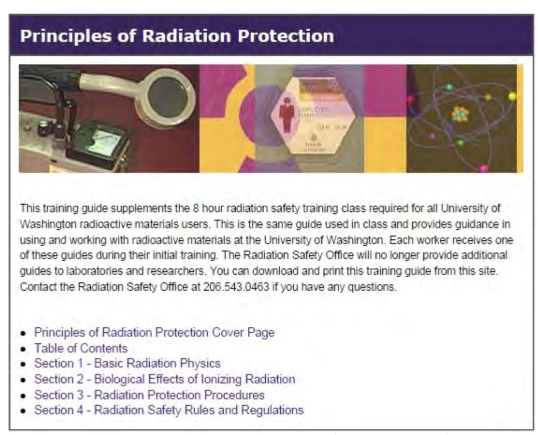

Figure 6.2-3. Example of UW safety courses (in-person and on-line) found at www.ehs.washington.edu.

The long standing and unique history of teaching students how to operate the tandem accelerator (Fig. 6.2-4) and ion-sources remains vital at CENPA today. Graduate and undergraduate students receive instruction in the theory and hands-on operation of our duoplasmatron ion source and 9-megavolt tandem Van de Graaff accelerator. This training brings together the laboratory technical skills & safety by practicing generating an ion beam, charging of the tandem terminal to multi megavolt potentials, tuning the ion beam through the tandem accelerator, and transporting the beam to an experimental target. After receiving such accelerator operations training (a.k.a. "crew training"), these students can operate the ion source and accelerator for their research. They are also be called upon to serve as crew operators during the research experiments of others to facilitate 24-hour accelerator operations.

Figure 6.2-4. Undergraduate students, Samuel Sexton (*left*) and Henry Gorrell (*right*), operating tandem accelerator from control consoles.

Recently, a CENPA staff developed course, "Basic Cryogenic Design and Operations," was provided and attended by staff and students in support of the ongoing ADMX research project ((Sec. 5.1)). The purpose of the course is to develop a crew of personnel, student and staff, that can operate both the Linde 1410 helium liquefier and the Janis He3/He4 dilution refrigerator, which can require 24-hour monitoring and adjustment during operation cycles. The following topics were covered in the course:

1. Data and techniques for basic cryostat design and for operation of the He liquefier and dilution refrigerator.
2. Zygmunt Wroblewski and Carl von Linde and the liquefaction of air.
3. Heike Kamerlingh Onnes and the liquefaction of natural helium.
4. The ADMX Linde 1410 Helium Liquefier.
5. Heinz London and the He3/He4 dilution refrigerator.
6. The ADMX Janis He3/He4 Dilution Refrigerator.
7. The ADMX Wang Superconducting Magnet Cryostat.
8. The ADMX Experimental Insert.
9. Leak checking and residual gas analysis for helium cryogenics.

CENPA hosted 6 official student group tours of the facility during this annual reporting period. These tours consist of an initial welcoming in our conference room, an audience appropriate introduction to the research performed at CENPA, and a tour through the CENPA laboratories provided by some combination of graduate students, faculty, or staff. Four of the tours, which included both public and home schooled students, were given to a total of 55 high school students, 10 middle school students, and 6 elementary students. A group of 16 undergraduate students from Central Washington University toured. We also welcomed approximately 50 University of Washington undergraduate students as part of the annual UW chapter of the Society of Physics Students (SPS) tour.

During the Spring 2016 Quarter, graduate student Diana Thompson performed research at CENPA, under faculty advisement and with engineering staff assistance & training, resulting in a Master of Science thesis[1] (degree granted August 2016) and poster presentation.[2] The research collected month long alpha particle energy spectra (Fig. 6.2-5) from the decay of technologically enhanced naturally occurring radioactive material (TENORM) in an effort to develop a faster, in-field radioassay technique.

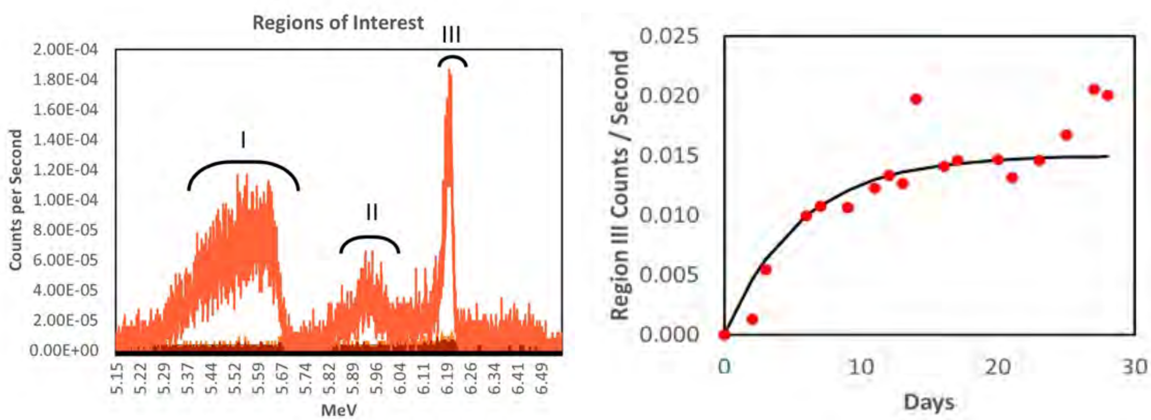

Figure 6.2-5. (*left*) month long alpha particle spectrum from TENORM sample; (*right*) time progression of alpha particle spectrum ROI peak III following Radon-222 ingrowth through to secular equilibrium.

[1] Diana Thompson, *Measurement of Alpha Decay from Radon-222 emanated from Radium-226 contaminated Barite Pipe Scale*, Master of Science Thesis, University of Washington, October 2016.

[2] D. S. Thompson, E. B. Smith, A. García, *Alpha Decay Measurements from Rn-222 Gas.* Poster session presented at the Health Physics Society (HPS) Annual Meeting, July 2016, Spokane, WA.

6.3 Accelerator-based lab class in nuclear physics

A. García, J. R. Pedersen, E. B. Smith, and D. I. Will

We have developed a graduate-level lecture and laboratory class for the purpose of teaching aspects of nuclear theory and techniques for nuclear physics experiments[1] (Fig. 6.3-1). This includes student operation of the tandem accelerator to achieve an ion beam on experimental targets.

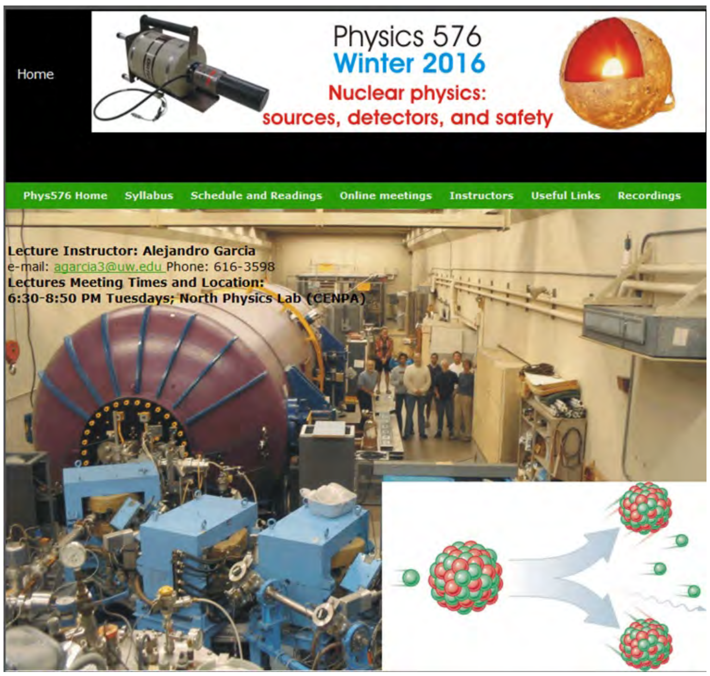

Figure 6.3-1. Home page for CENPA Phys 576 class.

The class met twice a week during the Winter 2016 quarter, once for a 1-1/2 hour lecture and again in groups for a 1-1/2 hour lab session. The list of subjects we covered were:

1. Atomic nucleus. Basics of nuclear physics, nuclear energy, orders of magnitude.
2. Attenuation of photon radiation. Solid-state detectors (Ge and Si).
3. Ranges of ions and electrons. The weak interaction. Radioactivity and radiation damage and health risks (α, β, γ, and neutron activity).
4. Deciphering a mystery γ spectrum measured using a Ge solid-state detector. Gauging the level of radioactivity and assessing health risks.
5. 9 megavolt tandem accelerator function, duoplasmatron ion source function, and ion beam optics. Tuning beam through tandem accelerator.
6. Rutherford back-scattering (RBS) spectra measured by scattering accelerated protons off foil targets and into Si solid-state detectors. Deciphering a mystery spectrum and the contents of a mystery foil (Fig. 6.3-2 *left*).

[1] Phys 576, Nuclear Physics: Sources, Detectors, and Safety, http://faculty.washington.edu/agarcia3/phys576.

7. Fission and fusion. The functioning of reactors.
8. Nuclear astrophysics: nucleosynthesis in stars.
9. Sources of positrons for positron emission tomography.
10. Resonance energy of (p,γ) nuclear reaction determined by irradiating a target with accelerated protons and detecting resulting γ's in a high purity germanium (HPGe) solid-state detector (Fig. 6.3-2 *right*).

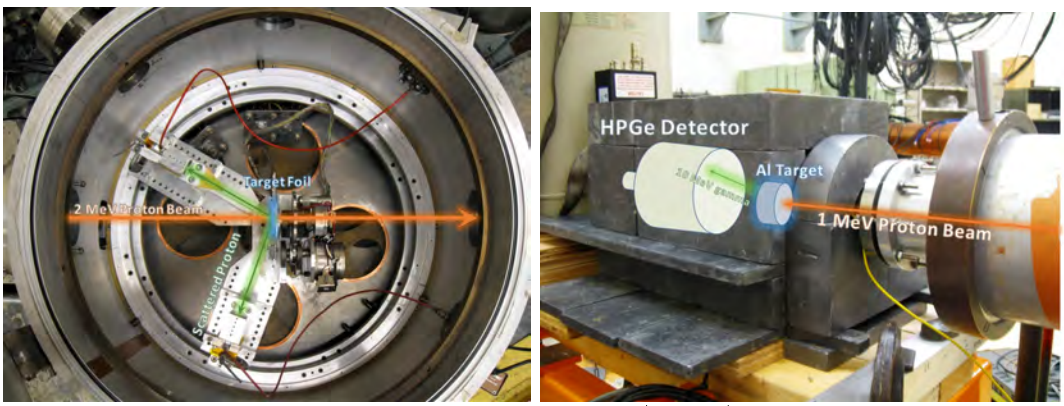

Figure 6.3-2. *Left*: RBS setup indicating 2 MeV protons (orange) incident on a thin foil target yielding back-scattered protons (green) detected in Si solid-state detectors. *Right*: (p,γ) nuclear resonance setup indicating 1 MeV incident protons (orange) incident on Aluminum target yielding in resonance emission γ's (green) detected in an HPGe solid-state detector.

Thirteen students attended the Winter Quarter 2016 sessions. They engaged enthusiastically in discussions during lectures and in laboratory sessions. A tour of the Boeing Radiation and Effects Laboratory (BREL) in Seattle was arranged by one of the Phys 576 students who was an employee of that facility.

7 Facilities

7.1 Facilities overview

E. B. Smith and D. I. Will

CENPA constantly updates and improves its facilities and provides the best possible resources and research environment for its users as new experiments emerge and as the demands of research change with time. These unique resources are each supported directly by CENPA staff, and include computing hardware & information technology, electronics shop, instrument shop, student shop, and programs & training for radiation safety, chemical safety, and general laboratory safety.

The computational facilities at CENPA remain at the front edge of technology. As always, personal desktop and portable computers are maintained and the technology kept current. The NPL Data Center (NPLDC), which previously contained a single high performance cluster, ATHENA, now provides the infrastructure to multiple clusters and department appliances (Sec. 7.3).

The FN tandem Van de Graaff accelerator is operated, modified, and maintained on a continuing basis (Sec. 7.2) to meet the needs of CENPA researchers and for hands-on student training (Sec. 6.3) (Sec. 6.2). We have made progress on the project to upgrade the existing control hardware and software used by the accelerator system with a PC based LabVIEW system.

The CENPA electronics shop provides modern surface-mount technology and miniature cable-manufacturing equipment on site and in appropriately clean areas. The shop continues to do custom design work for specialty preamplifiers as well as dedicated multichannel data-acquisition (DAQ) systems. The shop also interacts with the on-campus Washington Technology Center, taking advantage of much of the capital-intensive, high-tech equipment there that is more effectively used as a cost-shared facility. The electronics-shop staff also provides training for students and other staff members (Sec. 7.4).

The CENPA instrument shop is manned by three highly skilled instrument makers with vast knowledge of metallurgy, welding, and fabrication (Sec. 7.5). This shop has CNC machines, mills, lathes, and large-capacity machines. The instrument shop can provide engineering for all research projects. The CENPA student shop is headed by an instrument maker who provides safety training and instruction to students, staff, and faculty. This shop includes mills, lathes, drill presses, a laser cutter, 3D printer, and new CNC 3-axis mill.

Promoting the safety of researchers and of the environment has always been the culture at CENPA (Sec. 7.8). Through the proceeding year, we have moved forward on projects that are making safety even better, and have stepped up or disposal of hazardous materials.

Important changes to building security, and progress in removing large decommissioned infrastructure to increase space for new experiments have occurred the past year. New radiation safety equipment (detection and survey) has been added.

7.2 Van de Graaff accelerator and ion-source operations and development

M. J. Borusinski, A. T. Eberhardt*, H. T. Gorell†, B. E. Hamre, G. H. Leum, J. E. Oppor, J. R. Pedersen, D. A. Peterson, J. G. Reyes‡, S. S. Sexton, E. B. Smith, S. B. Troy§, T. D. Van Wechel, and D. I. Will

The only tandem entry occurred from Sept. 6-19, 2016. A failure to control the high-voltage (HV) Terminal Steerers, and anomalous flashing indicators for power and communications as seen from the LE bulkhead viewport were traced to a failed terminal computer +24VDC power supply. A new ACOPIAN model 24W210 power supply was installed, resulting in proper terminal computer operation. The LE, upper voltage pick-off pulley at the terminal was dragging and was thus replaced with a new pulley (NEC P/N 2DA00320). Both HE and LE pelletron chains were cleaned with isopropanol damped KimWipes. Replaced column resistor mounting bracket for first resistor next to terminal on HE side. Centered one top column resistor in it's shield in area directly under the second to last viewport on the HE. Lastly, a new set of sharp, thoriated corona points were installed (0.700" long, tip to brass base).

A fair amount of engineering development and maintenance was performed on the Ion Sources DECK during this reporting period. This included extensive servicing and mechanical documentation of the DEIS duoplasmatron (Fig. 7.2-1) ion source, repair of the analyzing magnet controls, and renewed operation of the beam chopping apparatus.

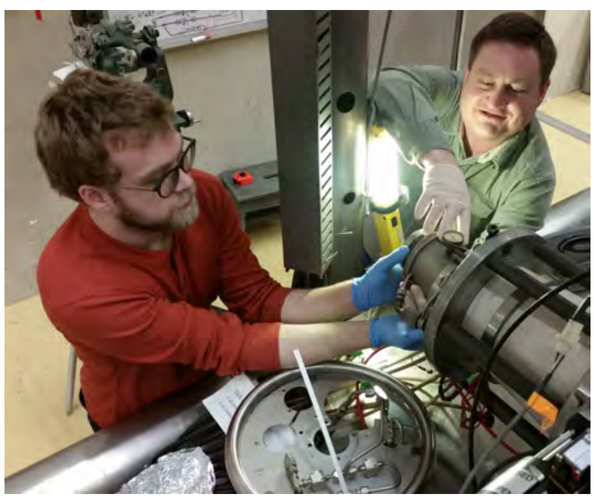

Figure 7.2-1. Research engineers Joben Pedersen (left) and Eric Smith (right) re-assembling the DEIS duoplasmatron after extensive servicing.

Over a period of several months in 2016, we began to observe slight drifting in the x position of the ion beam as detected in the signal from the Low Energy (LE) beam position

*Departed June, 2016.
†Arrived January, 2017.
‡Departed August, 2016.
§Arrived October, 2016.

wire scanner, which resulted in reduced beam transmission through the tandem accelerator. Eventually, this anomalous ion beam x drift was enough cause loss of beam current in the LE Faraday cup (immediately down beam from the LE wire scanner) and in the OFF DECK Faraday cup (between the Ion Sources DECK and the LE Farady cup). It was determined that the beam x position drift was occurring on the Ion Sources DECK, and was observed in the signal of the DECK IMAGE wire scanner, which is positioned down beam of the DECK analyzing magnet. The internal voltages of the DECK ANAC BOX #1, whose signals read & control the analyzing magnet power supply, were measured with a 10 Gohm input impedance ADC. The measurements revealed that the voltage reference device in the ANAC controller was intermittently drifting to erroneous values, and thus causing the analyzing magnet control signals to drift as well, steering the ion beam out of x position tune. Replacement of the Analog Devices LM311 voltage reference corrected the problem and stable beams are now achieved.

The ion beam chopping capability of the Ion Sources DECK was brought back to operational status for use in providing a chopped (a.k.a "pulsed") beam for testing of IBMS apparatus for the $g-2$ muon experiment (Sec. 4.16). A preliminary experiment confirmed the production of approximately 200 ns wide pulses of 10 MeV protons at 100 kHz delivered to the 30-degree Right 24" chamber. The chamber was set up with a gold foil target, Si solid-state detectors, and instrumentation to detect the Rutherford backscattered (RBS) protons (Fig. 7.2-2). A second experiment used 100-ns wide pulses of 10-MeV protons at 10 kHz delivered to the same 30-degree Right 24" chamber, but this time with a scintillating material and PMT detector. The PMT pulses from detected protons were used to measure time-of-flight (TOF) with respect to the beam chopper trigger, and the resulting TOF histogram confirmed a 100-ns wide pulse.

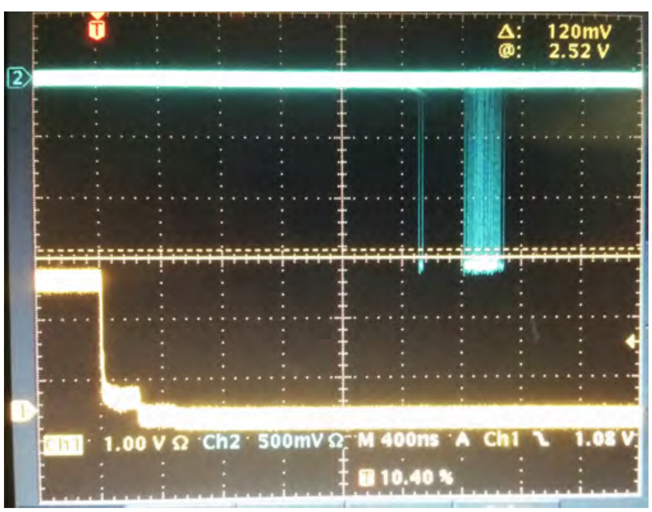

Figure 7.2-2. Oscilloscope display capture of many RBS proton detection events (narrow, negative going pulses on channel 2 (blue)) showing a narrowly defined beam pulse in time, and with a time-of-flight (TOF), with respect to the trigger (channel 1 (yellow)) falling edge, that is consistent with a 10 MeV proton traveling from the Ion Source DECK to the 30-degree Right 24" chamber.

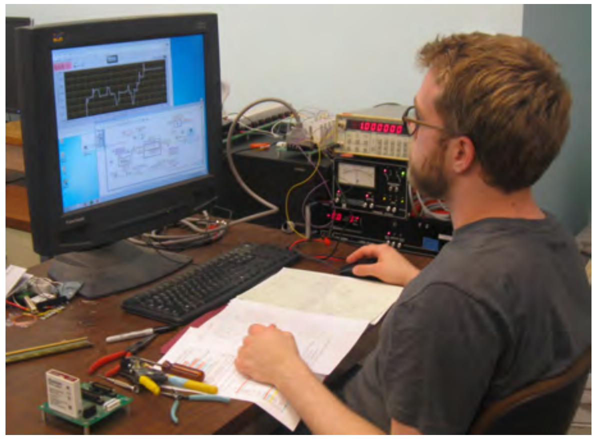

Figure 7.2-3. Research engineer Joben Pedersen creating LabVIEW controls for various accelerator system instruments.

We have made substantial progress towards upgrading the accelerator's control system during this reporting period. Using a LabVIEW program to drive PC based data acquisition (DAQ) boards to operate opto-isolated digital and analog I/O modules, we have been able to demonstrate communication with all the devices necessary to completely switch over to an upgraded vacuum control system. The computer hardware needed for the first phase of the control system upgrade (i.e. control of the High Energy (post accelerator) side of the accelerator system) has been acquired, and CAD models and wiring diagrams of the rack-mount housing for a first phase control system that will. system. Additionally, we've written and tested LabVIEW subroutines to control ion gauges, Pirani gauges, gate valves, and pumps, along with a failure diagnostics routine for our turbomolecular pumps (Fig. 7.2-3).

ACTIVITY SCHEDULED	**DAYS SCHEDULED**	**PERCENT of TIME**
Nuclear-physics research, accelerator	24	6.6
Development, maintenance, or crew training	88	24.1
Grand total	112	30.7

Table 7.2-1. Tandem Accelerator Operations April 1, 2016, to March 31, 2017.

During this annual reporting period from April 1, 2016, to March 31, 2017, the tandem pellet chains operated 214 hours, the sputter-ion-source (SpIS) operated 0 hours, and the duoplasmatron direct-extraction-ion source (DEIS) operated 330 hours. Additional statistics for accelerator operations are given in Table 7.2-1. Ion beams produced using the DEIS included 17.8 MeV ^{2}H for the ^{6}He experiment, 0.99 – 2.0 MeV ^{1}H for the Physics 576 class, 2.0 MeV & 10.0 MeV ^{1}H for $g-2$ muon IBMS, and 15.2 MeV ^{2}H for visiting experimenters.

7.3 Laboratory computer systems

G. T. Holman

CENPA is a mixed shop of Windows 7,10, Mac OS X and various Linux distributions. Windows 10 is installed on new workstations but we are still running a few Windows XP systems for data acquisition, DOS 6 on accelerator gordo controllers and an embedded Win 98 for a mechanical shop mill. As with every year, the IT focus was directed toward server consolidation, network security, process documentation and removal of redundant processes. We continue to utilize Xen virtualization for Autodesk Vault versions, Elogs, wiki, collaboration calendars, and document servers. The CENPA website and research group web pages are run on an upgraded server and have been migrated to Drupal 7 web framework. The NPL mail server still provides NPL presence but all email is relayed to UW email hardware. Workstations connect to UW delegated organizational unit (OU), which mostly removes the need to run a dedicated domain or LDAP server. The last remaining VMS Alphastation 500 'Emmy2' was officially retired this year (It was a race to see who retired first, Wick Haxton or Emmy 2).

Two Dell 510 20-TB servers (Lisa and Marie) continue to offer user storage, print server capability, and improved backup policy. Linux, Windows and Mac workstations are backed up to the Marie 20-TB raid farm which are backed up offsite using UW Trivoli backup service. Lisa runs the Crash Plan Pro backup application which supports all operating systems and provides differential and encrypted backups. Whereas workstations rely on Crash Plan Pro for backups, all servers utilize rsync. Marie provides 20 TB for research, user, and shared group data.

The NPL Data Center (NPLDC) provides legacy infrastructure supporting high-performance scientific-computing applications. The cluster is comprised of two specific cluster instances. The first cluster instance 'cenpa-mamba' runs the latest open-source Rocks software[1], runs the cvmfs (Cern-VM file system) client, and Frontier local squid cache server. The second cluster uses Rocks version 5.4, and most notably runs COMSOL, Cern ROOT and Geant. Both cluster instances use Torque/Maui via dedicated front ends. Approximately one third of the rack space is dedicated to non-cluster hardware: scratch storage, SQL, elogs, web applications, CAD workstations, and backup storage. These servers constitute over 200 TB of raw disk space.

Our computing and analysis facility consists of:

- A mix of Linux servers: Debian, Redhat, and Ubuntu distributions.
- Apple systems for the KATRIN, MAJORANA, and emiT groups.
- A VAXstation for the linac and vacuum systems control and display system.
- Various Windows XP desktop JAM systems (Java-based software for acquisition and analysis).
- A Shorewall Linux-based logical firewall to protect the bulk of CENPA's PCs and servers.

[1]http://www.rocksclusters.org/

7.4 Electronic equipment

D. A. Peterson and T. D. Van Wechel

The electronics shop is responsible for the design and construction of new laboratory electronic equipment as well as the maintenance and repair of existing CENPA electronics. Projects undertaken by the electronics shop in the past year include the following:

1. The design and production of the $g-2$ PbF_2 calorimeter SiPM readout and preamplifier boards (Fig. 7.4-1), power supplies, cables and 25 transition boxes for power and signal distribution are now complete and are being installed at Fermilab (Sec. 4.9).

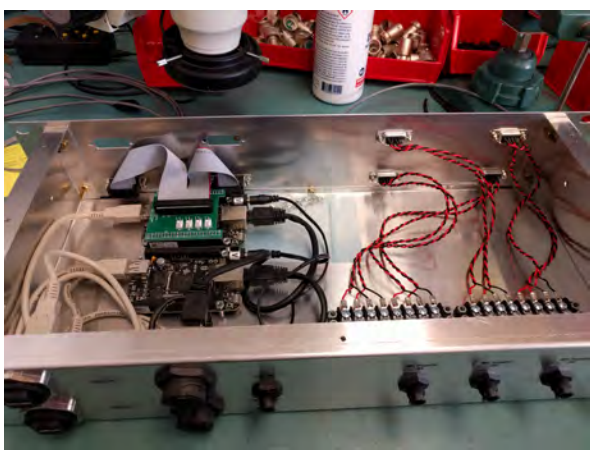

Figure 7.4-1. $g - 2$ transition box.

2. Production of the pulser/mixer NIM modules,the multiplexer/preamplifier boxes, power supplies, DAQ buffer board and cables for the $g-2$ NMR electronics upgrade have been completed (Fig. 7.4-2) (Sec. 4.18).

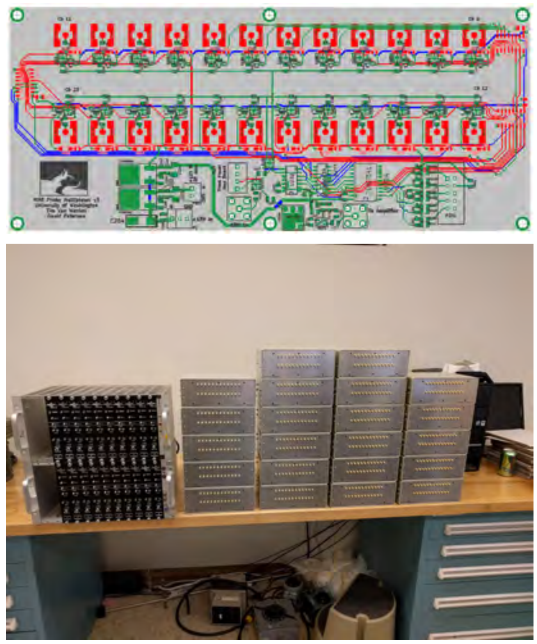

Figure 7.4-2. *Top*: $g-2$ NMR multiplexer PCB layout. *Bottom*: Completed $g-2$ NMR Pulser/Mixer NIM Modules and Multiplexer/Preamplifier Boxes.

3. Designed the high-voltage (HV) probe to Cornell digitizer adapter (Sec. 4.8) for the $g-2$ HV monitor has been completed.
4. Designed and prototyped a 16-channel board for the $g-2$ Inflector Beam Monitoring System (IBMS) (Sec. 4.16). Each of the channels has an 1x1 mm silicon-photomultiplier (SiPM) readout followed by a digital-controlled programmable-gain amplifier (Fig. 7.4-3).

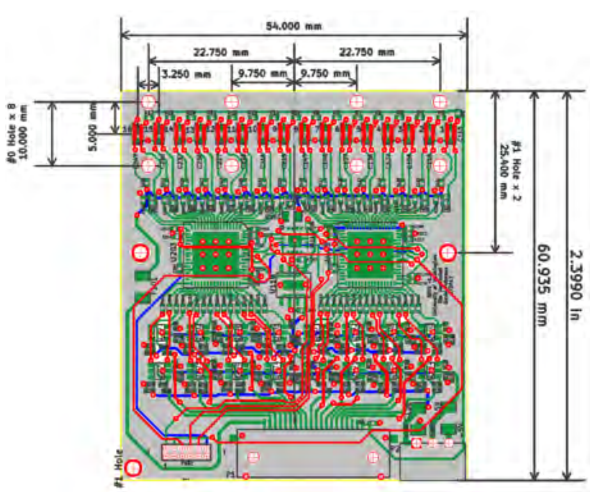

Figure 7.4-3. 16-channel $g-2$ IBMS PCB layout.

5. Assisted in development of a photo multiplier tube (PMT) base for the COHERENT experiment (Sec. 1.18).

6. Spice simulations to aid in the development of low noise electronics for electron detection for time-of-flight operation for the KATRIN neutrino-mass measurement (Sec. 1.5). We are developing a very low noise radio frequency (RF) preamplifier with psuedomorphic high electron-mobility transistors (pHEMT) in the first stage, followed by a Si-GE bipolar transistor second stage (Fig. 7.4-4).

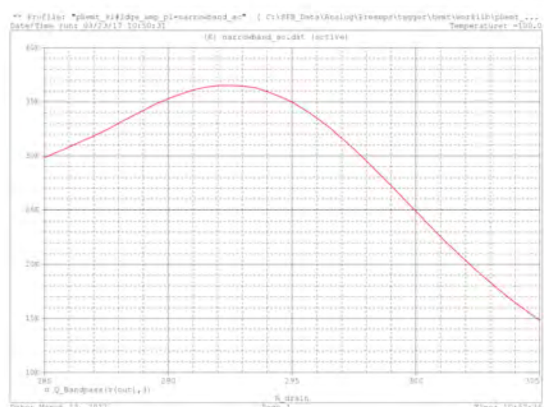

Figure 7.4-4. Spice simulation showing example of resonator Q enhanced by positive feedback versus the value of the pHEMT drain resistor.

7. Designed and built a relay based multiplexer for the HV monitoring system (Sec. 3.6) of the Magneto-Optical Trap(MOT2) for the ^{6}He experiment.
8. A Varactor Reflection Test fixture board was built for ADMX.

7.5 Instrument Shop

T. H. Burritt, J. H. Elms, D. R. Hyde, S. Kimes, and H. Simons

The CENPA instrument shop has given support to CENPA and several UW research groups. Projects completed this year include:

1. We machined, welded, soldered, leak tested, designed and work with all types of materials. In addition we often implemented complex procedures and processes.

2. Fabricated two back-up scintillator stays and two scintillator end-caps for KATRIN (Fig. 7.5-1).

Figure 7.5-1. *Left*: KATRIN Scintillator stays and end-cap. *Right*: Scintillator stays

3. Fabricated leak-tight vacuum chambers in both aluminum and stainless steel for KATRIN (Fig. 7.5-2) and ADMX.

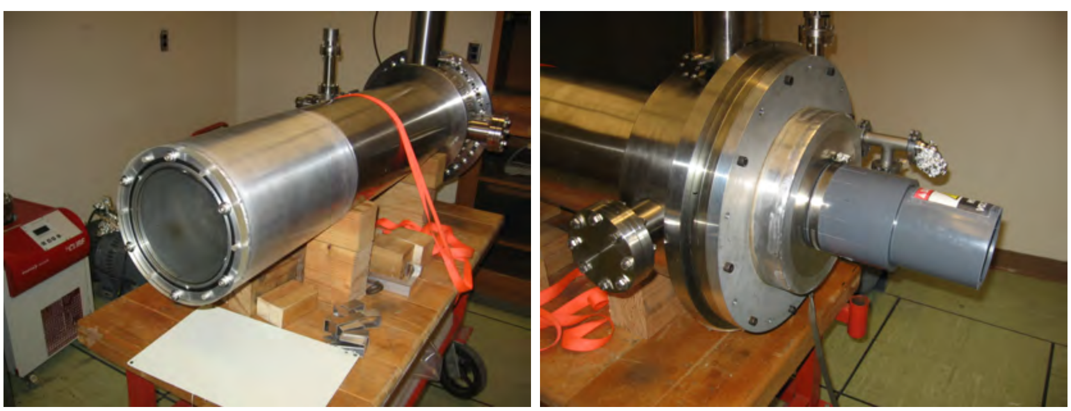

Figure 7.5-2. *Left*: KATRIN Vacuum Chamber. *Right*: KATRIN Vacuum Chamber Cover

4. Completed load testing for KATRIN (Fig. 7.5-3).

5. Fabricated 25 aluminum carts - tig welded and machined, 25 crystal-housing boxes, 25 electronic crates, and 7,000 small components for $g-2$ (Fig. 7.5-4).

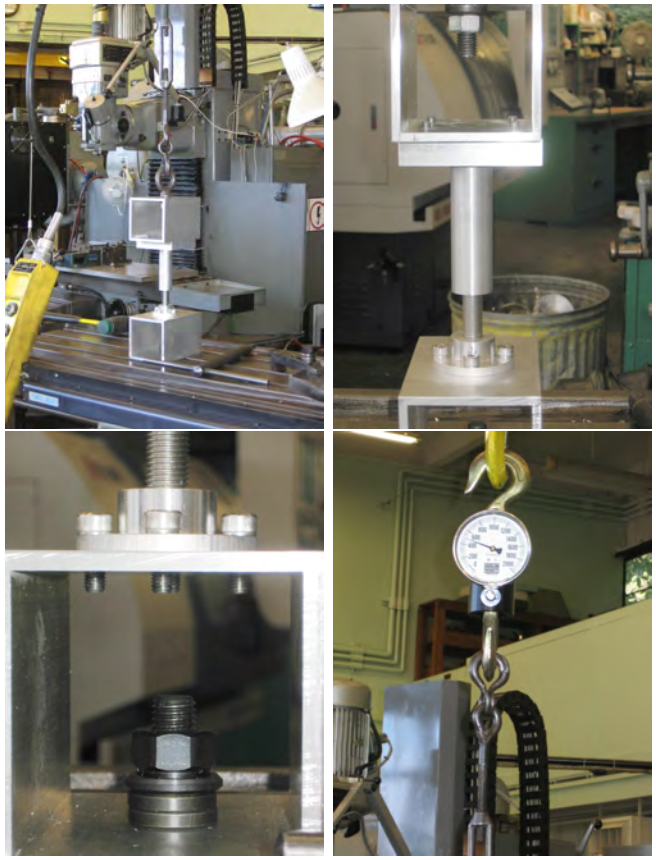

Figure 7.5-3. *Upper Left*: Test bed setup. *Upper Right*: Upper testing and gauge attachment. *Lower Left*: Test bed attachment. *Lower Right*: Load Gauge.

Figure 7.5-4. *Left*: Calorimeter cart back. *Right*: Calorimeter cart front.

6. Design and fabricated two super conductive magnets at 1.5-Tesla each. Developed procedures for winding and potting coils for ADMX Orpheus (Fig. 7.5-5).

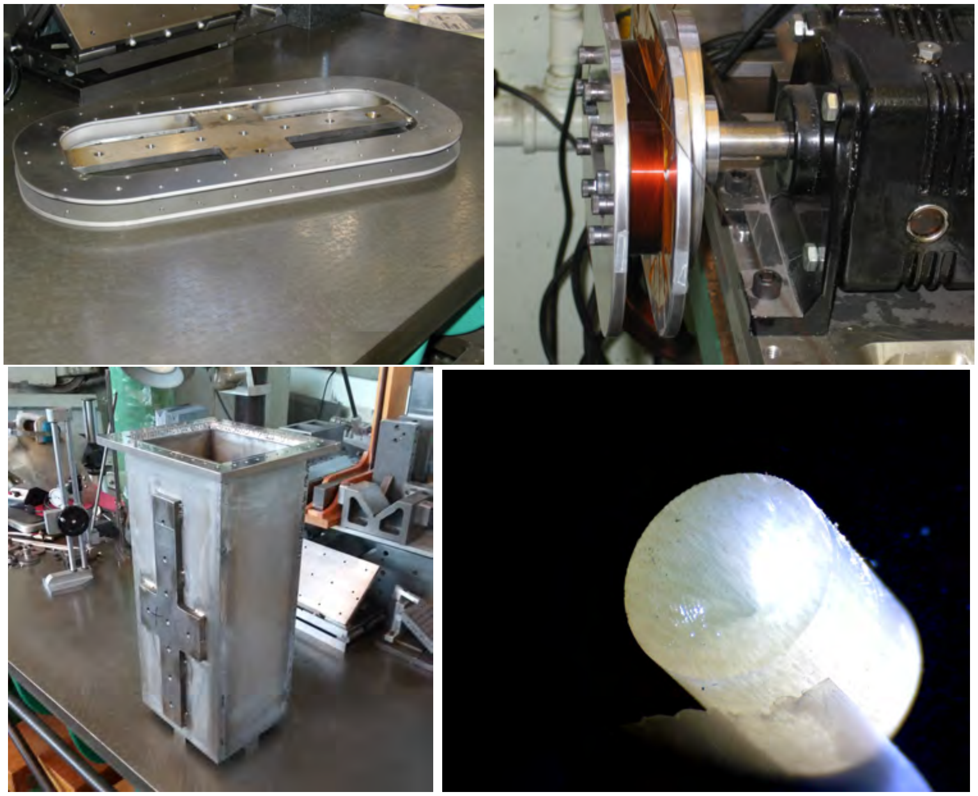

Figure 7.5-5. *Upper Left*: Magnet core. *Upper Right*: Winding development. *Lower Left*: Orpheus magnet mount and vacuum vessel. *Lower Right*: G-10 super conductor guide 0.250 inch diameter with 0.015 center hole. Filleted hole radius of 0.125.

7. Fabricated and modified transfer lines, hard soldered leak-tight and machined copper and stainless steel components for ADMX (Fig. 7.5-6).

Figure 7.5-6. Copper heat exchangers and transfer lines.

8. Designed, fabricated, and modified vessels and components for ADMX (Fig. 7.5-7).

Figure 7.5-7. ADMX aluminum vacuum vessel.

9. Fabricated parts, designed, and educated students and staff in solving problems related to high voltage, vacuum, thermal or magnetic for ADMX.

10. Fabricated wave guides and copper flanges for Project 8 (Sec. 1.15).

11. Fabricated new and repaired components for Van De Graaff accelerator materials using multiple materials (e.g. stainless, titanium, copper, mumetal, tantalum, nickel, maycore, tungsten vespel, and peek) (Sec. 7.2).

7.6 Student shop

D. R. Hyde

The student shop produced several small projects in addition to providing machine-tool training and safety training for the faculty, staff and students.

I drafted a proposal to the Student Technology Fund (STF) in order to obtain a Trak 3-axis CNC milling machine. The machine is now on line and producing parts for experiments. The first 2 below mentioned projects were manufactured by this machine.

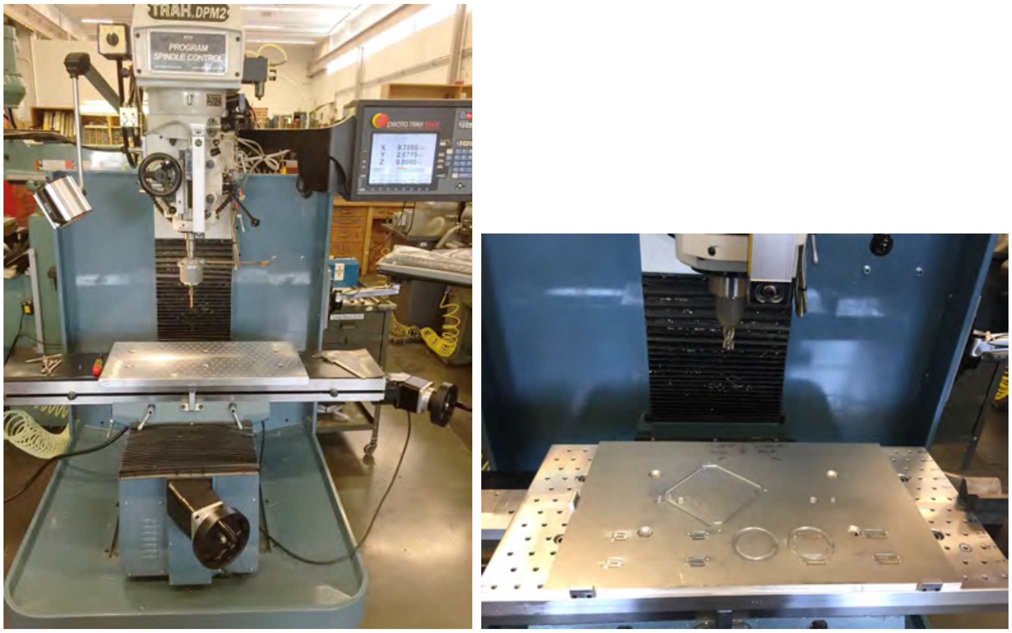

Figure 7.6-1. *Left*: 3-axis CNC milling machine. *Right*: $g-2$ calorimeter electronics rack.

1. Fabricated calorimeter electronics rack for $g-2$ (Fig. 7.6-1 *right*).
2. Modified TwinAx box for $g-2$.
3. Modified laser adjustment fixture for ^{6}He.
4. Fabricated copper block to stabilize detector instrument for ^{6}He.
5. Machined aluminum brackets for TRIMS (Sec. 1.9).
6. Fabricated scintillator frame for $g-2$.

7.7 Building maintenance, repairs, and upgrades

J. Pedersen, E. Smith, and D. I. Will

During the 2016 calendar year 151 Work Orders (WOs) were placed for the North Physics Laboratory buildings which house the CENPA research facility. For the Van de Graaff Accelerator Building 62 total WOs included the following: 35 Preventive Maintenance/Repair/Alterations (PM/R/Alts) by Facilities Services; 19 Service/Repair (S/R) by CENPA staff; and 8 Alterations (Alts) by CENPA staff. The alterations included an upgrade to the exterior door locks. These four WOs were as follows: Install 5 Alarm Lock Trilogy digital door locks with Medeco cylinders; Replace an additional 4 mechanical Russwin cylinders with Medeco cylinders; Cut an extra 5 Medeco keys; Rekey Exterior Door #4 for UW facilities services access via a Medeco to 2TAC key. These locks allow three modes. Everyone on the CENPA telephone list has been issued a six-digit code for keypad entry. Codes can easily be created when a new person arrives and can be readily de-activated upon departure. Some personnel have also been issued rfid-style key-cards upon request. Finally, brass Medeco security keys are in the hands of several senior personnel for use in case of battery or other electronic failure in the Trilogy locks. For the Cyclotron Building 56 total WOs included the following: 41 PM/R/Alts by Facilities Services, 12 S/R by CENPA staff, and 3 Alts estimates requested by CENPA staff. For the CENPA Instrument Shop 33 total WOs included the following: 26 PM/R/Alts by Facilities Services and 7 S/R by CENPA staff.

The high pressure insulating gas (1300 psig, 20% CO_2 in balance N_2) handling and storage system for the tandem accelerator has been upgraded to meet the Washington State Boiler Inspectors current requirements for special systems and vessels. This work is now complete and awaits inspection by the UW insurance inspector.

CENPA has upgraded its RadioActive Materials (RAM) detection and identification equipment and its dose rate measurement capability. During the past year UW Radiation Safety provided CENPA with one of several surplus Perkin Elmer TriCarb Liquid Scintillation Analyzers, model 2800TR, to meet the tritium detection needs of the TRIMS experiment. In addition, one of us (JRP) has assembled a portable electronics package for use with our High Purity Germanium detectors to rapidly identify accelerator-generated (and other) RAM via gamma spectroscopy. CENPA is assisting UW Radiation Safety with identification of RAM as needed across campus. Finally, as old dose rate meters fail beyond repair CENPA has upgraded with the purchase of a new Fluke 451 Ion Chamber Survey Meter and an S E International Geiger-Mueller-based Radiation Alert, Inspector model.

Due to the ongoing North Campus Housing Project (NCHP) to remove two aging dormitories and replace them with five new dormitories, our Gravity research group was awarded a grant from the project to devise an active vibration isolation system[1] (Sec. 2.5).

Finally, staff and students are removing and disposing of large portions of the decommissioned CENPA superconducting LINAC booster and its infrastructure to create space for the upcoming Orpheus Project of ADMX (Sec. 5.1) at the west end of our accelerator tunnel. During this reporting period, 3 tons of steel I-beams, 24 tons of steel shielding, 20 tons of concrete pillars, and several hundred feet of wire & cable was removed and recycled. All cryogenic valve boxes have been removed and staged outside the building, and are awaiting listing with UW Surplus along with all remaining cryostats.

[1] K. J. S. Stockton, Active Vibration Isolation Systems, Masters Thesis, March 2017.

7.8 Laboratory Safety

G. T. Holman, J. R. Pedersen, E. B. Smith, and D. I. Will

Providing an environment for safe research and promoting a culture of safety are activities strongly supported by the University of Washington and embraced by CENPA. That safety means not only the physical safety of UW students, faculty, and staff, but also the safety of the natural environment in which CENPA exists. The UW Environmental Health and Safety Department (EH&S) oversees all safety compliance on campus including areas such as building safety, radiation safety, chemical safety, occupational safety, and research safety.

UW EH&S has developed and maintains a UW Laboratory Safety Manual (LSM), which formulates the safety of UW laboratories around what the Washington Department of Labor and Industries calls a "Chemical Hygiene Plan (CHP)". Though a CHP is required for all laboratories that use hazardous chemicals, its formulation and scope can be applied beyond chemical safety to cover safety related to any laboratory hazards, and it is in this broad scope application that UW EH&S requires every CENPA laboratory to implement a CHP. After first requiring an identification of chemical and non-chemical hazards, and a specification of Standard Operator Procedures (SOPs), the CHP then requires the creation of a corresponding list of personal protective equipment (PPE) and training needed by personnel utilizing that laboratory.

At least once every 16-18 months, and at least once during this annual report period, UW EH&S performs a Laboratory Safety Survey of every laboratory at CENPA to review the laboratory's adherence to it's CHP. Additionally however, beginning this annual reporting period, CENPA has three laboratories participating in the University of Washington two-year Lab Safety Initiative (LSI) pilot program, which requires a Laboratory Safety Survey be performed three times over a 24-month period. The goal of the LSI program is to: a) identify and overcome barriers to safety in labs; b) develop and share best practices; c) reduce administrative burden; and d) lead to the development and implementation of services, approaches, and tools that significantly remove barriers and improve laboratory chemical safety throughout the University.

Over the past year, CENPA has made significant strides toward alignment with CHP formulation. We have divided the facility into many separate laboratory spaces, based primarily (but not exclusively) on rooms. Each laboratory space, though not restricted to a single research endeavor, has a clearly assigned laboratory supervisor charged with producing the broad scope CHP needed to address all safety aspects of research activities in that specific laboratory. Newly identified laboratory supervisors have spend much time on activities such as entering and checking inventory of chemicals online, creating SOPs, specifying training, and tracking personnel training. Additionally, CENPA staff have even developed a unique Safety Kiosk (Fig. 7.8-1 (left)) that has brought praise from the Lab Safety Initiative (LSI) pilot program. The inexpensive kiosk consists of a retractable shelf that contains a mounted notebook with WiFi connection to the UW LAN network. The notebook startup page is linked to a Safety Kiosk page on the CENPA website (Fig. 7.8-1 (right)), which contains links to the most current UW Laboratory Safety Manual, UW MyChem chemical management site, and other vital safety sites online. These Safety Kiosks are inexpensive enough and unobtrusive enough to allow one to be placed in every laboratory. CENPA already has the necessary equipment to install two more of these kiosks.

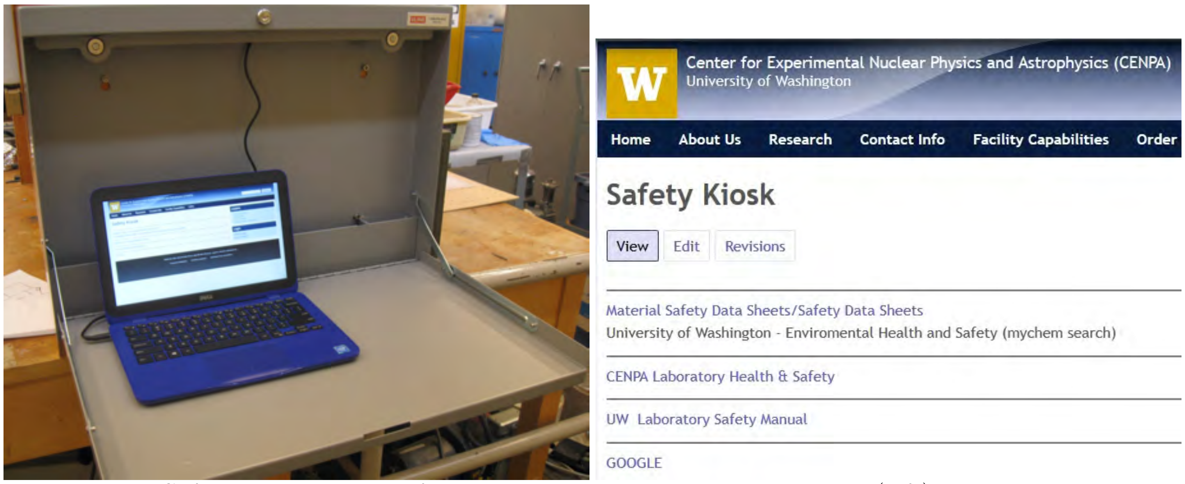

Figure 7.8-1. Safety Kiosk showing folding drawer with mounted notebook (left) displaying the newly created CENPA Safety Kiosk webpage (right) at statup.

The safe storage and disposal of the variety of hazardous materials needed to perform research at CENPA continued to receive attention and innovation this reporting period. In addition to stepping up our identification and disposal of unwanted or waste hazardous materials, we participated in a Collection of Hazardous and Unwanted Chemicals (CHUC) event offered by UW EH&S resulting in the removal of an entire cabinet (43”x64”x18”) of hazardous materials no longer needed at CENPA. Two additional CENPA staff members have been trained by CENPA engineers on the procedures for proper submission of hazardous materials to UW EH&S for disposal. We are also developing an in-house chemical inventory control application that will interface with the UW MyChem database and also provide additional information to CENPA personnel about chemical storage location and expiration.

8 CENPA Personnel

8.1 Faculty

Eric G. Adelberger[1]	Professor Emeritus
Hans Bichsel[1]	Affiliate Professor
John G. Cramer[1]	Professor Emeritus
Jason Detwiler	Assistant Professor
Peter J. Doe	Research Professor
Sanshiro Enomoto	Research Associate Professor
Martin Fertl[2]	Acting Assistant Professor
Xavier Fléchard[3,4]	Affiliate Professor
Alejandro García	Professor
Gerald Garvey[5]	Affiliate Professor
Jens H. Gundlach[1]	Professor
Blayne R. Heckel[1]	Professor; Chair
David W. Hertzog[6]	Professor; Acting Director
C. D. Hoyle[1,7]	Affiliate Professor
Peter Kammel	Research Professor
Jarek Kaspar[1]	Acting Assistant Professor
Woo-Joong Kim[8]	Affiliate Assistant Professor
Michael L. Miller[1,9]	Affiliate Research Assistant Professor
Diana Parno[1,10,11]	Affiliate Assistant Professor
R. G. Hamish Robertson[12]	Professor; Director
Leslie J Rosenberg[1]	Professor
Gray Rybka	Assistant Professor
Derek W. Storm[1]	Research Professor Emeritus
Thomas A. Trainor[13]	Research Professor Emeritus
Krishna Venkateswara[1]	Acting Assistant Professor
John F. Wilkerson[1,14]	Affiliate Professor

[1] Not supported by DOE CENPA grant.
[2] Postdoctoral position ended March 31, 2016. Faculty position commenced April 1, 2016.
[3] Professor from CEA/Saclay, on sabbatical at CENPA.
[4] Arrived April 1, 2016.
[5] Arrived October, 2016.
[6] Interim Director, February 2017.
[7] Affiliated faculty, Humboldt State University, Arcata, CA.
[8] Departed June, 2016. Assistant professor from Seattle University, on sabbatical at CENPA.
[9] Affiliated faculty.
[10] Departed December, 2016. Presently at Carnegie Mellon University, Pittsburgh, PA.
[11] Associate Director through November, 2016.
[12] Retired February, 2017.
[13] DOE supported through November 2014.
[14] Affiliated faculty, University of North Carolina, Chapel Hill, NC.

8.2 CENPA External Advisory Committee

Robert McKeown[1]	Jefferson Laboratory
Daniel McKinsey[1]	UC Berkeley
Michael Ramsey-Musolf[1]	University of Massachusetts, Amherst

8.3 Postdoctoral Research Associates

Clara Cuesta[2,3]
Mathieu Guigue[2,4]
Charles Hagedorn[2]
Rakshya Khatiwada[2]
Kim Siang Khaw
Arnaud Leredde[2,5]
Ana Malagon[2,6]
Richard Ottens[2]
Walter Pettus[7]
Daniel Salvat

8.4 Predoctoral Research Associates

Sebastian Alvis[8]
Yelena Bagdasarova[9]
Erin Board[2,10]
Christian Boutan[2,11]
Raahul Buch[2,12]
Micah Buuck[2]
Raphael Cervantes[2,13]
Nicole Crisosto[2,14]
Nick Du[2,15]
Ali Ashtari Esfahani[2]
Aaron Fienberg
Nathan Froemming
Brent Graner
Julieta Gruszko[2]
Ian Guinn
Jason Hempstead
Luke Kippenbrock
John G. Lee[2]
Erik Lentz[2]
Jonathan Leon[2,16]
Ting Lin
Brynn MacCoy[17]
Eric Machado
Eric Martin

[1] CENPA External Advisory Committee formed January 2014.
[2] Not supported by DOE CENPA grant.
[3] Departed February, 2017.
[4] Supported by Pacific Northwest National Laboratory.
[5] Supported by Argonne National Laboratory. Departed August, 2016.
[6] Departed September, 2016.
[7] Arrived May, 2016.
[8] Arrived September, 2016.
[9] Supported by CENPA DOE budget starting August, 2016.
[10] Arrived October, 2016.
[11] Graduated March, 2017.
[12] Arrived April, 2016.
[13] Arrived March, 2017.
[14] Visiting graduate student from University of Florida.
[15] Arrived June, 2016.
[16] Returned from leave of absence March, 2017.
[17] Arrived December, 2016.

Ethan Muldoon	Erik Shaw[2]
Michael Murray[1]	Matthias Smith
Rachel Osofsky	Kerkira Stockton[2,4]
Michael Ross[2]	Diana Thompson[2,5]
Nick Ruof[2,3]	Matthew Turner[2,6]
Rachel Ryan	Timothy Winchester[7]

8.5 University of Washington graduates taking research credit

Hannah Binney	David W. Hertzog, Advisor

8.6 University of Washington undergraduates taking research credit

Abdulla Alseiari	Jason Detwiler, Advisor
Andrew Eberhardt[8]	Jason Detwiler, Advisor
Eric Erkela	Jason Detwiler, Advisor
Xiong Feng	Jason Detwiler, Advisor
Zhenghao Fu[8]	Jason Detwiler, Advisor
Sean Gilligan	Alejandro García, Advisor
Kezhu Guo	Gray Rybka, Advisor
Jacob Herr	Gray Rybka, Advisor
Mikael Nils Hostage	Alejandro García, Advisor
Dustin Kasparek	Gray Rybka, Advisor
Matthew Kallandert[9]	R. G. Hamish Robertson, Advisor
Jacob Johnson	Gray Rybka, Advisor
Matthew Jones	Gray Rybka, Advisor
Yen Lee	Gray Rybka, Advisor
Aobo Li	Jason Detwiler, Advisor
Jocelin Liteanu	Jason Detwiler, Advisor
Anthony McIntosh	Gray Rybka, Advisor
Yujin Park	Gray Rybka, Advisor
Spencer Peters	Alejandro García, Advisor
Benjamin Phillips	Gray Rybka, Advisor
Joshua Povik	Gray Rybka, Advisor
Hira Shen	Gray Rybka, Advisor

[1] Graduated March, 2017.
[2] Not supported by DOE CENPA grant.
[3] Arrived September, 2016.
[4] Graduated with Master's degree and departed March, 2017.
[5] Graduated with Master's degree and departed October, 2016.
[6] On leave of absence beginning April, 2015. Presently at Microsoft.
[7] Graduated August, 2016. Currently teaching at Bellevue College and North Seattle College.
[8] Graduated June, 2016.
[9] Graduated June, 2016. Worked as volunteer after graduation.

Tun Sheng Tan	David W. Hertzog, Advisor
Kevin Thomas	Gray Rybka, Advisor
Khang Ton	Jason Detwiler, Advisor
Winnie Wang	David W. Hertzog, Advisor
Yu Xie	Jason Detwiler, Advisor

8.7 NSF Research Experience for Undergraduates participants

Wendy Collins	Skidmore College	Peter Kammel, Advisor
Annie Ramey	Grinnell College	Alejandro García, Advisor
Samantha Valenteen	University of Colorado Boulder	Gray Rybka, Advisor

8.8 Visiting students taking research credit

Frederik Otto[1]	Alejandro García, Advisor
Anthony Sanchez[2]	C. D. Hoyle, Advisor

8.9 Professional staff

John F. Amsbaugh	Research Engineer	Engineering, vacuum, cryogenics design
Tom H. Burritt	Shop Supervisor	Precision design, machining
Gary T. Holman[3]	Systems Manager	Computer systems
Aamar Ieso[4]	Research Scientist	ADMX
Hannah LeTourneau[5]	Research Engineer	Helium liquefier
Joben Pedersen[6]	Research Engineer	Accelerator, ion sources
Duncan J. Prindle, Ph.D.	Research Scientist	Heavy ion, muon research
Eric B. Smith	Research Engineer	Accelerator, ion sources
H. Erik Swanson, Ph.D.	Research Physicist	Precision experimental equipment
Timothy D. Van Wechel	Research Engineer	Analog and digital electronics design
Douglas I. Will	Senior Engineer	Cryogenics, ion sources, buildings

[1] Visiting student from Justus Liebig University Giessen.
[2] Visiting student from Humboldt State University.
[3] Acting Associate Director beginning December, 2016.
[4] Arrived August, 2016. Departed February, 2017.
[5] Departed August, 2016.
[6] Promoted to Research Engineer I in August, 2016.

8.10 Technical staff

James H. Elms	Instrument Maker
Nick Force	Engineering Technician
David R. Hyde	Instrument Maker
Seth Kimes	Engineering Technician
David A. Peterson	Electronics Technician
James Sloan[1]	Engineering Technician
Daniel Stromecki	Laboratory Technician

8.11 Administrative staff

Victoria A. Clarkson	Administrator
Ida Boeckstiegel	Fiscal Specialist

8.12 Part-time staff and student helpers

Michael Borusinski
Andrew Eberhardt[2]
Henry Gorrell[3]
Brett Hamre
Michael Huehn[4]
Mathew Kallander[5]
Grant Leum
Joshua Oppor
Ronaldo Ortez[6]
Josh Reyes[6]
Samuel Sexton
Hendrik Simons
Alex Zderic

8.13 Visitors & Volunteers

Christine Claessens[7]
Adam Cox[8]
Kiva Ramundo
Raphael Ostertag[9]
Agnes Seher[9]

[1]Departed December, 2016.
[2]Departed June, 2016.
[3]Arrived January, 2017.
[4]Departed December, 2016.
[5]Starting working as part-time staff after graduation June, 2016.
[6]Departed August, 2016.
[7]Visiting PhD student from the University of Mainz, working on TRIMS, June 2016.
[8]Departed September, 2016.
[9]Visiting student from Karlsruhe Institute of Technology.

9 Publications

Publications and presentations with a date of 2016 or 2017 are included below. Some entries from early 2016 may therefore also appear in the 2016 Annual Report.

9.1 Published papers

1. "Design and performance of SiPM-based readout of PbF_2 crystals for high-rate, precision timing applications," A. T. Fienberg, D. W. Hertzog, M. A. Huehn, J. Kaspar*, P. Kammel, K. S. Khaw, D. A. Peterson, M. W. Smith, T. D. Van Wechel, A. Chapelain, L. K. Gibbons, D. A. Sweigart, C. Ferrari, A. Fioretti, C. Gabbanini, G. Venanzoni, M. Iacovacci, S. Mastroianni, K. Giovanetti, W. Gohn, T. Gorringe, D. Pocanic, JINST **12**, no. 01, P01009 (2017); arXiv:1611.03180.†

2. "Electron Beam Test of Key Elements of the Laser-Based Calibration System for the Muon $g-2$ Experiment," A. Anastasi, A. Basti, F. Bedeschi, M. Bartolini, G. Cantatore, D. Cauz, G. Corradi, S. Dabagov, G. DI Sciascio, R. Di Stefano, A. Driutti, O. Escalante, C. Ferrari, A. T. Fienberg, A. Fioretti, C. Gabbanini, A. Gioiosa, D. Hampai, D. W. Hertzog, M. Iacovacci, M. Karuza, J. Kaspar, A. Liedl, A. Lusiani, F. Marignetti, S. Mastroianni, D. Moricciani, G. Pauletta, G. M. Piacentino, N. Raha, E. Rossi, L. Santi, G. Venanzoni, Nucl. Instrum. Meth. A **842**, 86 (2017); arXiv:1610.03210.†

3. "The calorimeter system of the new muon $g-2$ experiment at Fermilab," L. P. Alonzi, A. Anastasi, R. Bjorkquist, D. Cauz, G. Cantatore, S. Dabagov, G. Di Sciascio, R. Di Stefano, R. Fatemi, C. Ferrari, A T. Fienberg, A. Fioretti, A. Frankenthal, C. Gabbanini, L. K. Gibbons, K. Giovanetti, S. D. Goadhouse, W. P. Gohn, T. P. Gorringe, D. Hampai, D. W. Hertzog, M. Iacovacci, P. Kammel, M. Karuza, J. Kaspar, B. Kiburg, L. Li, F. Marignetti, S. Mastroianni, D. Moricciani, G. Pauletta, D. A. Peterson, D. Počanić, L. Santi, M. W. Smith, D. A. Sweigart, V. Tishchenko, T. D. Van Wechel, G. Venanzoni, K.B. Wall, P. Winter, K. Yai, Nucl. Instrum. Meth. A **824**, 718 (2016); doi:10.1016/j.nima.2015.11.041.†

4. "The calibration system of the new $g-2$ experiment at Fermilab," A. Anastasi, D. Babusci, G. Cantatore, D. Cauz, G. Corradi, S. Dabagov, P. Di Meo, G. Di Sciascio, R. Di Stefano, C. Ferrari, A. T. Fienberg, A. Fioretti, C. Gabbanini, D. Hampai, D. W. Hertzog, M. Iacovacci, M. Karuza, J. Kaspar, F. Marignetti, S. Mastroianni, D. Moricciani, G. Pauletta, L. Santi, G. Venanzoni, Nucl. Instrum. Meth. A **824**, 716 (2016). doi:10.1016/j.nima.2015; 11.059.†

An * denotes a CENPA author who is the lead author of or major contributor to a publication.
A † denotes a publication describing work fully or partially supported by the DOE grant.

5. "Measurement of a false electric dipole moment signal from ^{199}Hg atoms exposed to an inhomogeneous magnetic field," S. Afach, C. A. Baker, G. Ban, G. Bison, K. Bodek, Z. Chowdhuri, M. Daum, M. Fertl, B. Franke, P. Geltenbort, K. Green, M. G. D. Van Der Grinten, Z. Grujic, P. G. Harris, W. Heil, V. Hélaine, R. Henneck, M. Horras, P. Iaydijev, S. N. Ivanov, M. Kasprzak, Y. Kermaïdic, K. Kirch, P. Knowles, H.-C. Koch, S. Komposch, A. Kozela, J. Krempel, B. Lauss, T. Lefort, Y. Lemière, A. Mtchedlishvili, O. Naviliat-Cunic, J. M. Pendlebury, F. M. Piegsa, G. Pignol, P. N. Prashant, G. Quéméner, D. Rebreyend, D. Ries, S. Roccia, P. Schmidt-Wellenburg, N. Severijns, A. Weis, E. Wursten, G. Wyszynski, J. Zejma, J. Zenner, and G. Zsigmond, European Physical Journal D **69**, (2015); arXiv:1503.08651.

6. "A device for simultaneous spin analysis of ultracold neutrons," S. Afach, G. Ban, G. Bison, K. Bodek, Z. Chowdhuri, M. Daum, M. Fertl, B. Franke, P. Geltenbort, Z. D. Grujic, L. Hayen, V. Hélaine, R. Henneck, M. Kasprzak, Y. Kermaïdic, K. Kirch, S. Komposch, A. Kozela, J. Krempel, B. Lauss, T. Lefort, Y. Lemière, A. Mtchedlishvili, O. Naviliat-Cunic, F. M. Piegsa, G. Pignol, P. N. Prashant, G. Quéméner, M. Rawlik, D. Rebreyend, D. Ries, S. Roccia, D. Rozpedzik, P. Schmidt-Wellenburg, N. Severijns, A. Weis, E. Wursten, G. Wyszynski, J. Zejma, J. Zenner, and G. Zsigmond, European Physical Journal A **51**, (2015); arXiv:1502.06876.

7. "A prestorage method to measure neutron transmission of ultracold neutron guides," B. Blau, M. Daum, M. Fertl, P. Geltenbort, L. Göltl, R. Henneck, K. Kirch, A. Knecht, B. Lauss, P. Schmidt-Wellenburg, and G. Zsigmond, Nuclear Instruments and Methods in Physics Research, Section A: Accelerators, Spectrometers, Detectors and Associated Equipment **807** (2016); arXiv:1508.06144.

8. "Next generation muon g-2 experiment at FNAL," M. Fertl, Hyperfine Interactions **237** (2016), 94; arXiv:1610.07017.**†**

9. "High accuracy position response calibration method for a micro-channel plate ion detector," R. Hong*****, A. Leredde, Y. Bagdasarova, X. Fléchard, A. García, P. Müller, A. Knecht, E. Liénard, M. Kossin, M. G. Sternberg, H. E. Swanson, D. W. Zumwalt, Nucl. Instrum. Meth. A **835**, 42 (2016); arXiv:1605.08686.**†**

10. "Helicity and nuclear β-decay correlations," R. Hong*****, M. G. Sternberg, A. García*****, Am. J. Phys. **85** 45 (2017); arXiv:1604.07913.**†**

11. "The $2^+_1 \rightarrow 3^+_1$ gamma width in ^{22}Na and second class currents," S. Triambak, L. Phuthu, A. García*****, G. C. Harper, J. N. Orce, D. A. Short, S. P. R. Steininger, A. Diaz Varela, R. Dunlop, D. S. Jamieson, W. A. Richter, G. C. Ball, P. E. Garrett, C. E. Svensson, C. Wrede, Phys. Rev. C **95**, 035501 (2017); arXiv:1701.05545.**†**

An ***** denotes a CENPA author who is the lead author of or major contributor to a publication.
A **†** denotes a publication describing work fully or partially supported by the DOE grant.

12. "Detection system for neutron β decay correlations in the UCNB and Nab experiments," L. J. Broussard, B. A. Zeck, E. R. Adamek, S. Baeßler, N. Birge, M. Blatnik, J. D. Bowman, A. E. Brandt, M. Brown, J. Burkhart, N. B. Callahan, S. M. Clayton, C. Crawford, C. Cude-Woods, S. Currie, E. B. Dees, X. Ding, N. Fomin, E. Frlez, J. Fry, F. E. Gray, S. Hasan, K. P. Hickerson, J. Hoagland, A. T. Holley, T. M. Ito, A. Klein, H. Li, C.-Y. Liu, M. F. Makela, P. L. McGaughey, J. Mirabal-Martinez, C. L. Morris, J. D. Ortiz, R. W. Pattie Jr., S. I. Penttilä, B. Plaster, D. Počanić, J. C. Ramsey, A. Salas-Bacci, D. J. Salvat*, A. Saunders, S. J. Seestrom, S. K. L. Sjue, A. P. Sprow, Z. Tang, R. B. Vogelaar, B. Vorndick, Z. Wang, W. Wei, J. Wexler, W. S. Wilburn, T. L. Womack, A. R. Young, Nucl. Instrum. Meth. A **849** 83-93 (2016).

13. "Total cross sections for ultracold neutrons scattered from gases," S. J. Seestrom, E. R. Adamek, D. Barlow, M. Blatnik, L. J. Broussard, N. B. Callahan, S. M. Clayton, C. Cude-Woods, S. Currie, E. B. Dees, W. Fox, M. Hoffbauer, K. P. Hickerson, A. T. Holley, C.-Y. Liu, M. Makela, J. Medina, D. J. Morley, C. L. Morris, R. W. Pattie, Jr., J. Ramsey, A. Roberts, D. J. Salvat*, A. Saunders, E. I. Sharapov, S. K. L. Sjue, B. A. Slaughter, P. L. Walstrom, Z. Wang, J. Wexler, T. L. Womack, A. R. Young, J. Vanderwerp, and B. A. Zeck, Phys. Rev. C **95**, 015501 (2017).

14. "Newtonian-noise cancellation in large-scale interferometric GW detectors using seismic tiltmeters," J. Harms and K. Venkateswara, Classical and Quantum Gravity **33**, 234001 (2016).

15. "Subtracting tilt from a horizontal-seismometer using a ground-rotation-sensor," K. Venkateswara, C. A. Hagedorn, J. H. Gundlach, J. Kissel, J. Warner, H. Radkins, T. Shaffer, B. Lantz, F. Matichard, R. Mittleman, and R. Schofield, Bulletin of Seismological Society of America **107**, no. 2 (2017); doi.org/10.1785/0120160310.

16. "Tests of General Relativity with GW150914," B. P. Abbott *et. al.*, Physical Review Letters **116** 221101 (2016); arXiv:1602.03841.

17. "GW151226: Observation of Gravitational Waves from a 22-Solar-Mass Binary Black Hole Coalescence," B. P. Abbott *et. al.*, Physical Review Letters **116** 241103 (2016).

18. "Reduced Limit on the Permanent Electric Dipole Moment of ^{199}Hg," B. Graner, Y. Chen, E. G. Lindahl, and B. R. Heckel*, Phys. Rev. Lett. **116**, 161601 (2016); arXiv:1601.04339.†

19. "Measurement of muon annual modulation and muon-induced phosphorescence in NaI(Tl) crystals with DM-Ice17," J. Cherwinka, D. Grant, F. Halzen, K. M. Heeger, L. Hsu, A. J. F. Hubbard, A. Karle, M. Kauer, V. A. Kudryavtsev, K. E. Lim, C. Macdonald, R. H. Maruyama, S. M. Paling, W. Pettus*, Z. P. Pierpoint, B. N. Reilly, M. Robinson, P. Sandstrom, N. J. C. Spooner, S. Telfer, L. Yang, Phys. Rev. D **93**, 042001 (2016); arXiv:1509.02486.

An * denotes a CENPA author who is the lead author of or major contributor to a publication.
A † denotes a publication describing work fully or partially supported by the DOE grant.

20. "First search for a dark matter annual modulation signal with NaI(Tl) in the Southern Hemisphere by DM-Ice17," E. Barbosa de Souza, J. Cherwinka, A. Cole, A. C. Ezeribe, D. Grant, F. Halzen, K. M. Heeger, L. Hsu, A. J. F. Hubbard, J. H. Jo, A. Karle, M. Kauer, V. A. Kudryavtsev, K. E. Lim, C. Macdonald, R. H. Maruyama, F. Mouton, S. M. Paling, W. Pettus*****, Z. P. Pierpoint, B. N. Reilly, M. Robinson, F. R. Rogers, P. Sandstrom, A. Scarff, N. J. C. Spooner, S. Telfer, and L. Yang, Phys. Rev. D **95**, 032006 (2017); arXiv:1602.05939.

21. "Determining the neutrino mass with cyclotron radiation emission spectroscopy - project 8." A Ashtari Esfahani, D. Asner, S. Böser, R. Cervantes, C. Claessens, P. Doe, S. Doeleman, J. Fernandez, M. Fertl, E. Finn, J. Formaggio, D. Furse, M. Guigue, K. Heeger, A. M. Jones, K. Kazkaz, J. Kofron, C. Lamb, B. LaRoque, E. Machado, E. McBride, M. Miller, B. Monreal, P. Mohanmurthy, J. Nikkel, N. Oblath, W. Pettus, H. Robertson, L. Rosenberg, G. Rybka, D. Rysewyk, L. Saldaña, P. Slocum, M. Sternberg, J. Tedeschi, T. Thuemmler, B. VanDevender, L. Vertatschitsch, L. de Viveiros, M. Wachtendonk, J. Weintroub, N. Woods, A. Young, and E. Zayas. *Journal of Physics G: Nuclear and Particle Physics*, 2017; arXiv:1703.02037.**†**

22. "Measurements of d_2^n and A_1^n: Probing the neutron spin structure," D. Flay, M. Posik, D. S. Parno*****, K. Allada, W. Armstrong, T. Averett, F. Benmokhtar, W. Bertozzi, A. Camsonne, M. Canan, G. D. Cates, C. Chen, J.-P. Chen, S. Choi, E. Chudakov, F. Cusanno, M. M. Dalton, W. Deconinck, C. W. de Jager, X. Deng, A. Deur, C. Dutta, L. El Fassi, G. B. Franklin, M. Friend, H. Gao, F. Garibaldi, S. Gilad, R. Gilman, O. Glamazdin, S. Golge, J. Gomez, L. Guo, O. Hansen, D. W. Higinbotham, T. Holmstrom, J. Huang, C. Hyde, H. F. Ibrahim, X. Jiang, G. Jin, J. Katich, A. Kelleher, A. Kolarkar, W. Korsch, G. Kumbartzki, J. J. LeRose, R. Lindgren, N. Liyanage, E. Long, A. Lukhanin, V. Mamyan, D. McNulty, Z.-E. Meziani, R. Michaels, M. Mihovilovič, B. Moffit, N. Muangma, S. Nanda, A. Narayan, V. Nelyubin, B. Norum, Nuruzzaman, Y. Oh, J. C. Peng, X. Qian, Y. Qiang, A. Rakhman, S. Riordan, A. Saha, B. Sawatzky, M. H. Shabestari, A. Shahinyan, S. Širca, P. Solvignon, R. Subedi, V. Sulkosky, W. A. Tobias, W. Troth, D. Wang, Y. Wang, B. Wojtsekhowski, X. Yan, H. Yao, Y. Ye, Z. Ye, L. Yuan, X. Zhan, Y. Zhang, Y.-W. Zhang, B. Zhao, X. Zheng, Phys. Rev. D **94**, 052003 (2016). doi:10.1103/PhysRevD.94.052003

23. "A high-finesse Fabry-Perot cavity with a frequency-doubled green laser for precision Compton polarimetry at Jefferson Lab," A. Rakhman, M. Hafez, S. Nanda, F. Benmokhtar, A. Camsonne, G. Cates, M. Dalton, G. B. Franklin, M. Friend, R. Michaels, V. Nelyubin, D. S. Parno, K. Paschke, B. Quinn, P. A. Souder, W. A. Tobias, Nucl. Inst. Meth. A **822**, 82 (2016). doi:10.1016/j.nima.2016.03.085

An ***** denotes a CENPA author who is the lead author of or major contributor to a publication.
A **†** denotes a publication describing work fully or partially supported by the DOE grant.

24. "The Majorana Demonstrator radioassay program," N. Abgrall, I. J. Arnquist, F. T. Avignone III, H. O. Back, A. S. Barabash, F. E. Bertrand, M. Boswell, A. W. Bradley, V. Brudanin, M. Busch, M. Buuck, D. Byram, A. S. Caldwell, Y.-D. Chan, C. D. Christofferson, P.-H. Chu, C. Cuesta, J. A. Detwiler, J. A. Dunmore, Yu. Efremenko, H. Ejiri, S. R. Elliott, P. Finnerty, A. Galindo-Uribarri, V. M. Gehman, T. Gilliss, G. K. Giovanetti, J. Goett, M. P. Green, J. Gruszko, I. S. Guinn, V. E. Guiseppe, R. Henning, E. W. Hoppe, S. Howard, M. A. Howe, B. R. Jasinski, R. A. Johnson, K. J. Keeter, M. F. Kidd, O. Kochetov, S. I. Konovalov, R. T. Kouzes, B. D. LaFerriere, J. Leon, J. C. Loach, J. MacMullin, S. MacMullin, R. D. Martin, R. Massarczyk, S. Meijer, S. Mertens, M. L. Miller, J. L. Orrell, C. O'Shaughnessy, N. R. Overman, A. W. P. Poon, K. Pushkin, D. C. Radford, J. Rager, K. Rielage, R. G. H. Robertson, E. Romero-Romero, M. C. Ronquest, A. G. Schubert, B. Shanks, M. Shirchenko, K. J. Snavely, N. Snyder, D. Steele, A. M. Suriano, D. Tedeschi, J. E. Trimble, R. L. Varner, S. Vasilyev, K. Vetter, K. Vorren, B. R. White, J. F. Wilkerson, C. Wiseman, W. Xu, E. Yakushev, C.-H. Yu, V. Yumatov, and I. Zhitnikov, Nucl. Instr. Meth. Phys. Res. A, **828**, 22-36 (2016).†

25. "High voltage testing for the Majorana Demonstrator," N. Abgrall, I. J. Arnquist, F. T. Avignone III, A. S. Barabash, F. E. Bertrand, A. W. Bradley, V. Brudanin, M. Busch, M. Buuck, D. Byram, A. S. Caldwell, Y.-D. Chan, C. D. Christofferson, P.-H. Chu, C. Cuesta*, J. A. Detwiler, P. J. Doe, C. Dunagan, Yu. Efremenko, H. Ejiri, S. R. Elliott, Z. Fu, A. Galindo-Uribarri, G. K. Giovanetti, J. Goett, M. P. Green, J. Gruszko, I. S. Guinn, V. E. Guiseppe, R. Henning, E. W. Hoppe, S. Howard, M. A. Howe, B. R. Jasinski, K. J. Keeter, M. F. Kidd, S. I. Konovalov, R. T. Kouzes, B. D. LaFerriere, J. Leon, A. Lia, J. MacMullin, R. D. Martin, R. Massarczyk, S. Meijer, S. Mertens, J. L. Orrell, C. O'Shaughnessy, A. W. P. Poon, D. C. Radford, J. Rager, K. Rielage, R. G. H. Robertson, E. Romero-Romero, B. Shanks, M. Shirchenko, N. Snyder, A. M. Suriano, D. Tedeschi, A. Thompson, K. T. Ton, J. E. Trimble, R. L. Varner, S. Vasilyev, K. Vetter, K. Vorren, B. R. White, J. F. Wilkerson, C. Wiseman, W. Xu, E. Yakushev, C.-H. Yu, and V. Yumatov, Nucl. Inst. Meth. Phys. Res. A **823**, 83 (2016).†

26. "A Search for Electron Antineutrinos Associated with Gravitational-wave Events GW150914 and GW151226 Using KamLAND," A. Gando, Y. Gando, T. Hachiya, A. Hayashi, S. Hayashida, H. Ikeda, K. Inoue, K. Ishidoshiro, Y. Karino, M. Koga, S. Matsuda, T. Mitsui, K. Nakamura, S. Obara, T. Oura, H. Ozaki, I. Shimizu, Y. Shirahata, J. Shirai, A. Suzuki, T. Takai, K. Tamae, Y. Teraoka, K. Ueshima, H. Watanabe, A. Kozolov, Y. Takemoto, S. Yoshida, K. Fushimi, A. Piepke, T. I. Banks, B. E. Berger, B. K. Fujikawa, T. O'Donnell, J. G. Learned, J. Maricic, M. Sakai, L. A. Winslow, E. Krupczak, J. Ouellet, Y. Efremenko, H. J. Karwowski, D. M. Markoff, W. Tornow, J. A. Detwiler, S. Enomoto, and M. P. Decowski, Astrophys. J. Lett., **829**, L34 (2016).

An * denotes a CENPA author who is the lead author of or major contributor to a publication.
A † denotes a publication describing work fully or partially supported by the DOE grant.

27. "Search for Majorana Neutrinos near the Inverted Mass Hierarchy region with KamLAND-Zen," A. Gando, Y. Gando, T. Hachiya, A. Hayashi, S. Hayashida, H. Ikeda, K. Inoue, K. Ishidoshiro, Y. Karino, M. Koga, S. Matsuda, T. Mitsui, K. Nakamura, S. Obara, T. Oura, H. Ozaki, I. Shimizu, Y. Shirahata, J. Shirai, A. Suzuki, T. Takai, K. Tamae, Y. Teraoka, K. Ueshima, H. Watanabe, A. Kozolov, Y. Takemoto, S. Yoshida, K. Fushimi, T. I. Banks, B. E. Berger, B. K. Fujikawa, T. O'Donnell, L. A. Winslow, Y. Efremenko, H. J. Karwowski, D. M. Markoff, W. Tornow, J. A. Detwiler, S. Enomoto, and M. P. Decowski, Editor's Suggestion, Phys. Rev. Lett. **117**, 082503; Publisher's Note: Phys Rev. Lett. **117**, 109903 (2016).

28. "Commissioning of the vacuum system of the KATRIN Main Spectrometer," M. Arenz, M. Babutzka, M. Bahr, J. P. Barrett, S. Bauer, M. Beck, A. Beglarian, J. Behrens, T. Bergmann, U. Besserer, J. Blümer, L. I. Bodine, K. Bokeloh, J. Bonn, B. Bornschein, L. Bornschein, S. Büsch, T. H. Burritt, S. Chilingaryan, T. J. Corona, L. De Viveiros, P. J. Doe, O. Dragoun, G. Drexlin, S. Dyba, S. Ebenhöch, K. Eitel, E. Ellinger, S. Enomoto, M. Erhard, D. Eversheim, M. Fedkevych, A. Felden, S. Fischer, J. A. Formaggio, F. Fränkle, D. Furse, M. Ghilea, W. Gil, F. Glück, A. Gonzalez Urena, S. Görhardt, S. Groh, S. Grohmann, R. Grössle, R. Gumbsheimer, M. Hackenjos, V. Hannen, F. Harms, N. Haussmann, F. Heizmann, K. Helbing, W. Herz, S. Hickford, D. Hilk, B. Hillen, T. Höhn, B. Holzapfel, M. Hötzel, M. A. Howe, A. Huber, A. Jansen, N. Kernert, L. Kippenbrock, M. Kleesiek, M. Klein, A. Kopmann, A. Kosmider, A. Kovalk, B. Krasch, M. Kraus, H. Krause, M. Krause, L. Kuckert, B. Kuffner, L. La Cascio, O. Lebeda, B. Leiber, J. Letnev, V. M. Lobashev, A. Lokhov, E. Malcherek, M. Mark, E. L. Martin, S. Mertens, S. Mirz, B. Monreal, K. Müller, M. Neuberger, H. Neumann, S. Niemes, M. Noe, N. S. Oblath, A. Off, H.-W. Ortjohann, A. Osipowicz, E. Otten, D. S. Parno, P. Plischke, A. W. P. Poon, M. Prall, F. Priester, P. C.-O. Ranitzsch, J. Reich, O. Rest, R. G. H. Robertson, M. Röllig, S. Rosendahl, S. Rupp, M. Rysavy, K. Schlösser, M. Schlösser, K. Schönung, M. Schrank, J. Schwarz, W. Seiler, H. Seitz-Moskaliuk, J. Sentkerestiova, A. Skasyrskaya, M. Slezak, A. Spalek, M. Steidl, N. Steinbrink, M. Sturm, M. Suesser, H. H. Telle, T. Thümmler, N. Titov, I. Tkachev, N. Trost, A. Unru, K. Valerius, D. Venos, R. Vianden, S. Vöcking, B. L. Wall, N. Wandkowsky, M. Weber, C. Weinheimer, C. Weiss, S. Welte, J. Wendel, K. L. Wierman, J. F. Wilkerson, D. Winzen, J. Wolf, S. Wüstling, M. Zacher, S. Zadoroghny, M. Zboril, JINST **11**, P04011 (2016).**†**

9.2 Invited talks at conferences

1. "Direct Nuclear Probes of Neutrino Mass," D. S. Parno*****, Invited talk, APS April Meeting, Salt Lake City, UT, April, 2016.**†**

An ***** denotes a CENPA author who is the lead author of or major contributor to a publication.
A **†** denotes a publication describing work fully or partially supported by the DOE grant.

2. "Present status and future experiments in fundamental muon physics, Physics of Fundamental Symmetries and Interactions," D. W. Hertzog*, Invited talk, PSI2016, Villigen, Switzerland, October 16-20, 2016.†

3. "Frequency-based decay electron spectroscopy to probe the neutrino mass scale and chirality-flipping interactions," M. Fertl *, Invited talk, Physics of fundamental Symmetries and Interactions – PSI2016, PSI, Villigen, Switzerland, October, 2016.†

4. "Clocks to weigh Beyond Standard Model Physics: Muon g-2 and the Neutrino Mass Scale," M. Fertl*, Invited Semniar, Metrology Group Seminar, Laboratoire Kaster Brossel, Paris, France, October, 2016.†

5. "Weighing Beyond Standard Model Physics with Neutrinos," M. Fertl*, Physics Colloquium, University of Kentucky, Lexington, KY, USA , September, 2016.†

6. "Project 8: Towards cyclotron radiation emission spectroscopy of tritium", M. Fertl*, Invited talk, Determination of the absolute electron (anti)-neutrino mass, ECT*, Trento, Italy, April, 2016.†

7. "Using Cyclotron Radiation Spectroscopy to search for chirality-flipping interactions," A. García*, Invited talk at Workshop on Neutrinos in Nuclear Physics, Knoxville, July 29-31, 2016.†

8. "Direct Neutrino Mass Measurement with KATRIN" S. Enomoto*, Invited talk at the International Workshop on "Double Beta Decay and Underground Science" (DBD16), Osaka University, Osaka, Japan, November 8-10, 2016.

9. "Results from the Project 8 phase-1 cyclotron radiation emission spectroscopy detector." A. Ashtari Esfahani, S. Böser, C. Claessens, L. de Viveiros, P. J. Doe, S. Doeleman, M. Fertl, E. C. Finn, J. A. Formaggio, M. Guigue, K. M. Heeger, A. M. Jones, K. Kazkaz, B. H. LaRoque, E. Machado, B. Monreal, J. A. Nikkel, N. S. Oblath, R. G. H. Robertson, L. J. Rosenberg, G. Rybka, L. Saldaña, P. L. Slocum, J. R. Tedeschi, T. Thümmler, B. A. VanDevender, M. Wachtendonk, J. Weintroub, A. Young, and E. Zayas. In *Proceedings of Neutrino 2016, XXVII International Conference on Neutrino Physics and Astrophysics*, 2016; arXiv:1703.05760.†

10. "Project 8 detector upgrades for a tritium beta decay spectrum using cyclotron radiation." A. Ashtari Esfahani, S. Böser, C. Claessens, L. de Viveiros, P. J. Doe, S. Doeleman, M. Fertl, E. C. Finn, J. A. Formaggio, M. Guigue, K. M. Heeger, A. M. Jones, K. Kazkaz, B. H. LaRoque, E. Machado, B. Monreal, J. A. Nikkel, N. S. Oblath, R. G. H. Robertson, L. J. Rosenberg, G. Rybka, L. Saldaña, P. L. Slocum, J. R. Tedeschi, T. Thümmler, B. A. VanDevender, M. Wachtendonk, J. Weintroub, A. Young, and E. Zayas. In *Proceedings of Neutrino 2016, XXVII International Conference on Neutrino Physics and Astrophysics*, 2016; arXiv:1703.05761.†

An * denotes a CENPA author who is the lead author of or major contributor to a publication.
A † denotes a publication describing work fully or partially supported by the DOE grant.

11. "Project 8 phase III concept and design." A. Ashtari Esfahani, S. Böser, C. Claessens, L. de Viveiros, P. J. Doe, S. Doeleman, M. Fertl, E. C. Finn, J. A. Formaggio, M. Guigue, K. M. Heeger, A. M. Jones, K. Kazkaz, B. H. LaRoque, E. Machado, B. Monreal, J. A. Nikkel, N. S. Oblath, R. G. H. Robertson, L. J. Rosenberg, G. Rybka, L. Saldaña, P. L. Slocum, J. R. Tedeschi, T. Thümmler, B. A. VanDevender, M. Wachtendonk, J. Weintroub, A. Young, and E. Zayas. In *Proceedings of Neutrino 2016, XXVII International Conference on Neutrino Physics and Astrophysics*, 2016.†

12. "Progress toward measuring the mass of the neutrino," R. G. H. Robertson*, Colloquium, Oregon State University, Corvallis, OR, April 4, 2016.

13. "The Sun shines brightest at night: Reflections on the solar neutrino problem," R. G. H. Robertson*, Invited talk, APS April Meeting, Salt Lake City, UT April 16-19, 2016.

14. "The Sun shines brightest at night: Reflections on the solar neutrino problem," R. G. H. Robertson*, Invited talk, APS Northwest Section Meeting, Penticton, BC May 13-14, 2016.

15. "The Sun shines brightest at night: Reflections on the solar neutrino problem," R. G. H. Robertson*, Kemper Colloquium, Florida State University, Tallahassee, FL, September 29, 2016.

16. "Progress toward a direct measurement of the mass of the neutrino," R. G. H. Robertson*, Invited talk, International symposium on parity violation and neutrino physics (Inauguration of the T.D. Lee Institute); Shanghai, China, November 28-29, 2016.

17. "Progress toward a direct measurement of the mass of the neutrino," R. G. H. Robertson*, Invited talk, Neutrino Symposium: a Gerry Garvey Festschrift, Seattle, WA, December 10, 2016.

18. "Project 8: towards a direct measurement of the mass of the neutrino," R. G. H. Robertson*, Invited talk, Lake Louise Winter Institute, Lake Louise, AB, February 19-25, 2017.

19. "Electron Detection for KATRIN," D. S. Parno*, Invited talk at the Determination of the Absolute Electron (Anti)-Neutrino Mass workshop, ECT*, Trento, Italy, April 2016.†

20. "Direct Measurements of Neutrino Mass," D. S. Parno*, Invited talk at Symmetry Tests in Nuclei and Atoms, Kavli Institute for Theoretical Physics, Santa Barbara, California, September 2016.†

An * denotes a CENPA author who is the lead author of or major contributor to a publication.
A † denotes a publication describing work fully or partially supported by the DOE grant.

21. "The Majorana Demonstrator Neutrinoless Double-Beta Decay Search," J. A. Detwiler*, Center for Neutrino Physics Seminar, Virginia Polytechnic Institute and State University, March 2017.†

22. "2β or Not 2β: Majorana Neutrinos, Grand Unification, and the Existence of the Universe," J. A. Detwiler*, Physics Department Colloquium, University of Washington, November 2016.†

23. "Status and Initial Results from the Majorana Demonstrator," J. A. Detwiler*, Invited talk, 2016 Fall Meeting of the APS Division of Nuclear Physics, Vancouver, BC, Canada, October 2016.†

24. "Double-Beta Decay Experiments with ^{76}Ge," J. A. Detwiler*, Invited talk, International Workshop on Neutrino-Nuclear Responses for Double Beta Decays and Astro-Neutrino Interactions (NNR16), Osaka University, Osaka, Japan, September 2016.†

25. "^{76}Ge Double Beta Decay in Context," J. A. Detwiler*, Invited talk, Meeting on the Next Generation ^{76}Ge Experiment, Munich, Germany, April 2016.†

26. "Latest Results from KamLAND-Zen," SLAC Experimental Seminar, SLAC National Accelerator Laboratory, August, 2016.

9.3 Abstracts and contributed talks

1. "Background Model for the Majorana Demonstrator," C. Cuesta* on behalf of the Majorana Collaboration, XXVII Conference on Neutrino Physics and Astrophysics (Neutrino 2016), London, UK, July, 2016; arXiv:1405.1370.†

2. "Delayed Charge Recovery Discrimination of Passivated Surface Alpha Events in P-type Point-Contact Detectors," J. Gruszko* on behalf of the Majorana Collaboration, XXVII Conference on Neutrino Physics and Astrophysics (Neutrino 2016), London, UK, July, 2016; arXiv:1610.03054.†

3. "Environmental gamma radiation in the KATRIN Spectrometer Hall," L. Kippenbrock*, APS April Meeting 2016, Salt Lake City, UT, April, 2016.†

4. "Project 8: Towards cyclotron radiation emission spectroscopy of tritium," M. Fertl*, April Meeting of the American Physical Society, Washington D.C., USA, January, 2017.†

5. "Project 8: Towards cyclotron radiation emission spectroscopy of tritium," M. Fertl*, April Meeting of the American Physical Society, Salt Lake City, UT, USA, April, 2016.†

An * denotes a CENPA author who is the lead author of or major contributor to a publication.
A † denotes a publication describing work fully or partially supported by the DOE grant.

6. “Measurement of the electron shake-off in the β-decay of laser-trapped ^{6}He atoms,” R. Hong*, Y. Bagdasarova, A. García, D. W. Storm, M. G. Sternberg, H. E. Swanson, F. Wauters, D. W. Zumwalt, K. Bailey, A. Leredde, P. Müller, T. O’Connor, X. Fléchard, E. Liénard, A. Knecht, O. Naviliat-Cuncic, Contributed talk, April Meeting of The American Physical Society.†

7. “Production and trapping efficiency improvements for the He-6 experiment,” Y. Bagdasarova*, A. García, J. Pedersen, E. Smith, D. W. Storm, H. E. Swanson, K. Bailey, R. Hong, A. Leredde, P. Müller, T. O’Connor, X. Fléchard, E. Liénard, A. Knecht, O. Naviliat-Cuncic, F. Wauters, Contributed talk, 2016 Fall Meeting of the APS Division of Nuclear Physics, Vancouver, BC, Canada.†

8. “Searches for chirality-flipping interactions via cyclotron-radiation spectroscopy,” A. García*, M. Fertl, M. Guigue, P. Kammel, A. Leredde, P. Müller, R. G. H. Robertson, G. Rybka, G. Savard, H. E. Swanson, B. A. Vandevender, A. Young, Contributed talk, 2016 Fall Meeting of the APS Division of Nuclear Physics, Vancouver, BC, Canada.†

9. “Upgrades for the Project 8 Phase II Apparatus,” W. Pettus* on behalf of the Project 8 Collaboration, October, 2016, Fall Meeting of the APS Division of Nuclear Physics, Vancouver, BC, Canada.†

10. “Achieving a Precision Field in the Muon Storage Ring Magnet at Fermilab,” Erik Swanson* on behalf of The Muon g-2 Collaboration, October, 2016, Fall Meeting of the APS Division of Nuclear Physics, Vancouver, BC, Canada.†

11. “Background Model for the MAJORANA DEMONSTRATOR,” C. Cuesta*, N. Abgrall, I. J. Arnquist, I. J. , F. T. Avignone III, A. S. Barabash, F. E. Bertrand, A. W. Bradley, V. Brudanin, M. Busch, M. Buuck, A. S. Caldwell, Y.-D. Chan, C. D. Christofferson, P.-H. Chu, J. A. Detwiler, C. Dunagan, Yu. Efremenko, H. Ejiri, S. R. Elliott, A. Fullmer, A. Galindo-Uribarri, T. Gilliss, G. K. Giovanetti, M. P. Green, J. Gruszko, I. S. Guinn, V. E. Guiseppe, R. Henning, E. W. Hoppe, M. A. Howe, B. R. Jasinski, K. J. Keeter, M. F. Kidd, S. I. Konovalov, R. T. Kouzes, J. Leon, A. M. Lopez, J. MacMullin, R. D. Martin, R. Massarczyk, S. J. Meijer, S. Mertens, J. L. Orrell, C. O’Shaughnessy, A. W. P. Poon, D. C. Radford, J. Rager, K. Rielage, R. G. H. Robertson, E. Romero-Romero, B. Shanks, M. Shirchenko, A. M. Suriano, D. Tedeschi, J. E. Trimble, R. L. Varner, S. Vasilyev, K. Vetter, K. Vorren, B. R. White, J. F. Wilkerson, C. Wiseman, W. Xu, E. Yakushev, C.-H. Yu, V. Yumatov, and I. Zhitnikov, Proceedings of the XXVVII International Conference on Neutrino Physics and Astrophysics, Submitted to J. Phys.: Conf.; arXiv: 1610.01146†

12. “The Muon g-2 Experiment at Fermilab,”Chris Polly and Erik Swanson* behalf of The Muon g-2 Collaboration, August, 2016, ICHEP, Chicago IL.†

An * denotes a CENPA author who is the lead author of or major contributor to a publication.
A † denotes a publication describing work fully or partially supported by the DOE grant.

13. "TRIMS: Validating T_2 Molecular Effects for Neutrino Mass Experiments," Y.-T. Lin*, January, 2017, APS April Meeting 2017, Marriott Wardman Park, Washington, DC.†

14. "Initial Results from the MAJORANA DEMONSTRATOR," S. R. Elliott, N. Abgrall, I. J. Arnquist, I. J. , F. T. Avignone III, A. S. Barabash, F. E. Bertrand, A. W. Bradley, V. Brudanin, M. Busch, M. Buuck, A. S. Caldwell, Y.-D. Chan, C. D. Christofferson, P.-H. Chu, C. Cuesta, J. A. Detwiler, C. Dunagan, Yu. Efremenko, H. Ejiri, A. Fullmer, A. Galindo-Uribarri, T. Gilliss, G. K. Giovanetti, M. P. Green, J. Gruszko, I. S. Guinn, V. E. Guiseppe, R. Henning, E. W. Hoppe, M. A. Howe, B. R. Jasinski, K. J. Keeter, M. F. Kidd, S. I. Konovalov, R. T. Kouzes, J. Leon, A. M. Lopez, J. MacMullin, R. D. Martin, R. Massarczyk, S. J. Meijer, S. Mertens, J. L. Orrell, C. O'Shaughnessy, A. W. P. Poon, D. C. Radford, J. Rager, K. Rielage, R. G. H. Robertson, E. Romero-Romero, B. Shanks, M. Shirchenko, A. M. Suriano, D. Tedeschi, J. E. Trimble, R. L. Varner, S. Vasilyev, K. Vetter, K. Vorren, B. R. White, J. F. Wilkerson, C. Wiseman, W. Xu, E. Yakushev, C.-H. Yu, V. Yumatov, and I. Zhitnikov, Proceedings of the XXVVII International Conference on Neutrino Physics and Astrophysics, Submitted to J. Phys.: Conf.; arXiv: 1610.01210†

15. "Comparison of MAJORANA DEMONSTRATOR calibration data with simulation," Z. Fu* on behalf of the MAJORANA Collaboration, October, 2016, Fall Meeting of the APS Division of Nuclear Physics, Vancouver, BC, Canada.†

16. "Delayed charge recovery discrimination of passivated surface alpha events in P-type point-contact detectors," J. Gruszko*, N. Abgrall, I. J. Arnquist, I. J. , F. T. Avignone III, A. S. Barabash, F. E. Bertrand, A. W. Bradley, V. Brudanin, M. Busch, M. Buuck, A. S. Caldwell, Y.-D. Chan, C. D. Christofferson, P.-H. Chu, C. Cuesta, J. A. Detwiler, C. Dunagan, Yu. Efremenko, H. Ejiri, S. R. Elliott, A. Fullmer, A. Galindo-Uribarri, T. Gilliss, G. K. Giovanetti, M. P. Green, I. S. Guinn, V. E. Guiseppe, R. Henning, E. W. Hoppe, M. A. Howe, B. R. Jasinski, K. J. Keeter, M. F. Kidd, S. I. Konovalov, R. T. Kouzes, J. Leon, A. M. Lopez, J. MacMullin, R. D. Martin, R. Massarczyk, S. J. Meijer, S. Mertens, J. L. Orrell, C. O'Shaughnessy, A. W. P. Poon, D. C. Radford, J. Rager, K. Rielage, R. G. H. Robertson, E. Romero-Romero, B. Shanks, M. Shirchenko, A. M. Suriano, D. Tedeschi, J. E. Trimble, R. L. Varner, S. Vasilyev, K. Vetter, K. Vorren, B. R. White, J. F. Wilkerson, C. Wiseman, W. Xu, E. Yakushev, C.-H. Yu, V. Yumatov, and I. Zhitnikov, Proceedings of the XXVVII International Conference on Neutrino Physics and Astrophysics, Submitted to J. Phys.: Conf.; arXiv: 1610.03054†

17. "Precision energy measurement using the MAJORANA DEMONSTRATOR" I. Guinn* on behalf of the MAJORANA Collaboration, October, 2016, 2016 Fall Meering of the APS Division of Nuclear Physics, Vancouver, British Columbia, Canada.†

An * denotes a CENPA author who is the lead author of or major contributor to a publication.
A † denotes a publication describing work fully or partially supported by the DOE grant.

18. “Delayed charge recovery discrimination of passivated surface alpha events in P-type point-contact detectors,” J. Gruszko* on behalf of the MAJORANA Collaboration, July, 2016, XXVII International Conference on Neutrino Physics and Astrophysics, London, England.†

19. “A Waveform Library Technique for Multi-Site Identification with the MAJORANA DEMONSTRATOR,” M. Buuck* on behalf of the MAJORANA Collaboration, January, 2017, American Physical Society April Meeting 2017, Washington Marriott Wardman Park, Washington, DC.†

20. “A Single-Site Pulse Basis Technique for Multi-Site Event Tagging with the MAJORANA DEMONSTRATOR,” M. Buuck* on behalf of the MAJORANA Collaboration, July, 2016, National Nuclear Physics Summer School 2016, Massachusetts Institute of Technology, Cambridge, MA.†

21. “The MuSun experiment: first analysis of production data,” R. Ryan* on behalf of the MuSun collaboration, October, 2016, Conference on Physics of Fundamental Symmetries and Interactions (PSI2016), Paul Scherrer Institut, Switzerland.

9.4 Papers submitted or to be published

1. “Charge-state distribution of Li ions from the β decay of laser-trapped ^{6}He atoms,” R. Hong*, A. Leredde, Y. Bagdasarova, X. Fléchard, A. García*, A. Knecht, P. Müller, O. Naviliat-Cuncic, J. Pedersen, E. Smith, M. G. Sternberg, D. W. Storm, H. E. Swanson, F. Wauters, D. W. Zumwalt, arXiv:1703.07052 [nucl-ex]. Submitted to Phys. Rev. C.†

2. “Muon Flux Measurements at the Davis Campus of the Sanford Underground Research Facility with the Majorana Demonstrator Veto System,” N. Abgrall, E. Aguayo, F. T. Avignone III, A. S. Barabash, F. E. Bertrand, A. W. Bradley, V. Brudanin, M. Busch, M. Buuck, D. Byram, A. S. Caldwell, Y.-D. Chan, C. D. Christofferson, P.-H. Chu, C. Cuesta, J. A. Detwiler, C. Dunagan, Yu. Efremenko, H. Ejiri, S. R. Elliott, A. Galindo-Uribarri, T. Gilliss, G. K. Giovanetti, J. Goett, M. P. Green, J. Gruszko, I. S. Guinn, V. E. Guiseppe, R. Henning, E. W. Hoppe, S. Howard, M. A. Howe, B. R. Jasinski, K. J. Keeter, M. F. Kidd, S. I. Konovalov, R. T. Kouzes, B. D. LaFerriere, J. Leon, A. M. Lopez, J. MacMullin, R. D. Martin, R. Massarczyk, S. J. Meijer, S. Mertens, J. L. Orrell, C. O’Shaughnessy, N. R. Overman, A. W. P. Poon, D. C. Radford, J. Rager, K. Rielage, R. G. H. Robertson, E. Romero-Romero, M. C. Ronquest, C. Schmitt, B. Shanks, M. Shirchenko, N. Snyder, A. M. Suriano, D. Tedeschi, J. E. Trimble, R. L. Varner, S. Vasilyev, K. Vetter, K. Vorren, B. R. White, J. F. Wilkerson, C. Wiseman, W. Xu, E. Yakushev, C.-H. Yu, V. Yumatov, and I. Zhitnikov, arXiv:1602.07742 [nucl-ex], to appear in Astropart. Phys. (2017).†

An * denotes a CENPA author who is the lead author of or major contributor to a publication.
A † denotes a publication describing work fully or partially supported by the DOE grant.

3. "New limits on bosonic dark matter, solar axions, Pauli Exclusion Principle violation, and electron decay from the low-energy spectrum of the MAJORANA DEMONSTRATOR," N. Abgrall, I. J. Arnquist, I. J. , F. T. Avignone III, A. S. Barabash, F. E. Bertrand, A. W. Bradley, V. Brudanin, M. Busch, M. Buuck, A. S. Caldwell, Y. Chan, C. D. Christofferson, P.-H. Chu, C. Cuesta, J. A. Detwiler, C. Dunagan, Yu. Efremenko, H. Ejiri, S. R. Elliott, T. Gilliss, G. K. Giovanetti, J. Goett, M. P. Green, J. Gruszko, I. S. Guinn, V. E. Guiseppe, C. R. Haufe, R. Henning, E. W. Hoppe, S. Howard, M. A. Howe, B. R. Jasinski, K. J. Keeter, M. F. Kidd, S. I. Konovalov, R. T. Kouzes, A. M. Lopez, J. MacMullin, R. D. Martin, R. Massarczyk, S. J. Meijer, S. Mertens, C. O'Shaughnessy, A. W. P. Poon, D. C. Radford, J. Rager, A. Reine, K. Rielage, R. G. H. Robertson, B. Shanks, M. Shirchenko, A. M. Suriano, D. Tedeschi, J. E. Trimble, R. L. Varner, S. Vasilyev, K. Vetter, K. Vorren, B. R. White, J. F. Wilkerson, C. Wiseman, W. Xu, C.-H. Yu, V. Yumatov, I. Zhitnikov, and B X. Zhu, arXiv:1612.00886 [nucl-ex], to appear in PRL.†

4. "The MAJORANA DEMONSTRATOR calibration system," N. Abgrall, I. J. Arnquist, I. J. , F. T. Avignone III, A. S. Barabash, F. E. Bertrand, M. Boswell, A. W. Bradley, V. Brudanin, M. Busch, M. Buuck, A. S. Caldwell, C. D. Christofferson, P.-H. Chu, C. Cuesta, J. A. Detwiler, C. Dunagan, Yu. Efremenko, H. Ejiri, S. R. Elliott, Z. Fu, V. M. Gehman, T. Gilliss, G. K. Giovanetti, J. Goett, M. P. Green, J. Gruszko, I. S. Guinn, V. E. Guiseppe, C. R. Haufe, R. Henning, E. W. Hoppe, M. A. Howe, B. R. Jasinski, K. J. Keeter, M. F. Kidd, S. I. Konovalov, R. T. Kouzes, A. M. Lopez, J. MacMullin, R. D. Martin, R. Massarczyk, S. J. Meijer, S. Mertens, J. L. Orrell, C. O'Shaughnessy, A. W. P. Poon, D. C. Radford, J. Rager, A. Reine, K. Rielage, R. G. H. Robertson, B. Shanks, M. Shirchenko, A. M. Suriano, D. Tedeschi, J. E. Trimble, R. L. Varner, S. Vasilyev, K. Vetter, K. Vorren, B. R. White, J. F. Wilkerson, C. Wiseman, W. Xu, C.-H. Yu, V. Yumatov, I. Zhitnikov, and B X. Zhu, arXiv:1702.02466 [physics], submitted to Nucl. Inst. Meth. Phys. Res. A.†

9.5 Reports and white papers

1. "Nuclear Physics Exascale Requirements Review Report," J. Carlson, M. J. Savage, R. Gerber, J. Osborn, K. Riley, T. Straatsma, J. Wells, G. Fuller, B. Messer, A. Boehnlein, J A. Detwiler, P. Mantica, J. Porter, W. Nazarewicz, R. Edwards, P. Petreczky, M. Strickland, K. Antypas, T. Barnes, C. Lauzon, M. Fitzpatrick, A. Manning, M. Nelson, Vi. Skonicki, B. Cerny, and R. Coffey, US DOE NP/ASCR Meeting Report (2017).

An * denotes a CENPA author who is the lead author of or major contributor to a publication.
A † denotes a publication describing work fully or partially supported by the DOE grant.

9.6 Master's degrees granted

Measurement of Alpha Decay from Radon-222 emanated from Radium-226 contaminated Barite Pipe Scale, Diana Thompson, (October, 2016).

Active Vibration Isolation Systems, Kerkira Stockton, (March, 2017).

9.7 Ph.D. degrees granted

A search for hep solar neutrinos at the Sudbury Neutrino Observatory, Tim Winchester (August, 2016).

A Piezoelectrically Tuned RF-Cavity Search for Dark Matter Axions, Christian Boutan (February, 2017).

Muon-Catalyzed Fusion Effects in the Precision Measurement of Muon Capture on the Deuteron, Michael Murray (March, 2017).

An * denotes a CENPA author who is the lead author of or major contributor to a publication.
A † denotes a publication describing work fully or partially supported by the DOE grant.

BACK ROW: John Lee, Zhenghao Fu, Ethan Muldoon, Seth Kimes, Sean Fell, Erik Lentz, Martin Fertl, David Hyde, Jim Elms, Walter Pettus, Matthias Smith, Samuel Sexton, Joshua Oppor, Peter Doe, Ian Guinn, Nick Force

SECOND-TO-BACK ROW: Alejandro Garcia, Kim Siang Khaw, Krishna Venkateswara, Raphael Cervantes, Ting Lin, Nick Du, Eric Machado, Ali Ashtari Esfahani, Luke Kippenbrock, Henry Gorrell, Celia Chor, Nathan Froemming, Richard Ottens

SITTING (chairs): Jens Gundlach, Doug Will, Erik Swanson, Gerald Garvey, David Hertzog, Hamish Robertson, John Cramer, John Amsbaugh, Eric Smith, Gary Holman, David Peterson, Duncan Prindle, Derek Storm, Ida Boeckstiegel

SITTING (ground): Michael Ross, Rakshya Khatiwada, Charles Hagedorn, Jason Detwiler, Daniel Salvat, Peter Kammel, Rachel Ryan, Julieta Gruszko, Erik Shaw, Brett Hamre, Matthew Kallander, Micah Buuck, Brynn MacCoy